Modeling and Control of Robotics-assisted Needle Steering in Soft Tissue

by

Seyed Mohsen Khadem

A thesis submitted in partial fulfillment of the requirements for the degree of

Doctor of Philosophy

in

Biomedical Engineering

Department of Electrical and Computer Engineering
University of Alberta

Abstract

Percutaneous needle insertion is a common type of minimally invasive surgery used for diagnostic and therapeutic applications such as biopsy, drug delivery, and cancer treatment. Prostate brachytherapy is a needle-based intervention, which is used for cancer treatment. In brachytherapy the surgeon inserts a needle into a patient's body such that radioactive seeds pre-loaded in the needles can be placed in or near the tumor, where radiation released from the seeds kills the cancer cells. Efficiency of needle-based interventions highly depends on accurate control of the needle tip trajectory. For instance, mean targeting accuracy of current techniques used in brachytherapy is 5 mm, which is a relatively large inaccuracy as the average prostate is about 50 mm in diameter. Autonomous or semi-autonomous needle adjustment systems can be used to control the needle tip trajectory and enhance needle insertion accuracy.

This dissertation explores the modeling and control of robotics-assisted needle steering with the aim of enhancing the performance of needle-based interventions. This dissertation's main theme is to deploy a medical robot system with minimal modification to clinical settings. Prostate brachytherapy is studied as an example of needle-based interventions. Robotics-assisted needle steering strategies are proposed that can reduce needle targeting error in various clinical scenarios in prostate brachytherapy, which will benefit the individual patient, the surgeon, and the health-care system in the long run.

Modeling the needle deflection and its interaction with soft tissue is the first requirement for robotic needle steering. A needle steering model can be used for designing the needle steering controller or estimating the needle/tissue system states that are not observable using 2D imaging modalities. In this research, several needle steering models are proposed that can predict needle deflection in soft tissue as a function of needle steering control inputs such as insertion velocity and needle axial rotation. The models are also capable of estimating needle steering states such as needle shape or needle tip orientation in soft tissue, thus enabling applications in motion planning and real-time control of needle steering.

The models are implemented for 2D and 3D needle steering, as well as fully automatic and semi-automated needle steering. In the fully automated needle steering the robot

controls all the steering actions. In the semi-automated needle steering the robotic device shares the needle steering control inputs with the surgeon in the interest of ensuring the safety of the operation. Experimental results on synthetic and ex-vivo tissue samples demonstrate that the proposed strategies can significantly reduce needle targeting error in various scenarios in prostate brachytherapy. We also demonstrate that combining the proposed needle steering strategies with a novel flexible needle proposed in this research, provides new methods of reaching challenging targets to reduce number of conditions that are currently considered untreatable or inoperable.

Preface

The research conducted for this thesis is part of a multidisciplinary research collaboration, led by Dr. Nawaid Usmani and Professor Ron S. Sloboda from the Department of Oncology, University of Alberta, and Professor Mahdi Tavakoli being the lead collaborator at the Department of Electrical and Computer Engineering, University of Alberta.

The main goal of our research is to develop a robotics-assisted needle steering system that can improve the accuracy of needle-based interventions such as prostate brachytherapy. Brachytherapy is a popular treatment for men with early prostate cancer due to its high success rate, minimal side effects, and patient convenience. It involves the insertion of needles loaded with tiny radioactive seeds into the prostate. Once the needles are fully inserted, they are pulled back to permanently leave the seeds in locations inside and around the prostate, where high doses of radiation released from them kill the cancer cells. Accurate seed placement is a key factor that influences the effectiveness of the procedure. We intend to develop a robotic assistance for surgeons that will help them place seeds closer to their intended targets. The core theme of this research collaboration is motivated by the deployment of novel robotic-assisted system with minimal modifications to the current clinical setting. Our research will create a robotics-assisted needle adjustment assistant that will ensure seeds reach their intended targets in an accurate, repeatable and controlled manner.

Fig. 1 provides a flowchart showing high-level organization of this dissertation. This thesis includes: a detailed mechanics-based model of needle steering (Chapter 3), a novel controller that employs the mechanics-based model of needle steering for fully automated needle steering in 2D (Chapter 4), a novel semi-automated needle steering strategy for surgeon-in-the-loop 2D needle steering (Chapter 5), design of a highly flexible steerable needle (notched needle) that improves needles steerability (Chapter 6), and finally a 3D kinematic model of needle steering and two types of nonlinear controllers that employ the kinematic model for 3D fully robotic needle steering in soft tissue (Chapter 7).

This thesis including the literature review, the modeling sections, controller design, and data analysis is an original work by myself, Mohsen Khadem. I was also responsible for

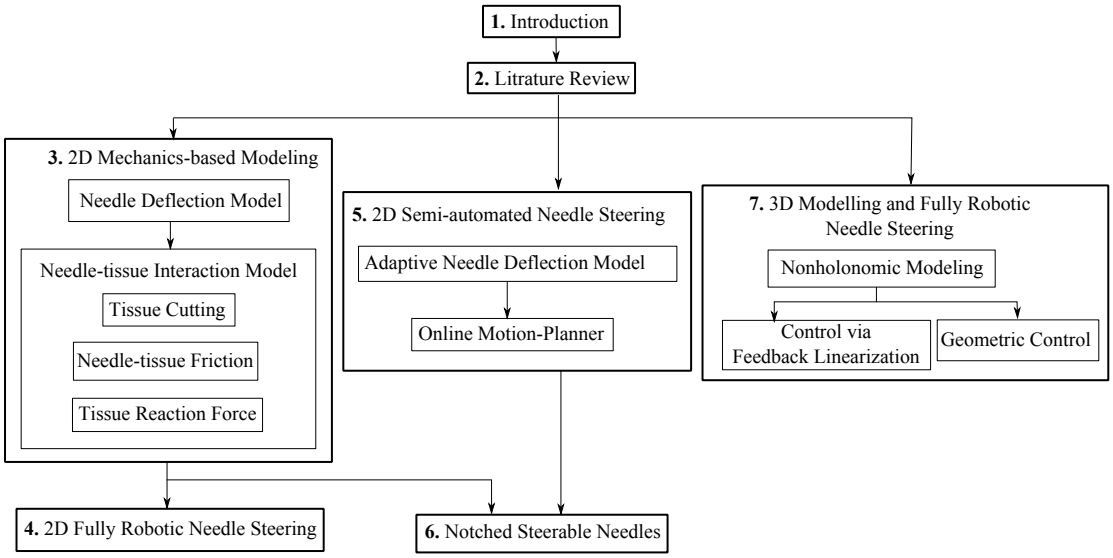

Figure 1: The high-level organization of this thesis. An arrow from one section to another indicates that the former chapter is prerequisite material for understanding the latter.

performing the experiments, the data collection and analysis as well as the manuscript composition. Professor Tavakoli was the supervisory author and was involved with concept formation and manuscript composition.

Parts of Section 3.2 of this thesis has been presented in 2015 IEEE International Conference on Robotics and Automation (ICRA) as M. Khadem, B. Fallahi, C. Rossa, R. S. Sloboda, N. Usmani, and M. Tavakoli, "A mechanics-based model for simulation and control of flexible needle insertion in soft tissue," in 2015 IEEE International Conference on Robotics and Automation (ICRA), 2015, pp. 2264-2269.

Sections 3.2 and 3.5 of this thesis has been published as M. Khadem, C. Rossa, N. Usmani, R. S. Sloboda, and M. Tavakoli, "A Two-Body Rigid/Flexible Model of Needle Steering Dynamics in Soft Tissue," IEEE/ASME Transactions on Mechatronics, vol. 21, pp. 2352-2364, 2016.

Sections 3.3.1 and 3.4 has been published as M. Khadem, C. Rossa, R. S. Sloboda, N. Usmani, and M. Tavakoli, "Mechanics of Tissue Cutting During Needle Insertion in Biological Tissue," IEEE Robotics and Automation Letters, vol. 1, pp. 800-807, 2016.

Chapter 4 has been published as M. Khadem, C. Rossa, R. S. Sloboda, N. Usmani, and

M. Tavakoli, "Ultrasound-Guided Model Predictive Control of Needle Steering in Biological Tissue," Journal of Medical Robotics Research, vol. 01, p. 1640007, 2016.

Chapter 5 has been published as M. Khadem, C. Rossa, N. Usmani, R. S. Sloboda, and M. Tavakoli, "Semi-Automated Needle Steering in Biological Tissue Using an Ultrasound-Based Deflection Predictor," Annals of Biomedical Engineering, pp. 1-15, 2016.

Section 6.2 was presented in 2016 IEEE International Conference on Advanced Intelligent Mechatronics (AIM) as M. Khadem, C. Rossa, N. Usmani, R. S. Sloboda, and M. Tavakoli, "Introducing notched flexible needles with increased deflection curvature in soft tissue," in 2016 IEEE International Conference on Advanced Intelligent Mechatronics (AIM), 2016, pp. 1186-1191.

Chapter 6 of this thesis has been submitted as M. Khadem, C. Rossa, N. Usmani, R. S. Sloboda, and M. Tavakoli, "Notched steerable needles with improved deflection curvature: efficacy in maneuvering around anatomical obstacles," IEEE Journal of Biomedical and Health Informatics, May 2017.

Section 7.3 has been presented in the American Control Conference (ACC) as M. Khadem, C. Rossa, N. Usmani, R. S. Sloboda, and M. Tavakoli, "Feedback-Linearization-based 3D Needle Steering in a Frenet-Serret Frame Using a Reduced Order Bicycle Model," in 2017 American Control Conference (ACC).

Sections 7.2 and 7.4 of this thesis is submitted as M. Khadem, C. Rossa, N. Usmani, R. S. Sloboda, and M. Tavakoli, "Geometric Modeling and Control of 3D Needle Steering," Automatica, April 2017.

The robotic setup referred to in Appendix A was designed by Thomas Lehman and has been published as T. Lehmann, M. Tavakoli, N. Usmani, and R. Sloboda, "Force-sensor based estimation of needle tip deflection in brachytherapy," Journal of Sensors, vol. 2013, p. 10, 2013. The hand-held apparatus referred to in Appendix A was designed by Dr. Carlos Rossa and has been published as C. Rossa, N. Usmani, R. Sloboda, and M. Tavakoli, "A hand-held assistant for semi-automated percutaneous needle steering," IEEE Transactions on Biomedical Engineering, vol 64, no. 3, pp. 637-648, 2016. The image processing algorithm employed in Sections 5.4 and 6.4.2 is developed by Michael Waine

and has been published as M. Waine, C. Rossa, R. Sloboda, and et al., "Needle tracking and deflection prediction for robot-assisted needle insertion using 2d ultrasound images," Journal of Medical Robotics Research, vol. 01, no. 01, p. 1640001, 2016. The image processing algorithm employed in Section 7.4.4 is developed by Jay Carrier and has been published as J. Carriere, C. Rossa, R. Sloboda, N. Usmani and M. Tavakoli, "Real-time needle shape prediction in soft-tissue based on image segmentation and particle filtering," 2016 IEEE International Conference on Advanced Intelligent Mechatronics (AIM), Banff, AB, 2016, pp. 1204-1209.

To my dearest parents

Acknowledgements

This thesis would not have been possible without the help of my supervisors, my research collaborators, and all my teachers at the University of Alberta. First and foremost, I thank my supervisor Professor Mahdi Tavakoli for his help and support. He has supported and encouraged me through my graduate studies with patience and enthusiasm, as well as financial and intellectual support. Without such a mentor, it is highly unlikely that I would have considered an academic career. This thesis would also not have been possible without the help of my co-supervisor Dr. Usmani and my unofficial co-supervisor Professor Sloboda. Their great efforts to explain things clearly and simply have been a source of inspiration for me. I have truly valued the many conversations I have had with each of them and I am grateful for having such excellent mentors.

The majority of the research was based on discussions with Dr. Carlos Rossa. I thank Carlos for all his help and time. He was always accessible and willing to help. I also thank Professor Roger Zemp for agreeing to be a member of my thesis committee. I have been fortunate enough to be part of Telerobotic and Biorobotic Systems (TBS) laboratory. I thank my colleagues at TBS, Thomas Lehmann, Jay Carrier, Bita Fallahi, and Michael Waine, for being so welcoming and helpful.

My doctoral studies would not have been possible without the financial support from the following funding sources: the Natural Sciences and Engineering Research Council (NSERC) of Canada under grant CHRP 446520, the Canadian Institutes of Health Research (CIHR) under grant CPG 127768. the Alberta Innovates - Health Solutions(AIHS) under grant CRIO 201201232, Alberta Innovates - Technology Solutions graduate student fellowship.

Finally, I would like to thank my parents for instilling the importance of a good education very early in life. I am grateful to my parents, my sister, and my brother for their constant encouragement and love.

Table of Contents

List of Tables

List of Figures

Chapter 1

Introduction

1.1 Motivation

Percutaneous needle insertion is a common type of minimally invasive surgery used for diagnostic and therapeutic applications such as biopsy, drug delivery, and cancer treatment. The efficiency of percutaneous needle insertion procedures highly depends on accurate control of the needle trajectory in soft tissue. In needle-based interventions, steerable flexible needles with beveled tips are used to enhance control over needle deflection. A flexible needle with an asymmetric beveled tip has an uneven distribution of forces at the tip, which causes the needle to bend. Using steerable needles, the surgeon can control tip deflection by rotating the needle and changing the orientation of the bevel tip, which causes the needle to bend in a different direction. The term "*needle steering*" implies control of the needle tip deflection as the needle is inserted via inputs such as insertion velocity and axial needle rotation. Considering factors such as tissue heterogeneity, uncertain needle-tissue interaction, inaccurate position sensing, and needle torsion effecting the targeting accuracy and given the limited control the surgeon over the inserted needle when manipulating its base, accurate steering and prediction of the needle tip during manual insertion is difficult.

An example of needle-based interventions is prostate brachytherapy used for cancer treatment. In brachytherapy, long and flexible needles loaded with radioactive seeds are inserted into the prostate, where the seeds are deposited. In the course of several months,

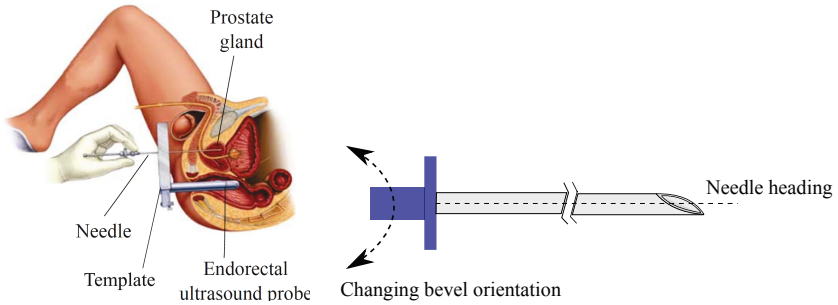

Figure 1.1: (a) A schematic of needle insertion in brachytherapy. The surgeon inserts long flexible needles through the patient's perineum in order to deliver radioactive seeds within the prostate gland. (b) A schematic of flexible needle with an asymmetric beveled tip.

radiation emitted from them will destroy adjacent tumor cells (see Fig. 1.1(a)). Accurate seed placement is a key factor that influences the effectiveness of the procedure. However, current techniques can place seeds with an accuracy of only about 5 mm. This is a substantial error given the average prostate size and narrows the scope of brachytherapy to primarily treating the entire prostate gland for patients with localized prostate cancer. A robotic surgeon's assistant that automatically controls the needle deflection in soft tissue can enhance needle targeting accuracy and help with achieving high quality implants. This will benefit the individual patient and the surgeon. In fact, the benefits of this research improving the accuracy of needle insertions will not only be limited to prostate brachytherapy, but will also be applicable to other procedures that involve precise insertion of needles (e.g., liver ablation, interventional radiology for image guided biopsies).

Fig. 1.2 shows a block diagram of automated needle steering system. Four subsystems that compose the automated closed-loop system are: 1) model of needle/tissue interaction, 2) needle steering controller, 3) sensor for detecting needle tip deflection in soft tissue, and 4) robotic steering device.

Modeling the needle deflection and its interaction with soft tissue is the first requirement for robotic needle steering and surgical planning. A needle steering model can be used for:

1. Designing the needle steering controller. A needle steering model that can be used for designing a controller relates various inputs such as insertion velocity, axial rotation

(bevel location adjustment), needle base lateral position, and needle base force/torque to needle tip deflection in tissue.

2. Estimating needle/tissue system states. The state variables in the needle/soft tissue system (e.g., needle shape or needle tip orientation) are not all measurable physical quantities, and observation of the immeasurable states via a realistic physical model will inform controller development.

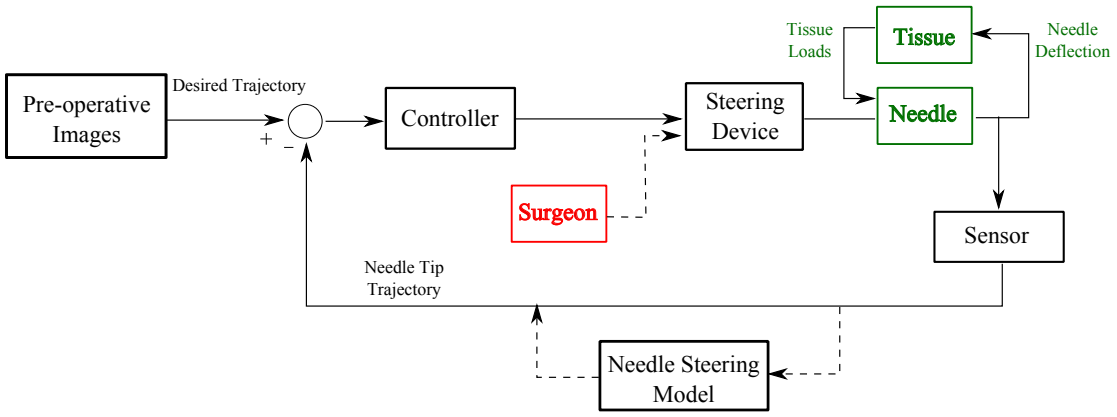

Figure 1.2: Block diagram of feedback control for robotics-assisted needle steering.

The next component of robotic needle steering system is the needle steering controller. Needle steering controllers can be classified based on the the control objective [1]. The first and simplest controller aims at navigating the needle tip to a desired point in tissue, regardless of what trajectory it takes. Applications of this controller are tissue sampling (biopsy) and percutaneous ablation. The second category comprises controllers whose control objective is to minimize the needle deflection at all depths. An example is transperineal prostate brachytherapy where the needle is controlled to follow a path as close as possible to a straight line such that strands of radioactive seeds can be deposited along the insertion path. The last category is the tracking problem, where the needle tip follows a pre-defined trajectory that is not necessarily a straight line. It is typically employed in cases where the needle must be maneuvered to avoid anatomical obstacles such as muscles, bones, or vessels.

It is also possible to categorize the needle steering controller based on the required level of automation. Typically, two main control actions are used to steer the needle in

combination with insertion, namely, axial rotation of the needle and lateral forces applied at the needle base. The needle steering controller can be either fully automated, meaning that the device performs both insertion and steering actions, or semi-automated, where insertion is performed by the surgeon while steering occurs automatically.

Closed-loop feedback control requires real-time measurement of needle deflection. During insertion imaging modalities such as X-ray, fluoroscopy and ultrasound are used to monitor the location of the needle in tissue. Alternative sensors such as optical fibers or force sensors can also be used to measure needle steering system states. The information is then fed back in the controller. Depending on the control approach employed and type of the sensor, state estimation using a needle steering model may also be necessary.

The last component is the needle steering device. The needle steering device can be designed based on the controller type. For fully robotic needle insertion, the robotic systems should be able to automatically insert a needle in tissue and undertake the necessary corrective actions to control its trajectory towards a target. In robotics-assisted needle insertion, the steering device should perform robotic adjustments to one of the aforementioned control inputs (e.g, axial needle rotation) while other inputs are directly applied by the surgeon. A robotic device used for semi-automated needle steering should be capable of sharing the control inputs with a human user.

This dissertation is concerned with implementing and testing a surgeon's assistant system to assess and substantially improve seed placement accuracy. A robotic needle insertion assistant will enable the physician to precisely steer a needle towards its intended location in a controlled manner. The assistant will be used for intraoperative adjustment of needle targets, and for continuous refinement of needle steering strategies. This thesis specifically explores: (1) modeling approaches for the development of a needle steering model, and (2) needle steering controllers for fully automated and semi-automated needle steering, as well as steering on a line and trajectory tracking with obstacle avoidance.

1.2 Dissertation Contributions and Overview

The major contributions of this dissertation are summarized as follows:

- **Mechanics-based Model of Needle Deflection and Fully Automated Needle Steering:** A computationally efficient needle steering model is developed that allows for real-time control of needle tip position in a robotic-assisted needle insertion scheme. The model includes a novel time-delayed tissue model that enables modeling of needle axial rotation during needle insertion. The needle steering model explicitly relates needle deflection to the insertion velocity, insertion force/torque, and axial rotation of needle. Therefore, these parameters can all be used as control commands for closed-loop needle steering. Experimental results demonstrate the ability of the model to describe needle tip position, needle shape, and force/torques at the needle base. Next, we demonstrate the feasibility of using mixed online image feedback and the mechanics-based model predictions for optimal needle steering and increasing targeting accuracy in needle-based interventions. A novel image-guided Model Predictive Controller is developed for fully robotic steering of needles in soft tissue, which can be used to target a specific point or to follow a desired trajectory and maneuver the needle tip around an obstacle.

- **Adaptive Model of Needle Deflection and Semi-automated Needle Steering:** A novel semi-automated strategy for steering needles in soft tissue is proposed, which can be used to target a specific point and maneuver the needle tip around an obstacle. The semi-automated needle steering system has two main components: (1) a real-time predictor for estimating future needle deflection as it is steered inside soft tissue, and (2) an online motion planner that calculates control decisions and steers the needle toward the target by iterative optimization of the needle deflection predictions. The predictor uses the ultrasound-based curvature information to estimate the needle deflection. Ex-vivo needle insertions are performed with and without obstacle to validate our approach. The results demonstrate the performance of the proposed needle steering strategy.

- **Design of Notched Steerable Needles:** A novel type of steerable needle is designed that is capable of achieving high deflection curvatures in soft tissue. The needle is developed by carving small notches on a standard needle shaft. By carving several consecutive notches on the needle shaft, the needle flexural strength and the needle's maximum achievable ROC are decreased. The Finite Element Method is used to model the notched needle deflection in tissue. The model is used with an optimization algorithm to optimize notch geometry and minimize needle ROC. A novel controller is developed and used to perform image-guided closed-loop needle steering experiments on a tissue phantom and demonstrate the feasibility of maneuvering around obstacles inside the tissue using the notched needle. Results show that by improving the needle ROC and its maneuverability we can extend the application of brachytherapy to deeper or more difficult-to-reach targets and enable optimal utilization of brachytherapy for more cancer patients.

- **Geometric Modeling and Control of 3D Needle Steering:** The previously proposed needle steering algorithms can be used for needle steering in a 2D and cannot be employed for trajectory tracking in 3D. Due to many factors such as uncertainty in needle/tissue interactions the needle might bent out of the desired 2D insertion plane. In the last chapter, a 3D automated needle steering system is proposed that can be used for 3D trajectory tracking. The system comprises a nonholonomic needle steering model and nonlinear controllers for 3D needle steering. Two types of controller are developed that employ the notched needles for 3D needle steering: 1) a nonlinear controller that stabilizes a reduced-order version of the nonholonomic model in a Serret-Frenet frame placed on the desired needle trajectory, and 2) a switching controller that inserts the needle up to the desired depth and as close as possible to the desired target location, and later performs a series of retraction and insertion motions that guides the needle toward the desired point. Validation experiments are performed on a phantom and ex-vivo animal tissues and the results are compared with manual needle insertions performed by skilled surgeons. The results demonstrate that the average error of our 3D needle steering system is less than manual needle insertions.

This thesis is organized as follows: Chapter 3 considers the details of the mechanics-based model of needle steering. In Chapter 4 a novel model predictive controller is developed that employs the mechanics-based model of needle steering for fully automated needle steering in 2D. In Chapter 5 the details of the proposed semi-automated needle steering strategy are presented. This includes the derivation of the equations for the adaptive needle deflection predictor, the method proposed for ensuring rapid convergence of the predictions, and the online needle motion planner for steering needle in soft tissue. Chapter 6 describes the design of the notched steerable needles. This chapter includes the development of an FEM model of needle deflection inside soft-tissue, the notched needle's design requirements, an optimization algorithm implemented to estimate the optimal location of the notches on the needle shaft for achieving a desired curvature, and validation of the notched steerable needle in achieving high curvatures in soft tissue and maneuvering around obstacles. Chapter 7 describes the 3D kinematic model of needle steering and design of two types of nonlinear controllers that employ the notched needles for 3D needle steering in soft tissue. We conclude and discuss future work in Chapter 8.

Chapter 2

Literature Review

2.1 Modeling Needle Deflection

Modeling of needle-tissue interaction makes it possible to steer flexible needles from outside the body to reach specified targets inside the body. Needle steering can be achieved using a variety of inputs including axial rotation, lateral base manipulation, and insertion velocity. A needle steering model estimates the needle trajectory inside tissue based on the aforementioned steering inputs, allowing for preoperative path planning and online needle trajectory control.

DiMaio and Salcudean [2], and Goksel *et al.* [3] are among the first researchers who used the Finite Element Method (FEM) to model the needle/tissue interaction in order to find the needle tip position. Alterovitz *et al.* presented a 2D FEM model of needle insertion considering the effect of the tip bevel [4]. Chentanez *et al.* expanded the model into 3D [5].

The simplest and perhaps the most widespread model of needle-tissue interaction is the nonholonomic model first introduced by Park *et al.* [6]. Park *et al.* developed a nonholonomic unicycle-like model to describe how an ideal needle with bevel tip moves through firm tissue. They assumed that the needle tip motion in tissue is constrained to a circular path similar to a unicycle mobile robot. Webster *et al.* extended this idea and developed and experimentally validated a kinematics-based model generalizing the unicycle

model [7]. The model describes the forward motion of beveled-tip needles in tissue as a bicycle with a fixed front wheel angle. A simplified 2-dimensional (2D) version is shown in Fig. 2.1. The model is composed of two hypothetical wheels placed at a distance a and b from the needle tip, and oriented by an angle ϕ with respect to each other. The steering angle makes it follow a circular path whose radius of curvature κ is empirically determined for a given needle and tissue. This arrangement constrains the needle motion to follow a path with a constant curvature, which can be reversed by rotating the needle base axially by 180 degrees. The two-parameter bicycle model can be reduced to a one-parameter unicycle model (a single wheel located directly at the needle tip) by appropriate simplifications that removes a while retaining κ.

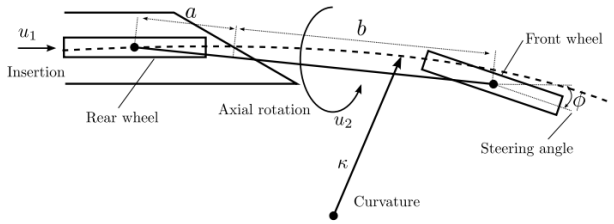

Figure 2.1: Configuration of nonholonomic model of needle steering tissue. The bicycle model of the needle composed of two wheels oriented by an angle ϕ with respect to each other. This figure is reproduced from [1] with permission from the authors.

Several research groups have used classical beam theories to develop fundamental mechanics-based models [8–10]. Yan *et al.* modeled needle interaction with the tissue as a beam connected to a series of springs [8]. Misra *et al.* used an energy-based formulation for a beam that is in contact with a nonlinear hyperplastic tissue to simulate needle steering [10]. This model accounts for lateral and axial deflection of the needle, tissue deformation, and input force applied at the needle base. Later, the same model was extended to include needle rotation during needle insertion [11]. Reed *et al.* studied effects of torsional friction on needle deflection dynamics [12]. They developed an estimator showed that the estimator allows the needle to maintain motion in a prescribed plane. Swensen *et al.* also investigated the torsional dynamics of the needle modeled as a beam and developed a model-based controller that compensates for the changing boundary conditions during subsurface needle insertion [13].

Design of needle steering planners and most types of feedback controllers requires a model of needle-tissue interaction that predicts the needle tip position given the inputs at the needle base such as insertion velocity and needle axial rotation. In the preceding models, a common approach for simulating needle deflection is using FEM [4,5]. Employing a comprehensive FEM model of tissue can be very time-consuming – more time-efficient ways to model tissue come at the expense of reduced accuracy. Also, some of the preceding models do not present sufficient control commands for real-time feedback control, which limits their application in real-time needle steering [8–10].

To the best of the author's knowledge, the nonholonomic kinematics-based models [6, 7] are the only models that has insertion velocity and axial needle rotation as inputs. The kinematics unicycle-like model has been widely used for robotic needle steering [14, 15]. The model does not account for needle-tissue interaction along the needle shaft and assumes the needle tip moves on a constant curvature path. Previous studies have shown that when the kinematic model is applied to path planning and control in soft tissues, there are non-negligible deviations between the model and experimental data [16].

2.2 Modeling Needle/Tissue Interaction

In needle insertion, puncturing the tissue surface and cutting through the tissue results in a relatively large cutting force at the needle tip. A flexible needle with an asymmetric bevelled tip has an uneven distribution of forces at the tip, which causes the needle to bend. Needle deflection results in tissue compression, which itself influences needle bending and changes the needle tip trajectory. For accurate needle steering, we need a sound understanding of the forces applied to the needle tip during needle insertion. The modelling of needle interaction forces during tissue cutting has been studied before for surgical planning and robotic needle steering [17, 18].

The needle-tissue interaction forces during needle steering in soft tissue can be categorized into four groups:

1. Tissue puncturing force, F_p: Puncturing happens at the contact point between the

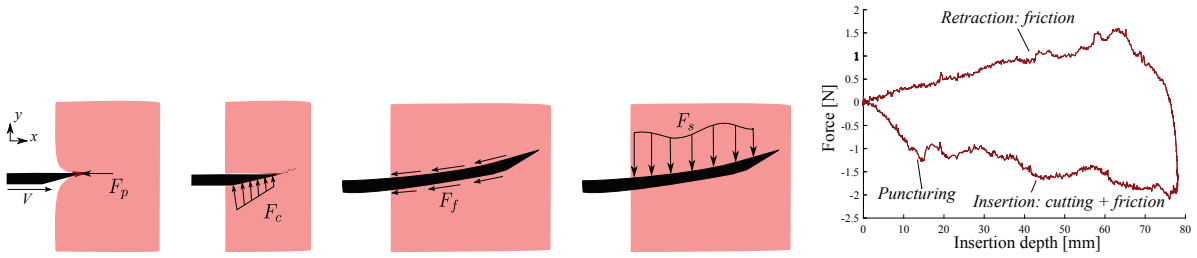

(a) (b) (c) (d) (e)

Figure 2.2: Needle-tissue interaction forces during needle insertion. (a) Tissue puncturing at the contact point between the needle tip and the tissue surface. (b) Tissue cutting including crack propagation into the tissue in response to needle displacement. (c) Needle-tissue friction force applied tangent to the needle shaft. (d) Tissue deformation forces applied perpendicular to the contact surface between the needle shaft and tissue. (e) Force versus displacement curve for needle insertion and retraction in porcine tissue at velocity of 5 mm/sec.

needle tip and the tissue surface, starts by deforming the tissue at its surface and continues until the contact force reaches its maximum and a crack is formed in the tissue surface.

2. Tissue cutting force, F_c: Cutting is a dynamic fracture event and starts when the initiated crack propagates into the tissue in response to the needle tip displacement.

3. Friction force, F_f: Friction is applied tangentially to the needle shaft and resists the motion of the needle.

4. Tissue deformation force, F_s: Tissue reaction forces applied perpendicularly to the contact surface between the needle shaft and the tissue.

Fig. 2.2 displays the above mentioned interaction forces. Fig. 2.2(e) shows these forces recorded during needle insertion and retraction in biological tissue.

In an experimental study, Okamura *et al.* performed ex-vivo tests on bovine liver and measured needle-tissue interaction forces [19]. They proposed a method for measuring friction and cutting force during needle insertion. Misra *et al.* incorporated a cohesive zone model to model tissue cutting [20]. They related the cutting force to the value of rupture toughness, which they proposed is constant for a specific tissue. They also used

a hyperelastic model of tissue to model tissue compression forces in needle insertion [10]. In these works the effect of velocity on needle insertion in biological materials has been neglected.

Heverly *et al.* experimentally studied cutting forces and proposed that two distinct phases exist in the evolution of the tissue cutting force [17]: the tissue deflection near the cutting edge and the tissue cutting characterized by a sudden decrease of the needle-tissue contact force. Moore *et al.* used the concept of elementary cutting tool edges, typically used in prediction of cutting forces in machining, to model cutting force in needle insertion [21]. Mahvash *et al* studied rupture of multilayered biological materials and studied needle-tissue contact forces during tissue puncturing [22]. They proposed that the cutting force when the needle punctures the tissue surface can be decreased by increasing insertion velocity; however, during the tissue cutting phase, fracture toughness and consequently the cutting force remains constant.

In most of the preceding studies, the effects of friction along the needle shaft on needle-tissue interaction are neglected [10,17,21]. Also these studies proposed a constant, velocity-independent cutting force during the tissue cutting phase [19, 20, 22]. Other researchers, however empirically studying the effects of cutting force, have reported velocity-dependent fracture toughness at the needle tip during tissue cutting [23, 24].

2.3 Control of Needle Steering

Several needle steering techniques have been developed that allow clinicians to adjust the needle path within a tissue to improve targeting accuracy. As discussed in Section 1.1, three types of needle steering controller are studied in the literature, namely, steering to a point, steering on a straight line, and trajectory tracking.

The first and simplest controller aims at navigating the needle tip to a desired point in tissue, regardless of what trajectory it takes. Typically, model-based predictive controllers are used for this purpose. The controller is composed of a needle-tissue model and a solver that minimizes a cost function. The cost function typically relates different steering actions,

i.e., twists or lateral motion of the needle shaft at different depths to the model-predicted targeting error. The objective of the controller is to reach a desired target with a minimum amount of control actions such that tissue trauma is minimized. The simplest controller of this type selects a single rotation depth that minimizes absolute value of targeting error, amongst a set of discrete rotation depth candidates, ranging from the current depth to the depth of the target [25]. When more than one rotation is allowed, optimization needs a multivariable and interactive solver. For instance, in [26], Rapidly-Exploring Random Tree (RRT) is used. RRT incrementally grows a tree of feasible control actions, and provides a quick high dimensional search subject to different optimization constraints [27]. Other ways to minimize the needle steering cost function involve solving for inverse kinematics models and create an optimal offline path planning [2, 28]. A variety of algorithms are available for solving such optimization problems. Several motion planning algorithms have been used [15, 29, 30], including an inverse kinematic solver, RRT based motion planner, and an online motion planner that accounts for sensing uncertainty.

The second type of controller concerns needle steering on a straight line. This type of needle steering can be seen as a particular case of third controller, i.e, trajectory tracking, where the reference trajectory is a straight line connecting the needle's entry point to the target point deep inside the tissue. The nonholonomic kinematics model [7] is widely used for trajectory tracking. Kallem and Cowan presented the unicycle model in generalized coordinates and used feedback linearization approach for 2D needle steering [31]. Minhas *et al.* presented the idea of duty-cycled spinning of the needle during insertion and showed that the curvature of the needle can be controlled via periodic needle rotations [32]. The major limitation of this method arises from the tissue trauma and drilling effect generated by such periods of constant rotation.

Mignon *et al.* [33] developed a robust 3D ultrasound needle detection approach integrated in a 3D needle steering system associated to a real-time path planning. The robustness of an existing algorithm is improved by limiting the needle detection to a curvilinear region of interest (ROI) using a mechanical-based prediction model.

Rucker *et al.* proposed a sliding-mode controller based on the unicycle model and used it to track a desired trajectory within the tissue [34]. Patil *et al.* developed an automatic

needle steering approach for reaching targets in 3D environments while avoiding obstacles [15]. Their approach relies on a rapidly exploring random tree (RRT) motion planner that calculates the optimal tip trajectory using the kinematics-based model of needle steering. Vrooijink *et al.* developed a needle steering system that uses 2-D ultrasound images to estimate the needle pose and an RRT motion planner that computes a feasible needle path toward the target based on the needle pose estimation [14]. Adebar *et al.* presented a method for 3D ultrasound guidance of robotic needle steering in biological tissue [35]. They used Doppler imaging combined with a piezo-actuated vibrating needle to track the needle tip in soft tissue and control the needle tip via duty-cycling. Abayazid *et al.* modified the kinematics-based model by accounting for the tissue cutting angle and used the model with an online motion planner for image-guided control of the needle tip deflection [11]. Maghsoudi and Jahed introduced and simulated a model-based robust controller to address needle insertion in the presence of tissue parameter uncertainty [36].

In general, the needle steering system is a nonlinear constrained system and most of the system states, namely, needle tip position and orientation, cannot be directly measured from 2D imaging systems. Thus, most of the presented needle steering strategies can only steer the needle in 2D and neglect needle deflection out of the 2D plane [11,31,32,36]. In some of the previous works, researchers assumed that all the needle states can be directly measured using electromagnetic tracking systems [15, 34], even though this limits the application of the needle steering controller in clinical practice. Several 3D needle steering algorithms are developed by incorporating image-based algorithms for calculating the needle pose in 2D ultrasound images and consequently estimating unicycle model parameters [14, 37]. However, no proof of convergence or stability were provided.

2.4 Design of Steerable Needles

As it was mentioned in Section 1.1, in needle interventions steerable flexible needles with asymmetric beveled tips are used to enhance control over needle deflection and reduce targeting error. Targeting errors are caused by human factors, imaging limitations, needle deflection, and needle/tissue reactions including soft tissue deformation, needle/tissue fric-

tion, and sliding of multilayered structures [38, 39]. A flexible needle with an asymmetric beveled tip has an uneven distribution of forces at the tip, which causes the needle to deflect from a straight path during the insertion. Using these needles, the surgeon can control tip deflection by axially rotating the needle and changing the orientation of the bevel tip, thus compensating for the effects of the aforementioned targeting errors. The beveled flexible needles have higher curvature compared to the stiff needles or needles with symmetric bevels. Using these needles surgeons can compensate any deviations caused by the aforementioned targeting error sources.

For needle insertions on a straight line, where the target and the needle insertion point are both on a straight line, stiff needles are used and axial rotations are performed only to compensate for small deviations from the straight line. However, to reach divergent targets or targets obscured by obstacles, needles with high curvature or small radius of curvature (ROC) are needed [40]. For instance in radiofrequency ablation (RFA) of liver, the minimum required needle's ROC for reaching the majority of the liver from a limited insertion site is estimated to be below 50 mm [41]. Another example is prostate brachytherapy. Brachytherapy is not prescribed for patients with large volume glands exceeding 50 cm^3 [42] or when there is severe pubic arch interference (PAI) [43]. Experimentally obtained mean ROC for 18G flexible brachytherapy needle is 700-1000 mm (depending on tissue type), which should be improved to enhance the needle maneuverability and extend the application of brachytherapy to deeper or more difficult-to-reach targets.

Steerable needles with high deflection curvature have been proposed for therapy in the liver [41], brain [44], breast [45], lung [46], and kidney [47]. Typically, researchers employ flexible nitinol wires instead of needle in their robotics-assisted needle steering strategies [14, 15, 32, 48]. The nitinol wire is highly flexible and has a higher curvature in comparison with the clinically used stainless steel needles. A mean ROC of 190 mm is reported for nitinol-based needles tested in synthetic tissue [7, 32]. Okazawa *et al.* [49] proposed a precurved stylet that could be rotated and translated relative to a straight needle shaft to manually steer a needle in tissue. Webster *et al.* [50], and Sears and Dupont [51] extended the concept of telescopic pre-curved tubes to develop active concentric tubes. The concentric tube robots can be used to avoid critical structures and reach targets in

the human body. With appropriate pre-curvature selections and deployment sequences, concentric tubes are able to obtain high curvatures and provide a large design space of possible curves [52]. However, relatively large dimensions and high cost of manufacturing of concentric tube robots have limited application of concentric tubes in cost-efficient needle-based interventions.

Several researchers have developed tip-bent steerable needles to improve needle deflection curvature in tissue [53]. The tip-bent needle consists of a flexible shaft with bent distal section. These needles can steer along highly curved paths as a result of the increased net lateral force acting at the bent distal end of the needle. Henken *et al.* developed an MRI steerable compatible needle with a manually controlled bent tip [54]. The outer diameter of the needle is 3.2 mm, which is relatively large compared to 1.3 mm 18G standard needles and can increase patient trauma. Swaney *et al.* [55] implemented a passive flexure in the bent tip of the needle to minimizing the tissue damage while maintaining the increased maximum nominal curvature. van de Berg *et al.* [56] extended the idea of tip-bent needles to develop a tendon-actuated bent-tip steerable needle.

To summarize, one can identify two main ways to increase the maneuverability of needles: 1) increasing needle flexibility, and 2) modify needle design to increase needle/tissue interaction forces that bend the needle. Needle flexibility is improved by employing softer materials or thinner needles. Interaction forces can be increased by decreasing the bevel tip angle, increasing the bevel surface, introducing a precurve near the tip, or a combination of the above [39]. Increasing needle/tissue interaction forces damages the tissue and consequently increases needle intervention's trauma. Also, very thin or bent-tip needles are incapable of providing a working channel inside the needle.

Chapter 3

2D Mechanics-based Modeling of Needle Steering

3.1 Objective

Needle-based interventions are common minimally invasive medical procedures. Robotics-assisted needle insertion can increase percutaneous medical procedures efficiency, which highly depends on accurate control of the needle tip trajectory. Modeling the needle deflection and the interaction between needle and soft tissue is an essential requirement for robotic needle steering and surgical planning and has been the topic of significant research efforts. Here, a novel hybrid model of needle-tissue interaction is presented. The hybrid modeling implies mixed use of ordinary differential equations (ODE) to model the surgeon's hand and/or a rigid needle carrier, as well as continuous partial differential equations (PDE) to model the needle-tissue interaction. The proposed model can be used for needle steering in robotic-assisted needle steering schemes. This chapter is organized as follows: In Section 3.2, details of the needle steering model including the modeling assumptions, kinematic and dynamic modeling, and model simplification are presented. In Sections 3.3 to 3.5, separate complementary models are developed to simulate interaction forces between the needle and its surrounding environment. In Section 3.6, the needle steering model is validated through intensive needle insertion experiments on synthetic and ex-vivo animal

tissues and results of the experiments are discussed. Concluding remarks are presented in Section 3.7.

3.2 Mechanics-based Needle Steering Model

Needle deflection is modeled as externally excited compliant beam attached to a rigid carrier. The elastic needle is modeled as a prismatic beam that deflects under various external forces, i.e., reaction forces from deformed soft tissue, needle-tissue friction, the grid template contact force, and tissue cutting force. The carrier has two translational and one rotational degrees of freedom (DoF). The carrier can be a physical component (e.g., the surgeon's hand or the needle inserting robot) or may simply be a virtual massless body with a body-fixed frame. Fig. 3.1(a) shows a schematic diagram of the needle insertion system. An advantage of the proposed modeling technique is that we can explicitly see the effects of the forces and torques applied to the carrier on needle deflection, and vice versa. By relating needle base force/torque to the needle deflection using the proposed model they can be used as feedback or control inputs in a robotically controlled needle steering.

The following assumptions are used in modeling the needle deflection during insertion into the tissue:

1. The needle has only 2D planar deflection and the insertion plane defined by initial orientation of the needle beveled tip.

2. The needle is modeled as homogeneous beam with constant cross section area that is infinitely stiff in shear.

3. Planar rotation of beam elements is small and rotary inertia of the needle due to needle bending is negligible.

4. The axis of the prismatic beam is incompressible and needle shortening due to axial compression is neglected. However, axial forces can affect needle bending dynamics when the deflection is large.

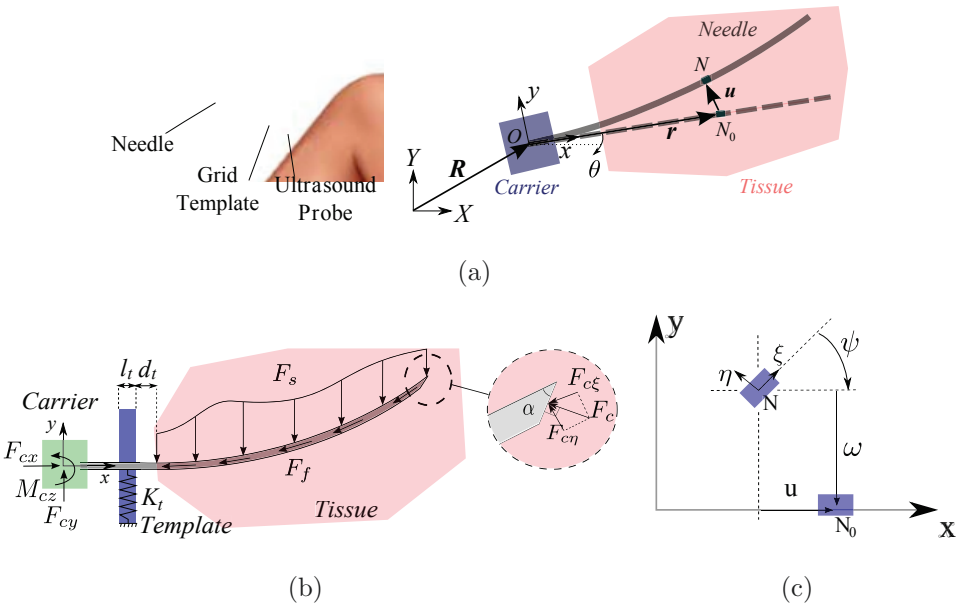

Figure 3.1: Needle insertion in brachytherapy. (a) The surgeon inserting the flexible needle in the tissue and a sketch of the needle insertion system consisting of a flexible needle attached to a rigid carrier. (b) Interaction forces acting on the length of the bevel-tip needle inserted into a soft tissue. (c) Needle element bending displacement.

5. The center of mass of the needle driving system is assumed to coincide with that of the carrier.

Assumptions 2 and 3 are Euler-Bernoulli beam theory assumptions [57], which hold for all slender brachytherapy needles. During needle steering, the needle tip might deviate and deflect out of plane. However, using the process presented in [12] and [13] we can minimize the out of plane deflection and maintain a 2D needle insertion. In the following, the generalized coordinates and kinematics of the needle-tissue system are introduced. Next, we use the variational formulation to model the dynamic motion of the needle inside the tissue. Finally, a mathematical approach is used to simplify the dynamic equations.

Throughout this chapter we use the following notation: s, $\boldsymbol{s}$ and $\mathbf{s}$ denote a scalar, a vector and a matrix, respectively. The following Table of nomenclatures summarizes the parameters and variables used throughout Section 3.2.

Table 3.1: Table of nomenclatures for Section 3.2

XY,xy,$\xi\eta$	Global inertial frame, carrier Body-fixed frame, and needle Body-fixed frame.
N	Generic point on the deflected needle.
N_0	Point N on the unbent needle.
$\boldsymbol{R}_N(x,t)$	Vector of coordinates of point N.
$\boldsymbol{R}^G(t)$	Vector of carrier mass center coordinates.
$\boldsymbol{r}(x)$	Vector of coordinates of N_0.
$\boldsymbol{u}(x,t)$	Displacement vector connecting N_0 to N.
$\mathbf{C}(t)$	Matrix of direction cosines.
$X(t)$,$Y(t)$	Displacement of carrier along X and Y axes.
$\theta(t)$	In-plane angle of rotation of carrier.
$\boldsymbol{\theta}(t)$	Vector of carrier Euler angles.
$u(x,t)$	Displacement of point N along x axis.
$\omega(x,t)$	Displacement of point N along y axis.
$\psi(x,t)$	In-plane angle of rotation of of point N.
$\boldsymbol{\psi}(x,t)$	Vector of point N Euler angles.
$\boldsymbol{V}(t)$	Velocity vector of the carrier center of mass.
$\dot{\boldsymbol{\theta}}(t)$	Angular velocity of xy relative to XY.
$\dot{\boldsymbol{u}}(x,t)$	Elastic velocity vector.
$\dot{\boldsymbol{\psi}}(x,t)$	Elastic angular velocity of $\xi\eta$ frame.
$\boldsymbol{V}_N(x,t)$	Velocity vector of point N of needle.
$\mathcal{L}$, $\overline{\delta\mathcal{W}}(t)$	Lagrangian and virtual work.
$T(t)$,$\mathcal{V}(t)$	Kinetic and potential energy of needle-carrier.
$\delta(.)$	Infinitesimal variation operator.
ℓ,A,I,α	Needle's length, cross-section area, second moment of inertia, and bevel angle.
ρ,E	Needle's density and Young's modulus.
m_c,$\mathbf{J}_c$	Carrier's mass and moment of inertia.
$\boldsymbol{g}$	Vector of gravitational field strength.
$\boldsymbol{F}_c(t)$	Vector of forces acting on the carrier.
$F_{cx}(t)$	Forces acting on the carrier along x axis.
$F_{cy}(t)$	Forces acting on the carrier along y axis.
$\boldsymbol{M}_c(t)$	Vector of torques acting on the carrier.

$M_{cz}(t)$	In-plane torque acting on the carrier.
$\boldsymbol{f}(x,t)$	Vector of distributed forces on needle shaft.
$f_x(x,t)$	Distributed interaction forces along x axis.
$f_y(x,t)$	Distributed interaction forces along y axis.
$F_s(x,t)$	Soft-tissue reaction force.
$F_f(x,t)$	Needle-tissue friction force.
$F_c(t)$	Tissue cutting force.
$F_{c\xi}(t)$	Axial and transverse cutting forces along ξ axis.
$F_{c\eta}(t)$	Axial and transverse cutting forces along η axis.
K_t,l_t,d_t	Template's stiffness, length, and distance from the tissue.
$x_t(t)$	Position of the template in xy.
H,δ	Unit step and Dirac delta functions.
$W_i(x)$	Assumed mode shapes of vibration, $i = 1, .., n$.
$\phi_i(t)$	Generalized coordinate, $i = 1, .., n$.
β_i	Vibration frequency constant, $i = 1, .., n$.
γ_i, κ_i	Vibration amplitude constants, $i = 1, .., n$.
$\boldsymbol{\phi}(t)$,$\mathbf{W}(x)$	Vectors of generalized coordinates and mode shapes.

3.2.1 Kinematics of Needle Steering

Fig. 3.1(a) shows a schematic diagram of the needle insertion system. A global inertial frame (XY) and a non-inertial frame (xy) fixed on the carrier at its mass center are defined. The generic point N_0 along the needle shaft when the needle is unbent coincides with the point N when the needle is deflected. The coordinates of point N of the deflected needle in the body-fixed frame (xy) is

$$\boldsymbol{R}_N = \mathbf{C}\boldsymbol{R}^G + \boldsymbol{r} + \boldsymbol{u} \tag{3.1}$$

where $\boldsymbol{R}^G = [X \quad Y \quad 0]^T$ is expressed in coordinates of the inertial frame, $\boldsymbol{r} = [x \quad 0 \quad 0]^T$, $\boldsymbol{u} = [u \quad \omega \quad 0]^T$, and $\mathbf{C}$ is the matrix of direction cosines and allows to transform a point from (XY) frame to (xy) frame. It should be emphasized that in our approach all the forces and torques applied to the needle and carrier are defined with respect to the non-

inertial frame (xy) attached to the carrier called the *body-fixed frame*. Thus, it is more convenient to define our generalized coordinates and velocities in the body-fixed frame – they are customarily referred to as pseudo-coordinates and pseudo-velocities, respectively [58].

The carrier has two translational DoF along X and Y, denoted by the vector $\boldsymbol{R}^G$ in XY frame. In addition to two translational DoFs, the carrier has a rotational DoF, θ, denoted by the vector of Eulerian-type angles $\boldsymbol{\theta} = [0 \;\; 0 \;\; \theta]^T$. According to the Assumption 1, the first two angles are zero. Point N on the needle has three DoFs in the body-fixed frame, namely ω, u and ψ, corresponding to displacements along x and y and the in-plane rotation, respectively (see Fig. 3.1(c)).

To model in-plane rotational motion of beam elements, we introduce a set of body-fixed frames ($\xi\eta$) attached to the cross-section of the beam at point N. Denoting the in-plane bending rotation of beam element by ψ and assuming it is small, we can express rotation of the $\xi\eta$ frame relative to the xy frame by the vector $\boldsymbol{\psi} = [0 \;\; 0 \;\; \psi]^T$.

Based on the presented configuration we have the vector of generalized coordinates $\boldsymbol{q} = [\boldsymbol{R}^{G^T} \;\; \boldsymbol{\theta}^T \;\; \boldsymbol{u}^T \;\; \boldsymbol{\psi}^T]^T$. Now, we can easily calculate the generalized velocities related to the derivatives of the generalized coordinates by

$$\begin{bmatrix} \boldsymbol{V}^T & \dot{\boldsymbol{\theta}}^T & \dot{\boldsymbol{u}}^T & \dot{\boldsymbol{\psi}}^T \end{bmatrix}^T = \begin{bmatrix} \mathbf{C} & 0 \\ 0 & \mathbf{I} \end{bmatrix} \dot{\boldsymbol{q}} \tag{3.2}$$

where I is a 9×9 identity matrix. All vectors in (3.2) are in body-fixed frame (xy). Now taking derivative of (3.1) with respect to time, we can write the kinematic equation of motion for point N in terms of generalized velocities as

$$\boldsymbol{V}_N = \boldsymbol{V} + \tilde{\dot{\boldsymbol{\theta}}}(\boldsymbol{u} + \boldsymbol{r}) + \dot{\boldsymbol{u}} = \boldsymbol{V} + (\tilde{\boldsymbol{u}}^T + \tilde{\boldsymbol{r}}^T)\dot{\boldsymbol{\theta}} + \dot{\boldsymbol{u}} \tag{3.3}$$

the superscript $\tilde{}$ denotes a skew symmetric matrix.

At this point, we introduce two equations that can be used to eliminate the redundant coordinates. Using Euler-Bernoulli assumptions we have

$$u(x,t) = -\frac{1}{2}\int_o^x \omega'(\zeta,t)^2 \, d\zeta, \quad \psi(x,t) = \omega'(x,t) \tag{3.4}$$

where ζ is a dummy integral variable and prime denotes partial derivative with respect to x. Above equations will be used later to write ψ and u in terms of other generalized coordinates and eliminate redundant degrees of freedom.

3.2.2 Variational Formulation of Needle Steering

Having all the kinematic equations that describe the motion of the needle and the carrier, we will use the variational formulation and extended Hamilton's principle to derive the dynamic equations of motion for the hybrid system. We note that $\boldsymbol{V}$ in (3.3) is defined in the body-fixed frame and based on (3.2), the components of $\boldsymbol{V}$ are not direct derivatives of generalized coordinates. $\boldsymbol{V}$ is typically called the derivative of pseudo-coordinates or pseudo-velocity vector. Similar to velocity, it is simpler to define all the forces and torques applied to the carrier and needle with reference to the body-fixed frame. Thus, it is more convenient to use the extended Hamilton's principle in terms of pseudo-coordinates. The extended Hamilton's principle is stated by $\int_{t_1}^{t_2}[\delta\mathcal{L} + \overline{\delta\mathcal{W}}]dt = 0$.

Before we can use the extended Hamilton's principle, it is essential to find the expressions for T, $\mathcal{V}$, and $\overline{\delta\mathcal{W}}$. Based on Assumption 3, the kinetic energy consists of only three parts, the translation of a beam element at a nominal position x, the translation of the carrier, and the carrier rotation. Using (3.3), we can write the kinetic energy as

$$\begin{aligned} T =& \frac{1}{2}\rho A \int_o^\ell \Big[\dot{\boldsymbol{u}}^T\dot{\boldsymbol{u}} + 2\,\boldsymbol{V}^T\dot{\boldsymbol{u}} + 2\,\boldsymbol{V}^T(\tilde{\boldsymbol{u}}^T + \tilde{\boldsymbol{r}}^T)\dot{\boldsymbol{\theta}} \\ &+ 2\dot{\boldsymbol{\theta}}^T(\tilde{\boldsymbol{u}} + \tilde{\boldsymbol{r}})\dot{\boldsymbol{u}}\Big]dx + \frac{1}{2}m_t\,\boldsymbol{V}^T\,\boldsymbol{V} + \frac{1}{2}\dot{\boldsymbol{\theta}}^T\mathbf{J}_t\dot{\boldsymbol{\theta}} \end{aligned} \tag{3.5}$$

where $\mathbf{J}_t = \mathbf{J}_c + \rho A\int_o^\ell(\tilde{\boldsymbol{u}} + \tilde{\boldsymbol{r}})(\tilde{\boldsymbol{u}} + \tilde{\boldsymbol{r}})^T dx$ and $m_t = m_c + \rho A\ell$ is the total mass of the needle-carrier system.

The potential energy of the system arises from two sources, gravity and needle flexibility. Considering Assumption 5, the gravitational potential energy of the needle is negligible. Also, from mechanics of materials, the bending potential energy of the deflected needle is equal to $\frac{1}{2}EI\int_o^l \psi'^2\,dx$ [57]. Replacing ψ using the kinematic constraint given by (3.4), the total potential energy can be expressed as

$$\mathcal{V} = -m_c\boldsymbol{g}^T\boldsymbol{R} + \frac{1}{2}EI\int_o^l \omega''^2\,dx \tag{3.6}$$

The non-conservative virtual work is due to the forces and torques applied to the carrier and a distributed force working on the length of the flexible needle. It can be written as

$$\overline{\delta \mathcal{W}} = \delta \boldsymbol{\theta}^T \boldsymbol{M}_c + \delta \boldsymbol{R}^T \mathbf{C}^T \boldsymbol{F}_c + \int_0^\ell \delta \boldsymbol{R}_N^T \boldsymbol{f} dx \tag{3.7}$$

where $\boldsymbol{M}_c = [0 \quad 0 \quad M_{cz}]^T$, $\boldsymbol{F}_c = [F_{cx} \quad F_{cy} \quad 0]^T$, and $\boldsymbol{f} = [f_x \quad f_y \quad 0]^T$. Fig. 3.1(b) shows a schematic of interaction forces on the needle carrier system. The elements of the distributed interaction force vector $\boldsymbol{f}$ can be obtained using Fig. 3.1(b) as

$$f_x = f_{cx} + f_{fx}, \quad f_y = f_{cy} + f_s + f_k + f_{fy} \tag{3.8}$$

where

$$\begin{aligned} f_s(x) &= F_s H_{l-X}(x), & f_k(x) &= K_t \omega [H_{x_t}(x) - H_{x_t+l_t}(x)] \\ f_{cx}(x) &= -F_{c\xi} - F_{c\eta}\omega'(l,t), & f_{cy}(x) &= [F_{c\eta} - F_{c\xi}\omega'(l,t)]\delta_\ell(x) \\ f_{fx}(x) &= F_f H_{l-X}(x), & f_{fy}(x) &= F_f \omega' H_{l-X}(x) \end{aligned} \tag{3.9}$$

where $x_t = \ell - X - d_t - l_t$. In (3.9), we have used assumption 3 and assumed $\tan(\omega') = \omega'$. The transverse and axial component of F_c in (3.9) can be related by the bevel angle using $F_{c\xi} = F_{c\eta} tan(\alpha)$ (see Fig. 3.1(b)). We note that some of the above mentioned forces are moving loads acting over a specific length of the needle. As the needle is inserted, their point of application or width will change accordingly. To define the limits of the force profile applied to the length of the beam, we use unit step (H) and Dirac delta (δ) functions. The shorthand notation $H_{x_0}(x) = H(x - x_0)$ and $\delta_{x_0}(x) = \delta(x - x_0)$ describes unit step and Dirac delta functions shifted by the constant x_0.

Note that in (3.9) we have used (3.4) to transform the contact forces shown in Fig. 3.1(b) from their point of application to the body-fixed frame. Consequently, all the forces given in (3.8) are in terms of the body-fixed frame (xy). Having all the reaction forces defined, we can continue to derive the virtual work ($\mathcal{W}$). Using (3.1), we can express the virtual displacement $\delta \boldsymbol{R}_N$ in the body fixed-frame as $\delta \boldsymbol{R}_N = \mathbf{C}\delta \boldsymbol{R} + (\tilde{\boldsymbol{u}}^T + \tilde{\boldsymbol{r}}^T)\delta\boldsymbol{\theta} + \delta \boldsymbol{u}$. Plugging $\delta \boldsymbol{R}_N$ into (3.7) gives

$$\overline{\delta \mathcal{W}} = \delta \boldsymbol{\theta}^T \boldsymbol{M}_c + \delta \boldsymbol{R}^T \mathbf{C}^T \boldsymbol{F}_c + \int_0^\ell [\delta \boldsymbol{R}^T \mathbf{C}^T \boldsymbol{f} + \delta \boldsymbol{\theta}^T (\tilde{\boldsymbol{u}} + \tilde{\boldsymbol{r}}) \boldsymbol{f} + \delta \boldsymbol{u}^T \boldsymbol{f}] dx \tag{3.10}$$

Combining (3.5), (3.6), and (3.10) and considering the geometrical constraints (3.4) and (3.4), we can write the Lagrangian in general functional form as $\mathcal{L} = \mathcal{L}(\boldsymbol{u}, \dot{\boldsymbol{u}}, \boldsymbol{u}', \boldsymbol{u}'', \boldsymbol{R}, \boldsymbol{V}, \boldsymbol{\theta}, \dot{\boldsymbol{\theta}})$.

Inserting the Lagrangian in the extended Hamilton's principle and following the mathematical procedure given in Appendix B, we can obtain

$$\begin{aligned}
&\int_{t_1}^{t_2} \delta \boldsymbol{R}^T \left[\mathbf{C}^T \left(-\frac{d}{dt}\left(\frac{\partial \mathcal{L}}{\partial \boldsymbol{V}}\right) - \tilde{\dot{\boldsymbol{\theta}}} \frac{\partial \mathcal{L}}{\partial \boldsymbol{V}} + \boldsymbol{F}_c + \int_o^\ell \boldsymbol{f}\, dx \right) \right. \\
&\left. + \frac{\partial \mathcal{L}}{\partial \boldsymbol{R}} \right] dt + \int_{t_1}^{t_2} \delta \boldsymbol{\theta}^T \left[-\frac{d}{dt}\left(\frac{\partial \mathcal{L}}{\partial \dot{\boldsymbol{\theta}}}\right) - \tilde{\boldsymbol{V}} \frac{\partial \mathcal{L}}{\partial \boldsymbol{V}} + \frac{\partial \mathcal{L}}{\partial \boldsymbol{\theta}} \right. \\
&\left. + \boldsymbol{M}_c + \int_o^\ell (\tilde{\boldsymbol{u}} + \tilde{\boldsymbol{r}}) \boldsymbol{f}\, dx \right] dt \\
&+ \int_{t_1}^{t_2} \int_o^\ell \delta \boldsymbol{u}^T \left[\frac{\partial \hat{\mathcal{L}}}{\partial \boldsymbol{u}} - \frac{d}{dt}\left(\frac{\partial \hat{\mathcal{L}}}{\partial \dot{\boldsymbol{u}}}\right) - \frac{d}{dx}\left(\frac{\partial \hat{\mathcal{L}}}{\partial \boldsymbol{u}'}\right) \right. \\
&\left. + \frac{d^2}{dx^2}\left(\frac{\partial \hat{\mathcal{L}}}{\partial \boldsymbol{u}''}\right) + \boldsymbol{f} \right] dx dt \\
&+ \int_{t_1}^{t_2} \left[\delta \boldsymbol{u}'^T \frac{\partial \hat{\mathcal{L}}}{\partial \boldsymbol{u}''} + \delta \boldsymbol{u}^T \left(\frac{\partial \hat{\mathcal{L}}}{\partial \boldsymbol{u}'} - \frac{d}{dx}\left(\frac{\partial \hat{\mathcal{L}}}{\partial \boldsymbol{u}''}\right) \right) \right] \Bigg|_0^\ell dt = 0
\end{aligned} \tag{3.11}$$

At this point we simplify the integrals in (3.11) to derive the hybrid equations for the needle-carrier system. The fundamental lemma of the calculus of variations tells us that the integrands in the four integrals in (3.11) must vanish. The first two integrals in (3.11) will give us the Lagrangian equations for the carrier. Following the mathematical approach presented in [58] we obtain the dynamic equations of the system.

We restrict the motion of the carrier to a linear insertion along the X direction (see Fig. 3.1(a)). However, using (3.11) we calculate all the force/torque applied to the carrier. From the first two integrals in (3.11) we obtain the dynamic equations of the rigid part in terms of quasi-coordinates

$$F_{cx} = m_c \ddot{X} - \int_0^\ell f_x \, dx \tag{3.12a}$$

$$F_{cy} = m_c g + \rho A \int_o^\ell \ddot{\omega}\, dx - \int_0^\ell f_y \, dx \tag{3.12b}$$

$$\begin{aligned}
M_{cz} = \int_0^\ell \Big\{ &-\rho A \left[\dot{\omega}\dot{X} + \omega \ddot{X} + \ddot{\omega}(u + x) \right] \\
&- \omega f_x + (x + u) f_y \Big\} \, dx
\end{aligned} \tag{3.12c}$$

where f_x and f_y are given by (3.8) and (3.9). Note that based on Assumption 2, we can say that u, the needle shortening along the x direction of the body-fixed frame, is small. Thus, we have neglected the term $\ddot{u}$ in derivation of (3.12).

Next, we will derive the equation of motion for the continuous part of the system. Inserting the forces given by (3.8) and (3.9) in the last two integrals in (3.11), taking integration by parts, and performing simple mathematical operations when appropriate, we obtain the PDE governing the motion of the needle as

$$EI\omega'''' + \rho A\ddot{\omega} + P\omega'' = Q \tag{3.13}$$

with P and Q being

$$Q = f_s + f_k + F_{c\eta}\delta_\ell(x) - F_{c\eta}\omega'^2\delta_\ell(x) \tag{3.14a}$$

$$P = F_{c\xi} + F_f(\ell - x)H_{\ell-X} + F_{c\eta}\omega'(\ell, t) \tag{3.14b}$$

subject to the following set of boundary conditions:

$$\omega(0,t) = 0, \quad \omega'(0,t) = 0, \quad \omega''(\ell,t) = 0, \quad \omega'''(\ell,t) = 0 \tag{3.15}$$

Equations (3.12) and (3.13) represent a set of coupled ordinary and partial differential equations describing the motion of the needle-carrier system. The partial differential equation (PDE) in (3.13) implies that the dimensionality of the problem is infinite. Also, the hybrid equations are nonlinear and complicated to solve. Next, we will simplify the equations by discretizing the continuous part and reducing the size of the model.

3.2.3 Discretization of the Continuous PDE

In this section, the continuous model in (3.13) is replaced by a discrete model following an approach known as Bubnov-Galerkin method [59]. The displacement field is approximated using $\omega(x,t) \simeq \hat{\omega}(x,t) = \sum_{i=1}^{n} \phi_i(t)W_i(x)$, where $W_i(x)$ $(i = 1, ..., n)$ are assumed functions representing the first n modes of vibration and $\phi_i(t)$ $(i = 1, ..., n)$ are the generalized coordinates or time functions expressing the deformation of the beam with respect to time. We select the mode shapes of a homogeneous clamped-free beam as the assumed functions.

This way we ensure that the assumed functions satisfy the differentiation requirements and geometrical and dynamic boundary conditions in (3.15). The mode shapes for the clamped-free beam are given by [60]

$$W_i(x) = \frac{1}{\kappa_i}\left[-\gamma_i\left(\cos(\frac{\beta_i x}{\ell}) - \cosh(\frac{\beta_i x}{\ell})\right) + \sin(\frac{\beta_i x}{\ell}) - \sinh(\frac{\beta_i x}{\ell})\right] \tag{3.16}$$

where β_i $(i = 1, ..., n)$ is a dimensionless constant corresponding to different modes of vibration. In this work, we will estimate the continuous model given in (3.13) using the first four modes. Values of the first four β_i for a clamped-free beam are 1.857, 4.694, 7.855 and 10.996, respectively [60]. γ and κ in (3.16) are given by

$$\begin{aligned} \gamma_i &= \frac{\sin\beta_i + \sinh\beta_i}{\cos\beta_i + \cosh\beta_i}, \\ \kappa_i &= -\gamma_i\left(\cos\beta_i - \cosh\beta_i\right) + \sin\beta_i - \sinh\beta_i \end{aligned} \tag{3.17}$$

Following the Bubnov-Galerkin method and inserting the approximated displacement field in (3.13) we can get a finite-dimensional model of needle steering as

$$\hat{\mathbf{M}}\ddot{\boldsymbol{\phi}} + \hat{\mathbf{K}}\boldsymbol{\phi} + \hat{\mathbf{R}}\boldsymbol{\phi} + \hat{\mathbf{T}}\boldsymbol{\phi} + \hat{\mathbf{G}}\boldsymbol{\phi}\boldsymbol{\phi}^T\boldsymbol{W}'(\ell) = \hat{\boldsymbol{S}}(\boldsymbol{\phi}) + \hat{\boldsymbol{V}} \tag{3.18}$$

where elements of matrices and vectors in (3.18) are given by

$$\begin{aligned} &\hat{M}_{ij} = \rho A\int_0^\ell W_j(x)W_i(x)dx, \quad \hat{K}_{ij} = EI\int_0^\ell W_j''''(x)W_i(x)dx, \\ &\hat{R}_{ij} = F_f\int_{\ell-X}^\ell(\ell - x)W_j''(x)W_i(x)dx + F_{c\xi}\int_0^\ell W_j''(x)W_i(x)dx, \\ &\hat{T}_{ij} = -K_t\int_{x_t}^{x_t+l_t} W_j(x)W_i(x)dx, \quad \hat{S}_i = \int_{\ell-X}^\ell F_s(x,t)W_i(x)dx, \\ &\hat{G}_{ij} = F_{c\eta}\Big[W_j'(\ell) + \int_0^\ell W_j''(x)W_i(x)dx\Big], \quad \hat{V}_i = F_{c\eta} \end{aligned} \tag{3.19}$$

By solving the above system of ODEs, the time functions $\phi_i(t)$ and consequently the needle deflection can be found. The matrices $\hat{\mathbf{M}}$ and $\hat{\mathbf{K}}$ are constant, positive definite, and symmetric and they correspond to the kinetic energy and the elastic linear forces in the beam. $\hat{\mathbf{T}}$ corresponds to the effects of reaction forces from the template. $\hat{\mathbf{R}}$ contains the effects of non-conservative axial forces. The last term on the right side of the system of differential equations in (3.18) is due to the rotation of needle tip as it bends under external

forces. $\hat{\boldsymbol{S}}$ shows the effects of tissue reaction force. $\hat{\boldsymbol{V}}$ corresponds to the transverse component of the cutting force acting at the tip of the needle. So far, we have modeled the dynamics of the coupled needle-carrier system. However, the interaction forces shown in Fig. 3.1(b), including the tissue reaction force (F_s) and the cutting force (F_c) are yet to be determined. In the next section we will model the needle/tissue interaction forces.

Fig. 3.1(b) shows a schematic of the interaction forces applied to the needle during needle insertion. The needle interactions with surrounding environment are modeled by axial and transverse distributed and concentrated loads that are applied to the portion of the needle that is inside the tissue. During needle insertion, the cutting force F_c is applied to the needle in a direction perpendicular to the beveled tip. The transverse and axial component of F_c are related using $F_{c\xi} = F_{c\eta} tan(\alpha)$ (see Fig. 3.1(b)). A force distribution F_s is used to model tissue reaction forces as the result of its deformation caused by needle bending. The grid template acts as a rigid support and is modeled by a stiff spring with stiffness of K_t. It is positioned at distance d_t from the tissue and has length l_t. Friction between the needle shaft and the tissue is modeled by an axially distributed load F_f tangent to the needle shaft. Fig. 3.1(b) displays the above mentioned interaction forces.

In the following, we will model the components of the needle/tissue interaction force including the tissue cutting force F_c, friction along the needle shaft F_f, and tissue reaction force F_s.

3.3 Tissue Cutting Model

Here, we develop several mechanical models of tissue cutting to calculate the cutting force F_c, shown in Fig. 3.1(b). Based on the experimental evaluations and the literature review presented in Section 2.2, cutting force explicitly depends on the tissue type and mechanical characteristics of the soft tissue. Here, we develop two different models for two different types of tissue: 1) synthetic phantom tissue or homogeneous tissue, and 2) multilayered heterogeneous tissue.

3.3.1 Cutting Force in Homogeneous Tissue

Modeling tissue cutting for needle steering and surgical planning has been the topic of significant research efforts [19, 20, 22]. In most previous studies cutting force is assumed to be constant [19]. However, experimental studies show that cutting force depends on insertion velocity [22]. Here, we propose a method based on principles of fracture mechanics in elastic materials to relate cutting force to velocity-dependent tissue fracture toughness. In this model it is assumption that the tissue around the needle tip is pure elastic and there is no delayed viscoelastic crack growth and the near tip plastic zone is small[61].

Fracture toughness, G_c, is a material property and a measure of resistance against crack growth in linear elastic materials. Based on the definition of fracture toughness, crack extension occurs when the rate of energy release in crack extension, G, is equal or greater than G_c.

Under plain strain condition, fracture toughness is $G_c = \frac{K_I^2}{E'}$, where $E' = \frac{E}{1-\nu^2}$. K_I is the stress intensity factor for mode I fracture. Mode I or opening mode corresponds to fracture in a body loaded by tensile forces such that the crack surfaces move apart in the direction of applied forces. Microscopic observations of tissue cutting have shown mode I crack best represents crack geometry during tissue cutting [10]. In dynamic fracture, the crack driving force should incorporate the effects of kinetic energy and crack velocity. It has been shown that the dynamic energy release rate in elastic material can be expressed as [61]

$$G(t) = \mathcal{A}(V)\frac{K_{ID}^2(V)}{E'} \tag{3.20}$$

Approximate expressions for $\mathcal{A}(V)$ and $K_{ID}(V)$ are [61]

$$\mathcal{A} = \left[(1 - hV)\left(1 - \frac{V}{c_r}\right)\right]^{-1}, \quad K_{ID} = \frac{K_{I0}}{1 - \left(\frac{V}{V_l}\right)^m} \tag{3.21}$$

where h is a function of shear and longitudinal wave speeds and constant for a given material and m is an experimentally determined constant. Clinical needle insertion velocities vary in between 5 to 50 mm/sec [62], which is significantly smaller than the Raleigh surface wave speed in soft tissue [63]. Also, h is zero for homogeneous isotropic materials and negligible

at low crack velocities for non-homogeneous materials [61]. Thus, we can assume $\mathcal{A}$ is equal to one.

(3.20) and (3.21) state that the dynamic stress intensity factor and consequently fracture toughness are functions of insertion velocity in the dynamic crack propagation, and that material resistance increases with crack speed. Based on (3.21), at low insertion speeds, K_{ID} is relatively insensitive to V but K_{ID} increases asymptotically as V reaches the limiting value of V_l. Now, we can use the equation proposed in [22] to relate cutting force to fracture toughness

$$F_c = G(t)w_c \tag{3.22}$$

w_c is the cutting width and equal to the needle outer diameter.

3.3.2 Cutting Force in Heterogeneous Tissue

We categorize the tissue cutting force in multilateral heterogeneous tissue into two separate groups:

1. Tissue cutting force during puncturing, F_P: Puncturing happens at the contact point between the needle tip and the tissue surface, starts by deforming the tissue at its surface and continues until the contact force reaches its maximum and a crack is formed in the tissue surface.

2. Tissue cutting force during insertion, F_C: Cutting is a dynamic fracture event and starts when the initiated crack propagates into the tissue in response to the needle tip displacement.

These two forces are shown in Fig. 2.2. The cutting force shown in Fig. 3.1(b), F_c, is equal to F_P during the puncturing phase or when it is traversing between two different layers of tissue, and it is equal to F_C during the insertion phase. In the following subsections we model the two phases of the cutting force.

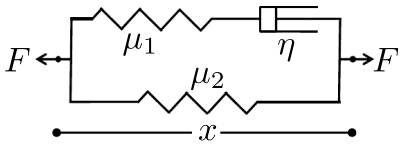

Figure 3.2: Standard linear viscoelastic model used to simulate needle interaction with a viscoelastic tissue during tissue puncturing. F is the applied force, μ_1 and μ_2 are the spring constants, η is the damping coefficient, and x is the needle tip displacement.

3.3.2.1 Tissue Cutting in Puncturing

Puncturing takes place at the beginning of needle insertion before the needle penetrates the tissue and when the needle tip travels between two different layers of biological tissue. For modeling purposes, we divide the tissue puncturing into two events: (1) Tissue Compression: The needle tip is pressed against the tissue surface and the contact force increases until it reaches its maximum. (2) Crack initiation: When the contact force at the needle tip reaches its maximum value, the tissue in the proximity of the needle tip (failure zone) is severely damaged. The molecular bonds in the failure zone break and a crack is formed in the tissue.

3.3.2.1.1 Tissue Compression We will employ a model known as standard linear solid to predict force-deformation response of a needle in contact with a biological tissue during the compression phase. The tissue is modelled as a Newtonian damper and two Hookean springs, one in parallel and one in series. The model has a time-dependent component that enables the modeling of creep, stress relaxation and hysteresis.

The model can be expressed as a first order differential equation

$$F + \frac{\eta}{\mu_1}\dot{F} = \mu_2 x + \eta\left(1 + \frac{\mu_2}{\mu_1}\right)\dot{x} \tag{3.23}$$

where F is the contact force, μ_1 and μ_2 are tissue stiffness, η is the tissue damping coefficient, x is the needle tip displacement, and dot denotes differentiation with respect to time t. Considering the responses of the system in (3.23) to a unit step force and displacement, and using the convolution integral, the contact force and displacement can be calculated

with respect to time as

$$x(t) = \int_0^t C(t-\tau)\frac{dF(\tau)}{d\tau}d\tau \tag{3.24a}$$

$$F(t) = \int_0^t G(t-\tau)\frac{dx(\tau)}{d\tau}d\tau \tag{3.24b}$$

where $C(t)$ and $G(t)$ are creep compliance and relaxation modulus, respectively, and are given by

$$C(t) = \frac{1}{E_R}\left[1-(1-\frac{\tau_1}{\tau_2})e^{-t/\tau_2}\right] \tag{3.25a}$$

$$G(t) = E_R\left[1-(1-\frac{\tau_2}{\tau_1})e^{-t/\tau_1}\right] \tag{3.25b}$$

where $E_R = \mu_2$ is the long-time or reference modulus of stiffness, and $\tau_1 = \eta/\mu_1$ and $\tau_2 = (\eta/\mu_2)(1+\mu_2/\mu_1)$ are intrinsic time scales characterizing the nature of the stress relaxation and creep and are called relaxation and retardation times, respectively [64]. Knowing the input force or displacement profile, one can use equation (3.24a) or (3.24b) to calculate needle-tissue contact displacement or force during tissue puncturing.

Now, to investigate needle-tissue interaction before the rupture happens, we study the case of needle insertion with a constant velocity V. Using (3.25b), we have

$$F_P = E_R\left[x_p - V(\tau_2-\tau_1)(e^{-\frac{x_p}{V\tau_1}}-1)\right] \tag{3.26}$$

where x_p is the tissue deformation at the contact point. The last term in (3.26) can be estimated by the first two terms of a Taylor series expansion and (3.26) reduces to

$$F_P = E_R x_p \frac{\tau_2}{\tau_1} \tag{3.27}$$

Equation (3.26) estimates tissue puncturing force as a nonlinear function of velocity. However, (3.27) states that for relatively high insertion velocities, the puncturing force is almost independent of the needle insertion velocity and increases linearly with respect to the tissue deformation. The velocity at which the puncturing force reaches 90% of its maximum value is called saturation velocity [22]. Using (3.26) and (3.27) and 3rd order Taylor expansion, we can calculate the saturation velocity as

$$V_s = 5\frac{x_p}{\tau_1} \tag{3.28}$$

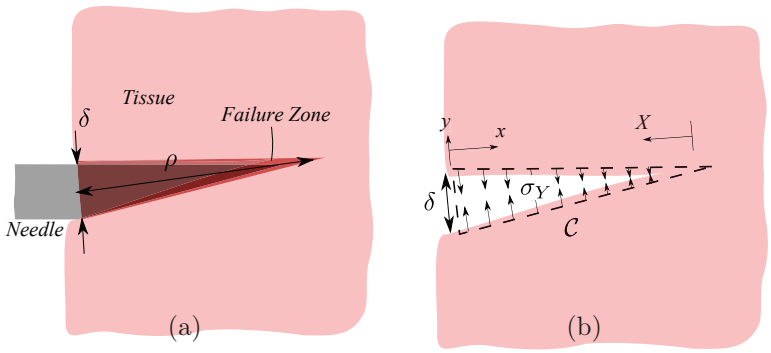

Figure 3.3: A schematic of the Strip-Yield zone model. (a) Plastic failure zone with the length of ρ near the needle tip. δ is the CTOD which is approximately equal to the needle outer diameter. (b) The plastic zone is modelled by a compressive stress σ_Y and $\mathcal{C}$ shown by the dashed line is a contour along the boundary of the Strip-Yield plastic zone.

The above equation can be used to estimate the optimal puncturing velocity for tissue cutting as a function of the tissue viscoelasic parameters and the tissue deformation. The puncturing force increases to its maximum until rupture happens. In the following a fracture mechanics-based analysis is used to calculate the maximum puncturing force.

3.3.2.1.2 Crack Initiation In general, failure and crack initiation are characterized by separation of atomic bonds of a material [61]. A local failure criterion typically used to predict crack initiation is the fracture toughness or the crack-resistant force per unit area of crack (G_c) and can include plastic, viscoelastic, or viscoplastic effects depending on the material. A crack initiates and grows when the energy released through crack extension equals or exceeds the fracture toughness. Here, we introduce two parameters typically used to characterize crack initiation and growth in materials, namely, crack-tip-opening displacement (CTOD) and the J contour integral. Next, we use the *Correspondence Principle*[65] to extend the definition of J integral and CTOD to viscoelastic materials and model time-dependent crack initiation in a viscoelastic tissue.

CTOD and the J integral can be defined and estimated using the Strip-Yield model first introduced by Dugdale [66]. The model is first introduced for small-scale crack in a body loaded by tensile forces such that the crack surfaces move apart in the direction of applied forces.In the Strip-Yield model, yielding is assumed to occur only in a narrow strip zone along the crack line. This strip yield zone or the failure zone is severely damaged and

contains voids and discontinuities. In the puncturing phase, when the puncturing force reaches a maximum value, the needle pushes into the failure zone. The failure zone is modelled by the closure yield stress σ_Y acting on the crack faces. Fig. 3.3 shows a strip yield zone with a length of ρ and the corresponding CTOD, δ.

Now we introduce the J integral as a measure of energy release rate in elastic-plastic materials per unit of crack advance. Considering an arbitrary counterclockwise path ($\mathcal{C}$) around the crack tip (see Fig 3.3(b)), the J integral is given by

$$J = \int_{\mathcal{C}} \left(w dy - \sigma_{ij} n_j \frac{\partial u_i}{\partial x} ds \right) \tag{3.29}$$

where w is the strain energy, σ_{ij} are components of the stress tensor, n_j are the components of the unit vector normal to $\mathcal{C}$, ds is a length increment along $\mathcal{C}$ and u_i are displacement vector components.

The J integral and CTOD are used to characterize crack initiation and growth in elastic-plastic fracture. However, these can not be simply used to model time-dependent crack initiation in viscoelastic soft tissue. In order to use the concept of the J integral and CTOD for viscoelastic fracture, we follow the approach proposed by Schapery [65] including the Correspondence Principle. Based on this principle, if the stresses and strains in the elastic body are σ^e_{ij} and ε^e_{ij}, respectively, while the corresponding quantities in the viscoelastic body are σ_{ij} and ε_{ij}, the stresses and strains are related as follows

$$\sigma_{ij} = \sigma^e_{ij}, \quad \varepsilon_{ij} = E_R C * \varepsilon^e_{ij} \; or \; \varepsilon^e_{ij} = \frac{1}{E_R} G * \varepsilon_{ij} \tag{3.30}$$

where $*$ is the mathematical shorthand for the convolution operation, E_R is the long-time modulus of stiffness, and C and G are given by (3.25). Equation (3.30) allows to find a solution for a viscoelastic problem by an analogy with the solution of the reference elastic problem. We can write the generalized time-dependent J integral using the Correspondence Principle

$$J_v = \int_{\mathcal{C}} \left(w^e dy - \sigma_{ij} n_j \frac{\partial u^e_i}{\partial x} ds \right) \tag{3.31}$$

where $.^e$ denotes pseudo values related to the elastic reference problem. Now, we compute the J integral for contour $\mathcal{C}$ shown in Fig. 3.3(b). Considering δ is relatively small ($\simeq 1.5mm$

for needle insertion), the first term in the integral in (3.31) vanishes because $dy = 0$. Also, the only surface tractions are in the y direction ($n_y = 1$ and $n_x = n_z = 0$), thus

$$J_v = \int_{\mathcal{C}} \sigma_{yy} \frac{\partial u_y^e}{\partial x} ds \tag{3.32}$$

Let us define a new coordinate XY at the crack tip with $X = \rho - x$. Note that u_y and σ_{yy} only depend on X and $u_y(X = \rho) = \delta/2$. Thus, J_v becomes

$$J_v = 2\int_0^{\rho} \sigma_{yy}(X) \frac{du_y^e(X)}{dX} dX = \int_0^{\delta^e} \sigma_{yy}(\delta^e) d\delta^e \tag{3.33}$$

Considering σ_{yy} is constant in the failure zone and equal to σ_Y we obtain

$$J_v = \sigma_Y \delta^e \tag{3.34}$$

Based on the Correspondence Principle, $\delta^e = \frac{1}{E_R} G * \delta$. Note that δ is the CTOD and its maximum value during rupture is equal to the needle outer diameter. Considering constant insertion velocity, we can approximate CTOD as a function of time and needle bevel angle, $\delta = 2Vt\tan(\alpha/2)$, where α is the bevel angle (see Fig. 3.5(a)). We can calculate δ^e as

$$\delta^e = G * \delta = 2V\tan(\alpha/2)\left[T + (\tau_1 - \tau_2)(e^{-T/\tau_1} - 1)\right] \tag{3.35}$$

where δ is the CTOD and T is the total time for insertion of the needle tip into the tissue. For constant insertion velocity T is equal to a/V where V is the insertion velocity and a is the length of the needle tip inserted in the tissue at the moment of rupture.

The energy required to advance the needle tip into the tissue is

$$\mathcal{G} = G_c a \delta \tag{3.36}$$

where G_c is the fracture toughness or the work required to advance the needle tip per unit area of crack. During the rupture event J_v is equal to the material resistance against the needle tip insertion $\mathcal{G}$. Also, the axial forces applied to the tip during rupture can be estimated by $F_P = 2\sigma_Y A_t \sin(\alpha/2)$ where, A_t is the contact area between the needle tip and the tissue. We can estimate the maximum puncturing force during crack initiation (F_P) using (3.36) and (3.37)

$$F_P = \frac{A_t G_c a \sin(\alpha/2)}{V\tan(\alpha/2)\left[T + (\tau_1 - \tau_2)(e^{-T/\tau_1} - 1)\right]} \tag{3.37}$$

Note that at relatively high insertion velocities where $T \ll \tau_1$, the dynamic part of (3.37) can be estimated by a second order Taylor series expansion. Also, for small bevel angles, $\tan(\alpha/2) = \sin(\alpha/2)$. Thus, (3.37) reduces to

$$F_P = A_t G_c \frac{\tau_1}{\tau_2} \tag{3.38}$$

Equation (3.38) implies that the maximum puncturing force during needle insertion is independent of insertion velocity and is a function of needle-tissue contact area, the ratio of relaxation and retardation time constants, and the rupture toughness of the material.

Using (3.38), we can quantify the maximum required force to puncture the tissue. Introducing (3.38) in (3.27) and (3.28) we can obtain the optimum insertion velocity for puncturing the tissue

$$V_{opt} = \frac{5 A_t G_c \tau_1}{E_R \tau_2^2} \tag{3.39}$$

3.3.2.2 Tissue Cutting in Insertion

Tissue cutting begins after the needle tip is completely inserted into the tissue and the initial crack in the tissue surface is formed. In this section we will use a criterion based on the rate of energy release per unit length of crack advance, to estimate the cutting force applied to the needle tip. As previously discussed, when J is equal to or larger than the material resistance (G_c), crack tip exceeds. It arrests when $J < G_c$. However, many materials do not fail catastrophically at a particular value of J and CTOD and display a rising resistance called the "R curve" [61]. The rise in the R curve is normally associated with the near tip plastic zone or viscoelastic behaviour of the material. The rising R curve typically reaches a steady-state value as the crack length increases. It can be also affected if the growing crack approaches tissue surface or a different layer of tissue.

Materials with rising R curves can be characterized by the fracture toughness at crack initiation, G_c. Using the definition of the R curve, the crack becomes unstable and propagates when

$$\frac{dJ}{da} \geq \frac{dR}{da} \tag{3.40}$$

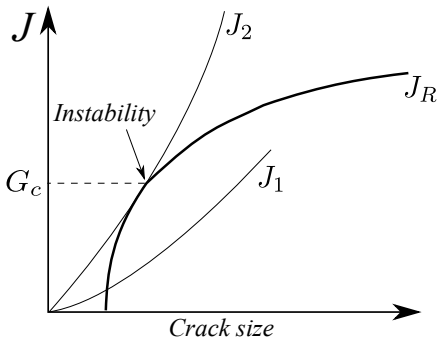

Figure 3.4: R curve and Diagram of J vs. crack length during needle insertion. J_R denotes value of critical J on R curve, J_1 and J_2 represent R curves for two insertions with different load-displacement profiles. J_2 curve is unstable and results in crack growth.

where a is the crack length. We will use the criterion given by (3.40) to predict tissue cutting and estimate the cutting force applied to the needle tip.

To model the needle-tip interaction with soft tissue, the tissue cutting is discretized into small incremental crack growths equal to the size of the needle tip. During tissue cutting, while the needle is being inserted, the tip pushes the tissue back and extends the crack until the CTOD is equal to or bigger than the needle outer diameter so the needle can advance into the tissue. A force distribution with a magnitude of F_C is used to model the needle tip-tissue interaction in the cutting phase (see Fig. 3.5(a)).

To calculate dJ/da, we use the general definition of the J integral given by

$$J = -\frac{d\Pi}{dA} \tag{3.41}$$

where $\Pi = \mathcal{U} - \mathcal{W}$, and $\mathcal{U}$ and $\mathcal{W}$ are the strain energy stored in the tissue and the work of the external forces, respectively.

From Fig. 3.5(a), we have

$$\delta = 2a\tan(\alpha/2) \tag{3.42}$$

Considering that cutting happens at relatively high insertion velocities, we can model the tissue near the needle tip as a linear elastic material. Note that the effects of tissue viscoelastic behaviour are modelled through a time-variant R curve. The cutting force F_C can be calculated using (3.42) as

$$F_C = \int_0^a E_T \delta da = E_T \tan(\alpha/2)a^2 \tag{3.43}$$

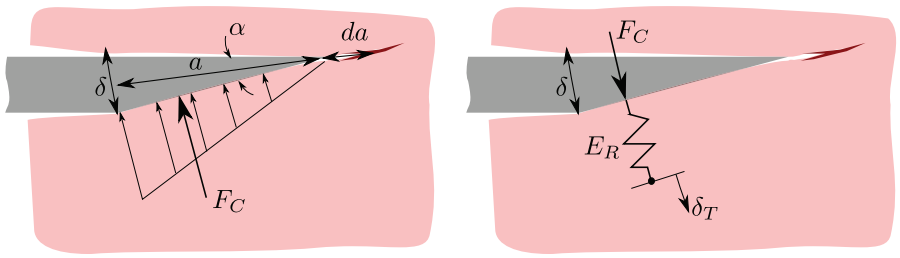

(a) (b)

Figure 3.5: Crack propagation in tissue cutting. (a) Needle tip-tissue interface during cutting represented by a force distribution with magnitude of F_C. δ is the CTOD, a is the needle tip length, da is the incremental crack growth. (b) modeling finite compliance and viscoelastic behaviour of tissue using a linear solid model element. $\delta_t = 0$ is the displacement of the tissue sufficiently far from the crack surface.

where E_T is the tissue stiffness per unit length.

First, we consider the case where the cutting force is constant as the crack grows inside the tissue. We can calculate $\mathcal{U}$ and $\mathcal{W}$ as

$$\mathcal{W} = F_C\delta = 2aF_C\tan(\alpha/2) \tag{3.44a}$$

$$\mathcal{U} = \int_0^{\delta} F_C\, d\delta = \frac{2}{3}aF_C\tan(\alpha/2) \tag{3.44b}$$

In (3.44), we have used (3.42) to simplify the integrals. Introducing (3.44) into (3.41) we have

$$J = -\frac{d\Pi}{dA} = -\frac{1}{w_c}\frac{d\Pi}{da} = \frac{4F_C\tan(\alpha/2)}{3w_c} \tag{3.45}$$

In (3.45), we used $dA = w_c da$, where w_c is the crack thickness equal to the needle outer diameter.

To consider the case where the cutting force is not constant and to simulate the finite compliance of the tissue surrounding a growing crack, we follow the approach proposed by Hutchinson and Paris [67]. In this method, a spring is placed at the interface between the needle tip and the tissue, The base of the spring is fixed at a remote distance and the J integral is calculated over a contour including the spring. The proposed modeling approach is schematically presented in Fig. 3.5(b).

From Fig. 3.5(b), the displacement of the tissue at a remote distance δ_T is

$$\delta_T = \delta^e + \frac{F_C}{E_R} = 0 \tag{3.46}$$

where E_R is the tissue long time stiffness modulus. Differentiating δ_T and J and assuming they only depend on load and crack length, we obtain

$$d\delta_T = \left(\frac{\partial \delta}{\partial a}\right)_{F_C} da + \left(\frac{\partial \delta}{\partial F_C}\right)_a dF_C + \frac{dF_C}{E_R} = 0 \tag{3.47a}$$

$$dJ = \left(\frac{\partial J}{\partial a}\right)_{F_C} da + \left(\frac{\partial J}{\partial F_C}\right)_a dF_C \tag{3.47b}$$

Fixing δ_T, dividing both sides of (3.47b) by da, and substituting dF_C/da from (3.47a), leads to

$$\left(\frac{dJ}{da}\right)_{\delta_T} = \left(\frac{\partial J}{\partial a}\right)_{F_C} - \left(\frac{\partial J}{\partial F_C}\right)_a \left(\frac{\partial \delta}{\partial a}\right)_{F_C} \left[\frac{1}{E_R} + \left(\frac{\partial \delta}{\partial F_C}\right)_a\right]^{-1} \tag{3.48}$$

Now, we can calculate the components of (3.48) using (3.42), (3.43), and (3.45)

$$\left(\frac{dJ}{da}\right)_{\delta_T} = \frac{4\tan^2(\alpha/2)}{\frac{3w_c}{E_R} + 6w_c\sqrt{\frac{\tan(\alpha/2)}{E_T F_C}}} \tag{3.49}$$

Inserting (3.49) in (3.40), we can approximate the cutting force as

$$F_C = \frac{\tan(\alpha/2)}{E_T}\left(\frac{2\tan^2(\alpha/2)}{3w_c dR/da} - \frac{1}{2E_R}\right)^{-2} \tag{3.50}$$

According to (3.50) in the case that the tissue around the cutting area is very soft ($E_R \to 0$), the crack propagation arrests and the CTOD increases while the cutting force significantly decreases. However, when the insertion velocity is high and the effects of tissue deformation around the crack can be neglected ($E_R \to \infty$), CTOD is constant and the cutting force is given by

$$F_C = \frac{9w_c^2(dR/da)^2}{4E_T\tan^3(\alpha/2)} \tag{3.51}$$

From (3.50) and (3.51), it can be inferred that at high insertion velocities when E_R is relatively high, the cutting force decreases. Also, the cutting force is a function of $\frac{(dR/da)^2}{E_T}$. As the stiffness of the crack surface (E_T) increases compared to the rate of energy release per unit of crack advancement dR/da, all the work applied to the crack tip leads to crack propagation rather than pushing up the crack surface, and consequently the needle slips through the tissue with a smaller cutting force.

Also, (3.50) states that the cutting force is not directly dependent on the crack length. However, depending on the R curve of the material it can be affected by velocity and crack length at the beginning of the insertion and when the R curve reaches its steady state, the value of the cutting force becomes almost constant. The rising R-curve can be estimated by the following exponential function

$$R(a) = b_0 \left[1 - exp(-b_1(a - b_2))\right] \tag{3.52}$$

where b_0, b_1, and b_2 are constant parameters. b_2 denotes the depth at which the crack initiate and a is the crack length equal to the insertion depth. Inserting (3.52) into (3.50) gives

$$F_C = \frac{\tan(\alpha/2)}{E_T} \left(\frac{2\tan^2(\alpha/2) exp(b_1(a - b_2))}{3 b_3 w_c} - \frac{1}{2E_R} \right)^{-2} \tag{3.53}$$

where $b_3 = b_0 b_1$. For relatively high insertion depths where $a >> b_2$, (3.53) simplifies to

$$F_C = \frac{4\tan(\alpha/2) E_R^2}{E_T} \tag{3.54}$$

Based on (3.53) and (3.54) the cutting force initially decreases with insertion depth and eventually converges to a constant value given by (3.54).

3.4 Needle-Tissue Friction Model

In modeling the friction force along the needle shaft, three regimes of interest exist that need to be investigated: (1) Presliding: the friction exists between needle and tissue while the needle is in the stuck state. (2) Break-away: the transition of the needle-tissue between the stuck state and the sliding state. (3) Sliding: contact forces exist in between the needle and soft tissue during the insertion.

The three stages can be accurately explained by LuGre model [68]. The model has been previously used to model needle-tissue friction forces [69]. LuGre model can simultaneously model all friction regimes. Fig. 3.6 shows a graphic representation of LuGre model. The model simulates a spring-damper like behaviour at the contact between surface asperities.

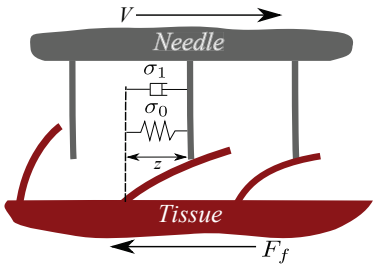

Figure 3.6: A schematic of elastic deformation of surface asperities at the microscopic level in LuGre friction model.

A complete description of this model can be found in [68]. LuGre model presents the following expression for the friction force:

$$\dot{z} = v - \sigma_0 \frac{|V|}{g(V)} z \tag{3.55a}$$

$$F_f = \sigma_0 z + \sigma_1 \dot{z} + \sigma_2 V \tag{3.55b}$$

where F_f is the friction force, z is the elastic deformation of surface asperities, and V is the velocity between the two surfaces in contact. Considering the translational motion of the needle and neglecting tissue displacement, V is equal to the needle insertion velocity. σ_0 is the stiffness coefficient of the microscopic deformations during the pre-sliding displacement, σ_1 is the damping coefficient associated with z, and σ_2 is the viscous damping coefficient. For systems with asymmetry in friction, different values for the parameters can be chosen for positive and negative directions of motion. The $g(v)$ term in (3.55a) captures the Stribeck's effect and is given by [70]

$$g(v) = f_c + (f_s - f_c)e^{-\Upsilon|v|} \tag{3.56}$$

where f_s is the stiction friction force, f_c the Coulomb friction, and Υ is a constant coefficient.

3.5 Tissue Reaction Force Model

The 2D distributed force F_s shown in Fig. 2.2 represents needle-tissue interaction forces due to tissue compression. In order to find F_s, first we calculate the tissue deformation

as a result of needle deflection. Next, we implement a viscoelastic tissue model to relate the tissue reaction force to the the tissue deformation and obtain F_s. The magnitude of the approximated interaction forces are relative to the total deformation of tissue caused by needle deflection. If we discretize an infinitesimal insertion of the needle into three parts, namely, pre-cutting, tissue cutting, and tissue deformation (see Fig. 3.7(a)). In the cutting phase, the needle cuts through the tissue and opens up a path called *cutting path*. Then, cutting force is applied perpendicularly to the tip and causes needle deflection. Consequently, the soft tissue is deformed by as much as the difference between the cutting path and the final needle position.

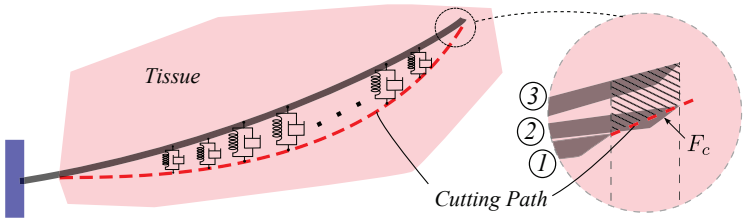

(a)

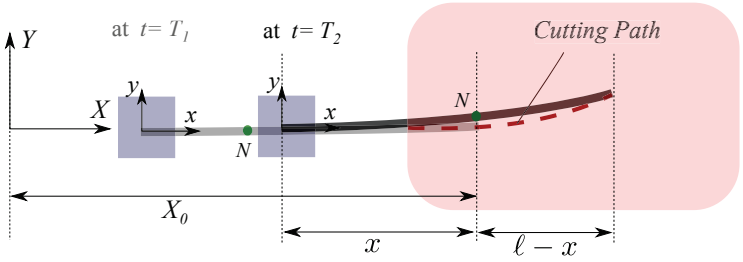

(b)

Figure 3.7: A schematic of needle insertion in soft tissue. (a) Infinitesimal tissue cutting consists of three steps: 1) needle at the beginning of insertion; 2) needle cutting through the tissue; 3) cutting force applied perpendicularly to the tip causing needle deflection and tissue deformation. Tissue deformation is the difference between the cutting path and the final needle position (hatched area) and less than the needle deflection from its unbent position. Tissue reaction force is modeled by series of Kelvin-Voigt viscoelastic elements placed in between the cutting path and the needle. (b) Schematic of needle insertion and cutting path at times T_1 and T_2.

To find the tissue reaction forces applied to a certain element of the needle, we calculate the amount of tissue deformation by comparing the global deflection of the needle element (i.e., needle shape) with the global position of needle tip (i.e., the cutting path) when it

was in the current position of the needle element. This fact is explained in Fig. 3.7(b). We are interested in finding the tissue deformation in the proximity of the point N on the needle, which is located at position X_0 with respect to the inertial frame at the present time ($t = T_2$). To this end, we need to find the needle cutting path and compare it to the current needle deflection. The cutting path is the needle tip deflection when it passed X_0 at a time $t = T_1 < T_2$. This has to be compared to the current deflection of the needle (position of point N) at $t = T_2$. The difference is the tissue deformation at position X_0 with respect to the inertial frame at the present time ($t = T_2$).

Based on Fig. 3.7(b), the tissue deformation is equal to $\omega(x,t) - \omega(\ell, t-\tau)$, where τ is the time delay used to find the cutting path at the current position of point N on the needle, and $\omega(\ell, t-\tau)$ is the deflection of the needle tip or the cutting path at time $t-\tau$. In Fig. 3.7(b), for element N of the needle, we have $\tau = T_2 - T_1$. Also, Assuming needle deflection is relatively small compared to the length of the needle, using Fig. 3.7(b) we can say $\tau = \frac{\ell - x}{V}$, where V is the needle insertion velocity. Now to relate tissue deformation to tissue reaction force, we use a conventional viscoelastic model known as the Kelvin-Voigt model. In Kelvin-Voigt model, tissue is modeled as a Hookean spring in parallel with a Newtonian damper. The tissue reaction force can be defined as

$$F_s(x,t) = K_s \left[\omega(x,t) - \omega(\ell, t-\tau)\right] + C_s \dot{\omega}(x) \tag{3.57}$$

where K_s and C_s are the tissue stiffness and damping coefficient per unit length of needle.

The presented novel tissue interaction model enables accounting for the effect of 180° axial rotation of the needle tip on the needle deflection. When the needle is axially rotated during the insertion, the orientation of the bevel tip changes and consequently the direction of the transverse component of cutting force changes too, causing the needle to bend in the opposite direction. The part of the needle that is already inside the tissue is forced to stay close to the path produced by the needle beforehand, i.e., the cutting path. Thus, the needle is confined in the tissue and the model can simulates multiple bending in the needle as a result of axial needle rotations.

The tissue reaction force model given by (3.57) is in fact a time-delayed system. F_s, the tissue reaction force is a function of the needle deflection at previous times. Control of time-

delayed systems is very challenging and, therefore, it is desirable to simplify the system. Here, a novel mathematical approach is presented to reduce the time-delayed system of differential equations to a simple system of ODEs. In our approach we use previous values of the system states to estimate the current ones. This idea was first proposed in [71].

Introducing (3.57) into $\hat{S}$ in (3.19) and substituting assumed-mode approximation for the needle deflection gives

$$\begin{aligned}\hat{S}_i = &\int_{\ell-X}^{\ell}\left[K_s\sum_{m=1}^{n}\phi_m(t)W_m(x)+C_s\sum_{k=1}^{n}\dot{\phi}_k(t)W_k(x)\right]W_i(x)dx\\ &-\int_{\ell-X}^{\ell}\left[K_s\sum_{j=1}^{n}\phi_j(t-\tau)\right]W_i(x)dx\end{aligned} \tag{3.58}$$

The second integral in (3.58) contains the delay term, τ. Now by expanding the delay term in (3.58) and replacing x as a function of the delay by $\tau = \frac{\ell-x}{V}$ gives

$$\begin{aligned}&\int_{\ell-X}^{\ell}\left[K_s\sum_{j=1}^{n}\phi_j(t-\tau)\right]W_i(x)dx =\\ &\frac{K_sV}{\kappa_i}\int_0^t\left[\sum_{j=1}^{n}\phi_j(t-\tau)\Big(\sin(\lambda_i\tau+\beta_i)-\gamma_i\cos(\lambda_i\tau+\beta_i)\Big)\right]d\tau+\\ &\frac{K_sV}{\kappa_i}\int_0^t\left[\sum_{k=1}^{n}\phi_k(t-\tau)\Big(-\sinh(\lambda_i\tau+\beta_i)+\gamma_i\cosh(\lambda_i\tau+\beta_i)\Big)\right]d\tau\end{aligned} \tag{3.59}$$

where $\lambda_i = \frac{-\beta_i V}{\ell}$. Close scrutiny of (3.59) reveals that the above technique has transformed the system of ODEs in (3.58) to a convolution integral. This is very promising because it facilitates solving (3.58) without having to deal with the system delay. Below, we tackle the problem by determining an equivalent system whose time response will take the form of the convolution integral in (3.59), i.e., the same as the time response of the ODE system in (3.58). To do so, first we take Laplace transform of the two terms on the right side of (3.59), next we sort out the equations and perform basic mathematical simplifications. Finally, taking inverse Laplace gives

$$\begin{aligned}\ddot{\varphi}_{ij}+\lambda_i^2\varphi_{ij} &= [\sin(\beta_i)-\gamma_i\cos(\beta_i)]\dot{\phi}_j+\lambda_i[\gamma_i\sin(\beta_i)+\cos(\beta_i)]\phi_j\\ \ddot{\chi}_{ij}-\lambda_i^2\chi_{ij} &= [-\sinh(\beta_i)+\gamma_i\cosh(\beta_i)]\dot{\phi}_j+\lambda_i[\gamma_i\sinh(\beta_i)-\cosh(\beta_i)]\phi_j\end{aligned}$$

With two new state variables

$$\begin{aligned}\varphi_{ij}(t) &= \int_0^t \phi_j(t-\tau)\Big(\sin(\lambda_i\tau+\beta_i) - \gamma_i\cos(\lambda_i\tau+\beta_i)\Big)d\tau,\\ \chi_{ij}(t) &= \int_0^t \phi_j(t-\tau)\Big(-\sinh(\lambda_i\tau+\beta_i) + \gamma_i\cosh(\lambda_i\tau+\beta_i)\Big)d\tau\end{aligned} \tag{3.60}$$

Using the new state variables, we can eliminate the delay in the needle steering model and rewrite the term corresponding to the tissue model ($\hat{S}$) in (3.19) as

$$\hat{\mathbf{D}}\dot{\boldsymbol{\phi}} + \hat{\mathbf{N}}\boldsymbol{\phi} + \boldsymbol{\varsigma} = 0 \tag{3.61}$$

where

$$\begin{aligned}&\hat{D}_{ij} = C_s\int_{\ell-X}^{\ell} W_j(x)W_i(x)dx, \quad \hat{N}_{ij} = K_s\int_{\ell-X}^{\ell} W_j(x)W_i(x)dx,\\ &\varsigma_i = -\frac{K_sV}{\kappa_i}\sum_{j=1}^{n}(\varphi_{ij}(t)+\chi_{ij}(t))\end{aligned} \tag{3.62}$$

Note that (3.61) is the needle-tissue interaction model and depends only on the needle shape and the tissue mechanical characteristics and we have eliminated the delay term. The main assumption of the proposed approach is that the continuous states and system dynamics remain almost unchanged during sampling time which is valid for control and simulatition of needle insertion at high sampling frequencies. (3.61) is a system of ODEs that should be solved in conjunction with the needle steering model in (3.18) to find the needle deflection.

3.6 Experimental Model Identification and Validation

In the following, a series of needle insertion experiments are performed to:

1. Identify the friction force model and validate its dependency on velocity as given by (3.55).

2. Identify and validate the tissue cutting force model. This includes: i) identifying the model for cutting in homogeneous tissue given by (3.20), ii) identifying the tissue puncturing model and statistically validating the dependency of the puncturing force

on the velocity as predicted by (3.26) and the maximum predicted puncturing force estimated by (3.38), and iii) identifying and validating the model for cutting force during insertion in heterogeneous tissue as predicted by (3.53) and (3.54).

3. Identify and validate the parameters of the time-delayed tissue reaction force model discussed in Section 3.5.

When all the models are identified separately, all the model parameters for various needle/tissue interaction models are inserted in the hybrid model of needle steering in (3.18). Then, the model predicted needle deflection is compared with experimental needle deflection to validate the comprehensive model of needle steering.

3.6.1 Materials and Equipment

In order to perform needle insertion into soft tissue, the setup shown in Appendix A, Fig. A.1 is used. Two different needles are used to perform insertions. One is a standard 18-gauge brachytherapy needle (Eckert & Ziegler BEBIG Inc., CT, USA) made of stainless steel. The second needle is more flexible and made of Nitinol wire (Kellogg's Research Labs, Plymouth, NH, USA) with a diameter of 1 mm and a length of 18 mm. The wire is inserted into the tip of a shortened needle with length of 1.2 mm and fixed in place with adhesive. The values of the needles physical parameters are given in Table 3.2. In order to evaluate the ability of the model in capturing the effects of the grid template on needle deflection, an 18G grid template is used in certain needle insertions.

Three types of tissue are used in the experiments: plastisol, porcine gelatin, and ex-vivo beef. The plastisol tissue is made of 80% (by volume) liquid plastic and 20% plastic softener (M-F Manufacturing Co., USA). The gelatin phantom is made by mixing porcine gelatin powder (Sigma-Aldrich Co., Canada) with water. The weight ratio of gelatin-to-water in the mixture is 18%. For ex-vivo tests, a piece of beef loin is used. Bovine tissue is embedded in gelatin to get a smoother surface on top, thus increasing the contact surface between the ultrasound probe and the tissue and as a result reducing noise in the ultrasound images. Young's elasticity moduli of the three tissues calculated using indentation tests,

Table 3.2: Values of constant known parameters of the model.

Brachytherapy needle							
E [GPa]	ℓ [m]	ρ [Kg/m^3]	r_{in} [m]	r_{out} [m]	A [m^2]	I [m^4]	α [°]
200	0.2	8030	0.5e-3	0.63e-3	4.81e-7	7.75e-14	20
Nitinol wire							
E [GPa]	ℓ [m]	ρ [Kg/m^3]	r_{out} [m]	A [m^2]	I [m^4]		α [°]
75	0.18	6500	0.5e-3	7.85e-7	1.962e-13		20
Grid template					Carrier		
K_t [N/m]		l_t [m]		d_t [m]	m_c [kg]		
10e7		0.02		0.005	0.045		

are reported in Table 3.7. The elasticity of the synthetic tissues are similar to what is found in animal tissue [72]. The values of the known model parameters used in simulations are given in Table 3.2.

3.6.2 Friction Model Validation

In order to identify the parameters of the friction force model, similar experiments as what is presented in [19] is used to separately measure the friction force by eliminating or minimizing the influence of other interaction forces such as the cutting force and the tissue compression force. First, a groove is hollowed out inside the tissue. Next the needle is inserted into the tissue and axial force is measured while the needle tip is in free space in the carved-out track. This force corresponds to needle-tissue friction force plus needle inertia forces. Knowing the acceleration profile and the mass of the needle plus its carrier, we can easily calculate the friction force per unit length of the needle.

To identify the friction model parameters, we employed the procedure based on friction-velocity mapping introduced in [73]. Friction-velocity mapping was developed by performing needle insertions under the aforementioned conditions at different insertion velocities. Five trials were performed. In each trial the needle base displacement was a sinusoidal

Table 3.3: Experimentally identified parameters of the friction model. Negative and positive directions of insertion are denoted by N and P, respectively.

Tissue		σ_0 [N/mm^2]	σ_1 [N.sec/mm^2]	σ_2 [N.sec/mm^2]	f_s [N/mm]	f_c [N/mm]	Υ [sec/mm]
Ex-vivo	N	0.0521	0.0145	-0.0051	0.294	1.0611	0.0078
	P	0.1415	0.0070	0.0049	0.262	0.0974	0.0051
Gelatin		2.86e4	1.75e2	1.62e3	26.20	3.80	27.3
Plastisol		9.71e3	-7.05e2	1.25e3	43.75	40.87	546.6

signal with an initial frequency of 0.05 Hz reaching to 0.2 Hz in 200 seconds, corresponding to insertion velocities of 5 to 40 mm/sec. The RMSE value of the friction force prediction for a single needle insertion and retraction in ex-vivo tissue is 0.0016 N/mm. The identified values of the friction model are listed in Table 3.3. Fig. 3.8 shows the result of friction identification including the estimated friction per unit length of the needle versus time for the ex-vivo tissue. Note that the magnitude of friction force directly depends on the contact area between the needle shaft and the tissue. In our ex-vivo tests, a bovine tissue with a thin layer of skin and thin layers of connective tissue was used. Thus, we assumed the friction model coefficients are the same for all the layers. Fig. 3.9 shows the experimental friction-velocity mapping for the three different tissues.

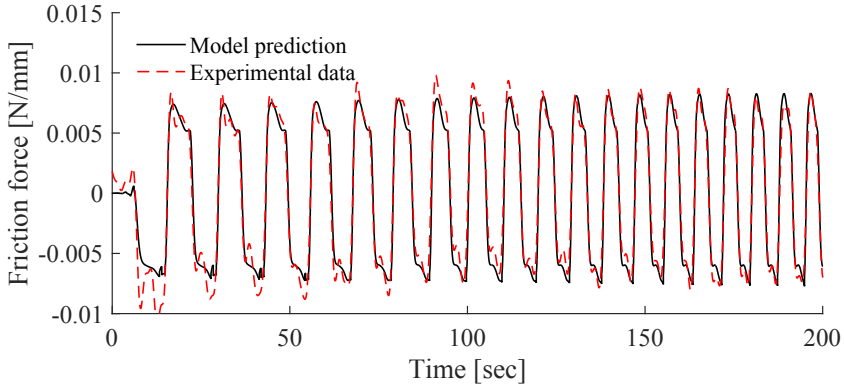

Figure 3.8: Experimental and model predicted friction force per unit length of the needle with respect to time.

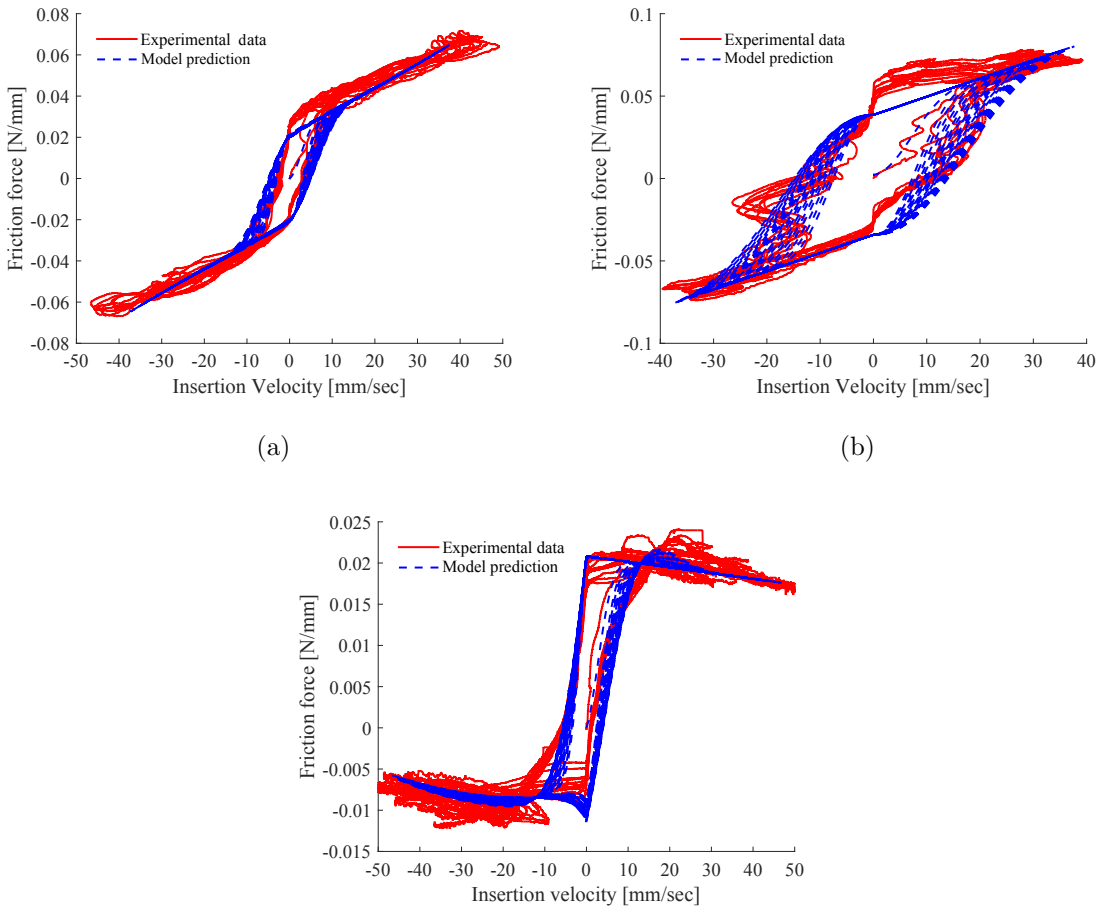

Figure 3.9: Estimated friction-velocity mapping and experimental data. (a) Gelatin (b) Plastisol (c) Bovine tissue

3.6.3 Tissue Cutting Model Validation

3.6.3.1 Tissue Cutting Model in Homogeneous Tissue

Experiments are designed and performed to identify the parameters of the cutting force model given by (3.20). To measure the magnitude of the cutting force, a shortened needle is inserted into the tissue at 30 different constant velocities between 5 and 40 mm/sec. Knowing the magnitude of friction from the model identified in the previous step, we can simply calculate the magnitude of the cutting force for different insertion velocities. Using measured values, the parameters of the fracture-based cutting force model presented by

Table 3.4: Experimentally identified parameters of the cutting force model for homogeneous tissue.

Tissues	V_l [m/sec]	K_{I0} [Pa $\sqrt{\text{m}}$]	m	$RMSE$ [N]
Gelatin	0.145	2.707e6	1.117	0.079
Plastisol	0.177	7.620e5	0.851	0.087

(3.20) and (3.21) are identified. Fig. 3.10 displays the mean cutting force over the trials versus needle insertion velocity. As predicted by (3.20) and (3.21), the average cutting force is an increasing function of velocity. The values of identified parameters are presented in Table 3.4. Root-mean-square error (RMSE) is calculated as $\sqrt{\frac{\sum_{k=1}^{n}(\hat{y}_k - y_k)^2}{n}}$ and is used as a measure of the differences between values predicted by each identified model, $\hat{y}$, and the values actually observed in the experiments, y, for n data points.

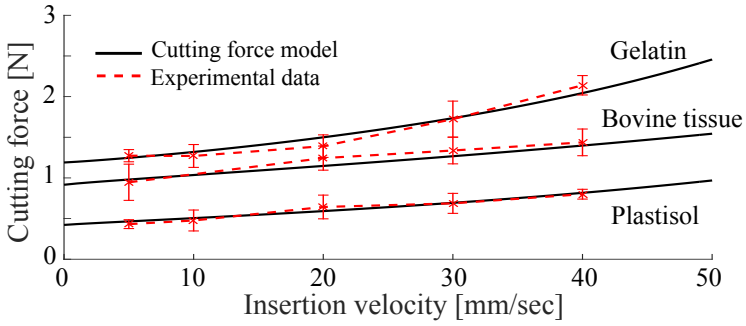

Figure 3.10: A comparison between experimentally-obtained cutting force in homogenous tissue and cutting force model prediction versus insertion velocity. Error bars denote standard deviation.

3.6.3.2 Tissue Cutting Model in Heterogeneous Tissue

First, we identify parameters of the tissue puncturing model. Relaxation tests are performed to identify the viscoelastic model given in (3.23). In the relaxation tests the needle is pressed against the tissue surface and the exerted forces are measured via the force sensor shown in Fig. A.1. In the experiments the needle is moved to five different depths (3, 5, 8, 10, and 12 mm) at three different velocities (5, 10, and 20 mm/sec). Three trials were performed for each combination of velocity and depth, leading to a total of 45 relaxation tests. Parameters of the model are identified by fitting the data to (3.23) using

Table 3.5: Experimentally identified parameters for the tissue puncturing model.

μ_1 [N/mm]	μ_2 [N/mm]	η [N.sec/mm]	τ_1 [sec]	τ_2 [sec]	RMSE [N]
0.0343	0.0557	0.0665	1.9388	5.0872	0.0183

the least-squares method. Tissue model predictions and experimental data for 6 mm tip displacement at three velocities are shown in Fig. 3.10. Table 3.5 provides the values of the identified parameters and Root-Mean-Squared-Error (RMSE) of the fitted model.

The next experiment is designed to validate the model-predicted maximum puncturing force given in (3.38). The needle is pressed against the tissue until the puncturing happens. We use the identified parameters of the viscoelastic model in (3.26) to estimate the force-displacement during the puncturing phase and compare it to the recorded data. Ten tissue puncturing experiments were performed. Two sample results are shown in Fig. 3.11(a). Maximum prediction error and RMSE of the prediction in the ten trials are 0.265 N and 0.107 N, respectively.

Also, fracture toughness (G_c) for the tissue is identified by fitting the model in (3.38) to the forces measured at the moment of puncturing. Magnitude of estimated rupture toughness per unit area of crack is 132.8 kN/m^3 which is consistent with previous experimentally measured values of rupture toughness for biological tissue samples [20]. In order to measure the magnitude of puncturing force, the needle was inserted in the tissue at 7 different velocities. 5 trials were performed for each velocity. The experimental value of maximum puncturing force for different velocities is shown in Fig. 3.11(b). As it is predicted by (3.38) and can be seen in Fig. 3.11(b) the maximum puncturing force at high insertion velocities is almost independent of insertion velocity. The estimated maximum puncturing force using (3.38) is 1.28 N with 95% confidence bounds of $\pm$0.1 N.

Now using the identified friction force and by subtracting it from recorded axial forces during needle insertion we can measure the cutting force in heterogenous tissue during the needle insertion. To identify the cutting force, the needle is manually inserted up to 25

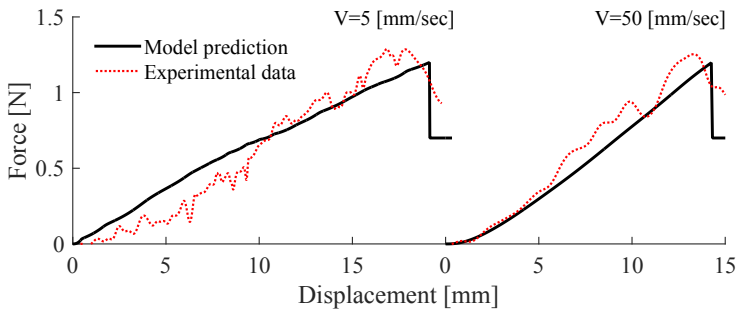

(a)

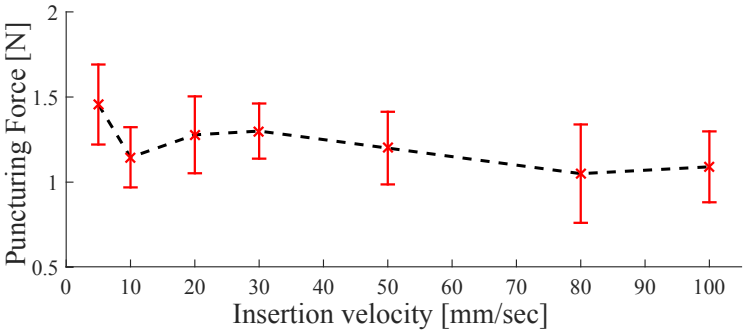

(b)

Figure 3.11: Result of tissue puncturing experiments. (a) Force versus deformation of tissue for velocities of 5 and 50 mm/sec. (b) Average of maximum puncturing force versus velocity. Error bars denote standard deviation.

different depths. Next, the axial force at the base of the needle is increased in steps of 0.05 N until the needle begins to move inside the tissue. Knowing the value of crack length at the moment of instability (the depth at which the needle suddenly moves in response to the applied force) and using (3.53) and (3.54), we can identify the parameters of the R-curve and estimate tissue stiffness at the crack surface (E_T). Identified values of the cutting force model are given in Table 3.6. The value of model predicted cutting force is presented in Fig.3.12.

3.6.4 Tissue Reaction Force Model Validation

The purpose of the next experiment is to identify the parameters of the viscoelastic model of the tissue (i.e., K_s and C_s). Several relaxation tests are performed to estimate the values of K_s and C_s. The relaxation test is performed by giving a position step input to the indenter

Table 3.6: Experimentally identified parameters of the cutting force model during insertion in heterogeneous tissue.

E_T	b_1	b_2	b_3
[N/mm^2]	[1/mm]	[mm]	[N/mm^2]
2.4e-3	0.07	5.1	500

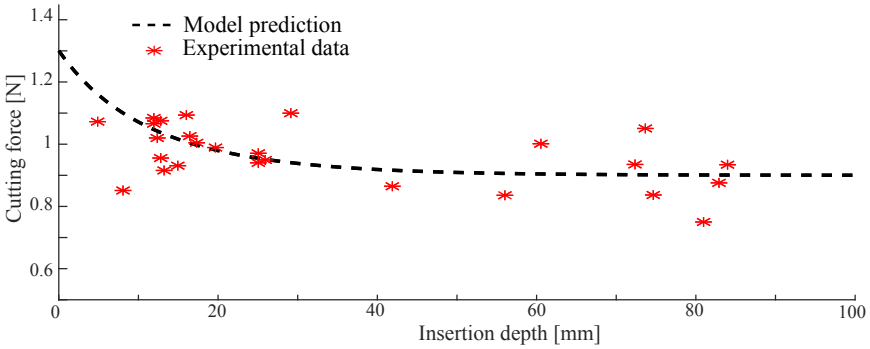

Figure 3.12: Experimental and model predicted cutting force vs insertion depth in heterogeneous tissue.

and measuring the exerted force. The experiments are performed with a insertion velocity of 10 mm/sec and indentation depths of 5, 8, 10 mm. Results of relaxation tests performed on plastisol tissue are shown in Fig. 3.13. We calculate tissue viscosity and tissue stiffness by fitting the data to the Kelvin-Voigt model using the least-squares method. Next, in order to calculate the values of K_s and C_s more precisely, we fitted the deflection data for three insertions at three different velocities (10, 20, and 50 mm/sec) to the proposed model of needle steering using nonlinear least-squares. Values of the identified parameters from the relaxation tests are used to define the initial values and lower and upper boundaries in the optimization. Table 3.7 provides the final values of the identified parameters and RMSE of the fitted models.

In the proposed research, the tissue puncturing is studied as a two phase event – tissue deformation and crack initiation. Equations (3.27) and (3.28) can be used to predict contact force between the needle tip and the tissue and its relation to tissue deformation and velocity in the deformation phase. Comparing force response of the needle-tissue system at constant velocities of 5 and 10 mm/sec in Fig. 3.11, we can see that in the deformation phase, the contact force increases with increasing velocity. This is consistent

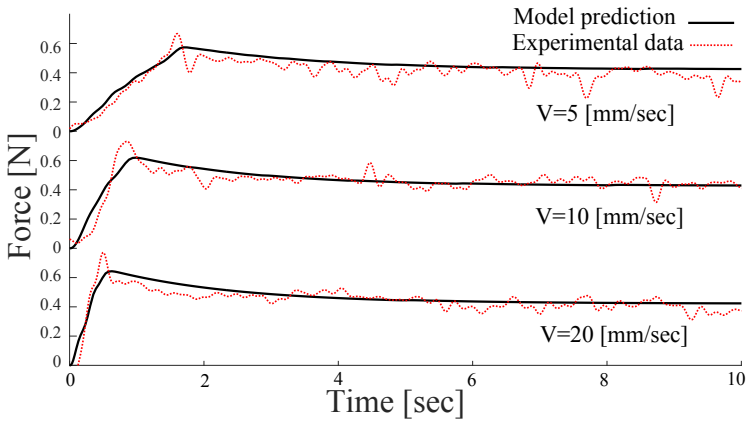

Figure 3.13: Results of relaxation tests performed on plastisol tissue. Needle force versus time during tissue deformation for velocities of 5, 10, and 20 mm/sec

Table 3.7: Experimentally identified parameters for tissue reaction model. 10 trials are performed for each tissue type.

Tissues	E [KPa]	K_s [N/m^2]	C_s [N.sec/m^2]	$RMSE$ [mm]
Gelatin	59.9±8	1.58e5	8.57e3	0.197
Plastisol	25.6±9	0.59e5	8.01e4	0.408
Beef	24.5±5	3.20e5	9.62e4	0.251

with (3.26). Also, according to (3.27), at high insertion velocities the force response of the system is almost independent of velocity and the force increases linearly with the needle tip displacement. This can be seen by comparing the force responses for velocities of 10 and 20 mm/sec in Fig. 3.13, where the ratio of force to the needle tip displacement is almost the same. 1.081 and 0.985 for velocities of 10 mm/sec and 20 mm/sec, respectively.

3.6.5 Needle Steering Model Validation and Discussions

In this section, we intend to 1) validate all the needle/tissue interaction models combined, and 2) validate the needle steering model presented in Section 3.2.

In order to evaluate our proposed analytical needle/tissue interaction models, we compare the experimentally obtained axial forces applied to the needle during a full needle

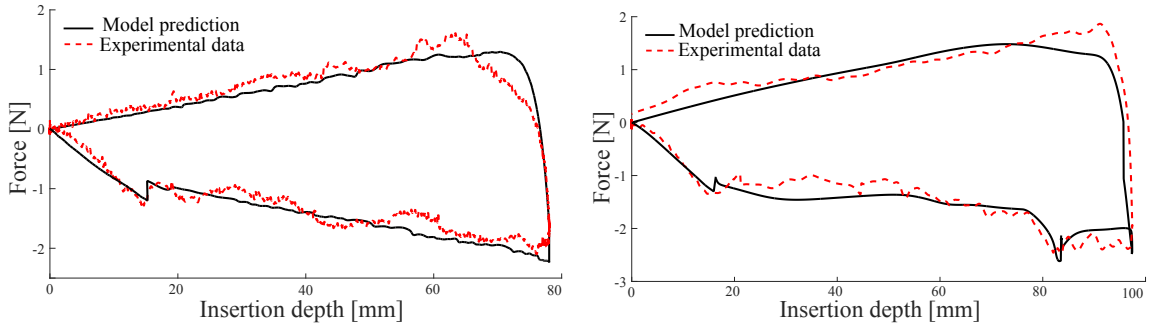

(a) V=5 mm/sec

(b) V=100 mm/sec

Figure 3.14: Model prediction and experimental data for axial force during needle insertion and retraction at velocities of (a) 5 mm/sec and (b) 100 mm/sec.

insertion and retraction to the predictions of the identified models. Note that the main three interaction forces studied in this work (i.e., puncturing, cutting, and friction force) can simply be added together to model the overall forces applied to the needle shaft. At the puncturing phase the needle is still outside the tissue and the cutting force and friction are zero. When the needle tip is inserted into the tissue the puncturing force is zero and we have a combination of cutting force and friction (see Fig. 2.2(e)). Friction is an axial force along the needle shaft and the cutting force is a force applied perpendicular to the needle tip (Fig. 2.2(c)). Thus the cutting force has two components, an axial and a transverse component. Neglecting the effects of tissue deformation one can say that the axial force recorded at the base of the needle during the needle insertion is the summ of friction and the axial component of the cutting force. During needle retraction the cutting force is zero and there is only friction along the needle shaft.

Combining the force models together as discussed above we can model all the interaction forces during insertion and retraction. Results for insertion velocities of 5 and 100 mm/sec are shown in Fig. 3.14. Note that in Fig. 3.14(b) the needle passes through different layers of tissue and there are two puncturing phases at depths of 16.5 (at the beginning of insertion) and 82 mm. RMSE and maximum error of force prediction for velocity of 5 mm/sec are 0.104 N and 0.81 N, respectively. RMSE and maximum error for insertion at 100 mm/sec are 0.182 N and 0.73 N, respectively. It is clear from the figure that the models successfully estimate needle interaction forces with the tissue in all phases of insertion including tissue

cutting and puncturing.

Now we can validate the whole needle steering model by comparing the model predicted needle deflection with experimental needle deflections performed in various tissue types. In the validation experiments, the insertion depth is fixed for each needle type – 140 mm for the brachytherapy needle and 120 mm for the Nitinol wire. The needle tip deflection is computed through image processing. For the gelatin and plastisol tissues, images are acquired using the HD camera (see Fig. A.1). For insertions in the bovine tissue, ultrasound images are used to find the needle deflection using the method proposed in [74]. The values of the known model parameters used in simulations are given in Table 3.2. The stiffness of the spring modeling the template is arbitrarily chosen to be very large (10e7 N/m).

Fig. 3.15 shows the needle deflection for the different needles inserted in tissues at velocities of 5, 20, and 40 mm/sec. Table 3.8 compares the experimental and model prediction of tip deflection values at 6 different velocities for insertion, each of which has been attempted 5 times. Final tip position in the experiments $\omega_{exp}(\ell)$, final tip position in the simulation $\omega_{sim}(\ell)$, maximum tip error e_{max}, and standard deviation of final tip position $\sigma(\ell)$ are listed in Table 3.8. The largest deviation in final tip deflection was observed for plastisol at insertion velocity of 50 mm/sec (7%), while the smallest difference was observed for gelatin at insertion velocity of 5 mm/sec (3.2%).

We performed experiments involving 180^o axial rotation of the needle. The brachytherapy needle is inserted in tissues at a speed of 5 mm/s while either a single rotation is performed at a depth of 40 or 80 mm, or double rotations are performed at depths of 40 and 80 mm. Four needle insertions are performed for each scenario. The resulting needle tip deflection is shown in Fig. 3.15. The results of this experiment are summarized in Table 3.8. The model captures the effect of axial tip rotation on the needle deflection for all three tissues and the maximum error in predicting the tip position is 0.74 mm at a depth of 135 mm for insertion in gelatin with a double rotation. In model predictions, when the needle is axially rotated, there is a small jump in needle trajectory that corresponds to a sudden change of the cutting force orientation. However, this sudden deflection is small (a maximum of 0.61 mm in plastisol). The magnitude of this jump depends on the value of the velocity of needle rotation, cutting force, and tissue characteristics.

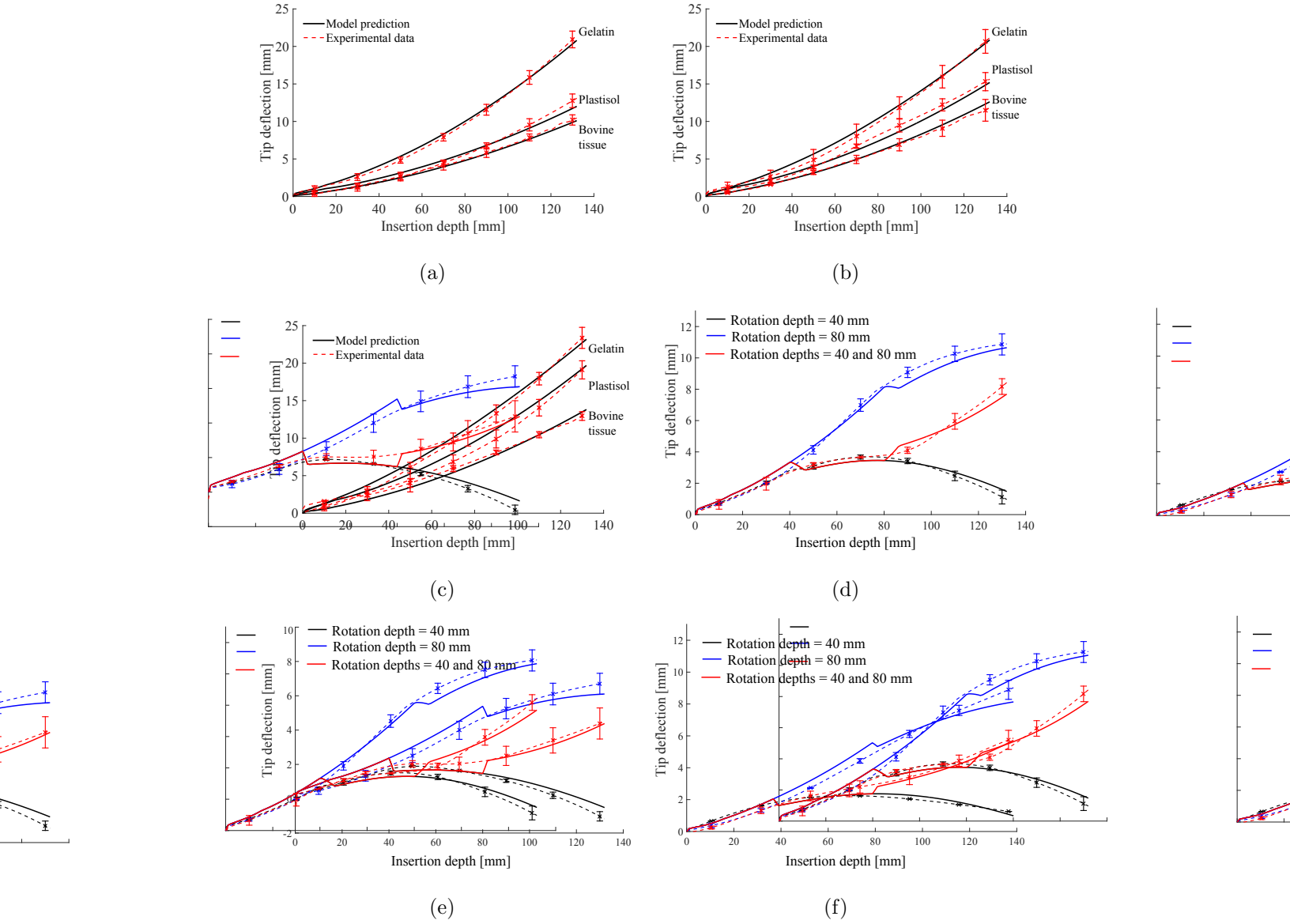

Figure 3.15: A comparison of experimentally-obtained needle tip deflections and the corresponding model predictions for needle insertion in plastisol, gelatin, and bovine tissue. (a) V=5 [mm/sec] without axial rotations. (b) V=20 [mm/sec] without axial rotations. (c) V=40 [mm/sec] without axial rotations. (d) V=5 [mm/sec] with axial rotations in gelatin. (e) V=5 [mm/sec] with axial rotations in plastisol. (f) V=5 [mm/sec] with axial rotations in bovine tissue. Solid and dashed lines denote model prediction and experimental data, respectively.

Table 3.8: Results of insertion of the needle at different velocities with and without axial rotation(s).

		Gelatin					Plastisol					Bovine tissue				
V [mm/sec]	Rotation depth(s)	$\omega_{exp}(\ell)$ [mm]	$\omega_{sim}(\ell)$ [mm]	e_{max} [mm]	$\sigma(\ell)$ [mm]	RMSE [mm]	$\omega_{exp}(\ell)$ [mm]	$\omega_{sim}(\ell)$ [mm]	e_{max} [mm]	$\sigma(\ell)$ [mm]	RMSE [mm]	$\omega_{exp}(\ell)$ [mm]	$\omega_{sim}(\ell)$ [mm]	e_{max} [mm]	$\sigma(\ell)$ [mm]	RMSE [mm]
5	–	21.47	20.80	0.67	1.11	0.348	13.09	12.20	0.88	0.91	0.576	10.44	10.11	0.47	0.68	0.189
10	–	22.04	21.11	0.93	0.94	0.421	13.85	13.48	0.49	0.56	0.442	10.25	11.16	0.91	0.43	0.373
20	–	21.14	20.85	0.49	1.50	0.466	15.62	15.39	0.63	1.01	0.423	11.85	12.61	0.72	1.14	0.278
30	–	22.51	22.14	0.82	1.32	0.507	16.95	18.36	1.41	1.15	0.621	12.44	13.21	0.77	0.72	0.279
40	–	23.91	23.17	0.72	1.35	0.524	19.63	19.88	0.64	1.18	1.008	13.27	13.80	0.67	0.58	0.625
50	–	25.12	26.02	1.21	2.10	0.642	23.2	25.33	1.59	1.78	0.726	–	–	–	–	–
5	40 mm	0.96	1.47	0.36	0.54	0.261	-1.17	-0.51	0.60	0.37	0.334	1.21	0.98	0.25	0.12	0.154
5	80 mm	10.89	10.65	0.72	0.77	0.380	6.75	6.10	0.68	0.62	0.437	9.02	8.13	0.70	0.59	0.403
5	40 & 80 mm	8.42	7.68	0.74	0.65	0.332	4.44	4.28	0.51	0.92	0.306	5.85	5.62	0.45	0.60	0.271

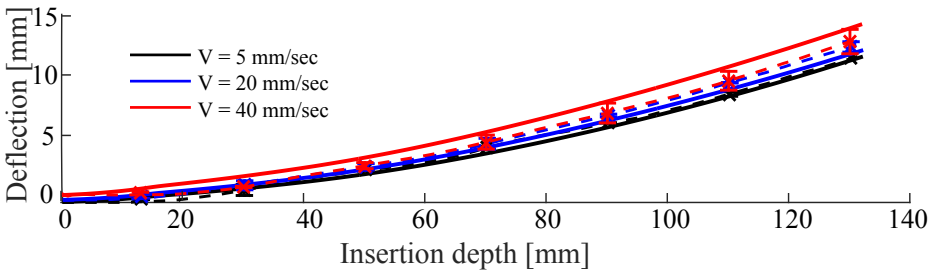

Figure 3.16: Experimental needle tip deflection and model prediction for needle insertion in plastisol with the grid template. Solid and dashed lines denote model prediction and experimental data, respectively.

Fig. 3.16 shows results of needle insertions performed with the template for the plastisol tissue at velocities of 5, 20 and 40 mm/sec. Five insertions were performed for each velocity. As expected, the template decreases the total needle deflection by restraining the needle motion outside the tissue. Also, the template reduces the effect of insertion velocity on the needle tip deflection – the difference between the final tip deflections at velocities of 5 and 50 mm/sec is less than 4 mm. Results show the model can perfectly explain the template effect on needle deflection with maximum final tip error of 0.72 mm. Next, insertions were performed using the more flexible needle made of Nitinol wire. Fig. 3.17(a) and Fig. 3.17(b) present the results of experimental needle insertions in synthetic tissues compared to model predictions. Needle was inserted at a velocity of 5 mm/sec with and without rotation(s). Four needle insertions were performed for each scenario. In all of the experiments with the wire, the template was used. Results indicate that the model is in good agreement with the experimental results. The maximum error in predicting the tip deflection is 1.1 mm at a depth of 121 mm for insertion in plastisol. Also, the maximum error of the model in predicting the final tip position is 0.432 mm for insertions with double rotation in plastisol.

To validate the model in terms of the dynamics of the carrier, we compare the force/torque predicted by (3.12a) with the needle base force/torque measured during needle insertions. Fig. 3.18(a) shows a comparison of experimentally-obtained axial and lateral forces and in-plane torque applied to the needle's base during needle insertion in plastisol for three different trials and the model predictions. Based on results the model accurately captures the effect of needle deflection on axial and lateral needle base forces. Maximum RMSEs between model predictions and average experimental value of axial and lateral forces are

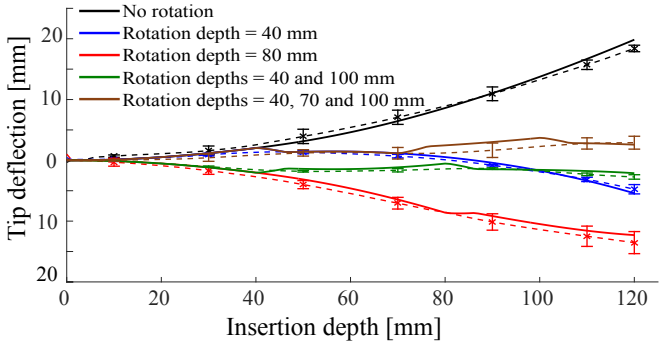

(a)

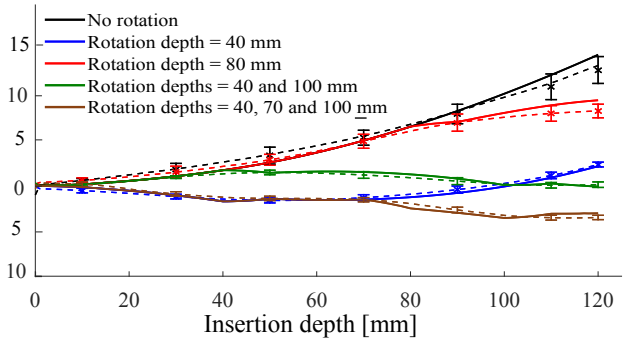

(b)

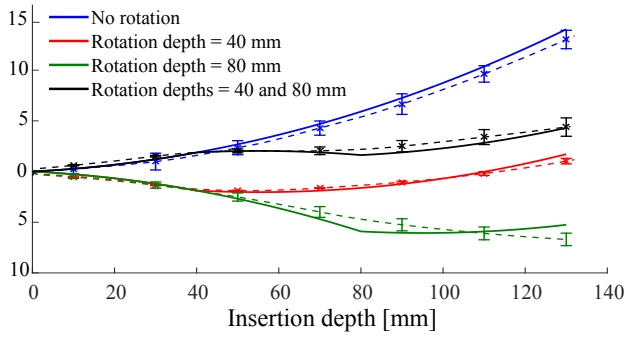

(c)

Figure 3.17: A comparison of experimentally-obtained needle tip deflections and the corresponding model predictions for needle insertion using a flexible Nitinol wire at a constant insertion velocity of 5 mm/sec with and without axial rotation in (a) gelatin and (b) plastisol. (c) A comparison of kinematics-based model predictions and experimentally-obtained needle tip deflections for needle insertion at a constant velocity of 5 mm/sec with and without axial rotation in plastisol. Solid and dashed lines denote model prediction and experimental data, respectively.

0.185 N and 0.073 N, respectively, for the insertion with double rotation. Maximum RMSE of model prediction for torque is 0.009 N.m for the insertion with single rotation.

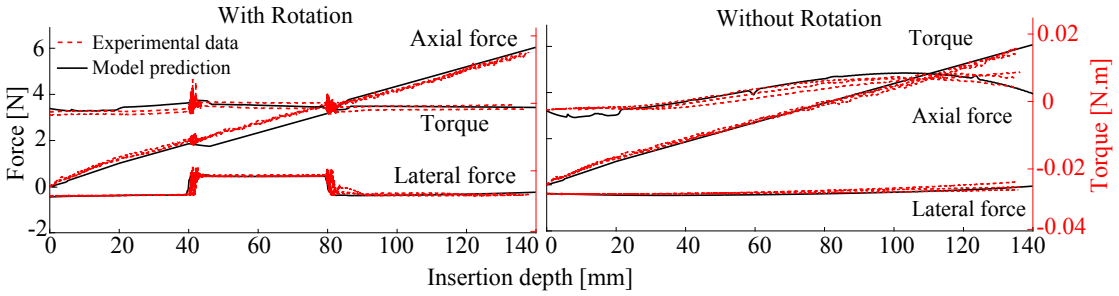

(a)

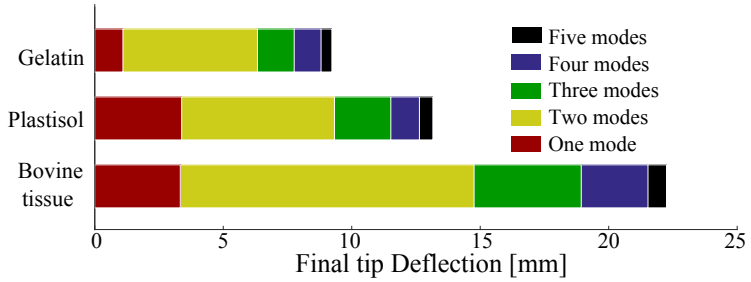

(b)

Figure 3.18: (a) A comparison of experimentally-obtained needle base forces and torque and the corresponding model predictions for needle insertion in plastisol at constant insertion velocity of 5mm/sec with no axial rotation and with double rotation at depths of 40 and 80 mm. (b) Model prediction of final tip deflection at insertion depth of 140 mm and constant insertion velocity of 5 mm/sec for different number of assumed modes.

As a part of model simplification discussed in 3.2.3, we replaced the infinite-dimensional model by a discrete model. The PDE used in modeling the needle deflection is approximated by a linear combination of four arbitrarily assumed shape modes. Increasing the number of modes can enhance the accuracy of discretization method. However, it will make the model computationally inefficient for real-time control purposes. Let us investigate the trade-off between the computational efficiency and the prediction accuracy of the model. Fig. 3.18(b) shows model prediction of the final tip deflection at an insertion depth of 140 mm and for a constant insertion velocity of 5 mm/sec in three tissues for different numbers of assumed modes. Based on the results, needle tip deflection accuracy initially increases as we increase the number of modes. However, after the 4th mode, the change in the final

Table 3.9: Comparison of experimental data and kinematics-based model prediction.

	Gelatin			Plastisol		
	$\omega_{sim}(\ell)$ [mm]	e_{max} [mm]	RMSE [mm]	$\omega_{sim}(\ell)$ [mm]	e_{max} [mm]	RMSE [mm]
V=5 [mm/sec]	19.7	1.28	0.527	14.03	0.61	0.841
V=20 [mm/sec]	19.7	1.49	0.738	14.03	2.72	0.987
V=40 [mm/sec]	19.7	3.72	1.067	14.03	7.68	1.201
Rotation at 40 mm	4.5	2.86	1.505	-1.7	0.53	0.782
Rotation at 80 mm	10.8	0.36	1.327	5.24	1.81	1.208
Rotations at 40 & 80 mm	9.8	1.63	0.912	4.30	0.72	0.822

tip deflection is less than 1 mm – a maximum of 0.756 mm for gelatin and minimum of 0.24 mm for bovine tissue. Thus increasing the number of assumed modes any further is not necessary. We were able to solve the 4-mode model on an Intel Core i7 (2.93 GHz) machine with 4 GB memory at a sampling frequency of 10 kHz in a total computation time of 0.28 sec. Thus, four assumed modes are sufficient for developing an accurate model that can be used in control of needle steering.

Finally, we compare the accuracy of our model with the kinematics-based models. For the sake of comparison, we have only used the bicycle model as it is reported to have better accuracy [7] than the unicycle model [6]. Needle insertions are performed with axial rotation(s) at constant velocity of 5 mm/sec and without axial rotation at constant velocities of 5, 20 and 40 mm/sec. Results are presented in Table 3.9 and Fig. 3.17(c). The model parameters are identified as proposed in [7]. Compared to our model, the kinematics-based model shows a similar fit to experimental data for fixed insertion velocity of 5 mm/sec and with no rotation. However, the model's accuracy decreases when the needle is axially rotated. This is partly because it fits the model parameters empirically for every experimental condition (e.g., every constant insertion velocity and depth of rotation) while our model requires only one global parameter fit. Also, one of the main assumptions of the bicycle model is that the needle is flexible relative to the tissue, meaning that it can be steered without causing large tissue deformations. Thus, the model has been widely

used for steering of flexible wires in soft tissues. However, when applied to path planning and control in softer tissues using standard brachytherapy needles, which are three times stiffer than a Nitinol wire, there is significant error in the kinematic model predictions. Compared to the kinematic model, the proposed model demonstrates good accuracy in both soft material and stiff material for both wire and needle. Lastly, compared to the kinematic model, the proposed model accepts as input a *variable* insertion velocity.

3.7 Concluding Remarks

In this chapter, a novel approach is used to develop a dynamic model of needle steering in soft tissue. The needle deflection is modeled as an externally excited compliant beam attached to a rigid carrier. The elastic needle is modeled as a prismatic beam that deflects under various external forces, i.e., reaction forces from deformed soft tissue, needle-tissue friction, the grid template contact force, and tissue cutting force. Several mechanics-based models are developed to model the mentioned needle/tissue interactions during the needle insertion. Using a needle driving robot, experiments are performed on synthetic and ex-vivo tissue samples to identify the model parameters and validate the analytical predictions. The results demonstrate that the proposed approach accurately predicts needle insertion forces in synthetic and inhomogeneous biological tissue.

The needle/tissue interaction models are implemented in the needle steering model to accurately predict needle deflection inside tissue. The needle steering model relates needle deflection to insertion velocity and axial rotation of the needle, which can be regarded as control inputs for needle steering. The results also demonstrate that the model is computationally efficient and allows for real-time control of the needle tip position in a robotic-assisted needle insertion context. Needle insertion experiments are performed on synthetic and ex-vivo animal tissue using two different needles to validate the needle steering model. In the collected experimental data, the maximum error of the 2D model in predicting the needle tip position in the insertion plane was 1.59 mm in case of no axial rotation and 0.74 mm with axial rotation. The results confirm the model's accuracy and capability in capturing the effects of insertion velocity and axial needle rotation on needle deflection, thus

enabling future applications in pre-surgery motion planning, optimized trajectory design and real-time control of needle steering. In the next section, we use the presented model for controlled robotic needle steering.

Chapter 4

2D Robotic Needle Steering

4.1 Objective

In this chapter, we present a novel needle steering controller based on model predictive control theory. The goal is to steer the needle tip to follow a desired trajectory and reach a target point in the tissue. The desired tip trajectory can be a straight line toward the target location or a path around patient-specific anatomical obstacles. Obstacles are sensitive or impenetrable anatomical regions in the proximity of the target point such as glands, blood vessels or bones. Given preoperative medical images the clinician can specify the insertion location and target region as well as sensitive structures and obstacles.

Fig. 4.1 shows a block diagram of our closed-loop control algorithm for ultrasound-based guidance of needle steering. The three main components of the needle steering system are highlighted in Fig. 4.1. The first one is the mechanics-based needle steering model presented in Chapter 3 that predicts the needle deflection and accepts needle tip rotation as an input.

The second component is a needle tip tracking system that estimates the needle deflection from the ultrasound images. Ultrasound image feedback is given to the model (the first component) as the initial condition in the sense that the needle steering model employs the estimated needle deflection at the present time to predict needle tip trajectory in the future steps. The third component is a nonlinear model predictive controller (MPC) that steers the needle inside the tissue by rotating the needle's beveled tip. The MPC controller

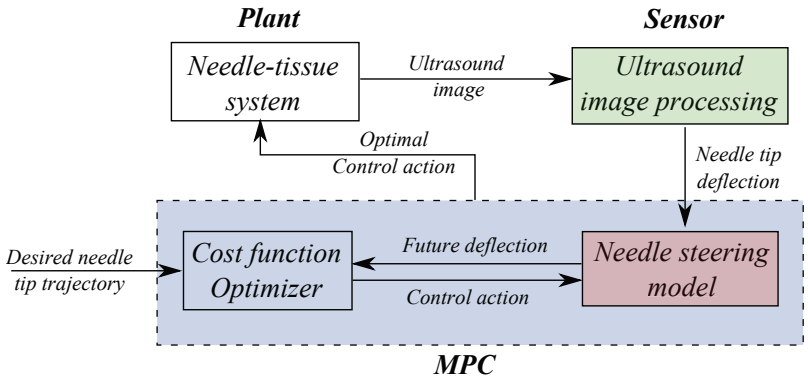

Figure 4.1: Scheme of the MPC closed-loop components.

calculates the control decisions based on iterative optimization of a cost function. The cost function evaluates the difference between the predictions of the needle steering model and the desired tip trajectory.

Fig. 6.8 shows the procedure used in the proposed MPC approach to find the optimal control inputs. First, the needle tip position is determined using the ultrasound images. Using the needle steering model and image-based feedback multiple needle tip trajectories are simulated for different depths of rotation. Next, the MPC controller selects the optimal path and the corresponding depth of rotation and uses the inputs to steer the needle towards a target point.

The rest of this chapter is organized as follows: In Section 4.2, small modifications are performed on the needle steering model so it can be implemented in the MPC context discussed above. In Section 4.3, the process of needle tracking from ultrasound images is discussed. Details of the proposed MPC scheme are presented in Section 4.4. In Section 4.5, experiments are performed on an ex-vivo animal tissue to validate the needle steering model, evaluate the needle tracking and steering algorithms, and demonstrate that the presented framework is applicable to clinical needle-based interventions.

4.2 Mechanics-based Needle Steering Model

In Chapter 3, a the mechanics-based model of needle steering is presented that predicts the needle deflection and accepts needle tip rotation as an input. The models initial conditions

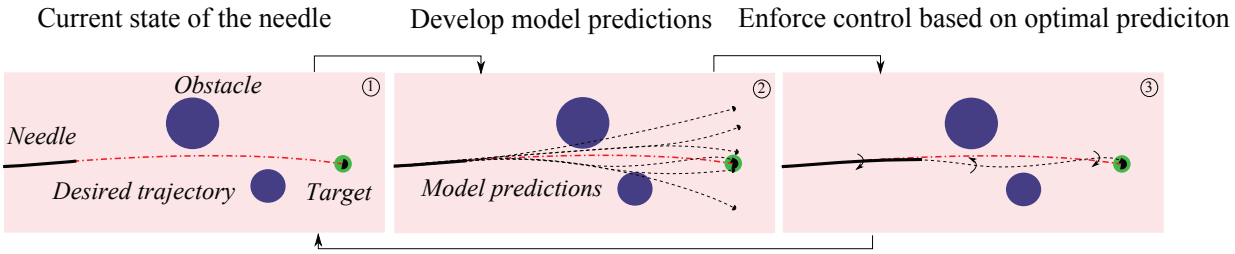

Figure 4.2: Ultrasound-guided model predictive needle steering steps. (1) The current position of the needle tip is estimated from ultrasound images. (2) The position of needle tip is used as initial condition in the needle steering model. Since the model accepts needle axial rotation as an input, an optimization algorithm is used to generate multiple needle tip trajectories corresponding to needle rotation at various future depths. (3) The closest path to the desired trajectory that has the minimum amount of tissue deformation and the least number of needle rotations is selected as the optimal path. The control input (depth of axial rotation) corresponding to the optimal path is used to steer the needle. Since the needle tip will inevitably deviate from its model prediction because of tissue inhomogeneity and uncertainties in model parameters, the above MPC loop is repeated to continually monitor and compensate for needle tip deviations.

are given by (3.15). The initial conditions state that the clamped side of the needle is assumed to have no deflection and have a slope of zero. The tip of the needle is assumed to experience no bending moment and the initial displacement at the tip of the needle is zero. However, in our MPC-based needle steering approach we need to predict the needle deflection in the future steps from arbitrary and feasible initial conditions, i.e., initial deflection ω_0 at a given insertion depth d_0 (see Fig. 4.3). Thus, we modify the needle steering model boundary conditions as follows

$$\omega(0,t) = 0, \quad \omega'(0,t) = 0, \quad \omega'''(\ell,t) = 0, \quad \omega(\ell,t) = \omega_0 \tag{4.1}$$

where prime denotes a derivative with respect to x. Note that ω_0 is the needle tip initial deflection. At the beginning of the insertion it is equal to zero. During the needle insertion, ω_0 is estimated using ultrasound images.

We also have to modify the tissue reaction force model presented in Section 3.5. To calculate the tissue deformation during needle insertion, we propose a method composed of two different steps corresponding to two phases of needle-tissue interaction:

1. Phase 1– Needle-tissue interaction forces given initial tip deflection.

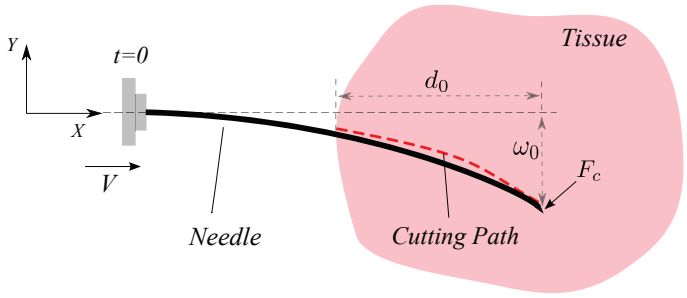

Figure 4.3: Initial configuration of partially inserted needle in tissue. ω_0 is the initial deflection of the needle tip, d_0 is the length of the part of the needle that is already inserted in the tissue, and F_c is the tissue cutting force applied to the needle tip

2. Phase 2– Needle-tissue interaction as the needle is further inserted in the tissue.

Note that in Section 3.5 we only considered the second phase of insertion as the model only predicted needle deflection starting from zero deflection and zero depth (i.e, $\omega_0 = d_0 = 0$). Let us use the concept of cutting path discussed in Section 3.5 to calculate tissue reaction force in the first phase. Cutting path is the path that the needle tip cuts through in the tissue during insertion. The amount of tissue deformation at the onset of insertion is the difference between the cutting path and the needle shape. Now, we modify the needle reaction model given by (3.57) to estimate tissue reaction during phase 1:

$$F_{s0} = K_s \left[\omega(x,t) - CP(x)\right] + C_s \dot{\omega}(x,t) \tag{4.2}$$

where, K_s is the tissue stiffness, C_s is the tissue viscous damping coefficient, and F_{s0} denotes the tissue forces applied to the part of the needle that is initially inserted in the tissue and CP is the cutting path. By definition, the cutting path is equal to the path followed by the needle tip. Thus, by tracking the needle tip in the incoming image frames, we can calculate the cutting path at any time instant. In the proposed image-guided needle steering approach, CP is measured from the ultrasound images and given to the model in preparation for the model-based optimization.

The tissue deformation forces in the second phase of needle-tissue interaction is the same as the one proposed by (3.57) in Section 3.5:

$$F_s = K_s \left[\omega(x,t) - \omega(\ell, t-\tau)\right] + C_s \dot{\omega}(x,t) \tag{4.3}$$

where ℓ is the needle length, and τ denotes the time difference between deflection of a generic point of a needle positioned at present time and the cutting path (i.e., needle tip deflection) at a specific time in the past. Now, we can replace the tissue reaction force f_s in the needle steering model given by (3.13), (3.14a), and (3.14b) with the modified tissue reaction force given by

$$f_s = F_{s0}[H_{\ell - Vt - d_0} - H_{\ell - Vt}](x) + F_s H_{\ell - Vt}(x) \tag{4.4}$$

The shorthand notation $H_{x_0}(x) = H(x - x_0)$ describes unit step function shifted by the constant x_0. In (4.4), the initial needle-tissue interaction force ($Fs0$) are only applied to the needle up to the initial insertion depth d_0, and the needle-tissue force profile for the cutting phase (Fs) is applied to the part of the needle that passes the initial insertion depth d_0 . Note that the presented force profile enables modeling of 180° rotations of the needle tip and can accommodate any number of rotations.

We can follow the same procedure implemented in Section. 3.2.3 to discretize the continuous PDE. The only difference is that based on (4.1), we have non-homogeneous boundary conditions. We use substitution of variables to convert the non-homogeneous boundary conditions to homogeneous. We introduce the new field variable $\eta(x,t)$ satisfying the following equation:

$$\omega(x,t) = \eta(x,t) + \lambda(x)\omega_0 \tag{4.5}$$

Substituting (4.5) in the boundary conditions in (4.1) gives

$$\begin{aligned} &\eta(0,t) + \lambda(0)\omega_0 = 0 \\ &\eta'(0,t) + \lambda'(0)\omega_0 = 0 \\ &\eta'''(\ell,t) + \lambda'''(\ell)\omega_0 = 0 \\ &\eta(\ell,t) + \lambda(\ell)\omega_0 = \omega_0 \end{aligned} \tag{4.6}$$

Based on (4.6), in order to have homogeneous boundary conditions, we must have

$$\lambda(0) = 0, \quad \lambda'(0) = 0, \quad \lambda'''(\ell) = 0, \quad \lambda(\ell) = 1 \tag{4.7}$$

We choose $\lambda(x)$ as a 2nd order polynomial satisfying (4.7)

$$\lambda(x) = \left(\frac{x}{\ell}\right)^2 \tag{4.8}$$

By substituting (4.8) and (4.5) into (3.13), we can obtain the needle steering model in terms of the new field variable $\eta(x,t)$, with the following homogeneous boundary conditions:

$$\eta(0,t) = 0, \quad \eta'(0,t) = 0, \quad \eta'''(\ell,t) = 0, \quad \eta(\ell,t) = 0 \tag{4.9}$$

Note that $\eta(x,t)$ calculated using the above procedure is not a unique function. However, the solution of the original model in (3.13) can be correctly determined by the new field variable. At this point, the same discretization procedure presented in Section. 3.2.3 can be used to derive the system of ODEs representing the needle steering system.

4.3 Needle Tracking in Ultrasound Images

In this section, a method for estimating the needle tip trajectory from ultrasound images is presented. The needle tip location and cutting path are estimated based on partial observations of the needle axial cross sections within a small region of 2D transverse ultrasound images. As discussed earlier, the cutting path represents the history of the needle tip deflections from the beginning of insertion up to the current time. Thus, by locating the tip position, we can also estimate the cutting path.

Researchers has previously developed needle detection algorithms using 3D volumetric images [75–77]. For instance, Ding *et al.* developed a 3D segmentation algorithm for locating the needle and implanted seeds in brachytherapy procedures [78]. Uhercik *et al.* proposed a method for detecting the position and orientation of long surgical tools in 3D ultrasound images using Random Sample Consensus (RANSAC) algorithm[79]. Zhao *et al.* implemented a Kalman filter technique in RANSAC algorithm for tracking micro-tools in 3D [78]. Tracking needle trajectory in 3D ultrasound images is computationally less efficient compared to 2D needle tracking. Also, state-of-the-art 3D ultrasound machines are very costly and not available in most hospitals. Thus, it is more convenient to use 2D ultrasound images for needle tracking especially for real-time applications. In needle-based medical procedures, 2D ultrasound imaging can be used to acquire transverse and sagittal images. The planes are defined in reference to the anatomical planes of the human body.

In the transverse images, an axial cross section of the needle can be detected and in sagittal images a small portion of the needle shaft is visible.

Previous efforts in detecting needle tip in 2D sagittal images include the work performed by Okazawa *et al.*, who proposed a Hough transform based detection scheme [80]. Kaya *et al.* used Gabor filtering and the utilization of RANSAC to improve needle segmentation [81]. From our group, Carrier *et al.* used RANSAC processing in combination with a simple mechanics-based needle model to predict the entire needle shape using partial observation of needle in 2D ultrasound images [82]. In brachytherapy, aligning the US probe with the sagittal plane that contains the needle is not always possible using endorectal probes.

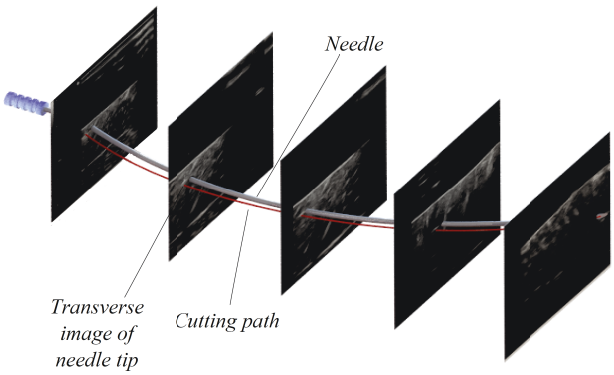

Figure 4.4: ultrasound-based needle tracking. Multiple transverse images of needle tip are obtained and used to reconstruct the needle tip trajectory (cutting path) in real-time.

Recently, researchers have developed needle tip detection strategies for tip tracking in 2D transverse ultrasound images. Transverse ultrasound images eliminate complications with probe alignment found in sagittal imaging. Vrooijink *et al.* presented a method for online flexible needle tracking in 3D using 2D ultrasound images [14]. They used a combination of median filtering, thresholding, and Hough transform to find the center of the needle cross section in transverse images visualizing the needle tip. Abayazid *et al.* also used 2D ultrasound to estimate needle tip pose and track the needle tip in 3D during the insertion [83]. From our group, Waine *et al.* used images from an ultrasound probe moving along the shaft of a inserted needle to estimate needle tip deflection [84]. In this approach, possible needle locations are identified in the image using a mix of filtering and thresholding. Later, RANSAC algorithm is used to find the needle tip position and predict

the needle shape.

Below, we propose a new approach to track the needle tip trajectory and estimate the cutting path using 2D transverse images. Several consecutive image processing steps are combined to determine the needle tip location in each of the transverse images and to construct the tissue cutting path (see Fig. 4.4). In prostate brachytherapy, transverse images of needle close to the tip are acquired by inserting the endorectal probe as shown in Fig. 1.1(a). Here, we use a robotically driven ultrasound probe that follows the needle tip to capture real-time transverse images of the needle. Details of the experimental setup used to capture transverse images of the needle tip is discussed in Section 4.5.

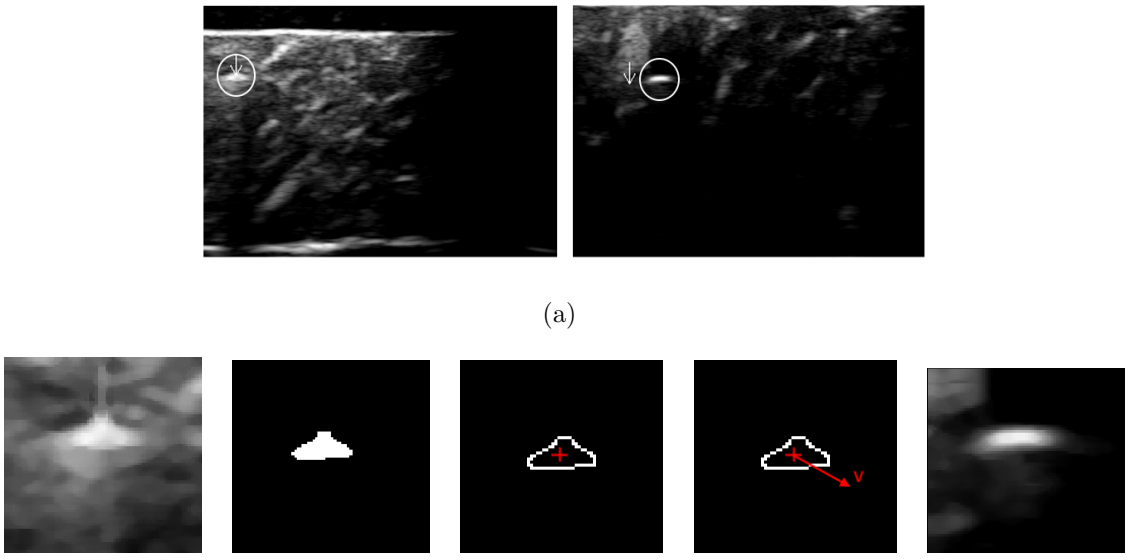

(a)

(b) (c) (d) (e) (f)

Figure 4.5: The image processing algorithm for locating the needle tip. (a) Two subsequent transverse ultrasound images in which needle is circled in white and the position of the needle in the first frame is shown with an arrow. (b) The region of interest in the first frame is selected around the needle tip. (c) The grayscale image is smoothed to filter out the artifacts and iterative thresholding is performed to separate the needle cross section from image background. (d) SUSAN corner detection is applied and the needle tip centroid (needle tip deflection) is calculated in the selected ROI. (e) The motion vector of the needle tip in the transverse images is calculated by minimizing the sum of squared differences between the current ROI and the one from the previous frame. (f) The motion vector is used to select the ROI in the next frame.

Here is our proposed algorithm for needle tip tracking:

Fig. 4.5 shows how the image processing algorithm is applied to determine the needle tip

Algorithm 4.1: US-based needle tip tracking algorithm

1. A region of interest (ROI) around the initial position of the needle tip in the first frame of the ultrasound images is selected manually(Fig. 4.5(b)).

2. The selected ROI is processed using a series of image processing techniques including median filtering and iterative thresholding to reduce image noise and separate the needle tip from the image background (Fig. 4.5(c)).

3. SUSAN corner detection algorithm [85] is used to find centroid of the needle axial cross section in the ROI (Fig. 4.5(d)).

4. A motion vector estimation algorithm is used to estimate 2D translational motion of the needle tip in the transverse images. The results are extrapolated to predict the position of the ROI in the next frame (Fig. 4.5(e) and Fig. 4.5(f)). The algorithm is repeated from Step 2 using the selected ROI.

position. After manually selecting a window of 75 by 75 pixels around the initial position of the needle in the first frame, median filtering and thresholding are used to reduce speckles and eliminate small artifacts in the ultrasound image. For thresholding the image inside this ROI, first we select an initial value T for the threshold and the image is segmented. This produces two groups of pixels consisting of pixels with gray level values bigger and smaller than T. Next, the averaged gray level for the pixels in two groups are computed and used as the next value of the threshold T. This process is continued until the differences in T between different iterations is smaller than a predefined threshold.

As mentioned previously, the SUSAN (i.e., Smallest Univalue Segment Assimilating Nucleus) edge detector is used to estimate the position of the needle cross section's centroid [85]. Following the SUSAN algorithm, a circular mask is placed around a pixel in the ROI; this pixel is called the nucleus. Next, the number of the pixels within the circular mask that have similar brightness to the nucleus are calculated. These pixels define the univalue segment assimilating nucleus or USAN. Later the USAN size is compared to the geometric threshold to produce an edge strength image. Geometric threshold is usually chosen as 3/4

and 2/3 of maximum size of USAN for detecting edges and corners, respectively. Finally, we select a nucleus that has the maximum size of USAN and is placed within the edges estimated using the SUSAN method as the needle tip centroid. An advantage of this method compared to other corner detectors is that SUSAN does not use the derivatives operator, which makes it faster and less sensitive to noise. Also, we select a circular template with the diameter of 21 pixels which is almost equal to the outer diameter of the needle (1.27 mm). By incorporating a geometrically exact template in SUSAN algorithm, we ensure that the algorithm selects the biggest blob that matches the needle shape rather than selecting the comet tail artifacts (CAT) commonly seen in the ultrasound images [83].

In the final step, we estimate the motion vector of the needle in 2D images to select the next ROI. The motion vector is calculated between 2 adjacent frames and only used to select the ROI in the upcoming frame. Under the assumption that all pixels in the ROI undergo a translational motion denoted by one 2D motion vector, we can estimate the motion vector by minimizing the sum of squared differences (SSD) between the two displaced frames. The SSD is given by

$$SSD(\mu, \nu) = \sum_{x,y} \left[I(x + \varepsilon, y + \nu) - I(x, y) \right]^2 \tag{4.10}$$

where the pixel intensity at position (x, y) is given by $I(x, y)$ and ε and ν are components of motion vector in the x and y directions, respectively.

In order to calculate the motion vector, a fast template search algorithm is presented. In this method, we search between neighbouring pixels of the centroid in the current frame to find the pixel in which the sum of squared differences (SSD) between the current and previous frames is minimum. In the fast search algorithm, first a 20 by 20 window of pixels around the located needle tip is selected. Then, we simply move the center of the template on 16 randomly selected neighbouring pixels and calculate the SSD over the whole area spanned by the template. The pixel in which the magnitude of SSD is minimum is selected as the new centroid. Next, we accelerate the algorithm by cutting down the search step size by two and repeat the search around the newly selected centroid. The search is continued until the search step becomes one. Finally, the motion of the newly found matched template is equal to (ε, ν) in (4.10).

After the needle tip position is determined, the cutting path can be estimated by fitting a 3rd-order polynomial to the tip position using the linear least squares method. Each pixel in the ultrasound image is 0.063 mm. This is the maximum accuracy for estimating the cutting path. However, considering the error of image processing and needle tracking, this error can be larger. The cutting path and current needle tip position will be used as the feedback in the closed-loop control of needle steering discussed in the next section.

4.4 Model Predictive Control for Needle Steering

MPC is an advanced optimal control technique widely applied in the area of process industry [86]. The main advantage of MPC is its simplicity to define and handle constraints. MPC uses the discrete model of the process (e.g., needle steering) in order to predict and optimize the future behaviour of the system as shown in Fig. 4.1. Given the last measurement available at the present time (t_n), the controller predicts the dynamic behaviour of the system over the horizon N based on the model of the system. Only the first element of the predicted optimal input sequence is applied to the plant until the next measurement is available. Subsequently, the horizon is shifted one step forward and a new optimization problem is formulated and solved [87]. In our case, the control input is a binary signal corresponding to 180° axial rotation of the needle.

We can discretize the needle steering model as

$$\omega_u(k+1) = f(CP, \omega_0, \omega_u(k), u(k)), \qquad k = 0, ..., N-1 \tag{4.11}$$

Using (4.11), we obtain predictions $\omega_u(k+1)$ for the deflection of the needle tip at the time t_{n+k} in the future. In (4.11), f is our model that gives the future needle deflection $\omega_u(k+1)$ as the function of the current control value $u(k)$ and the current needle deflection $\omega(k)$. The cutting path CP and the initial tip deflection ω_0 are the initial conditions for solving f. CP and ω_0 are obtained from the ultrasound images as discussed in Section 4.3. Starting from the current state $\omega(n)$, for any given control sequence $u(0), ..., u(N-1)$ over the horizon length $N \geqslant 2$, we can now use (4.11) to construct the prediction trajectory ω_u.

Next, we use optimal control in order to determine $u(0), ..., u(N-1)$ such that ω_u is as close as possible to our desired trajectory ω_d. To this end, we define a cost function $\mathcal{L}(\omega_u(k), u(k))$ that depends on the distance between $\omega_u(k)$ and $\omega_d = 0$ for $u(0), ..., u(N-1)$. In here, we not only allow for penalizing the deviation of the output from the reference but also the distance of the control values $u(k)$ to a reference control u_d, which here we choose as u_d. By penalizing $u(k)$, we can minimize the number of needle rotations and limit the amount of tissue cutting during the insertion. A common and popular choice for this purpose is the quadratic function

$$\mathcal{L}(\omega_u, u) = \| \omega - \omega_d(n) \|^2 + \Lambda \| u \|^2 \tag{4.12}$$

where $\| \cdot \|$ denotes the Euclidean norm and Λ is a weighting parameter that penalizes the control action. The optimal control problem now becomes

$$\text{minimize} \quad \mathcal{J}(n, \omega(n), u(0)) = \sum_{k=0}^{N-1} \mathcal{L}(n+k, \omega_u(k), u(k)) \tag{4.13}$$

with respect to all admissible control sequences $u(0), ..., u(N-1)$ with ω_u found from (4.11).

Let us assume that this optimal control problem has a solution given by $u^*(0), ..., u^*(N-1)$ where $\cdot^*$ denotes the internal optimal control variable. In order to get the desired feedback value μ_n at t_n, we now set $\mu_n := u^*(0)$, i.e., we apply the first element of the optimal control sequence. This procedure is sketched in Fig. 4.6. At the following time instants $t_{n+1}, t_{n+2}, ...$, we repeat the procedure with the new ultrasound-based measurements at $\omega(n+1), \omega(n+2), ...$ in order to derive the feedback values $\mu_{n+1}, \mu_{n+2}, ...$. In other words, we obtain the feedback law μ by an iterative online optimization of our model predictions over a moving horizon.

In the following section, details of the nonlinear model predictive control (NMPC) algorithm are discussed. The additional term "nonlinear" indicates that our model is not a linear map.

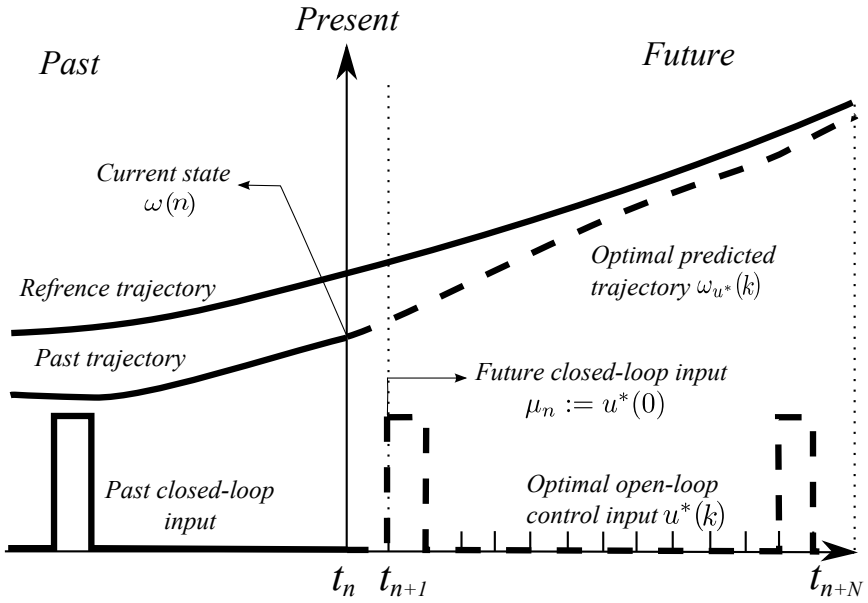

Figure 4.6: Illustration of the MPC step at time t_n

4.4.1 Model Predictive Algorithm

The NMPC algorithm for constrained control of needle tip trajectory for tracking a desired time varying trajectory at each sampling time t_n, $n = 0, 1, 2, ...,$ is:

In Algorithm 4.2, $w_k, k = 0, ..., N-1$, are weights on summands of the cost function. Using the weights, we can penalize the cost function at a certain time or insertion depth. For instance by setting $w_{N-1} = 1$ and $w_k = 0$ for $k = 0, ..., N-2$, the focus of the optimization will be on minimizing the error of the needle steering at the final tip position (target point) rather than tracking a certain trajectory at different depths. Also, U_{max} is the constraint we put on the number of needle tip rotations. We intend to minimize the number of needle rotations to limit the tissue damage during needle insertion. Typically, during the insertion of needles into a patient, the surgeon limits the number of the needle rotations. This is due to concerns from physicians that increasing the number of needle rotations will lead to a drilling motion which will increase tissue cutting and damage the surrounding tissue. This has been previously investigated [55, 62]. In the proposed approach this has been done in two different ways: (1) By penalizing the control action in the cost function in (4.12), and (2) by limiting the total number of rotations in each optimization step . Constraining u can be also useful for computational reasons because the optimal control problem is easier

Algorithm 4.2: Nonlinear Model Predictive Control algorithm for needle steering

1. Measure the cutting path CP and the needle tip deflection ω_0 from the ultrasound images .

2. Solve the following optimal control problem for the current state of the system $\omega(n)$ to obtain the optimal control sequence $u^*(k)$:

$$\begin{aligned} &\text{minimize} \\ &\mathcal{J}(n, \omega(n), u(0)) = \sum_{k=0}^{N-1} w_k \mathcal{L}(n+k, \omega_u(k), u(k)) \\ &\text{subject to} \quad \omega_u(k+1) = f(CP, \omega_0, \omega_u(k), u(k)) \\ &\text{and} \quad \sum_{k=0}^{N-1} u(k) - U_{max} \leqslant 0 \end{aligned}$$

3. Define the NMPC control command $\mu_n := u^*(0)$ and use this value as control command in next sampling time.

to solve if the control variable is penalized.

The optimal control problem must be solved multiple times in each iterate of the NMPC procedure. Thus we need to use an algorithm that is able to find a good enough solution in a reasonable amount of time. Below, we will use simulated annealing (SA) to find a good approximation to the global optimum of the problem. Simulated annealing is a generic probabilistic metaheuristic method for solving bound-constrained optimization problems. The method models the physical process of heating a material and then slowly lowering the temperature to decrease defects, thus minimizing the system energy [88]. In an optimization problem, as the number of possible solutions gets large, it becomes too computationally intensive to check every possible itinerary. SA is effective at tracking down the best possible solution in a specified fixed optimization time [89]. The method can handle nonlinear constrained problems and have been previously used in autonomous robotic path planning [90, 91].

The inputs to the optimization algorithm are the maximum allowable computation

time (t_c), the initial temperature (T_0), and the annealing parameter (k). Temperature is a parameter in simulated annealing that affects the algorithm in two ways: (1) Changing the distance of a trial point from the current point, and (2) changing the probability of accepting a trial point with a higher objective function value. Trial points correspond to the control input. The binary control input sequence is characterized by two components, namely the number of needle rotations and the depths at which the rotations take place.

The simulated annealing algorithm for solving the finite horizon nonlinear optimal control is as follows:

As mentioned previously, t_c is the computation time of the optimization process. This time is large compared to the sampling period. Also, the computational delay caused by step (2) in Algorithm 4.2 is not negligible and needs to be considered. In the next section, we present a method to compensate for this delay.

4.4.2 Delay Compensation

In this section, we employ our needle steering model as a predictor in the NMPC scheme to compensate for the computation delay. Without the delay compensation proposed here, the solution to the optimal control problem and calculation of the required control action (i.e., depth of needle rotation) will be subject to delay. This means that the robot will not be able to apply the control command on time. For instance, assume the optimal depth to perform a rotation for correcting the needle path is calculated to be 40 mm. However, when the controller wants to apply this command, the needle will be at a depth of 45 mm (because the needle keeps moving while the optimization problem is being solved).

Close scrutiny of Algorithm 4.2 shows that steps (1) to (3) correspond to different physical tasks: ultrasound-based measurements, computing optimal control input, and applying the control to the physical plant. These tasks are operated by individual components, namely, the sensor, the MPC controller, and the plant (see Fig. 4.1). The idea behind the compensation approach is to run the NMPC controller component with a predefined time offset (t_{max}). This offset causes the controller to compute a control command ahead of time, such that the computed control command value is readily available at the time it is

Algorithm 4.3: SA algorithm for solving the nonlinear MPC problem

1. Starting from an initial point and an initial temperature, the algorithm generates a random initial point. The distance of the trial point from the current point is chosen using normal probability distribution with a scale depending on the current temperature. Step length is equal to the current temperature, and direction is chosen to be uniformly random.

2. The algorithm determines whether the new point is better or worse than the current point. If the new point is better, it becomes the next point. If not, then the algorithm can still make it the next point using the following acceptance probability function:

$$P_a = \frac{1}{1 + exp\left(\frac{\Delta}{max(T)}\right)}$$

where Δ is the difference between the new and the old cost functions, and T is the temperature.

3. The algorithm lowers the temperature while storing the best point found so far using

$$T = \frac{T_0}{k}$$

where k denotes the annealing parameter and is chosen to be the same as the iteration number.

4. The algorithm stops when the average change in the objective function is small relative to a predefined tolerance, or when it reaches the optimization time limit (t_c).

supposed to be applied to the plant. This offset should be chosen larger than the maximal computing time required to solve the optimal control problem (t_c). At time t_n, the optimal control problem is solved with a prediction $\hat{\omega}(n)$ of the initial value $\omega(n)$ based on the available sensor measurement at time t_n. This prediction is performed using the developed needle steering model, which is also used for the NMPC prediction.

In order to perform this prediction, the control commands to be applied to the plant

during the computation time interval and have been computed before by the NMPC controller are needed to be stored using a buffer. Thus, we extend the scheme given in Fig. 4.1 by adding the required predictor and buffer to the controller. The structure of the resulting scheme is shown in Fig. 4.7(a) and the scheduling structure for the delay compensation strategy is sketched in Fig. 4.7(b). Other than delay compensation, advantage of this method is that we can run the three components of the system as separate algorithms in parallel.

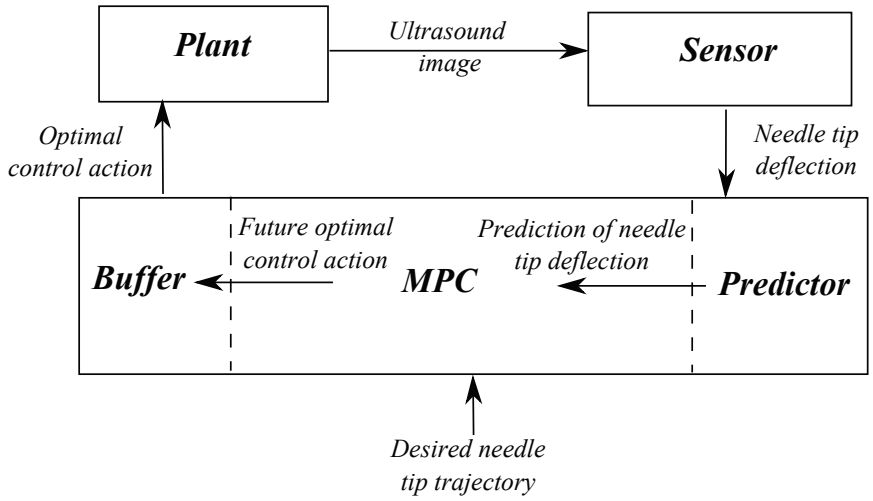

(a)

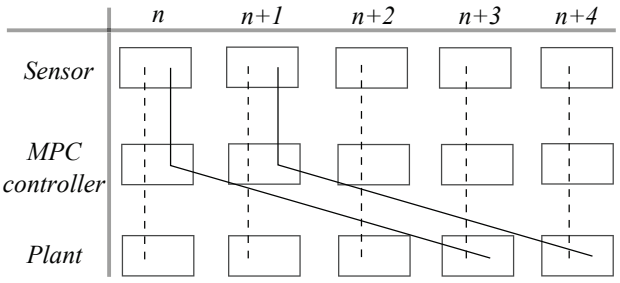

(b)

Figure 4.7: A schematic of the delay compensation strategy. (a) Block diagram of the time decoupled closed-loop NMPC control with delay compensation. (b) Comparison of scheduling structure between NMPC (dashed line) and NMPC with delay compensation with $t_{max} = 3 * \text{sampling time}$ (solid line)

As discussed before, solving Step (2) of Algorithm 4.2, is computationally demanding. Thus, t_{max} can be relatively larger than the sampling time. Consequently, at the start of the

needle insertion for a certain time (t_{max}) no control command will be available. To avoid this situation we solve the optimal control problem offline once before the insertion begins. Then, we use the acquired optimal control command at the beginning of the insertion.

In the next section we present the experiments performed on ex-vivo tissue phantom to validate the proposed needle steering model and our MPC based needle steering strategy.

4.5 Experimental Evaluation

In this section needle insertion experiments are designed and performed on soft tissue samples. The goal of the experiments is validating the proposed needle steering strategy.

In order to perform needle insertion into soft tissue, the setup shown in Appendix A, Fig. A.1 is used. The needle used to perform insertions is a standard 18-gauge brachytherapy needle (Eckert & Ziegler BEBIG Inc., Oxford, CT, USA) made of stainless steel, with an outer diameter of 1.27 mm, an inner diameter of 1 mm. Beef loin tissue is used in the needle steering experiments. Bovine tissue is embedded in gelatin to get a smoother surface on top. This increases the contact surface between the ultrasound probe and the tissue and consequently reduces the noise in the ultrasound images. Same tissue was used in all the experiments. The identification process discussed in Section. 3.6 is used to identify the needle steering model parameters.

We considered a circular target region of 2 mm for all the experiments described below. The targeting accuracy of the needle tip is calculated by measuring the distance between the center of the target and the final needle tip position. The MPC control algorithm is executed on an Intel i7 3.33 GHz PC. The time offset t_{max} required for cost function optimization in the MPC, is set equal to 10 seconds, which is a sufficiently short-time interval for clinical applications that require needle insertion depth ranging from 100 mm to 150 mm[62]. During the optimization, the needle model is used to generate a minimum of 20 needle trajectory predictions. The needle insertion and rotational velocities used during the experiments are 2 mm/s and 300 rpm, respectively, and the total depth of insertion is 140 mm. In the experiments, the needle tip is inserted in the tissue for 5 mm by hand

prior to robotic needle insertion to fix the entry point.

Two virtual scenarios are used in the experiments and we executed our system 5 times for each experimental scenario.

- **Scenario I** The needle is steered to follow a straight line and reach a target placed at the depth 140 mm. This is similar to the needle insertion in brachytherapy where the seeds should be placed along a straight line within the tissue.
- **Scenario II** A 4 mm circular obstacle is positioned at 70 mm between the needle entry point in the tissue and the target. The needle is steered to reach a target at the depth of 140 mm while avoiding the obstacle. Obstacles are sensitive or impenetrable anatomical regions in the proximity of the target point such as blood vessels.

In the first scenario the model prediction horizon is set to 10 sec corresponding to insertion depth of 20 mm. In the first scenario, the needle is inserted at a constant velocity of 2 mm/s and the model prediction horizon is set to 10 sec corresponding to the insertion depth of 20 mm. Goal of the first scenario is to steer the needle on a straight line and we want the controller to focus on minimizing the trajectory tracking error regardless of the target position. It is clear that by tracking a straight line leading to the target we will be able to reach the target. In the second scenario the prediction horizon is the maximum insertion depth, i.e. 70 sec for insertion depth of 140 mm. The goal of the second scenario is to steer the needle to reach a target at the depth of 140 mm while avoiding an obstacle placed at the depth of 70 mm. In this scenario we plan to follow a curve going around the obstacle and reaching the target and minimize the targeting error. Thus in this scenario we select the prediction horizon equal to the total insertion depth to include the targeting error in the optimal control problem. The desired tip trajectory is a 3rd order polynomial starting from the entry point and ending at the target location with maximum distance of 3 mm from the centroid of the obstacle. The number of allowable rotations in the prediction horizon (U_{max}) is three for both scenarios.

A representative results for scenario (1) and (2) are given in Fig.4.8(a) and Fig.4.8(b), respectively. The experimental results are provided in Table 4.1. The maximum, mean and standard deviation of targeting error are reported.

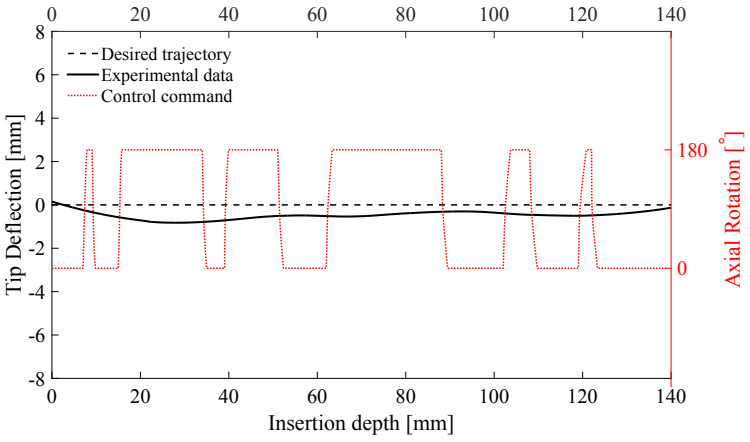

(a)

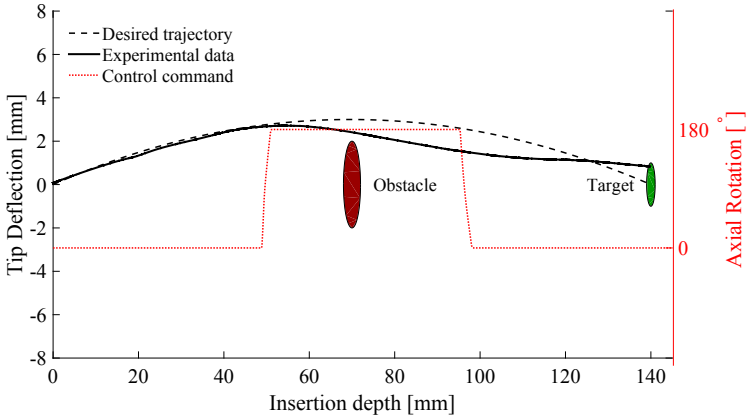

(b)

Figure 4.8: Representative experimental needle steering results and corresponding controller input command (a) Scenario I–needle steering with the aim of moving on a straight line. (b) Scenario II–needle steering with the aim of manoeuvring around an obstacle.

The maximum targeting error in the first and second scenario are 2.10 mm and 2.85 mm, respectively. Also, the minimum distance from the obstacle in the second scenario is 1.4 mm. Currently, average seed placement errors by experienced brachytherapists are in the range of about 6.3 mm [14, 92]. Another study showed that prostate biopsies via rigid needles show average targeting errors of 5.5 to 6 mm [93]. Thus, with the proposed needle steering strategy targeting accuracy can be improved by almost 50%.

Table 4.1: Result of needle steering experiments. Maximum number of axial rotations rot, mean targeting error e_{mean}, maximum targeting error e_{max}, standard deviation of targeting error σ are listed.

	rot	e_{max} [mm]	e_{mean} [mm]	σ [mm]
Scenario I	13	2.10	1.75	0.61
Scenario II	7	2.85	2.25	0.97

4.6 Concluding Remarks

This chapter combines a needle deflection model, image processing techniques, and a model predictive controller to accurately steer bevel tipped flexible needles with the aim of reaching desired target location inside soft tissues. The proposed image processing algorithm combined with the needle deflection model make the foundations of a model predictive controller for needle steering. The needle steering controller provides accurate targeting while avoiding anatomical obstacles such as sensitive or impenetrable structures. We experimentally evaluated our approach by performing needle insertion experiments in ex-vivo tissue. The experimental results demonstrate that our needle steering approach successfully guides the needle to desired targets with and without the presence of obstacles with an average error of less than 2 mm and 3 mm, respectively, which is within clinically acceptable thresholds.

Identified values for some of the needle steering model parameters (such as the tissue cutting force and tissue stiffness) are only the nominal values and the magnitude of these parameters might change during the needle insertion due to factors such as tissue inhomogeneity. Using the proposed feedback controller, we are able to correct uncertain perturbations caused by deviation of parameters from their nominal values.

The main drawback of the proposed system is 2D needle steering. During clinical needle steering the needle tip might deviate and deflect out of plane. Many factors such as tissue inhomogeneity can cause out of plane needle deflection. Also, we have only considered the fully robotic needle insertion. In fully robotic needle steering the goal is to calculate a needle steering control input (needle axial rotation) assuming the rest of the inputs are fixed

at known values such that needle targeting accuracy is improved. A possible intermediate step between manual and fully-robotic insertion is semi-manual needle insertion, in which automatic robot-assisted adjustments are performed to one of the control inputs while other inputs are directly applied by the surgeon. For instance, the surgeon is in charge of needle insertion in the interest of ensuring the safety of the operation and to maintain continuous engagement, while the needle tip bevel location is controlled robotically. In the next chapter, we propose a needle steering strategy for surgeon-in-the-loop semi-automated needle steering.

Chapter 5

2D Semi-automated Needle Steering

5.1 Objective

In this chapter, we propose a novel automated surgeon-in-the-loop strategy for semi-automated needle steering in soft tissue, which can be used to target a specific point and maneuver the needle tip around an obstacle. The system is composed of two parts:

(1) An adaptive real-time needle deflection predictor. The predictor incorporates the ultrasound-based depth-varying radii of curvature to predict needle deflections in future steps. A method known as Homotopy Analysis Method (HAM) is used to develop the predictor. We assume that the needle curvature belongs to a certain homotopy – a group of functions (e.g., circles and ellipses) that can continuously deform and change shape. The deformation of the functions is governed by a nonlinear differential equation known as the zero-order deformation equation to match the curvature of the needle. We use real-time visual feedback from the ultrasound images to select the best curve from the homotopy and use that to predict the needle deflections in future steps. The predictor developed using HAM accounts for 180° needle axial rotations and changes in the needle deflection radius of curvature due to factors such as tissue in-homogeneity and varying insertion velocity.

(2) A novel online motion planner that is informed by the predictions of the HAM-based predictor and automatically rotates the needle while the needle is manually inserted in order to steer the needle toward the desired target.

Two main features of the proposed semi-automated needle steering strategy are:

(1) The controler relies on an adaptive needle deflection predictor. The performance of model-based controllers highly relies on accurate models for precise needle position prediction. The well-known kinematic model that is widely used for control assumes that as the needle is inserted, it moves on a constant curvature path, which is not always the case [94]. Previous studies have shown that when the kinematic model is applied to path planning and control in soft tissues, there are non-negligible deviations between the model and experimental data due to tissue nonhomogeneity or uncertainty in the nominal values of the model parameters [16]. Here, we develop a needle deflection predictor that accounts for changes in the needle deflection radius of curvature due to factors such as tissue inhomogeneity and variations of the insertion velocity. The predictor uses the well-known nonholonomic kinematic model of needle steering [7] to initially estimate the needle deflection, and then employs the HAM method [95] to update the predictions online.

(2) The controller includes the surgeon in the control loop. The previous studies including the controler presented in previous chapter have only considered the fully robotic needle insertion [14, 15, 34–36]. In fully robotic needle steering the goal is to calculate a needle steering control input (mainly needle axial rotation) assuming the rest of the inputs are fixed at known values such that needle targeting accuracy is improved. A possible intermediate step between fully-manual and fully-robotic insertion is semi-manual needle insertion, in which automatic robot-assisted adjustments are performed to one of the control inputs while other inputs are directly applied by the surgeon. Here, we propose a semi-automated needle steering strategy, in which the surgeon is in charge of needle insertion in the interest of ensuring the safety of the operation and to maintain continuous engagement, while the needle tip bevel location is controlled robotically.

This chapter is organized as follows: In Section 5.2.1, the Homotopy Analysis Method used for developing the needle deflection predictor is introduced. Section 5.2.2 includes the derivation of the equations for the HAM-based needle deflection predictor, the method proposed for ensuring rapid convergence of the predictions are presented in Section 5.2.3, and the online needle motion planner for semi-automated needle steering in soft tissue is discussed in Section 5.3. In Section. 5.4, experiments are performed to validate the needle

steering strategy.

5.2 Needle Deflection Prediction

5.2.1 Introduction to The Homotopy Analysis Method

The homotopy analysis method is a mathematical technique to solve nonlinear ordinary/partial differential equations [95]. Here, we will present a modified version of the HAM applicable to *non-homogeneous* nonlinear differential equations. Let us consider the nonlinear differential equation

$$\mathcal{N}[y(x)] = f(x), \quad \mathcal{B}[y, y'] = 0 \tag{5.1}$$

where $\mathcal{N}$ is a nonlinear operator that represents a nonlinear equation, x denotes the independent variable, prime denotes differentiation with respect to x, $y(x)$ is an unknown function, $f(x)$ is a known analytic function, and $\mathcal{B}$ is a boundary operator defining the boundary conditions. By means of the homotopy method first presented by Liao [96], one can construct the so-called zero-order deformation equation as

$$(1-q)\mathcal{L}[y(x) - y_0(x)] = c_0 q\,[\mathcal{N}[y(x)] - f(x)] \tag{5.2}$$

where $q \in [0, 1]$ is the homotopy parameter, $c_0 \neq 0$ is a convergence-control parameter, $\mathcal{L}$ is an auxiliary linear operator, and $y_0(x)$ is the initial guess of $y(x)$. It is important to note that one has great freedom to choose the auxiliary linear operator $\mathcal{L}$ in HAM.

From (5.2), we have

$$\begin{aligned} y(x) &= y_0(x) \qquad \text{when } q = 0 \\ N[y(x)] &= f(x) \qquad \text{when } q = 1 \end{aligned} \tag{5.3}$$

Thus, as q increases from 0 to 1, the homotopy presented by (5.2) continuously deforms from the initial guess to the solution of the original nonlinear equation in (5.1). So, the solution $y(x)$ depends on the homotopy parameter and can be expressed more accurately

as $y(x;q)$. Expanding $y(x;q)$ using Maclaurin series with respect to q, one has

$$y(x;q) = y_0(x) + \sum_{n=1}^{+\infty} y_n(x) q^n \tag{5.4}$$

where

$$y_n(x) = \mathcal{D}_n[y(x;q)] = \frac{1}{n!} \frac{\partial^n y(x;q)}{\partial q^n}\bigg|_{q=0} \tag{5.5}$$

$\mathcal{D}_n[\cdot]$ is called the nth-order homotopy derivative operator. If the auxiliary linear operator, the initial guess, and the convergence-control parameter are chosen properly, the series in (5.4) converges at $q = 1$. Then we have the mth-order homotopy-approximation of the solution to the nonlinear equation as

$$\widehat{y}(x) \approx y_0(x) + \sum_{n=1}^{m} y_n(x) \tag{5.6}$$

In order to calculate $y_n(x)$ $(n = 1, ..., m)$, we differentiate (5.1) n times with respect to q. Then dividing by $n!$ and setting $q = 0$, we get the nth-order deformation equation

$$\mathcal{L}[y_n(x) - \chi_n y_{n-1}(x)] = c_0 \mathcal{D}_{n-1} \left[\mathcal{N}[y(x)] + (1 - \chi_n) f(x)\right] \tag{5.7}$$

where

$$\chi_n(x) = \begin{cases} 0, & \text{if } n \leqslant 1 \\ 1, & \text{if } n > 1 \end{cases} \tag{5.8}$$

$y_n(x,t)$ (for $n \geqslant 1$) is governed by the *linear* equation given by (5.7) with the linear boundary conditions that come from the original problem and can be easily solved in real-time. Solving (5.7), one can successively obtain homotopy approximation of the solution of the nonlinear differential equation in 5.1.

5.2.2 HAM-based Needle Deflection Prediction

Here, the needle deflection predictor developed using the HAM is introduced. As discussed in Section. 5.2.1, HAM is a mathematical technique to solve nonlinear ordinary/partial differential equations [95]. This method is based on the concept of homotopy, a fundamental concept in topology and differential geometry. A homotopy describes a continuous variation

or deformation. For instance, a circle can be continuously deformed into an ellipse. Such a deformation is called a homotopy between the two functions describing the circle and the ellipse. We will use the concept of HAM to estimate the continuous deformation of needle as it is being inserted into the tissue.

In our approach, it is assumed that the needle deflection is initially given by the well-known kinematics model of needle steering [7]. Next, we use the kinematics-based model and the homotopy analysis method to develop the general deformation equation governing the needle tip deflection called the *nth-order deformation equation*. Finally, ultrasound-based feedback of needle position in is used to solve the deformation equation and predict needle deflection in future steps.

Let us assume $\kappa(x)$ is the signed curvature of the needle tip trajectory and x is the insertion depth. If the needle deflection is given in Cartesian coordinates as $y(x)$, then (assuming $y(x)$ is differentiable up to the 2^{nd} order) from basic geometry we have

$$\kappa(x) = \frac{y''(x)}{(1 + y'^2(x))^{\frac{3}{2}}} \tag{5.9}$$

During insertions, the ultrasound probe acquires transverse images of the needle tip. We can use the method presented in [97] to estimate the needle tip trajectory and its curvature (κ) from the ultrasound images. The sign of κ corresponds to the needle tip orientation and changes after each 180° axial rotation of the needle. Having an approximation of the curvature, using (5.9) we can define the general nth-order deformation equation governing the deformation of the needle (see Appendix) and use the HAM method to calculate the needle tip deflection. This process is developed in the following.

We can rewrite (5.9) as

$$y''^2(x) - \text{sgn}(\kappa)\kappa^2(x)[3y'^2(x) + 3y'^4(x) + y'^6(x)] = \text{sgn}(\kappa)\kappa^2(x) \tag{5.10}$$

subject to the initial conditions

$$y(0) = Y_0 \ , \quad y'(0) = Y_0' \tag{5.11}$$

where sgn(.) is the sign function. Y_0 is the initial deflection of the needle tip and Y_0' is the first derivative of the needle deflection, both evaluated at $x = 0$. Y_0' corresponds to the

initial angle of the needle tip with respect to the insertion axis. Note that the predictor estimates the needle deflection in the future steps from arbitrary initial conditions, i.e., the initial deflection ($y(0) = Y_0$). Y_0 is equal to zero at the beginning of the insertion. However, after each needle rotation it is updated to the needle tip deflection immediately prior to rotation. The same approach is used for $y'(y'(0) = Y_0')$. Using this method, we achieve a continuous tip trajectory during needle insertion with multiple axial rotations.

To solve (5.10) and (5.11) by means of the homotopy analysis method, we choose the initial approximation of the needle deflection using the kinematics model of needle steering [7] as:

$$y(x) = r - \sqrt{r^2 - x^2} \tag{5.12}$$

where $r = \frac{1}{\kappa}$ is an initial approximation of the needle radius of curvature. Expanding (5.12) using binomial series

$$y(x) = \frac{x^2}{2r} + \frac{x^4}{8r^3} + \frac{x^6}{16r^5} + ... \tag{5.13}$$

Neglecting terms of orders higher than three and modifying (5.13) based on the initial conditions in (5.11), we obtain the initial approximation of deflection ($y_0(x)$) as

$$y_0(x) = \frac{\kappa}{2}x^2 + Y_0'x + Y_0 \tag{5.14}$$

Note that the above equation satisfies the initial conditions in (5.11) and gives a linear approximation of the needle deflection based on the kinematics-based model of needle steering. Next, we choose the auxiliary linear operator

$$\mathcal{L}[y(x)] = y''(x) \tag{5.15}$$

$\mathcal{L}$ in an auxiliary linear operator that is used to estimate the nonlinear differential equation in (5.11). One has great freedom to choose the auxiliary linear operator in HAM. Inserting (5.10), (5.13), and (5.15) into (5.7), we construct the zeroth-order deformation equation as

$$\begin{aligned} y_n''(x) - \chi_n y_{n-1}''(x) = c_0 \mathcal{D}_{n-1}\Big[& y''^2(x) \\ & - \operatorname{sgn}(\kappa)\kappa^2(x)\left(3y'^2 + 3y'^4 + y'^6\right) - \operatorname{sgn}(\kappa)\kappa^2(x)(1-\chi_n)\Big] \end{aligned} \tag{5.16}$$

subject to initial conditions

$$y_n(0) = 0\ , \quad y_n'(0) = 0 \tag{5.17}$$

n in (5.16) determines the order of approximation. Solving (5.16), we can successively obtain a homotopy approximation of the needle deflection given by (5.10). The first three approximations are

$$y_0(x) = \frac{\kappa}{2}x^2 + Y_0'x + Y_0 \tag{5.18a}$$

$$y_1''(x) = c_0[y_0''^2 - \kappa^2(3y_0'^2 + 3y_0'^4 + y_0'^6 + 1)] \tag{5.18b}$$

$$y_2''(x) = y_1'' + c_0[2y_0''y_1'' - \kappa^2(6y_0'y_1' + 12y_0'^3y_1' + 6y_0'^5y_1')] \tag{5.18c}$$

Note that based on (5.17), the integration constants for solving the above equations are zero. Following the above approach, the approximate nth-order solution of the deformation equation for $n \geqslant 1$ is

$$\begin{aligned} y_n(x) = \int_0^x \int_0^x \Bigg\{ & \chi_n y_{n-1}''(x) + c_0 \sum_{k=0}^{n-1} y_k'' y_{n-k-1}'' \\ & + c_0 \mathrm{sgn}(\kappa)\kappa^2 \Bigg[(\chi_n - 1) - 3\sum_{k=0}^{n-1} y_k' y_{n-k-1}' \\ & - 3\sum_{k=0}^{n-1} y_{n-k-1}' \sum_{m=0}^{k} y_{k-m}' \sum_{j=0}^{m} y_{m-j}' y_j' \\ & - \sum_{k=0}^{n-1} y_{n-k-1}' \sum_{m=0}^{k} y_{k-m}' \sum_{j=0}^{m} y_{m-j}' \sum_{p=0}^{j} y_{j-p}' \sum_{l=0}^{p} y_{p-l}' y_l' \Bigg] \Bigg\} dx \end{aligned} \tag{5.19}$$

Based on (5.18) we infer that the predictor starts by predicting the needle deflection using the linearized kinematics-based model in (5.18a) (our initial approximation). Then, it implements the approximate curvature acquired from the ultrasound images (κ) to enhance the needle deflection estimation using (5.18b) and (5.18c).

The proposed adaptive predictor enhances the needle deflection prediction by improving upon a function from the homotopy defined by the zero-order deformation equation in (5.16) based on ultrasound image feedback. The final needle deflection prediction is robust against noise in the ultrasound-based deflection feedback because it belongs to a homotopy group their deformation is restricted by the zeroth-order deformation equation. Another advantage of HAM is that its performance and convergence is independent of any small/large scale parameters [96]; note that as the straight needle deflects during the insertion, its radius of curvature varies from ∞ to a finite value. The HAM-based method

is independent of the size of the nonlinear equation parameters. All the nth-order deformation equations given by (5.19) are linear and easy to solve. Also, the only parameters of the predictor are the initial estimate of curvature of the needle (κ) and the initial angle of the needle ($Y'(0)$), which can be approximated using a few trial needle insertions. However, experimental results will show that the predictor's performance is robust against uncertainty in the initial value of r.

The convergence control parameter (c_0) in (5.19) guarantees convergence of the approximations to the original solution (5.10). In the next section, we quantify the performance of the proposed needle deflection predictor and propose a semi-analytical approach to calculate the optimal convergence-control parameter (c_0) that ensures rapid convergence of the deflection predictions to the actual value.

5.2.3 Rapid Convergence of Predictions

In the following, we use a semi-analytic method to estimate the optimal convergence-control parameter (c_0) and quantify the convergence of the needle deflection predictions. In order to choose a proper value of c_0, we use the mean squared residual defined by

$$E_m(c_0) = \frac{1}{N+1}\sum_{k=0}^{N}[\triangle_m(x_k; c_0)]^2 \tag{5.20}$$

where N is an integer, $\triangle_m(x_k; c_0)$ is the residual of the governing nonlinear equation given by

$$\triangle_m(x_k; c_0) = \widehat{y}''^2(x) - \kappa^2(3\widehat{y}'^2(x) + 3\widehat{y}'^4(x) + \widehat{y}'^6(x) + 1) \tag{5.21}$$

and $\widehat{y}$ is given by (5.6). $E_m(c_0)$ can be used as a measure of accuracy of the proposed predictor and helps us to select the optimal value of c_0 for rapid convergence of the predictions.

Fig. 5.1(a) shows the experimental needle deflection during an insertion with the constant velocity of 5 mm/sec, compared with the results of the homotopy-based predictor for zero, 2nd, 4th, 8th, and 10th order approximation. The initial radius of curvature for predicting needle deflection (r) was arbitrary selected to be 500 mm. Also, the convergence-

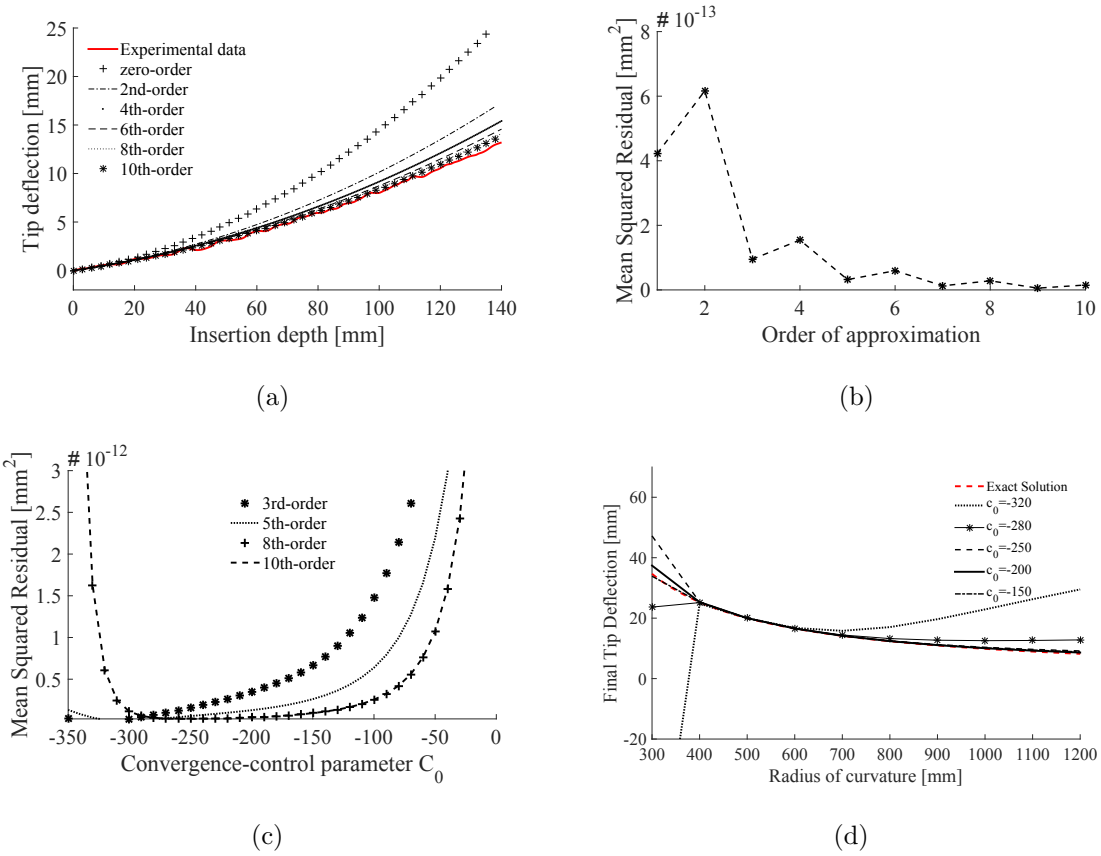

Figure 5.1: Needle deflection during an insertion with a constant velocity of 5 mm/sec. (a) Comparison of homotopy-based predictions for zero, 2nd, 4th, 8th, and 10th order approximation with experimental data. (b) Mean residual error with respect to the order of approximation. 500 data points are used to estimate E_m. (c) Mean residual error for the 3rd, 5th, 8th, and 10th order approximations with respect to the convergence-control parameter. (d) Comparison of exact solution for the final needle tip deflection at a depth of 140 mm under the assumption of constant radius of curvature with the 10-th order homotopy approximation for different values of c_0.

control parameter (c_0) is -250. The mean squared residuals for different orders of approximation are shown in Fig. 5.1(b). Based on the results, the model prediction converges to the actual value as the order of approximation increases for the given value of $c_0 = -150$. In order to investigate the effect of c_0, we plot the mean squared residual with respect to c_0 for the 3rd, 5th, 8th, and 10th order approximations. As can be seen in Fig. 5.1(c), the predictions are convergent for any c_0 between -300 to -200. This distance is typically called the *radius of convergence*.

To further investigate the effect of c_0 and estimate the radius of convergence, we simulate

a scenario in which the radius of curvature is constant and the kinematics-based model accurately predicts the needle deflection. In this case, the needle tip deflection is given by (5.12). The comparison of the exact needle tip deflection at a depth of 140 mm with the 10th-order approximations for different values of c_0 is shown in Fig. 5.1(d). The results show that for a large radius of curvature, high values of $|c_0|$ are non-convergent. Also, the convergence radius of the needle tip deflection becomes smaller as the needle radius of curvature decreases (or the curvature κ increases). This motivates us to define c_0 as

$$c_0^* = -\frac{a}{\kappa} \tag{5.22}$$

where c_0^* is the optimal convergence-control parameter, and based on the results of Fig. 5.1(c) and Fig. 5.1(d), a is a constant between 0.4 and 0.6. We can set the value of $|c_0^*|$ to be smaller than 300 to ensure convergence at high radii of curvature. Using (5.22), we can ensure rapid convergence of the needle deflection predictions to the actual needle deflection. Equation (5.22) can be understood more clearly by comparing the 1st-order approximation of the predictor with the kinematics-based model given in (5.13). Once again, considering that the radius of curvature is constant, from (5.13) and (5.18b) we have

$$y(x) = \frac{x^2}{2r} + \frac{x^4}{8r^3} + \frac{x^6}{16r^5} + .. \tag{5.23a}$$

$$y_1(x) = c_0(\frac{x^4}{4r^4} + \frac{x^6}{10r^6} + \frac{x^8}{48r^8}) \tag{5.23b}$$

By comparing the 1st-order approximation of needle deflection $(y_0(x) + y_1(x))$ given by (5.23) with (5.13), it can be inferred that the optimal c_0, which ensures rapid convergence of the deflection predictions, should be a function of r or $1/\kappa$.

5.3 Online Motion Planner

In the proposed human-in-the-loop needle steering scheme (see Fig. 5.2), the surgeon inserts the needle while the robot axially rotates the needle at appropriate depths to minimize targeting error and maneuver the needle around anatomical obstacles. In most needle-based interventions such as prostate brachytherapy, the target is typically defined on a straight line starting at the entry point in tissue and up to a certain depth. A grid template placed

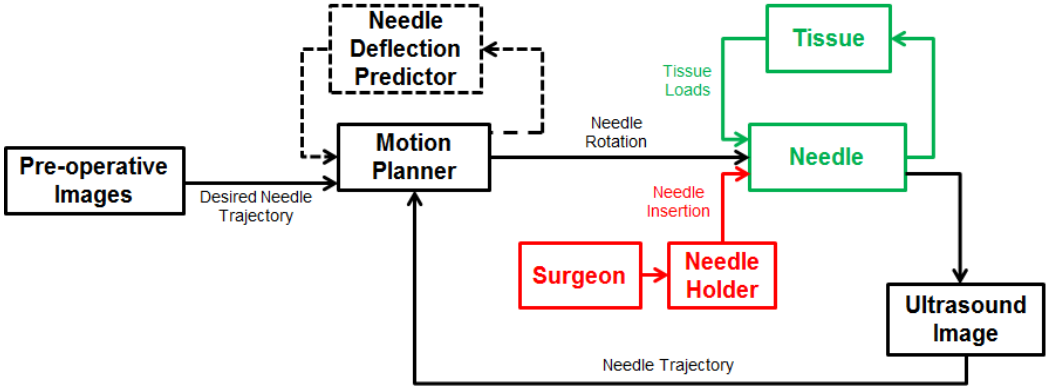

Figure 5.2: Overview of needle steering algorithm, which relies on an online motion planner for closed-loop steering of the needle to the desired target while avoiding anatomical obstacles. As the surgeon pushes the needle in soft tissue using a robotic hand-held instrument, the instrument automatically rotates the needle axially at appropriate depths in order to reach a desired target. The desired target trajectory is obtained using the pre-operative images. The control actions, i.e., rotation depths, are calculated iteratively by the motion planner, which is informed by the current deflection of the needle tip calculated in real-time from the ultrasound images.

outside the tissue is used to position the needle in a fixed insertion plane that contains the target. Also, the surgeon can use other control inputs such as insertion velocity, lateral manipulation of the needle base, and tissue palpation to compensate for out of plane needle deflection. Hence, there is no need to generate 3D trajectories and we will limit the motion planner to the 2D insertion plane. Fig. 5.2 shows a block diagram of our closed-loop control algorithm for semi-automated needle steering.

Our motion planner uses a graph-based search algorithm known as the A^* algorithm. Given the inputs specified previously (e.g., target and obstacle locations), the motion planner computes a large number of plans using the adaptive HAM-based deflection predictor and selects the best plan. The output of the planner is the set of needle 180° rotation depth(s) that will steer the needle tip to the target while avoiding obstacles.

To design the online motion planner we present the needle steering problem in the needle *configuration space*, $\mathcal{C}$. Assuming the needle moves in the 2D insertion plane, the needle *workspace* is a Euclidean space $\mathcal{W} = \mathbb{R}^2$. Let $\mathcal{O}_1, ..., \mathcal{O}_p$ be the obstacles in the workspace. It is assumed that both the geometry and position of the obstacles are known from the preoperative images. The motion planning problem is as follows: given an initial

and a target position of the needle tip in $\mathcal{W}$, find (if it exists) a path, i.e., a sequence of needle axial rotations, that steers the needle between the initial and target positions while avoiding collisions with the obstacles $\mathcal{O}_1, ..., \mathcal{O}_p$.

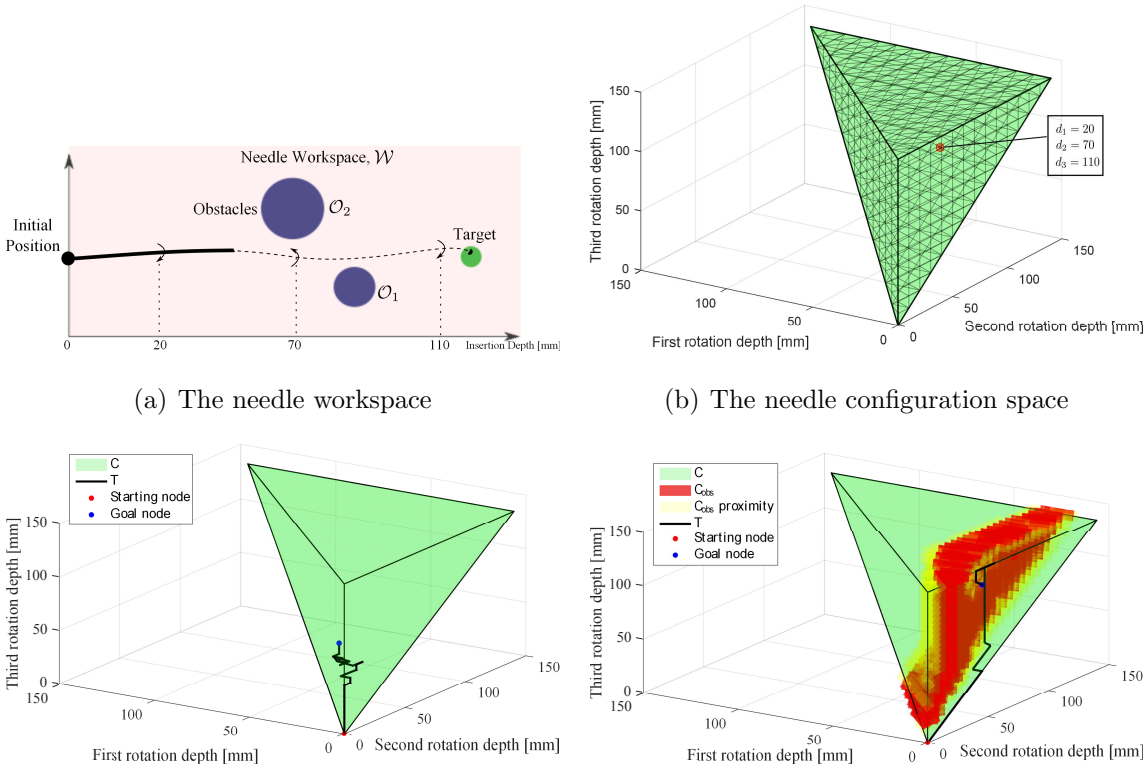

(a) The needle workspace

(b) The needle configuration space

(c) Motion planning without obstacle

(d) Motion planning with obstacle

Figure 5.3: Graphical representation of (a) needle workspace and (b) needle configuration space for a maximum of 3 axial rotations and a maximum insertion depth of 140 mm. A sequence of rotations at depths of 20, 70, and 110 mm in the workspace corresponds to a single point in the needle configuration space. Representative results of motion planning in the configuration space (c) without an obstacle and (d) with a 4-mm circular obstacle positioned at the depth of 70 mm between the needle entry point in the tissue and the target.

We refer to the space of possible control actions (i.e., depth(s) of needle rotation(s)), whose values identify the configuration of the needle tip in the workspace, as the configuration space, $\mathcal{C}$. Considering symmetry of rotation depths (e.g., rotations at depths of 40 and 80 mm are equal to rotations at 80 and 40 mm) the configuration space is an n-dimensional simplex, where n is the number of axial rotations. For instance, if the maximum allowable number of rotations is 3, the configuration space forms a tetrahedron. Fig. 5.3(a) and

Fig. 5.3(b) show the workspace and the configuration space for maximum of 3 rotations, respectively. The motion planner searches through the configuration space to find a sequence of control actions that steers the needle toward the target position while avoiding collisions. In order to solve the planning problem we decompose the configuration space into several disjoint cells. Assuming the distance between two consecutive rotations is at least 5 mm we can decompose $\mathcal{C}$ into several smaller simplices shown in Fig. 5.3(b). This is a valid assumption since two close 180° axial rotations are equal to one full rotation of the needle tip and this action has no effect on needle deflection.

In order to characterize paths that represent a solution in the configuration space – those that avoid collisions between needle tip and obstacles – it is necessary to build the image of the obstacles in the configuration space. Assuming the obstacles are closed in $\mathcal{W}$, we define $\mathcal{C}_{obs}$ as the union of all subsets of the configuration space that cause a collision. The free configuration is the subset of $\mathcal{C}$ that does not cause a collision and is given by $\mathcal{C}_{free} = \mathcal{C} - \mathcal{C}_{obs}$. We build the $\mathcal{C}_{obs}$ through an exhaustive offline search. To find the $\mathcal{C}_{obs}$ we estimate the needle trajectory using the HAM-based predictor at every node in the decomposed configuration space. The boundary of $\mathcal{C}_{obs}$ is the locus of configurations that put the needle in contact with an obstacle. Fig. 5.3(d) shows the image of a circular obstacle in $\mathcal{C}$. The obstacle is 4 mm in diameter and is placed at the depth of 70 mm between the initial entry point in the tissue and the target at the depth of 140 mm. The red area corresponds to a collision and the yellow area is the area in the proximity of the obstacle and corresponds to the needle tip passing the obstacle within a minimum distance of less than 1 mm. The obstacle proximity area is considered to be part of $\mathcal{C}_{obs}$ in order to compensate for unpredictable motion of the obstacle during the insertion.

Assuming that the initial guess for a configuration in $\mathcal{C}_{obs}$ is N_s and the goal configuration that actually steers the needle toward the target is N_g, planning a collision free motion for the needle means generating a safe path between N_s and N_g in $\mathcal{C}_{free}$. For this purpose we use a graph-based search algorithm known as A^* [98]. A^* visits the nodes of the decomposed configuration space iteratively starting from N_s, storing only the minimum paths from N_s to the visited nodes in a tree $\mathcal{T}$. The algorithm employs a cost function $F(N_i)$ for each

visited node during the search.

$$F(N_i) = G(N_i) + H(N_i) \tag{5.24}$$

where

$$G(N_i) = \Lambda \dim(N_i) \tag{5.25a}$$

$$H(N_i) = \|y - y_{tg}\| \tag{5.25b}$$

$H(N_i)$ is the targeting cost function and is the Euclidean distance between the final needle tip position y and the target position y_{tg} in the needle workspace, calculated online using the HAM-based predictions during the iterations. $G(N_i)$ is the cost of the path from $N_{(i-1)}$ to N_i. G is equal to a constant Λ multiplied by the number of rotations $\dim(N_i)$. G increases as the number of rotations increases. One of the goals of the needle steering algorithm is to minimize the patient operative trauma (i.e. tissue damage) by limiting the number of needle axial rotations. The algorithm advances the tree toward the nodes that contain fewer rotations, i.e, the nodes on the faces, edges, or vertices of the n-dimensional simplex. In the following a pseudocode description of the motion planner algorithm is given.

In Algorithm 5.1 we maintain two lists: $OPEN$ and $CLOSED$. $OPEN$ consists of nodes that have been visited but not expanded, meaning that the neighboring nodes have not been explored yet. This is the list of pending tasks. $CLOSED$ consists of nodes that have been visited and expanded (neighboring nodes have been explored already and included in the open list, if this was the case). The `ADJ(`N_g`)` function in Algorithm 5.1 finds the neighboring nodes that are directly connected to node N_i in $\mathcal{C}$. The motion planner accepts the starting node N_s, the minimum allowable cost function F_{min}, and the maximum run time τ as inputs and calculates the target node N_g corresponding to a sequence of rotation depths with an optimal cost function as the output.

Results of the simulation of the motion planner with and without an obstacle are shown in Fig. 5.3(c) and Fig. 5.3(d). The goal is to steer the needle from an initial depth of 0 toward a target placed at a depth of 140 mm. In the simulations, the maximum allowable

Algorithm 5.1: $N_g \longleftarrow$ `Motion_Planner` (F_{min}, N_s, τ)

```
Insert N_s in OPEN with F(N_s) = G(N_s) + H(N_s)
Add N_s to T
while OPEN ≠ ∅ ∧ t < τ do
    N_g ⟵ Find the node in the OPEN with minimum F
    if F(N_g) ≤ F_min then
        Break
    for ∀N_i ∈ ADJ(N_g)∩C_free do
        if N_i ∉ OPEN ∪ CLOSED then
            Insert N_i in OPEN & Update F(N_i)
            Add N_i to T with pointer toward N_g
    Insert N_g in CLOSED
    t ⟵ Update time
```

number of rotations is 3 and we used the HAM-based predictor with constant curvature $\kappa = 0.002$ mm. The starting point is at 0 depth and the run time is set to 1 second. The final targeting error for simulations with and without the obstacle is 0.1 mm and 0.15 mm, respectively. The optimal rotation depths are 25, 35, and 60 mm for insertion without the obstacle and 45 and 125 mm for insertion in the presence of the obstacle. In the next section, we perform needle insertion experiments in ex-vivo biological and synthetic tissue samples to validate the HAM-based predictor and the proposed needle steering strategy.

5.4 Experimental Results and Discussion

Several needle insertion experiments are performed to verify the needle deflection predictor's accuracy. In order to perform needle insertion into soft tissue, the setup shown in Appendix A, Fig. A.2 is used. During the insertions, the ultrasound probe follows the needle tip and acquires transverse images of the needle tip in ex-vivo tissue. The method presented by Waine *et al.* [97] is used to estimate the needle deflection and radius of cur-

vature from the axial ultrasound images. The estimated radius of curvature is used in the HAM-based predictor to calculate needle deflection in future steps. Two types of soft tissue are used in the experiments – homogeneous plastisol tissue and heterogeneous ex-vivo bovine tissue.

A standard 18-gauge brachytherapy needle (Eckert & Ziegler BEBIG Inc., Oxford, CT, USA) is used in the experiments. Plastisol-based and ex-vivo bovine tissue are used in the experiments. The plastisol tissue is made of 80% (by volume) liquid plastic and 20% plastic softener (M-F Manufacturing Co., USA). The stiffness of the plastisol tissue, estimated through indentation tests, is 35 ± 5 kPa. Bovine tissue is embedded in gelatin to ensure good acoustic contact between the ultrasound probe and the tissue and reduce the noise in the ultrasound images.

In the experiments the brachytherapy needle is inserted to a total depth of 130 mm in the soft tissue with and without axial rotation at different insertion velocities. Fig. 5.4 shows the representative results for needle deflection in bovine tissue compared to the initial prediction using the kinematics-based model and the predictor estimations updated online. The results are shown for three scenarios: insertions with constant velocities of 5 (Fig. 5.4(a)) and 30 mms^{-}1 (Fig. 5.4(b)) without axial rotation, and insertion at a velocity of 5 mms^{-}1 with rotation at a depth of 40 mm (Fig. 5.4(c)).

In order to identify the kinematics-based model parameters, the needle is inserted in soft tissue at 10 different insertion velocities between 5 and 50 mms^{-}1, which is in the range of clinical needle insertions [62]. Later the method proposed by Webster et al. [7] is used to estimate the mean, maximum, and minimum curvature (κ) and initial insertion angle ($Y'(0)$). These values are reported in Table. 5.1. The mean curvature and initial angle are used for initial prediction (dashed line in Fig. 5.4).

Table 5.2 compares the experimental and model predictions of the tip deflection values. According to the results given in Table 5.2 and shown in Figs. 5.4(a), 5.4(b), and 5.4(c), the adaptive needle deflection predictor is more accurate than the kinematics-based model. The kinematics- based model's accuracy decreases as insertion velocity is increased. This is mainly due to the fact that the model considers a constant, velocity-independent radius

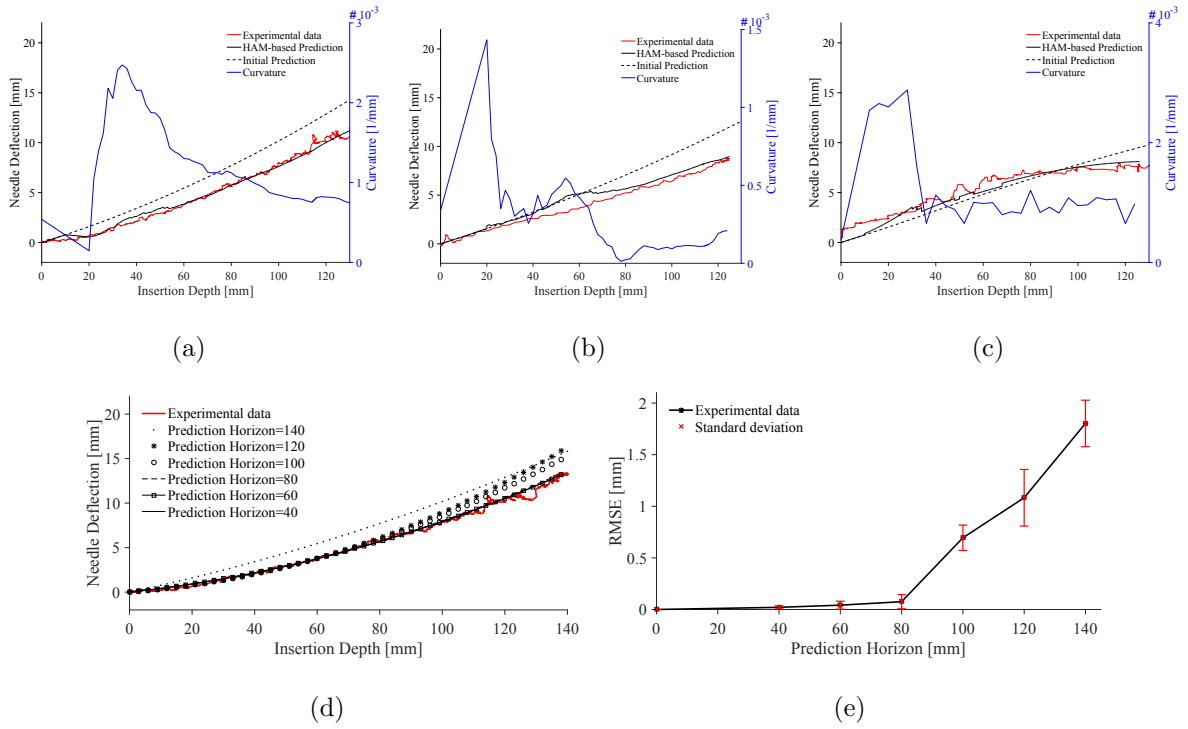

Figure 5.4: Results of experimental validation of the deflection predictor. Comparison of measured needle deflection in ex-vivo needle insertions, HAM-based predictions, and initial prediction using Kinematics-based model at (a) Insertion velocity of 5 mms^{-}1, (b) Insertion velocity of 30 mms^{-}1, and (c) Insertion velocity of 5 mms^{-}1 with rotation at depth of 40 mm. (d) Comparison of experimental data with HAM-based predictions with different prediction horizons. (e) RMSE of the homotopy based prediction for different prediction horizons. Error bars denote the standard deviation of the RMSE for 6 different insertions.

of curvature for the needle tip trajectory and neglects the effects of tissue in-homogeneity, friction along the needle shaft, and velocity-dependent cutting force on tip deflection.

However, it is evident that the adaptive closed-loop predictor is more accurate because it implements the real-time image-based feedback of the needle curvature to compensate for unpredicted deviations from the initial prediction. In order to compare the models more precisely, the kinematics-based model prediction is compared with the predictions of the HAM-base predictor informed by the partial feedback of the needle deflection. For instance, needle is inserted 40 mm in the tissue and the feedback of needle deflection at the depth of 40 mm is used to predict needle deflection up to the depth of 140 mm. Fig. 5.4(d) and 5.4(e) show the error of the homotopy-based predictions for different prediction hori-

Table 5.1: Identified parameters for the kinematics-based model. Maximum curvature (κ_{max}), minimum curvature (κ_{min}), and maximum of initial insertion angle ($Y'(0)$) are listed.

	$\kappa_{max}[mm^{-1}]$	$\kappa_{min}[mm^{-1}]$	$Y'(0)[rad]$
Plastisol	2.9×10^{-3}	6.66×10^{-4}	0.074
Beef	2.03×10^{-3}	4.5×10^{-4}	0.051

Table 5.2: Results of needle steering experiments and HAM-based predictions. Insertions are performed at multiple insertion velocities without axial rotation and at an insertion velocity of 5 mm/sec with rotation(s).

	Plastisol			Beef		
	e_0 [mm]	e_{end} [mm]	RMSE [mm]	e_0 [mm]	e_{end} [mm]	RMSE [mm]
V=5 [mm sec^{-1}]	1.9	0.12	0.10	2.3	0.08	0.09
V=10 [mm sec^{-1}]	2.10	0.09	0.13	2.8	0.22	0.25
V=30 [mm sec^{-1}]	3.38	0.11	0.25	3.4	0.20	0.56
Rotation at 40 mm	1.09	0.24	0.30	1.78	0.53	0.17
Rotations at 40 & 80 mm	0.46	0.263	0.18	0.74	0.72	0.22

zons. In the experiments the needle is inserted to a total depth of 140 mm. Therefore, a prediction horizon of 100 mm corresponds to updating the model up to a depth of 40 mm and then using it to predict needle deflection over the next 100 mm. A prediction horizon of 140 mm corresponds to the offline prediction using the kinematics-based model. It is evident that prediction accuracy decreases as the prediction horizon increases. Note that we are using the optimal convergence-control parameter calculated previously which ensures convergence to the ultrasound-based estimated curvature and because the predictor uses the kinematics-based model for initial prediction, the model error is guaranteed to be less than the kinematics-based model for any prediction horizon. The maximum RMSE is 1.3 mm corresponding to the final tip prediction error of 1.05 mm.

We performed several experiments to evaluate the performance of the online motion

Table 5.3: Results of needle steering experiments. Maximum number of axial rotations rot, mean targeting error e_{mean}, maximum targeting error e_{max}, and mean of out of plane deflection e_{out} for 10 trials are listed.

	Plastisol		Beef	
	Scenario I	Scenario II	Scenario I	Scenario II
rot	9	5	11	4
e_{max} [mm]	0.87	1.05	1.08	1.22
e_{mean} [mm]	0.51	0.74	0.71	0.87
e_{out} [mm]	0.41	0.55	0.68	0.81

planner. The needle is inserted by hand while the motion planner controls the needle axial rotation. The maximum run time for the planner is set to 1 s and the maximum allowable number of rotations during each run is set to 3. The total depth of insertion is 140 mm, which is in the range of clinical needle insertions. Two virtual scenarios are used in the experiments per each tissue type and we executed our system 10 times for each experimental scenario:

1. The needle is steered to reach a target placed at a depth of 140 mm. This is similar to needle insertion in brachytherapy, where the needle should be inserted along a straight line within the tissue.

2. A 4 mm circular obstacle is positioned at a depth of 70 mm between the needle entry point in the tissue and the target. The needle is steered to reach a target at the depth of 140 mm while avoiding the obstacle. The target diameter is selected to be 2 mm.

The representative results for scenario (1) and (2) in two different types of tissue are shown in Fig. 5.5 and 5.6. The experimental results are summarized in Table 5.3. The maximum targeting error in the first and second scenario are 1.08 and 1.22 mm, respectively, both for insertions in ex vivo tissue. Also, the maximum out of plane deflection is 0.87 and occurs in the ex-vivo heterogeneous tissue.

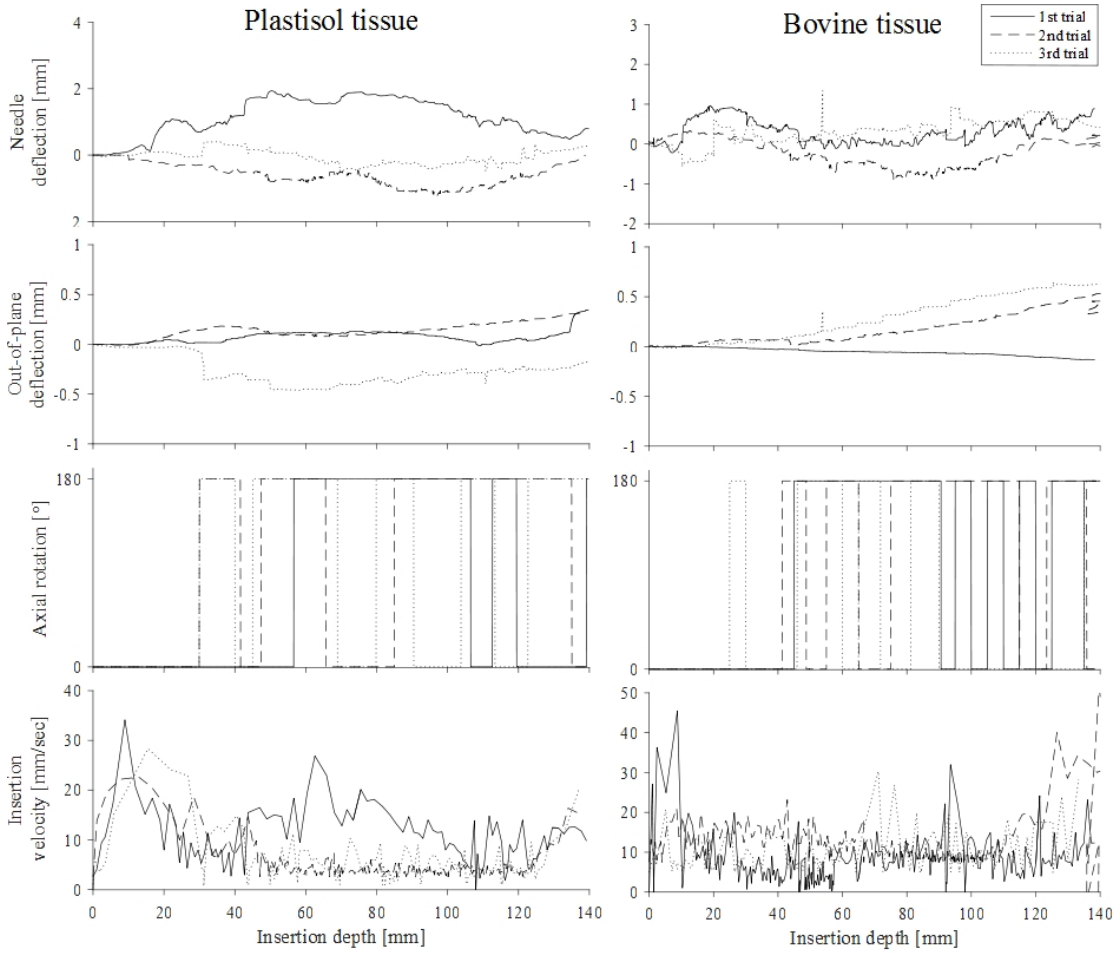

Figure 5.5: Representative experimental results for needle steering without obstacle in plastisol tissue and ex-vivo bovine tissue for three trials per each insertion scenario and corresponding controller input command (i.e., needle axial rotation), needle out- of-plane deflection, and insertion velocity.

5.5 Concluding Remarks

In this section, we presented an adaptive real-time predictor based on the homotopy analysis method for estimation of future needle deflections as the needle is steered inside soft-tissue. Some of the features of the proposed method are: (1) the model uses a depth-varying radius of curvature and is able to predict changes in the needle curvature due to the variations in the insertion velocity or tissue inhomogeneity. (2) As the straight needle deflects, its radius of curvature varies from ∞ to a finite value. The HAM based method is independent of magnitude of radius of curvature and other parameters of the model and

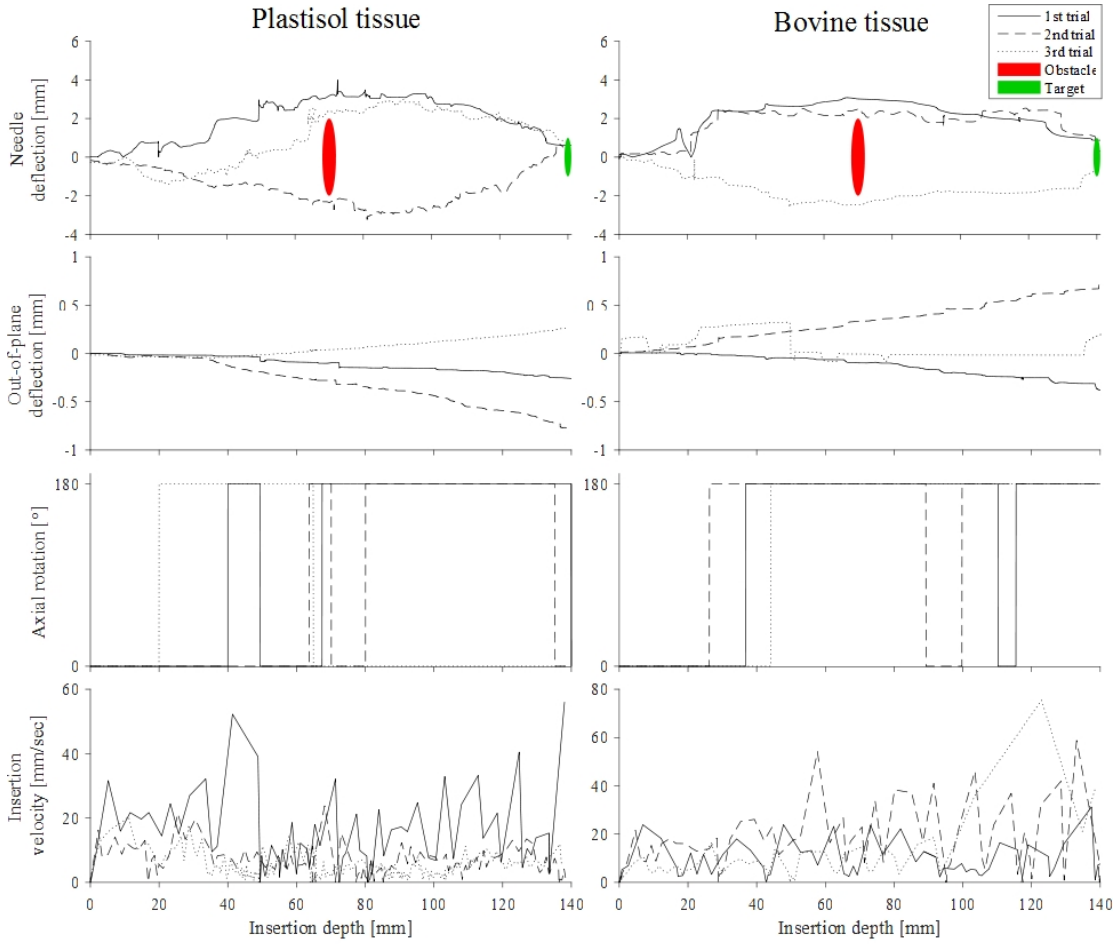

Figure 5.6: Representative experimental results for needle steering with obstacle avoidance in plastisol and ex vivo bovine tissue for three trials per each insertion scenario and corresponding controller input command (i.e., needle axial rotation), needle out- of-plane deflection, and insertion velocity.

predicts needle deflection with good accuracy. (3) The only parameters of the predictor are the average radius of curvature of the needle and the initial angle of the needle with respect to the insertion axis. The experimental results showed, the predictor performance is robust against uncertainty in the initial value of these parameters.

The predictor is implemented in a novel motion planner that steers the needle inside the tissue toward a predefined target. In contrast to existing systems, our approach relies on a semi-automated needle steering scheme. In our needle steering system the robot only controls the needle axial rotation while the surgeon inserts the needle. The experimental results demonstrate that our needle deflection predictor can accurately estimate tip position

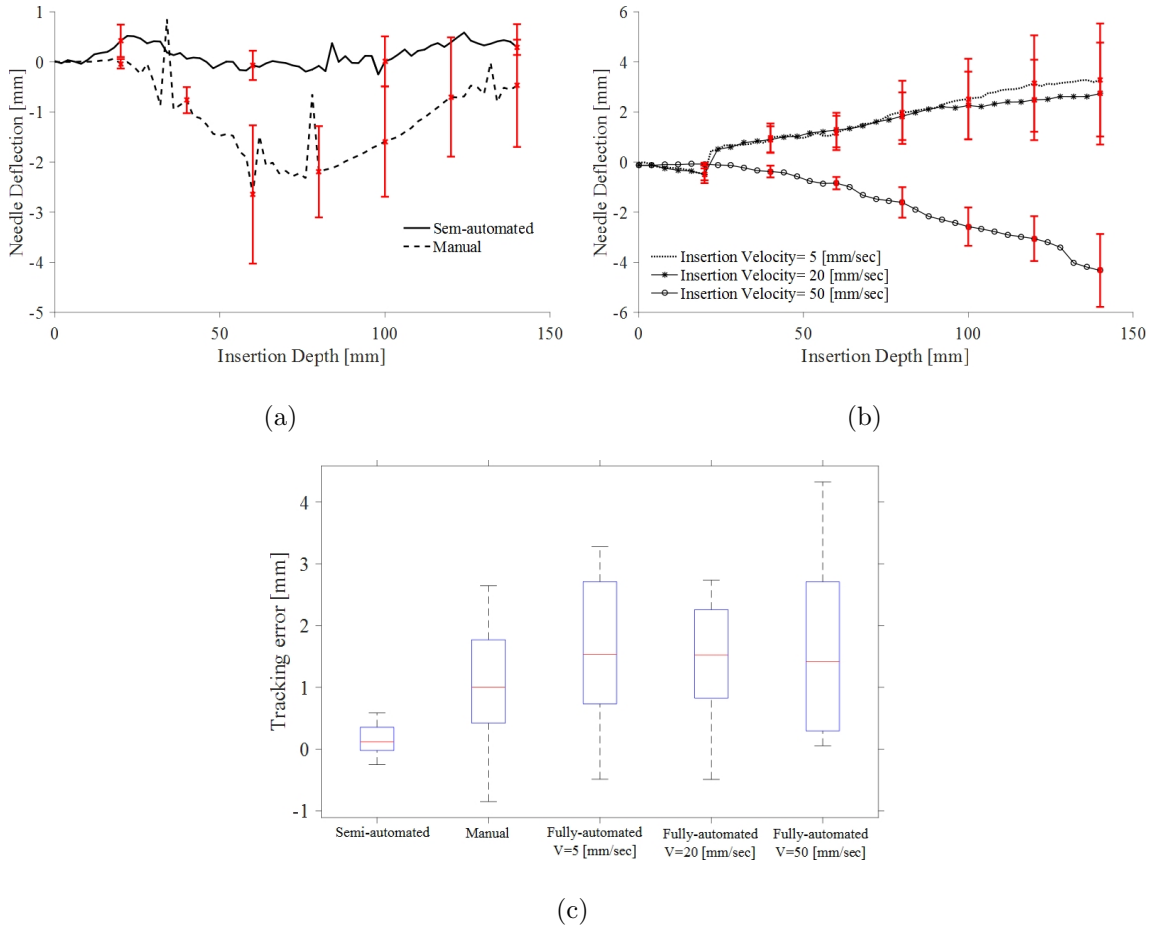

Figure 5.7: (a) A comparison between semi-automated needle steering and manual needle insertion. Averaged data for 10 trials are reported and the red bars denote the standard deviation. (b) A comparison between fully automated needle steering at different insertion velocities. Averaged data for 10 trials are reported and the red bars denote the standard deviation. (c) Accuracy results for different needle insertion scenarios. For each group, red line indicates median error, blue box indicates 25th and 75th percentile, and whiskers indicate minimum and maximum error.

in real-time and the motion planner can steer the needle toward the target position with a maximum in-plane error of 1.22 mm and maximum out of plane error of 0.87. Many factors such as needle torsional dynamics and tissue inhomogeneity can cause needle out-of-plane deflection. In our human-in-the-loop approach, the robot only controls needle axial rotation. Thus, the surgeon can use other control inputs such as insertion velocity, lateral manipulation of the needle base, and tissue palpation to compensate for out of plane needle deflection.

The maximum targeting error of the proposed approach is 1.08 mm for needle insertion on a straight line. In a recent study from our group, seed placement accuracy in prostate brachytherapy is measured using post-implant ultrasound images [99]. 1619 seeds using 357 strands were implanted in 15 patients prostate glands. Of the 1619 seeds implanted, 1196 (73.87%) were confidently identified in post-implant images. The overall mean in-plane and out-of-plane displacements were 13 and 15 mm, respectively, which is higher than our proposed method. However, this error includes the image processing error, error in registering images before and after the surgery, and errors due to prostate motion and deformation.

To furthermore elaborate the effectiveness of semi-automated needle steering and for benchmarking our controlled needle insertion strategy, we have performed several fully automated and manual needle insertions and compared the results with semi-automated needle insertion. Three scenarios are used in the experiments and 10 trials were performed for each experimental scenario:

1. Fully automated needle insertion – Needle insertion and rotation is controlled by a robot to reach a desired target inside the tissue. The needle is robotically inserted at velocities of 5, 20, and 50 mm/sec, which is in the range of clinical needle insertion velocities [62].

2. Semi-automated approach – The surgeon is in charge of needle insertion to ensure the safety of the procedure, while the robot is in charge of controlling the needle trajectory via axial rotations of the needle. Insertions are performed using the device shown in Fig.A.2.

3. Manual insertions – In manual needle insertions, the surgeon inserts the needle using the hand-held device shown in Fig.A.2 and he can rotate the needle 180 degrees axially by pressing a knob located in the control console. Real time visual image feedback of needle tip were provided to the surgeon during the insertions. Manual insertions are performed by a skilled brachytherapist.

In all scenarios, the needle is steered to follow a straight line and reach a target at

the depth of 140 mm (similar to clinical needle insertions in brachytherapy). Results are shown in Fig. 5.7. Based on Fig. 5.7, human-in-the-loop strategy is more accurate than manual. Fig 5.7(c) shows that the standard deviation of the error of the proposed approach is smaller than manual needle insertion. This means our approach gives the same performance at different trials. Also, the semi-automated approach is more precise than fully automated needle steering. Results demonstrated that the needle tracking error increases as the insertion velocity increases. The reason is that the motion planner has less time to compensate for tracking errors at higher velocities. Also mean out-of-plane needle deflection for fully automated needle insertion is 3.2 mm, which is 260% more than the semi-automated out of- plane error. Based on the results, the proposed approach shows more precision and repeatability compared to conventional needle insertion strategies.

Chapter 6

Notched Steerable Needles

6.1 Objective

As it was discussed in Section 2.4, for needle insertions on a straight line, where the target and the needle insertion point are both on a straight line, stiff needles are used and axial rotations are performed only to compensate for small deviations from the straight line. However, to reach divergent targets or targets obscured by obstacles, needles with high curvature or small radius of curvature (ROC) are needed [40]. An example is prostate brachytherapy. In brachytherapy is not prescribed for patients with large volume glands exceeding 50 cm^3 [42] or when there is severe pubic arch interference (PAI) [43]. Experimentally obtained mean ROC for 18G flexible brachytherapy needle is 700-1000 mm (see Section 3.6.5), which should be improved to enhance the needle maneuverability and extend the application of brachytherapy to deeper or more difficult-to-reach targets.

Based on the literature review presented in Section 2.4, one can identify two main ways to increase the maneuverability of needles: 1) increasing needle flexibility, and 2) modify needle design to increase needle/tissue interaction forces that bend the needle. Needle flexibility is improved by employing softer materials or thinner needles. Interaction forces can be increased by decreasing the bevel tip angle, increasing the bevel surface, introducing a precurve near the tip, or a combination of the above [39]. Increasing needle/tissue interaction forces damages the tissue and consequently increases needle intervention's trauma.

Also, very thin or bent-tip needles are incapable of providing a working channel inside the needle.

In this chapter, we modify commercially available disposable brachytherapy needles to develop a needle with improved deflection curvature and enhanced maneuverability. A novel notched needle is developed by carving small notches on a standard needle shaft as shown in Fig.6.1. By carving several consecutive notches on the needle shaft, the needle flexural strength and the needle's maximum achievable ROC are decreased. An optimization algorithm is employed to optimize notch geometry and minimize needle ROC. A novel controller is developed and used to perform image-guided closed-loop needle steering experiments on a tissue phantom and demonstrate the feasibility of maneuvering around obstacles inside the tissue using the notched needle. We simulated a clinical scenario in prostate brachytherapy, where the target is obscured by pubic arch and standard needles can not reach it. Results demonstrate that the new needles can avoid an anatomical obstacle and reach the target. Thus, by improving the needle ROC and its maneuverability we can extend the application of brachytherapy to deeper or more difficult-to-reach targets and enable optimal utilization of brachytherapy for more cancer patients. The width of the notches are smaller than the diameter of payloads. Thus, the needle provides a safe working channel for delivering payloads to target locations.

We remark that the goal of the proposed research is not changing the current clinical setting and replacing the current needles with the new proposed notched needle. Highly flexible needles have been previously proposed for therapies in the brain [44], breast [45], lung [46], liver [41] and kidney [47]. They can be used based on the requirements of the needle-based interventions. We intend to provide another option in terms of needle selection so that surgeons can perform successful needle insertions in certain clinical scenarios where high needle deflection ROC is required.

This section is divided into three main sections, namely, modeling, design, and controlled needle steering. In Section 6.2, we develop a model of needle deflection inside soft-tissue using finite element method (FEM). Open-loop needle insertion experiments are performed in Section 6.2.2 to validate the model. In Section 6.3, we describe the notched needle's design requirements and implement an optimization algorithm to estimate the op-

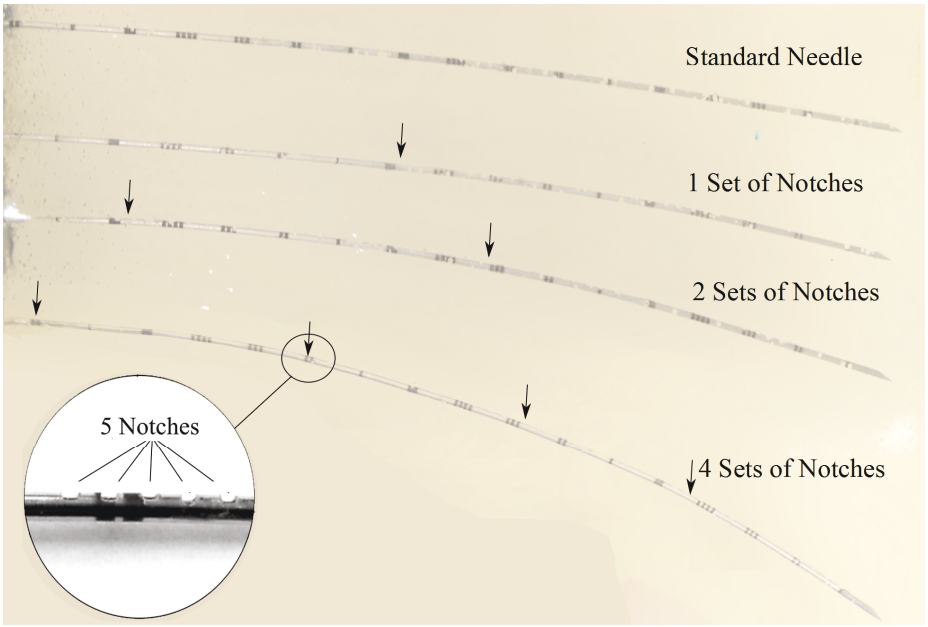

Figure 6.1: A Comparison between deflection of a standard 18G brachytherapy needle and notched needles. Representative experimental needle insertion results for 140 mm insertion of needles with 0, 1, 2, and 4 sets of notches in plastisol tissue phantom are presented. Arrows show location of notches on the needle shaft.

timal location of the notches on the needle shaft for achieving a desired curvature. Next, in Section 6.4 a modified version of the online motion planner developed in Section 5.3 is used for obstacle avoidance in needle steering. Validation of the notched steerable needle in achieving high curvatures in soft tissue and maneuvering around obstacles is presented in Section 6.4.2. Results of the experiments are discussed in Section 6.5.

6.2 Modeling of Notched Needles

Here, we use the finite element method (FEM) to develop a 2D model of the notched needle. The needle is modeled as a beam with a non-constant cross section due to several notches made along the needle shaft. The needle/tissue interaction forces including the tissue cutting force F_c, tissue deformation force F_s, and needle/tissue friction F_f are modeled as external excitation forces (see Fig. 6.4(a)). It is assumed that the needle is comprised of two parts. First part of the needle is outside the tissue, confined by the grid template. The template is used for guiding and positioning the needle during the insertion. The second

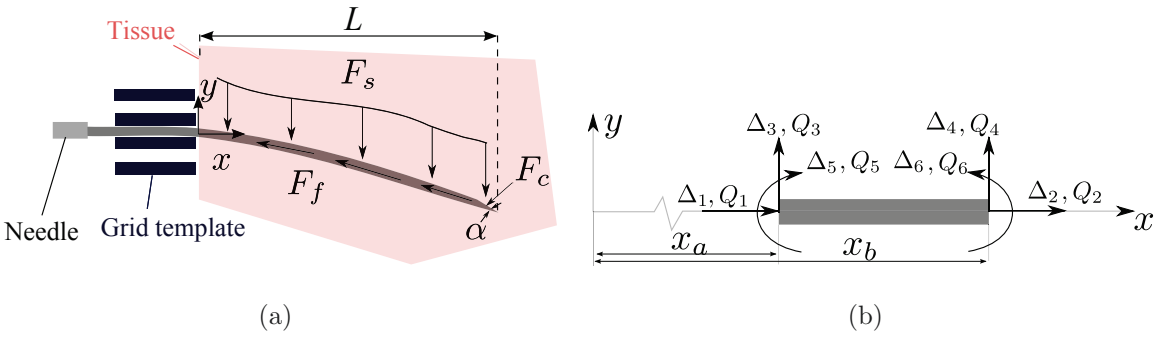

Figure 6.2: Bending behavior of needle modeled as a straight beam under transverse and axial loads: (a) A schematic of needle inside the tissue, F_s, F_c, and F_f are the tissue deformation force, tissue cutting force, and friction along the needle shaft, respectively,α is the needle bevel angle and L is the length of the needle inside the tissue .(b) Generalized force and displacement degrees of freedom of an element of the beam.

part of the needle is inside the tissue. We employ Euler-Bernoulli hypothesis [57] to model the section of the needle that is inside the tissue as a clamped-free beam. To model large needle deflections, we use a modified Euler-Bernoulli beam theory that considers the effects of large rotation of the needle elements and needle shortening along the insertion axis. In the following, first we develop the 2D FEM model of the needle, next we incorporate several needle/tissue interaction models into the FEM model as external nodal forces to develop the final model.

6.2.1 FEM model

We apply the Euler-Bernoulli hypothesis to model the needle as a clamped-free slender beam, which is valid for small deflections of a beam [57]. To model large needle deflections, we modify the Euler-Bernoulli beam theory by considering the effects of large rotation of the needle elements and needle shortening along the insertion axis. This will lead to a nonlinear beam equation, which will be solved iteratively using FEM.

Based on Fig. 6.2(a) and using the Euler-Bernoulli assumption [57], the components of the displacement field are

$$u_1 = u(x) - y\frac{d\omega}{dx}, \quad u_2 = \omega(x), \quad u_3 = 0 \tag{6.1}$$

Using the Green strain tensor and the displacement field in (6.3), we can calculate the

strain components. The only non-zero strain component is

$$\varepsilon_{xx} = [\frac{du}{dx} + \frac{1}{2}(\frac{dw}{dx})^2] - y\frac{d^2\omega}{dx^2} \tag{6.2}$$

In deriving (6.2), we used the small strain assumption (i.e., $(\frac{\partial u_1}{\partial x})^2 = 0$). However, the rotation of beam elements (i.e., $\frac{\partial u_2}{\partial x}$) is non-zero. Now, we use the principle of virtual displacement to derive the nonlinear equations of the deflected beam. Following the variational formulation discussed in Section 3.2.2, we get the nonlinear model of needle deflection

$$\begin{aligned} &-\frac{d}{dx}\left\{EA[\frac{du}{dx} + \frac{1}{2}(\frac{d\omega}{dx})^2]\right\} - f = 0 \\ &\frac{d^2}{dx^2}(EI\frac{d^2\omega}{dx^2}) - \frac{d}{dx}\left\{EA\frac{d\omega}{dx}[\frac{du}{dx} + \frac{1}{2}(\frac{d\omega}{dx})^2]\right\} - q = 0 \end{aligned} \tag{6.3}$$

ω and u are the longitudinal displacement and the transverse deflection, respectively, E is the modulus of elasticity, I is the second moment of inertia of needle cross section, and A is the needle cross section area. f and q are the distributed axial and transverse loads given by

$$\begin{aligned} f &= F_f + F_{cx}\delta(L) \\ q &= F_s + F_{cy}\delta(L) \end{aligned} \tag{6.4}$$

where F_s and F_f are the tissue deformation force and friction along the needle shaft (measured per unit length). $F_{cx} = F_c \sin(\alpha)$ and $F_{cy} = F_c \cos(\alpha)$ are the axial and transverse components of tissue cutting force, respectively, and α is the needle tip's bevel angle. F_c is the total cutting force defined as the normal force applied to the needle beveled tip as it cuts through the tissue (see Fig. 6.2(a)). $\delta(\cdot)$ is the Dirac delta function.

Now, we can use (6.4) to build a weak formulation of the problem. Let the axial displacement $u(x)$ and the transverse displacement $\omega(x)$ for each element be approximated by

$$u(x) \approx \Sigma_{j=1}^{2}\Delta_j\psi_j(x), \quad \omega(x) \approx \Sigma_{k=1}^{4}\Delta_{k+2}\phi_k(x) \tag{6.5}$$

where $\Delta_i(x)$ $(i = 1, 2, 3, 4)$ are generalized virtual displacements of element e of the needle shown in Fig. 6.2(b). $\psi_j(x)$, $j = 1, 2$, are the linear Lagrange interpolation functions and $\phi_k(x)$, $k = 1, 2, 3, 4$, are the Hermite cubic interpolation functions [100] satisfying the differentiability conditions in (6.3). Substituting the approximations in (6.3), we can build

a weak formulation of (6.3) and obtain the following FEM equations for an element e of the beam beginning at x_a and ending at x_b.

$$\begin{bmatrix} K^{11} & K^{12} \\ K^{21} & K^{22} \end{bmatrix} \begin{bmatrix} \Delta \end{bmatrix} = \begin{bmatrix} F^1 \\ F^2 \end{bmatrix} \tag{6.6}$$

where

$$K_{ij}^{11} = E \int_{x_a}^{x_b} A^e \frac{d\psi_i}{dx} \frac{d\psi_j}{dx} dx, \tag{6.7a}$$

$$K_{ik}^{12} = \frac{1}{2} E \int_{x_a}^{x_b} A^e \frac{d\omega}{dx} \frac{d\psi_i}{dx} \frac{d\phi_k}{dx} dx \tag{6.7b}$$

$$K_{mj}^{21} = E \int_{x_a}^{x_b} A^e \frac{d\omega}{dx} \frac{d\psi_j}{dx} \frac{d\phi_m}{dx} dx \tag{6.7c}$$

$$K_{mk}^{22} = E \int_{x_a}^{x_b} \left[I^e \frac{d^2\phi_m}{dx^2} \frac{d^2\phi_k}{dx^2} + \frac{1}{2} A^e \left(\frac{d\omega}{dx} \right)^2 \frac{d\phi_m}{dx} \frac{d\phi_k}{dx} \right] dx \tag{6.7d}$$

$$F_i^1 = \int_{x_a}^{x_b} (F_f + F_{cx}\delta_\ell)\psi_i dx + Q_i, \tag{6.7e}$$

$$F_m^2 = \int_{x_a}^{x_b} (F_s + F_{cy}\delta_\ell)\phi_m dx + Q_{m+2} \tag{6.7f}$$

with $i, j = 1, 2$ and $k, m = 1, 2, 3, 4$. Q_i is the generalized forces of element e shown in Fig. 6.2(b). (6.6) gives the equation of motion for each element of the beam. By assembling the resulting equations for all the beam elements in a matrix and enforcing boundary conditions for a clamped-free beam, we obtain the final FEM model of the needle deflection as

$$K(\Delta)\Delta = F(\Delta) \tag{6.8}$$

where K is the stiffness matrix and is a function of displacement of nodes Δ. F is the vector of nodal forces. K^{12}, K^{21}, K^{22}, and F^2 in (6.7) include nonlinear terms. Thus, the FEM problem given by (6.8) is nonlinear and should be solved iteratively. To solve the FEM problem, the Newton's iteration procedure is used [100].

So far, we have modeled the needle bending. However, the interaction forces shown in Fig. 6.4(a) are yet to be determined. To calculate these forces, we implement the models we developed in Chapter 3. First we use a simplified friction model. Friction can be estimated as a function of insertion velocity per needle length using

$$f = \mu_c \text{sgn}(V) + \mu_v V \tag{6.9}$$

where μ_c and μ_v are the Coulomb and viscous friction coefficients, respectively, and V is the insertion velocity. Also the cutting force applied to the needle tip can be modeled using the model given in Section 3.3.1. Based on the mode, for a specific tissue and a given insertion velocity, cutting force can be assumed constant. To model the tissue reaction forces we implement the *time-delayed* tissue model presented in Section 3.5. In the model, the magnitude of tissue deformation during the needle insertion is estimated as the difference between the cutting path (i.e., the needle tip trajectory across time) and the needle shape. Under this assumption, the distributed tissue reaction force is given by

$$F_s = E_S[\omega(x,t) - \omega(L, t-\tau)] \tag{6.10}$$

where L is the length of the needle inserted in the tissue, E_S is the tissue stiffness, $\tau = \frac{\ell - L}{V}$, ℓ is the total length of the needle, and V is the insertion velocity. F_s in (6.10), depends on both tissue properties and the amount of needle deflection. See Section 3.5 for more details.

In our *quasi-static* simulations, first we divide the total insertion depth into several small insertion steps, d_s. The simulation begins at the onset of insertion, needle initial length L is equal to d_s, with zero needle deflection, zero tissue reaction force, and only the cutting force applied to the needle tip. In the next step, $L = 2d_s$. We use the resulting needle tip deflection from the previous step and the model (6.10) to estimate the current tissue reaction force along the needle length. Estimated forces are implemented in the FEM model as nodal forces and the needle deflection is calculated. This approach is continued until the needle reaches the final depth.

We can compute the strains and stresses in the notched needle by post-processing the FEM and estimate the factor of safety of the notched needle as a measure of the strength of the needle in withstanding the expected loads applied to the needle. The axial stress in the beam is given by $\sigma_{xx} = E\varepsilon_{xx}$, where ε_{xx} is the summation of extensional and bending components of strain given by (6.2). The factor of safety can be obtained by:

$$FS = \frac{\sigma_{TS}}{\sigma_{max}} \tag{6.11}$$

σ_{max} is the maximum stress in the needle, and σ_{TS} is the material ultimate tensile strength.

6.2.2 Results

In this section, needle insertion experiments are performed using the setup shown in Appendix A, Fig. A.1 to verify the proposed FEM model and evaluate notched needle performance in achieving high deflection curvatures. In order to identify the tissue cutting force, the tissue stiffness per unit length of the needle and the friction force per unit length of the needle, we follow the approach discussed in Section 3.6. The values of the parameters of the needle steering model identified for constant insertion velocity of 5 mm/sec and known mechanical characteristics of the needle are given in Table 6.1.

Results of needle deflection simulations using the parameters given in Table 6.1 are presented in Fig. 6.4. The simulations are performed for needle deflection in free space under 0.05 N load and the needle insertion in soft tissue up to a depth of 140 mm without rotation and with rotation at the depth of 70 mm. Simulations are performed for a standard needle and a notched needle with 3 sets of notches. Based on the simulation results, the mean ROCs of the notched needle in and outside the tissue is 53% and 70% smaller than the standard needle both, respectively. The highest estimated stresses for both needles in free space are at the needle base and almost similar ($\sim$ 18 MPa). The maximum stress for notched needle in soft tissue is near the notch closest to the needle tip in insertion with rotation and is equal to 1.25 MPa. Considering that the maximum strength of a needle made out of stainless steel Grade 316 is 480 MPa, the safety factor of the proposed notched needle is 380. This is a relatively high safety factor and ensures the needle will not break during the insertion.

Figure 6.3: The 3D printed template used for carving notches on the needle.

We compare model predictions with experimentally obtained needle deflection to validate the model. In the experiments, sets of 5 equidistant notches with depth 0.3 mm and width 0.4 mm are manually carved at different locations on the needle shaft. The distance between each consecutive notch in a single set is selected to be 1.5 mm. Needle insertions

Table 6.1: Experimentally identified parameters and constant known parameters of the FEM model

Identified Parameters		
E_S [N/m^2]	F_c [N.sec/m^2]	F_f [N/m]
1.190×10^5	0.963	4.208
Known Parameters		
E [GPa]	ℓ [m]	α [°]
200	0.2	20
I [m^4]		A [m^2]
Un-notched 7.75×10^{-14}		Un-notched 4.81×10^{-7}
Notched 6.8×10^{-14}		Notched 2.40×10^{-7}

are performed with a standard 18G brachytherapy needle (Eckert & Ziegler BEBIG Inc., CT, USA) and 18G brachytherapy needles with 1, 2, and 4 sets of notches. A single set of notches is carved in the middle of the needle, double sets are carved at the lengths of 66 and 133 mm, and quadraple sets are placed at lengths of 40, 80, 120, and 160 mm. The procedure introduced in [97] is used to calculate needle deflection from the ultrasound images. To validate the FEM model, we perform simulations using the parameters given in Table 6.1 and compare the results with the experimentally obtained needle deflections. The results are shown in Fig. 6.5. In the experiments, 6 insertions were performed at a constant insertion velocity of 5 mm/sec for each needle type.

Table 6.2 summarizes the experimental results. Experimental mean ROC, ROC_{exp}, model predictions mean ROC of the deflected needle, ROC_{model}, as well as the prediction error, ROC_{error}, and root mean squared error (RMSE) of predicting ROC during the needle insertion are reported. The needle ROC reported in here and commonly assumed to be constant in the literature is the needle ROC in the local frame of the needle tip. The needle trajectories seen in in Fig. 6.5 are from a point of view of a fixed inertial-frame. We note that the local tip frame and the global inertial frame coincide when the insertion velocity is constant and the needle is not rotated. Thus, the data for the needle insertions without rotation are used to identify the needle's ROC. Throughout this chapter, the ROC is calculated by fitting a circle to the global needle deflection when the needle is not rotated

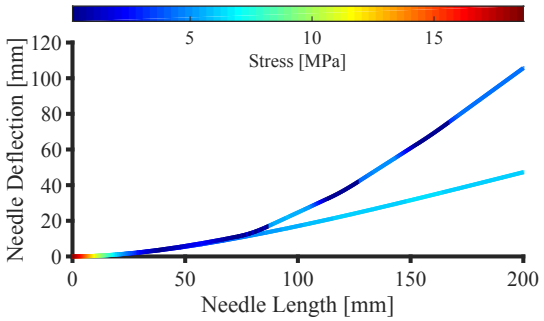

(a) Needle in free space

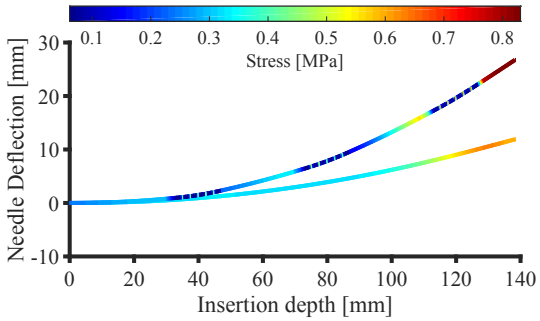

(b) Needle in soft tissue

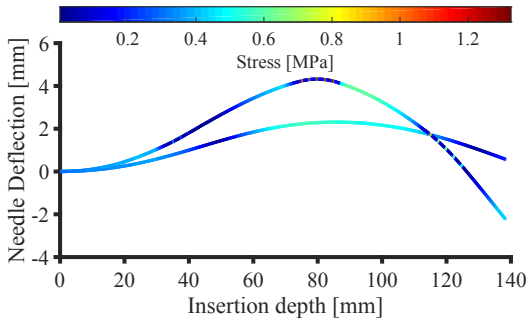

(c) Needle in soft tissue with axial rotation

Figure 6.4: Results of FEM model simulations. Simulations are performed for a standard needle and a notched needle with 3 sets of notches. The FEM model consists of 120 elements and the insertion is performed at 0.25 mm steps. A tolerance of 10^{-4} mm and a maximum allowable iteration number of 100 (per each insertion increment) are used in the FEM analysis and the iteration procedure. (a) Needle deflection in free space under 0.05 N load applied to the needle tip. (b) Needle insertion in soft tissue up to a depth of 140 mm without rotation. (c) Needle insertion in soft tissue up to a depth of 140 mm with rotation at the depth of 70 mm.

using nonlinear least-square method.

We also performed some experiments involving 180° axial rotation of the needle. A notched needle with two sets notches is inserted to a total depth of 140 mm at a speed of 5 mm/s, while either a single rotation is performed at a depth of 80 mm, or double rotations are performed at depths of 30 and 80 mm. 10 needle insertions are performed for each scenario. The maximum error in predicting the tip position is 1.74 mm at a depth of for insertion with double rotations.

The experimental results show that carving four sets of equally spaced notches on the needle shaft improves the needle deflection curvature by 67%. The FEM model is capable

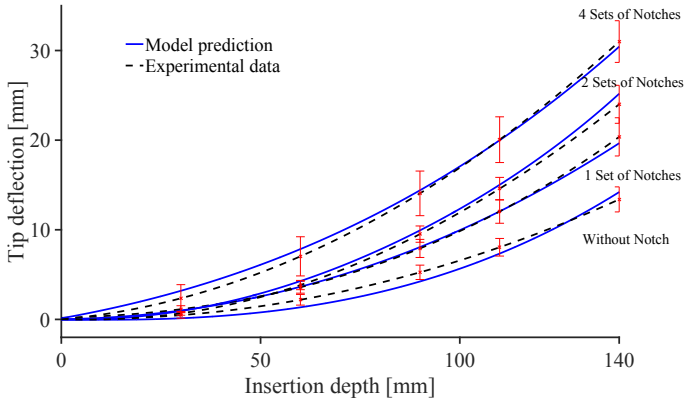

(a) Without axial rotation

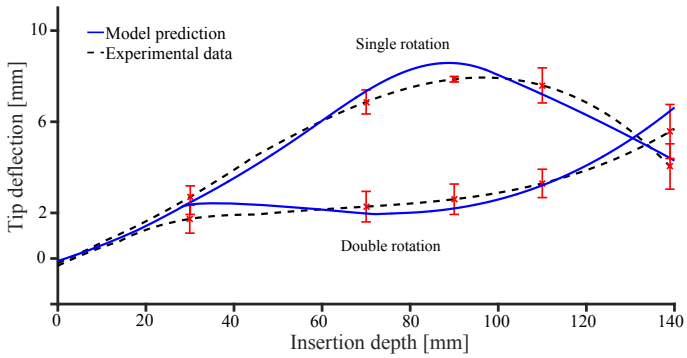

(b) With axial rotation

Figure 6.5: A comparison of experimentally-obtained needle deflections and the corresponding model predictions for (a) needles with 0, 1, 2, and 4 set(s) of notches without rotation, and (b) needle with 2 sets of notches with single rotation at a depth of 80 mm and double rotations at depths of 30 and 80 mm. Error bars denote standard deviation.

of predicting the needle curvature with an accuracy of of 89%. The largest deviation in final tip deflection was observed for the needle with one set of notches (6%).

6.3 Design of Notched Needles

The FEM model presented in Section 6.2 accepts the notch geometry (e.g., notch depth, width, and the location of the notches on the needle shaft) as the initial parameters. In this section, the model is employed in an optimization algorithm to estimate the number of notches and the optimal geometry of the notches required to achieve the highest possi-

Table 6.2: Comparison of experimental data and model predictions.

Number of Notch Sets	ROC_{exp}	ROC_{model}	ROC_{error}	RMSE [mm]
0	616	583	5.3%	6.85
1	452	478	5.7%	3.01
2	367	340	7.3%	4.09
4	205	233	10%	7.64

ble curvature (or lowest ROC), while maintaining a reasonable safety factor. We will use the particle swarm algorithm (PSO) to calculate optimal design soloution. PSO was first proposed by Kennedy and Eberhart [101] and has been proved to be useful on diverse engineering design applications such as structral shape optimization and topology optimization [102]. In the following, we introduce the optimal problem for designing the notches and briefly discuss a modified PSO algorithm for solving the optimal problem.

6.3.1 Optimal Notch Design

The notched needle design involves carving several sets of notches on different locations on the needle shaft. Each set includes several consecutive notches. It is assumed the notch width and depth are both 0.5 mm. These design parameters are assumed constant to ensure the needle can provide a safe channel for delivering payloads with a diameter bigger than 0.5 mm. In the optimal design problem the number of sets of notches (N_s), the number of notches in each set (N_n), the distance between notches in each set (d_n), and each sets location on the needle shaft (d_s) are being optimized towards the minimization of the mean needle ROC during needle insertion to the depth of 140 mm. The number of sets and notches in each set are integers and varies between 1 and 10. To restricts the optimization to feasible solutions, constraints are imposed on the distance between the notches in each set [0.5, 5] mm and the notch sets' locations on needle shaft [0, 200] mm.

In total, the problem has variable dimentionalty of 13 (maximum of 10 different notch set locations, the distance between notches, the number of notches, and the number of

sets). The optimal problem can be programmed as a mixed integer constrained nonlinear optimization problem:

$$\begin{aligned} &\text{cost}(\overrightarrow{X}) = \min_{\overrightarrow{X}} \;\; ROC(\overrightarrow{X}) + \Lambda \frac{1}{FS(\overrightarrow{X})} \\ &\text{subject to} \quad A.\overrightarrow{X} \leq b \\ &\text{where } \overrightarrow{X} = (N_s, N_n, d_s, d_n), \\ &\; N_s, N_n \in \mathbb{N}, \; d_n \in \mathbb{R}, \; d_s \in \mathbb{R}^{10} \end{aligned} \tag{6.12}$$

A is a m-by-13 matrix, where m is the number of inequality constraints and b is a vector of length m. Λ is a weighting parameter that penalizes low safety factors.

The PSO makes use of velocity vector $\overrightarrow{V}$ to update the particles' position $\overrightarrow{X}$ in a swarm. Each particle corresponds to an initial solution of the optimal problem. The position of a particle i at iteration $k+1$ is updated by

$$\overrightarrow{X}^i_{k+1} = \overrightarrow{X}^i_k + \overrightarrow{V}^i_{k+1} \tag{6.13}$$

Velocity is updated based on the memory gained by each particle, as well as the knowledge gained by the swarm as a whole. Velocity for each particle is given by

$$\overrightarrow{V}^i_{k+1} = w\overrightarrow{V}^i_k + c_1 r_1(\overrightarrow{P}^i_k - \overrightarrow{X}^i_k) + c_2 r_2(\overrightarrow{P}^g_k - \overrightarrow{X}^g_k) \tag{6.14}$$

$\overrightarrow{V}^i_k$ is the velocity at iteration k, r_1 and r_2 represents random numbers between 0 and 1, $\overrightarrow{P}^i_k$ and $\overrightarrow{P}^g_k$ denote the best ever particle position and global best position up to iteration k, respectively. c_1 and c_2 are constants and vary between 0 and 1. w is the inertia weight. Based on the particle and velocity update rules and the optimal problem in (6.12), the algorithm is constructed.

In Algorithm 6.1, three modifications are performed (compared to the standard PSO algorithm) to satisfy the constraints.

1. All the design variables for each particle are randomly initialized to satisfy the lower and upper bounds imposed by the constraints.
2. In calculating $\overrightarrow{P}^i$ and $\overrightarrow{P}^g$, only the feasible particles that satisfy the constraints are counted.

Algorithm 6.1: Particle Swarm Optimization

1 `Initialize all particles` $\overrightarrow{X}_0^i = \overrightarrow{X}_{min} + r(\overrightarrow{X}_{max} - \overrightarrow{X}_{min}),\ \ \overrightarrow{V}_0^i = 0,\ k = 0$
2 **while** $k <$ *Max_iteration* **do**
3 **for** $\forall \overrightarrow{X}_k^i \in$ swarm **do**
4 **if** $A.\overrightarrow{X}_k^i \leq b$ **then**
5 **if** $cost(\overrightarrow{X}^i) < cost(\overrightarrow{P}^i)$ **then**
6 $\overrightarrow{P}^i = \overrightarrow{X}^i$
7 **if** $cost(\overrightarrow{X}^i) < cost(\overrightarrow{P}^g)$ **then**
8 $\overrightarrow{P}^g = \overrightarrow{X}^i$
9 **for** $\forall \overrightarrow{X}_k^i \in$ swarm **do**
10 $\overrightarrow{V}_{k+1}^i = w\overrightarrow{V}_k^i + c_1 r_1(\overrightarrow{P}_k^i - \overrightarrow{X}_k^i) + c_2 r_2(\overrightarrow{P}_k^g - \overrightarrow{X}_k^g)\ \overrightarrow{X}_{k+1}^i = \overrightarrow{X}_k^i + \overrightarrow{V}_{k+1}^i$
11 **if** $A.\overrightarrow{X}_{k+1}^i \leq b$ **then**
12 $w = 0$
13 **Go to** 14
14 $k = k + 1$

3. The velocity vector of a particle that violates the constraints is restricted to a usable direction that will reduce the cost function while pointing backwards to feasible directions [103]. During the iterations, a new position for the violated constraint particles is defined by setting the inertia parameter w in (6.14) to zero. The new velocity is a weighted average of previous particles and points toward feasible regions of the design space. To update discrete design variables, a criterion known as the Nearest Vertex Approach (NVA) is used [104]. The NVA approximates the discrete-domain location to the nearest integer of the local discrete variable on the basis of the Euclidean distance. This method is used for the two aforementioned discrete variables, namely, the number of sets of notches (N_s) and the number of notches in each set (N_n).

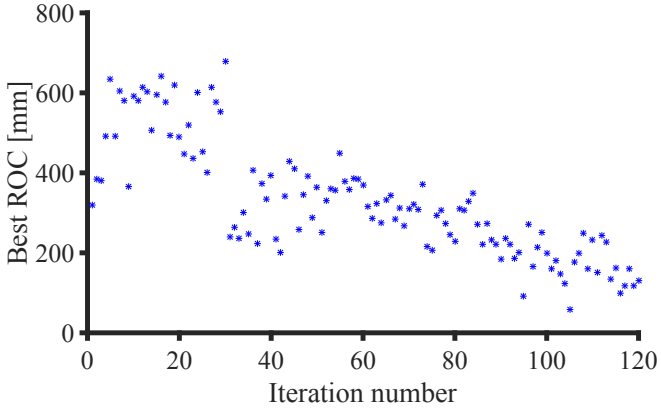

Figure 6.6: Results of PSO optimization for estimating optimal needle ROC with respect to notch geometry and placement.

6.3.2 Optimization Results

Using Algorithm 6.1, the optimization is performed to estimate the optimal notch positions for achieving the maximum allowable deflection curvature. Both c_1 and c_2 in (6.14) are 0.5 and the inertia weight w is initially equal to 0.1. The number of particles in the swarm is 20 and the maximum number of iterations is 120. Fig 6.6 shows the best solutions (optimal ROC) at different steps of the simulation. The global best ROC after 100 iterations is 131 mm for 5 sets of 6 notches. The center of the notch sets are placed at 88, 106, 153, 170, 190 mm on needle shaft. The width of the notches is 0.5 mm and the distance between each notch in a set is 1.5 mm. The estimated safety factor of the optimal solution is 285. We will use this needle in the following section to perform controlled needle steering with obstacle avoidance.

6.4 Steering and Obstacle Avoidance

In this section, we briefly introduce an online motion planner used for ultrasound-guided needle steering. The motion planner is a modified version of the planner introduced in Section 5.3. Using the planner, several controlled experimental needle insertions are performed to validate the efficiency of the notched needles in maneuvering obstacles.

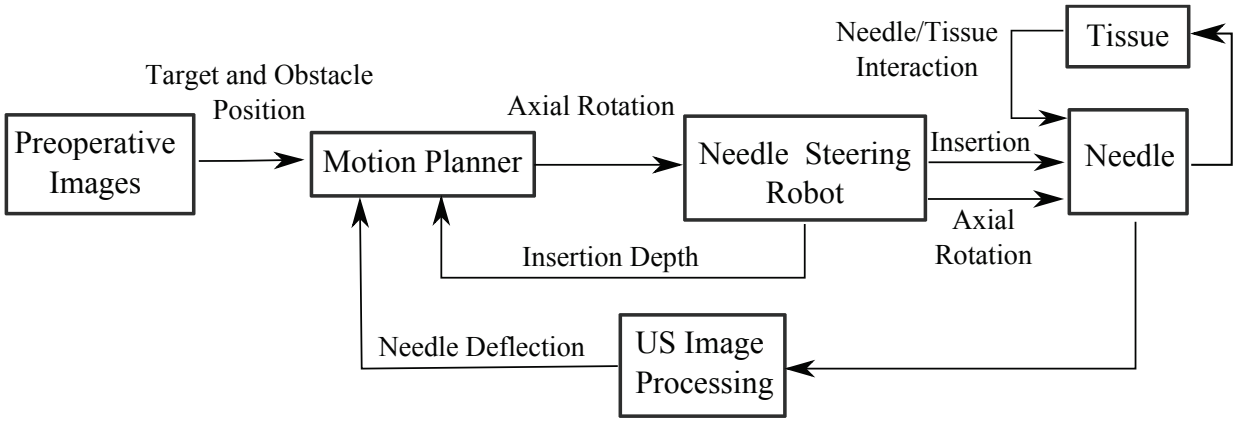

Figure 6.7: Block diagram of the needle steering system.

6.4.1 Online Motion Planner

A schematic of the proposed needle steering scheme is shown Fig. 6.7. The setup shown in Fig. A.1 is used to axially rotate the needle at appropriate depths during the insertion with the aim of minimizing targeting error while maneuvering the needle around anatomical obstacles. An online motion planner is used to calculate the control inputs (i.e., appropriate rotation depths) during the needle insertion. Given the inputs specified preoperatively (e.g., target and obstacle locations), the motion planner computes a large number of plans using the well-known kinematics based model of needle deflection [7] and selects the best plan using the Rapid Random Tree (RRT) algorithm [105]. The output of the planner is the set of needle 180° rotation depth(s) that steers the needle to the target while avoiding obstacles. The kinematics-based model described in Section 2.1 assumes the needle moves on a path with a constant ROC. The only parameter of the model is the needle ROC [7] that is calculated in previous sections. The model has been widely used for image-guided needle steering in tissue [14, 32].

To design the online motion planner, the needle steering problem is defined in the needle *configuration space*, $\mathcal{C}$. Assuming the needle moves in the 2D insertion plane, the needle *workspace* is a Euclidean space $\mathcal{W} = \mathbb{R}^2$. The configuration space, $\mathcal{C}$, is the space of possible control actions (i.e., depth(s) of needle rotation(s)), whose values identify the configuration of the needle tip in the workspace. The motion planning problem is: given an initial and a target position of the needle tip in $\mathcal{W}$, find (if it exists) a sequence of needle axial rotations

that steers the needle between the initial and target positions while avoiding collisions with the obstacles. Considering symmetry of rotation depths (e.g., rotations at depths of 40 and 80 mm and rotations at 80 and 40 mm are equal) the configuration space is an n-dimensional simplex, where n is the number of rotations. For instance, if the maximum allowable number of rotations is 3, the configuration space forms a tetrahedron. Fig. 6.8 shows the workspace and Fig. 6.9(a) shows the configuration space for maximum of 3 rotations. The motion planner searches through the configuration space to find a sequence of rotation depths that steers the needle toward the target position while avoiding collisions. In order to solve the planning problem we decompose the configuration space into several disjoint cells. Assuming the distance between two consecutive rotations is at least 5 mm we can decompose $\mathcal{C}$ into several smaller simplices shown in Fig. 6.9(a).

In order to characterize paths that represent a solution in the configuration space – those that avoid collisions between needle tip and obstacles – it is necessary to build the image of the obstacles in the configuration space. Assuming the obstacles are closed, we define $\mathcal{C}_{obs}$ as the union of all subsets of the configuration space that cause a collision. To find the $\mathcal{C}_{obs}$ we estimate the needle trajectory using the FEM model at every vertex in the decomposed configuration space. The boundary of $\mathcal{C}_{obs}$ is the locus of configurations that put the needle in contact with an obstacle. Same approach can be used to find the goal region in configuration space. The goal region is defined as a set of rotation depth that will lead the needle tip to the proximity of the target while avoiding obstacles (see Fig. 6.9(b) and 6.9(c)). Now we can use the RRT algorithm to search the obstacle free space in $\mathcal{C}$ and find the optimal solution that steers the needle toward goal region. Description of the RRT motion planner algorithm is given in Algorithm 6.2.

The inputs of the RRT are the current depth D_0, the number of allowed rotations N, and the computation time available for planning T_{max}. The algorithm builds the free configuration space , $\mathcal{C}_{free}$, which is the subset of $\mathcal{C}$ that does not cause a collision. Then it generates a random candidate q_{rand} from the N-dimentional configuration space. Next, `Near_Vertex` runs through all the vertices (candidate rotation depths) in $\mathcal{C}_{free}$ to find the closest vertex to q_{rand}. `New_Conf` produces a new candidate configuration q_{new} on the segment joining q_{near} to q_{rand} at a predefined arbitrary distance δ from q_{near}. The random

Algorithm 6.2: Motion Planner

```
Initialize configuration space
C_free = C(N, D_0) − C_obs
while q_goal = ∅ ∧ t < T_max do
    q_rand = Rand_conf(C_free)  q_near = Near_Vertex(q_rand, C_free)
     q_new = New_Conf(q_rand, q_near)  path = Needle_model(q_new, ROC)
     T ← Add_Vertex(q_new)
    if path ∈ Goal then
        q_goal = q_new
    Update T
```

tree $\mathcal{T}$ is expanded by incorporating q_{new} and the segment joining it to q_{near}. Next, needle tip path and targeting accuracy are obtained by inputting the selected rotation depths in the kinematics-based model of needle steering. When the needle path for the newly added configuration is found to lie in the target region (*Goal*), or when the computation times exceeds T_{max} the RRT planner terminates. Once the algorithm stops, the output q_{goal} contains the best set of rotation depths that will bring the needle towards *Goal* region. RRT expansion procedure results in a very efficient exploration of $\mathcal{C}$ and the procedure for generating new candidates in RRT is intrinsically biased toward regions of $\mathcal{C}$ that have not been visited.

6.4.2 Results

Two scenarios are used in the experiments to validate the performance of the notched needle in enhancing targeting accuracy in needle steering.

1. The needle is steered on a straight line to reach a target placed at a depth of 140 mm.

2. The needle is steered to reach a target at the depth of 140 mm while avoiding the obstacle in the proximity of the target.

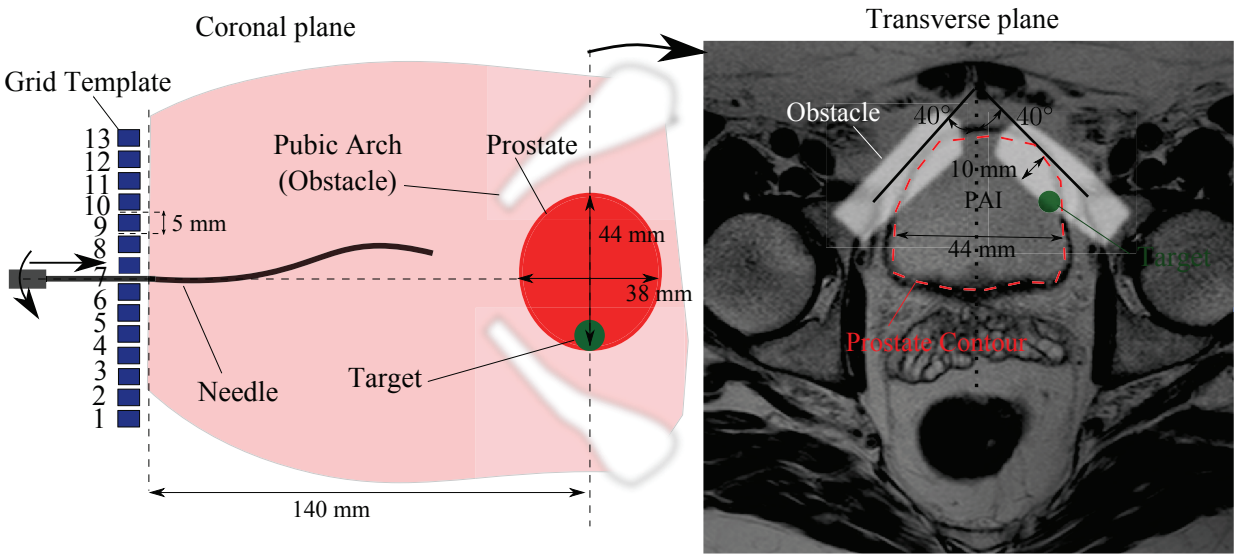

Figure 6.8: Needle workspace in prostate brachytherapy in coronal and transverse plane. In brachytherapy the needle passing through a grid template is inserted in tissue, such that radioactive sources loaded in the needles can be placed near the tumor. The grid template has 13 holes placed 5 mm apart. In the transverse plane, the MR image with the narrowest pubic arch section is overlaid on that with the largest prostate contour in one patient. The image was obtained with the patient in the supine position. The angles of the right and left pubic arches are 40°. The patient has 10 mm overlap of the pubic arch with the prostate margin.

The 1st scenario is similar to conventional needle insertion in prostate brachytherapy, where the needle should be inserted along a straight line within the tissue. The 2nd scenario represents needle steering when there is a severe PAI. PAI is common when the prostate volume is larger than 50 cm^3[43]. PAI is also observed in the presence of a narrow pubic arch even in patients with a small prostate volume [106]. Brachytherapy is often not presceribed in case of PAI. PAI occurs in less than 10% of patients with early signs of prostate cancer [106]. Here, to validate the performance of the notched needles in obstacle avoidance we simulate a very severe case of PAI reported in the literature [106] (see Fig. 6.8).

In this scenario, there is a 10 mm interference between pubic arch and the prostate. The right and left angles to the inner border of the pubic arch are 40°. The prostate is 44 mm in width, 31 mm in height, and 38 mm in length. The prostate dimentions are selected based on the average prostate size reported for men between the ages of 40 and 50 [107]. The 2 mm circular target is placed on one side of the prostate in a plane in the middle of

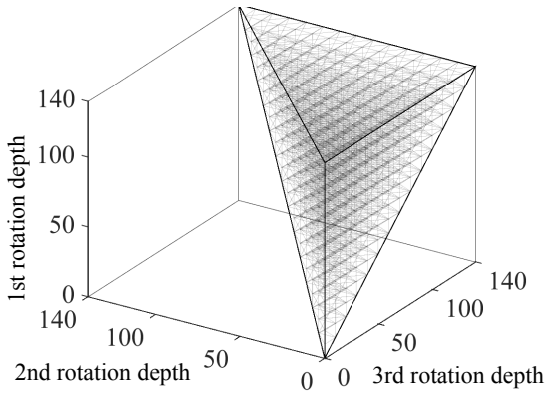

(a) Needle steering configuration space

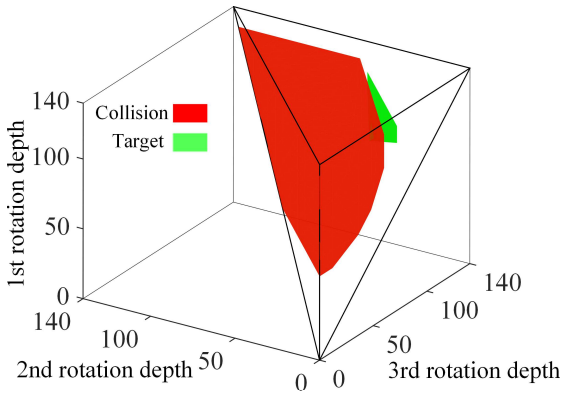

(b) Regions of goal and collision for standard needle

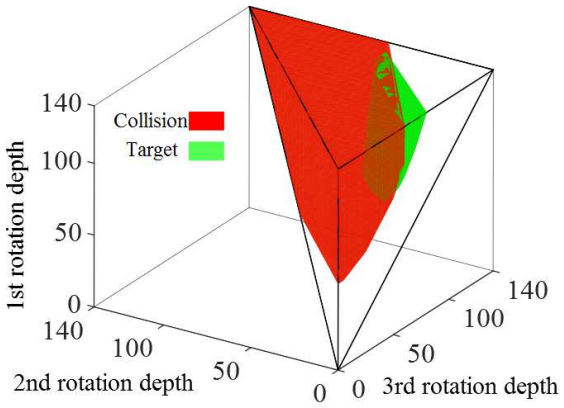

(c) Regions of goal and collision for notched needle

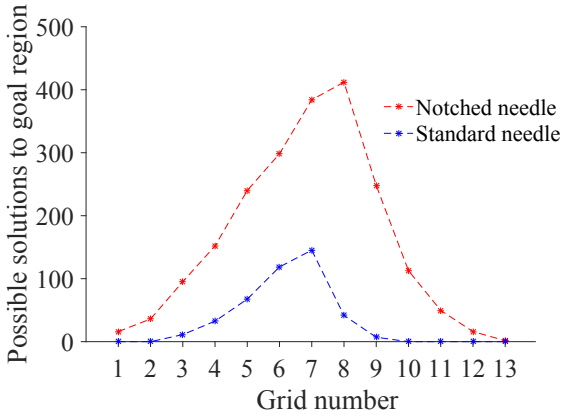

(d) Number of needle steering solutions vs. needle point of entry

Figure 6.9: (a) Needle configuration space for a maximum of 3 axial rotations and a maximum insertion depth of 140 mm. (b) The configuration space for needle insertion from grid 5 with obstacle avoidance for the scenario shown in Fig. 6.8. The regions of obstacle collision and goal achievement are shown in red and green, respectively.(c) The configuration space for insertion of the notched needle from grid 5 with obstacle avoidance for the scenario shown in Fig. 6.8. (d) Comparison of offline path planning with the notched and standard needle. Number of possible solutions, i.e, sets of rotation that will steer the needle to the target while avoiding obstacles, are shown with respect to the selected template grid for insertion (see Fig. 6.8)

the prostate that contains the largest prostate contour.

Results of the offline simulation of the motion planner with and without an obstacle are shown in Fig. 6.9. The goal is to steer the needle towards a target placed at a depth of 140 mm in the presence of PAI. In the simulations, the maximum allowable number of rotations

is 3 and we used the FEM model of notched needle described in Section 6.2 to calculate the obstacle and the target region. We build the obstacle collision region ($\mathcal{C}_{obs}$) and the goal region through an exhaustive offline search. We estimate the needle trajectory using the FEM model at every node in the decomposed configuration space. In the simulations, the needle is inserted from grid point number 5 in the template (see Fig. 6.8). Based on the simulation results shown in Fig. 6.9(b) and Fig. 6.9(c), the obstacle region for both needles are almost the same. However, the target region for the notched needle is 215% larger than the standard needle target region, which indicates that the possibility of reaching to the target with the notched needle is more than the standard needle in the presence of PAI.

The number of possible control actions (i.e., sequence of rotation depths that steer the needle to the target) as a function of the insertion point (i.e., the grid number) for the two needles is shown in Fig. 6.9(d). The number of the possible control actions is significantly larger for the notched needle regardless of the insertion location. The best grid points for the notched needle and the standard needle are 8 and 7, respectively. We will use these grid points in the experiments.

Results of needle steering experiments for the notched needle designed in Section 6.3 and the standard 18G brachytherapy needle are shown in Fig. 6.10 and Fig. 6.11, respectively. In the experiments, the online motion planner is used to steer the needle. The planner uses the Kinematics-based model and the ROC for the needles are 583 and 131 mm, respectively (see Sections 6.2.2 and 6.3.2). Experimental results for the two scenarios and the two needles are summarized in Table 6.3. The mean targeting error for 10 insertions e_{mean}, maximum targeting error e_{max}, and mean of out of plane deflection for 10 trials e_{out} are reported. The maximum targeting error for the notched needle in the first and second scenario are 1.21 mm and 1.85 mm, respectively. Also, the maximum out of plane deflection for the notched needle is 1.35 mm and occurs in the needle steering with obstacle avoidance.

6.5 Concluding Remarks

The experimental validation results described in Sections 6.2.2, and 6.4.2 demonstrate that the notched needle is able to achieve higher deflection curvature in soft tissue than the

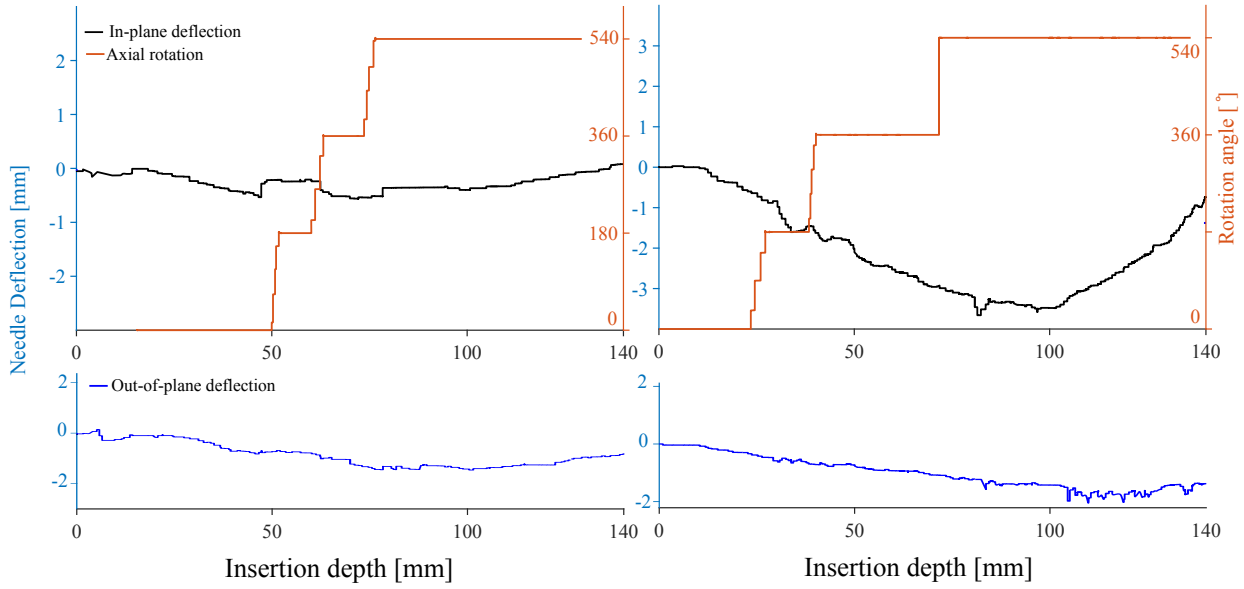

(a) Notched needle

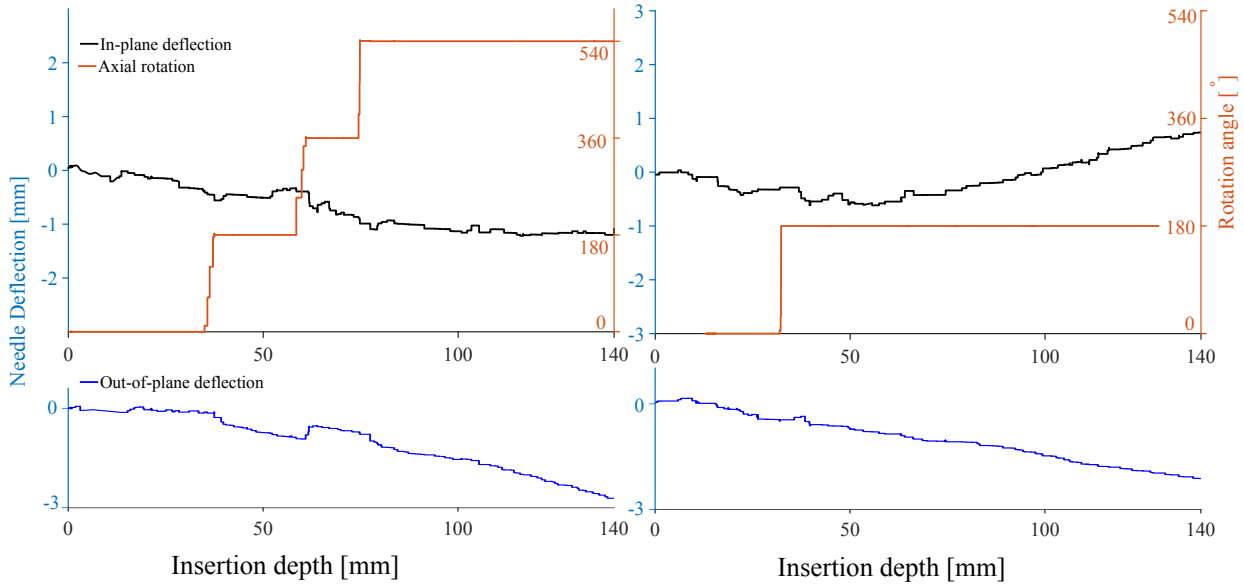

(b) Standard needle

Figure 6.10: Representative experimental needle steering results for needle insertion on a straight line (a) notched needle, (b) standard 18G brachytherapy needle. Corresponding controller input command (i.e, needle axial rotation), needle out-of-plane deflection, and insertion velocity are shown in the figures.

standard needle (75% smaller ROC). We compared the performance of the designed notch needle with a standard brachytherapy needle in two different case studies. The first case intends to steer the needle on a straight line. The second case steers the needle toward

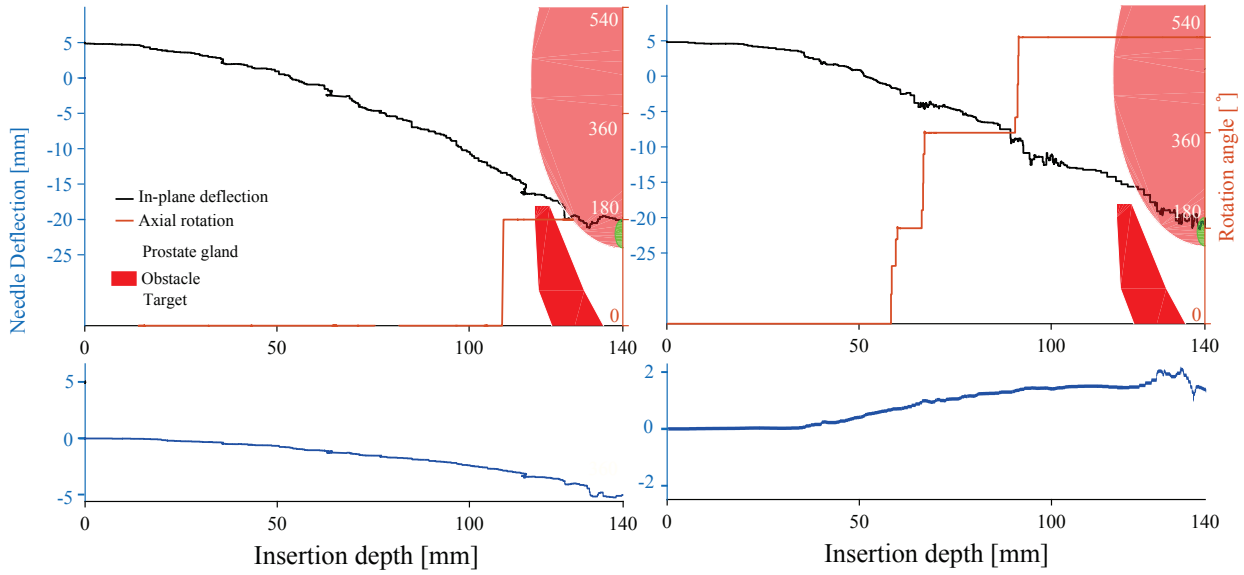

(a) Notched needle

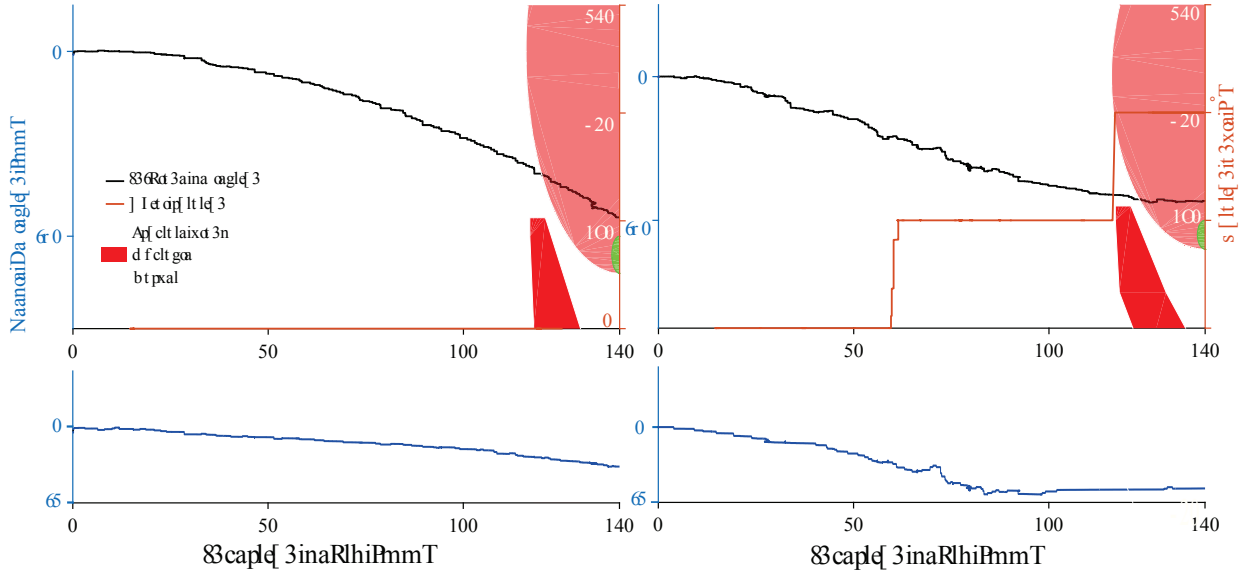

(b) Standard needle

Figure 6.11: Representative experimental needle steering results for needle insertion with obstacle avoidance for (a) notched needle, (b) standard 18G brachytherapy needle. Corresponding controller input command (i.e, needle axial rotation), needle out-of-plane deflection, and insertion velocity are shown in the figures.

a target partially obscured by an anatomical obstacle. Both needles showed the same performance for the first scenario. However, in the second scenario the motion planner mostly fails to steer the standard needle to the target in the presence of PAI (see Fig. 6.11). 40% of the insertions using the standard needle collides with the obstacle and the minimum

Table 6.3: Comparison of experimental data and model predictions.

	Notched needle		Standard needle	
	1st scenario	2nd scenario	1st scenario	2nd scenario
e_{max}	1.21	1.85	1.16	5.6
e_{mean}	0.90	1.26	0.85	4.1
e_{out}	0.62	1.35	1.05	1.67
σ	0.25	0.46	0.28	0.77

targeting error when the needle passes the obstacle is 3.80 mm, which is 3 times more than the notched needle. Changing the point of entry can increase the needle insertion accuracy. We performed several other insertions from different grid points. 5 insertion trials were performed for each grid point. Changing the point of entry for the standard needles from 7 to 5,6, and 8 increased the possibility of collision. Results demonstrate that 47% of the insertions made from the grid points No. 5, 6, and 8 lead to collision, unlike the insertions from grid point 7 where no collision was detected. Thus, grid point 7 is more suitable for standard needles.

In most needle-based interventions such as prostate brachytherapy, the target is typically defined on a straight line starting at the entry point in tissue and up to a certain depth. The grid template placed outside the tissue is used to position the needle in a fixed insertion plane that contains the target. However, due to many factors such as needle/tissue reaction forces and tissue in-homogeneity the needles bend out of the deflection plane and reduce needle insertion accuracy. The designed notched needles tend to bend in one plane and have less out-of-plane deflection compared to the standard needles. Conventional needles have constant isotropic flexural strength. However, the designed notched needles have less flexural strength in the needle deflection plane and more strength in the plane normal to the needle deflection plane. The notches on the needle shaft reduce the overall needle's flexural strength defined as the needle's modulus of elasticity times second moment of inertia (EI). The notches are carved in a plane that is perpendicular to the deflection plane (i.e., normal to the bevel, see Fig. 6.1). Thus, the second moment of

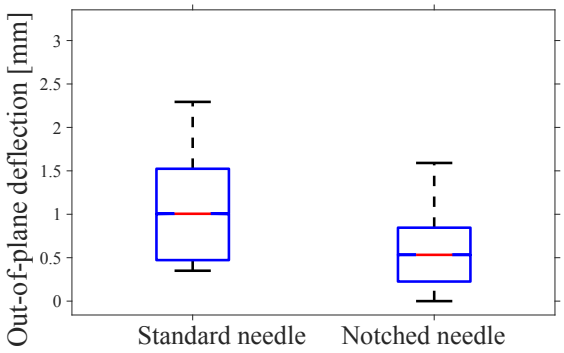

Figure 6.12: A comparison between out-of-plane deflection of the notched needle and the standard needle. Experimental data for 10 trials are reported. Red line indicates median error, blue box indicates 25th and 75th percentile, and whiskers indicate minimum and maximum error.

inertia in the deflection plane is smaller than the normal plane. For a notch with a depth of 5 mm, the needle flexural strength in the deflection plane in the proximity of the notch is 417% smaller than the flexural strength in the normal plane. Thus, the notched needle is more resistant to out-of-plane deflection and is disposed to bend in one plane. Fig. 6.12 shows the mean and the standard deviation of the out-of-plane deflection for the notched needle and the standard needle in needle insertion on a straight line for 10 trials. Based on the results, the notched needle shows less out-of-plane deflection compared to conventional needles.

In designing the notched needles, it is assumed that the notch width and depth are both 0.5 mm, which is smaller than the inner diameter of the needle. These design parameters are assumed constant to ensure the needle can provide a safe channel for delivering payloads with a diameter bigger than 0.5 mm, which is the case for radioactive seeds in prostate brachytherapy. However, there is a risk of leaking for delivering or preserving liquids. This can be avoided by coating the needles with super-elastic materials that does not increase needle rigidity but reduce the chance of leakage. Feasibility of silicone coating of surgical needles has been previously studied in the literature [108]. A soft coating also reduces the contact between the notches and the tissue, thus, eliminating the possibility of damaging the tissue. We intend to investigate the possibilities of coating the notched needles in future work.

In the next chapter, we will use the notched needles with a novel needle steering system

to robotically steer the needle in 3D space.

Chapter 7

3D Geometric Modeling and Robotic Needle Steering

7.1 Objectives

The 3D needle steering system is a highly nonlinear constrained system and most of the system states, namely, needle tip position and orientation, cannot be directly measured from 2D imaging systems. Thus, most of the previous needle steering strategies studied in the litrature can only steer the needle in 2D and neglect needle deflection out of the 2D plane [11,31,32,36]. In some of the previous works, researchers assumed that all the needle states can be directly measured using electromagnetic tracking systems [15,34], even though this limits the application of the needle steering controller in clinical practice. Several 3D needle steering algorithms are developed by incorporating image-based algorithms for calculating the needle pose in 2D ultrasound images and consequently estimating unicycle model parameters [14, 37]. However, no proof of convergence or stability were provided. Also, to the best of the author's knowledge, none of the previous studies propose a method for correcting final targeting error that can occur due to many factors such as uncertain tissue interactions or target motion.

In this section, we propose a nonholonomic model of needle steering that is fully controllable. We show that this type of system cannot be asymptotically stabilized using a

continuous state feedback. Then, we present two different type of controllers for 3D needle steering:

1. Nonlinear feedback-linearization-based controller: The proposed model is presented in a local coordinate system using the Serret-Frenet frame. By means of this transformation, the needle steering problem is converted to the regulation of the distance from a desired curved trajectory. Then, using the transformed model, a novel nonlinear controller is developed to steer the needle in 3D while avoiding anatomical obstacles. The performance of the proposed approach is verified through several simulated scenarios.

2. Geometric controller for 3D needle steering via retraction/insertion: A two-step controller is proposed for 3D needle steering. The proposed approach implements needle retraction/insertion motion to correct any undesired targeting errors. The proposed 3D needle steering system can be used in all clinical needle insertion scenarios to improve needle steering accuracy and extend the application of needle-based interventions to deeper or more difficult-to-reach targets. The needle steering system relies only on 2D ultrasound images to steer the needle. Inspired by clinical needle insertion, the designed controller inserts the needle up to the desired depth and as close as possible to the desired target location, and later performs a series of retraction and insertion motions that guides the needle toward the desired point. To the best of the author's knowledge, this is the first 3D needle steering system that incorporates the retraction/insertion of the needle – which is common in clinical needle insertions – to precisely steer the needle to a desired point. The proposed insertion/retraction based controller can also be combined with previous 3D [14, 15, 34] or 2D planar needle steering strategies [31, 37] to enhance their targeting accuracy. The stability of the control system is shown and several needle insertion experiments are performed to validate the needle steering system.

This Chapter is organized as follows: Section 7.2 describes the 3D kinematic model of needle steering. Section 7.3 details the feedback-linearization-based controller. This includes the conversion of the system into the chained form, the control law that allows

the path following, and the controller validation results. Section 7.4 details the geometric controller, including the details of a geometric reduction method used to transform the system to a *normal form*, design of the controller, simulation results, and experimental validation results. Concluding results appear in Section 7.5.

7.2 Nonholonomic Model of Needle Steering

Here, we present a nonholonomic model of needle steering based on the bicycle-like model of needle steering first presented in [7]. The bicycle model is a generalization of a nonholonomic mobile robot model and assumes that the needle is torsionally stiff and the insertions and twists applied to the needle base are directly transmitted to the tip. The motion of the needle is then determined only by the motion of the needle tip. The needle tip bends under the asymmetric distribution of forces applied to the beveled tip and follows a path with a constant radius of curvature in a plane defined by the orientation of the needle beveled tip.

To track a desired 3D trajectory using the bicycle model, one needs to control the needle tip position and the needle tip orientation (6 states of the system). However, tracking the needle tip with a 2D imaging systems typically enable us to measure only the position of the needle and not its orientation. Here, inspired by the work in [6, 7], we introduce a reduced-order nonholonomic model of needle steering that is later used to design a needle steering controller.

Fig. 7.1 shows a schematic of 3D needle steering in tissue. A global inertial coordinate frame xyz is fixed on the needle point of entry in the tissue and a local body-fixed frame $x'y'z'$ is attached to the needle tip. The two frames initially coincide. Let $v, \omega \in \mathbb{R}$ denote the needle insertion and rotation velocities expressed in the local frame. The beveled tip of the needle always lies in the local $x'y'$ plane. Thus, the needle tip follows a path in the $x'y'$ plane and the needle rotation around the y'-axis is assumed to be negligible. The configuration space of the needle tip is given by $\mathcal{Q} = \mathbb{R}^3 \times S^1 \times S^1$ and is parameterized by the general coordinates $q = [x, y, z, \phi, \theta]^T$, denoting the position of the needle tip in 3D, the orientation of the needle tip (roll angle), and the angle of the needle tip as it deflects (pitch angle).

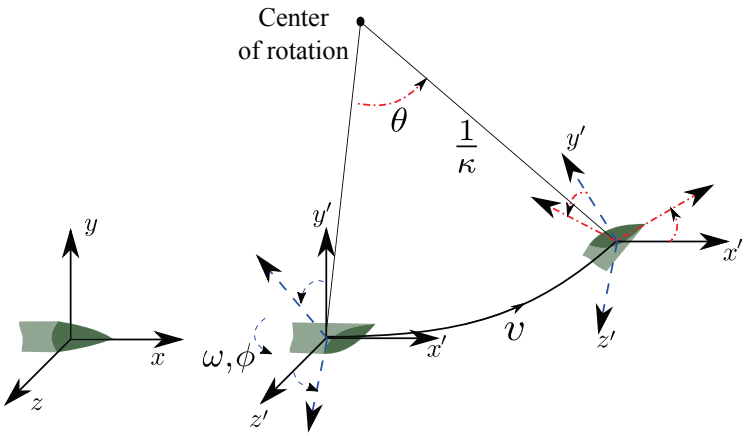

Figure 7.1: A schematic of needle steering in tissue. An inertial coordinate frame xyz is fixed at the needle point of entry and the needle tip position is $[x, y, z]^T \in \mathbb{R}^3$. a local body-fixed frame $x'y'z'$ attached to the needle tip initially coincides with the inertial frame. The needle is inserted and follows a constant curvature path in $x'y'$ plane while rotating around the z'-axis with an angle of θ. The needle can also rotate axially about x' by an angle ϕ. Needle rotation about the y'-axis is restricted by the surrounding tissue and is assumed to be negligible. The needle tip motion can be fully defined by a set of generalized coordinates $q = [x, y, z, \phi, \theta]^T$.

The needle tip follows a constant curvature path along the x' axis of the local frame at the velocity of v. It is also assumed that during the insertion, the needle tip rotation around z' axis is a linear function of the needle insertion velocity [7]:

$$\dot{\theta} = \kappa v \tag{7.1}$$

κ is the needle tip deflection curvature, which depends on the mechanical characteristics of the tissue and the needle. The needle tip follows a constant curvature path along x' axis at the velocity of v and the needle tip velocity is zero in y' and z' directions. Thus, we have

$$R^T \ [\dot{x} \ \ \dot{y} \ \ \dot{z}]^T = [\dot{x'} \ \ \dot{y'} \ \ \dot{z'}]^T = [v \ \ 0 \ \ 0]^T \tag{7.2}$$

R is the rotation matrix corresponding to two consecutive rotations around the local x' and z' axes and allows to rotate any vector from the local needle tip frame to the global coordinate frame. Using (7.1) and (7.2), we can construct the following set of Pfaffian constraints

$$A(q)\dot{q} = 0 \tag{7.3}$$

where

$$A = \begin{bmatrix} -\mathrm{C}\theta & \mathrm{S}\theta\mathrm{C}\phi & \mathrm{S}\theta\mathrm{S}\phi & 0 & -\frac{1}{\kappa} \\ -\mathrm{S}\theta & \mathrm{C}\theta\mathrm{C}\phi & \mathrm{C}\theta\mathrm{S}\phi & 0 & 0 \\ 0 & -\mathrm{S}\phi & \mathrm{C}\phi & 0 & 0 \end{bmatrix} \tag{7.4}$$

Throughout this chapter, shorthand notations S and C describe $\sin(\cdot)$ and $\cos(\cdot)$, respectively.

Equation (7.3) defines three nonholonomic constraints that decrease the system degree of freedom (DoF) from 5 to 2. However, they do not introduce any loss of accessibility in $\mathcal{Q}$. Considering the 5-dimensional configuration space, the admissible generalized velocities at each configuration $q \in \mathcal{Q}$ belongs to the 2-dimensional null space of matrix $A(q)$. Denoting by $\{g_1(q), g_2(q)\}$ a basis of the null space $\mathcal{N}(A(q))$, the admissible trajectories for the needle tip can be characterized as the solution of $g_1(q)u_1 + g_2(q)u_2$, where u_1 and $u_2 \in \mathbb{R}$ are the input vectors for the two remaining DoFs. The bases of $\mathcal{N}(A(q))$ can be easily calculated from (7.4) as

$$\begin{aligned} g_1(q) =& [\mathrm{C}\theta \quad \mathrm{S}\theta\mathrm{C}\phi \quad \mathrm{S}\theta\mathrm{S}\phi \quad 0 \quad \kappa]^T \\ g_2(q) =& [0 \quad 0 \quad 0 \quad 1 \quad 0]^T \end{aligned} \tag{7.5}$$

The bases are not unique. However, with the above selected bases, the input vectors have a clear physical interpretation and are equal to the insertion velocity v and the axial rotation velocity ω. Now using (7.5), we can build the nonholonomic model of needle steering as

$$\begin{bmatrix} \dot{x} \\ \dot{y} \\ \dot{z} \\ \dot{\phi} \\ \dot{\theta} \end{bmatrix} = \begin{bmatrix} \mathrm{C}\theta \\ \mathrm{S}\theta\mathrm{C}\phi \\ \mathrm{S}\theta\mathrm{S}\phi \\ 0 \\ \kappa \end{bmatrix} v + \begin{bmatrix} 0 \\ 0 \\ 0 \\ 1 \\ 0 \end{bmatrix} \omega \tag{7.6}$$

Let q^e denote an equilibrium solution of the system in (7.6) corresponding to $v = \omega = 0$. The following observations can be made about the nonholonomic system:

1. Using successive Lie brackets, it can be shown that the rank of the system's accessibility distribution is 5. Thus, the system is strongly accessible at q^e. Also, the system has

a nonholonomy degree of 3 and the constraint distribution given in (7.3) is completely nonholonomic.

2. The system in (7.6) is driftless and affine in the inputs. Considering the accessibility rank, the system is controllable at q^e.

3. Based on the Brockett's theory (see [109]), a necessary condition for the existence of c^1 asymptotically stabilizing feedback law for (7.6) is that the image of the mapping $(q, v, w) \rightarrow (v\mathrm{C}\theta, v\mathrm{S}\theta\mathrm{C}\phi, v\mathrm{S}\theta\mathrm{S}\phi, \omega, \kappa v)$ contain some neighborhood of q^e. The system fails to satisfy this condition. For instance, in a neighborhood of zero, where $\kappa v = 0$, i.e., $v = 0$, no points of the form $[\epsilon\ 0\ 0\ 0\ 0]^T$, $\epsilon \neq 0$ are in its image. Thus, the nonholonomic system is not asymptotically staibilizable using a smooth feedback law.

Based on the above discussion, a single equilibrium of (7.6) cannot be asymptotically stabilized using linear feedback, feedback linearization, or any other control approach that uses smooth feedback. One can stabilize such a system to an equilibrium sub-manifold of the system via smooth feedback [110, 111] or use switching control to stabilize the system on an equilibrium point [112]. Another option is to transform the model into a form that is continuously stablizable [113].

In the next sections, we use the model to design two different needle steering controllers. In the first approach, we transform the reduce-order model of needle steering, using a Frenet-Serret frame placed on an arbitrary desired 3D trajectory. By means of the transformation to the Frenet-Serret frame, the needle steering problem is converted to the regulation of the distance of the needle tip from a desired curved trajectory without the need for observing or direct control of the needle tip orientation. Later a nonlinear controller is developed for stabilizing the transformed system. In the second approach, first we transform the system's model to a *normal form* that is easy to analyze. Next, inspired by the work in [110] and [112], we will design a two-step controller for 3D needle steering that entails: 1) Smooth stabilization of the needle on an equilibrium manifold with desired predefined features and 2) stabilizing the needle on an equilibrium point in the manifold via a non-smooth feedback law that involves the retraction/insertion of the needle.

7.3 Feedback-Linearization-based 3D Needle Steering

7.3.1 Transformation to Frenet-Serret Frame

Here, we transform the reduce-order model of needle steering, using a Frenet-Serret frame placed on an arbitrary desired 3D trajectory. By means of the transformation to the Frenet-Serret frame, the needle steering problem is converted to the regulation of the distance of the needle tip from a desired curved trajectory without the need for observing or direct control of the needle tip orientation. In differential geometry, the Frenet-Serret frame is commonly used to describe the kinematic properties of a particle moving along a continuous, differentiable curve in 3D. Following this approach, the needle tip motion is expressed in terms of the desired path parameters (curvilinear abscissa s, path curvature c, and path torsion τ).

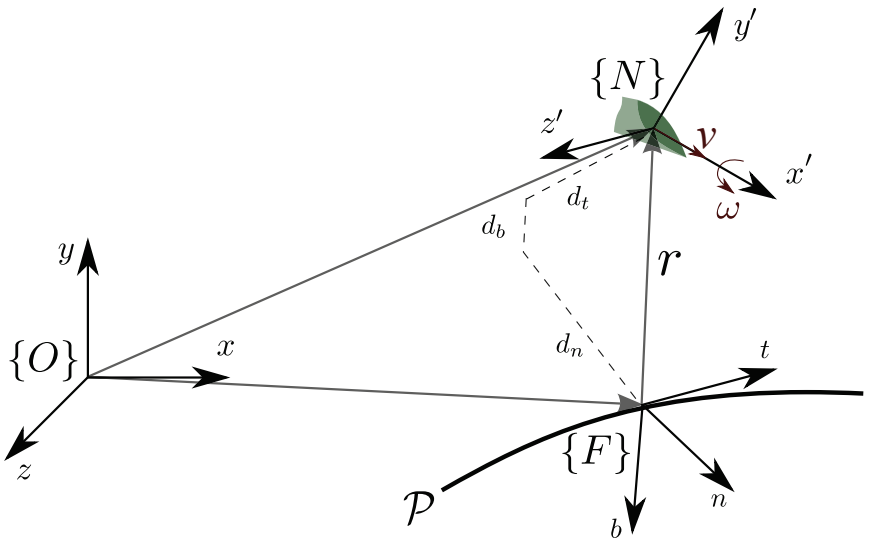

Figure 7.2: Illustration of the needle path following problem.

The needle tip and the path ($\mathcal{P}$) to be followed are presented in Fig. 7.2, where $\{F\}$ is the orthogonal projection of the needle tip frame $\{N\}$ on the path. The tangent, normal, and bi-normal unit vectors of the Frenet-Serret frame associated with $\{F\}$ are t, n, and b. Let d_n and d_b denote the signed distances between frame $\{N\}$ and the origin of frame $\{F\}$. Let s be the path's abscissa, c the path's curvature, and τ its torsion. c and τ are assumed to be continuous bounded functions of s with bounded derivatives. Based on Frenet-Serret

formulas, the angular velocity of F is given by ${}^{F}W_F = [\tau\dot{s} \;\; 0 \;\; c\dot{s}]^T$. The goal of the path following problem is to set the needle tip distance from the path (d_n and d_b) to zero, while aligning the linear velocity of the needle tip v with the tangent of the reference path t via manipulation of needle tip angular velocity ω.

Let ${}^{F}R_N(\phi_e, \psi_e, \theta_e)$ be the rotation matrix from the Frenet-Serret frame to the needle frame, which aligns the velocity vector and tangent vector to the path t. ${}^{F}R_W$ is locally parameterized by Z-Y-X Eulerian angles. Writing the linear velocity of the needle frame in the Frenet-Serret frame yields

$$ {}^{F}R_N(\phi_e, \psi_e, \theta_e){}^{N}V_N = {}^{F}V_F + \frac{d^{F}\overrightarrow{FN}}{dt} + {}^{F}W_F \times {}^{F}\overrightarrow{FN} \tag{7.7} $$

where ${}^{N}V_N = [v \;\; 0 \;\; 0]^T$ is the vector velocity of needle tip in needle frame $\{N\}$, ${}^{F}V_F = [\dot{s} \;\; 0 \;\; 0]^T$ is the $\{F\}$ frame linear velocity and, ${}^{F}\overrightarrow{FN} = [0 \;\; d_n \;\; d_b]^T$ is the vector of needle tip position in frame $\{F\}$.

We can also compute the needle frame angular velocity relative to the Frenet-Serret frame as

$$ {}^{N}W_{N,F} = {}^{N}W_N - {}^{N}R_F(\phi_e, \psi_e, \theta_e){}^{F}W_F \tag{7.8} $$

where ${}^{N}W_N = [0 \;\; 0 \;\; \kappa v]^T + R^T(\theta)[\omega \;\; 0 \;\; 0]^T$, and ${}^{N}W_{N,F}$ is given by

$$ {}^{N}W_{N,F} = \begin{bmatrix} \dot{\phi}_e \\ 0 \\ 0 \end{bmatrix} + R^T(\phi_e) \begin{bmatrix} 0 \\ \dot{\psi}_e \\ 0 \end{bmatrix} + \left(R(\psi_e)R(\phi_e)\right)^T \begin{bmatrix} 0 \\ 0 \\ \dot{\theta}_e \end{bmatrix} \tag{7.9} $$

Solving (7.7) for $\dot{s}$, $\dot{d}_n$ and $\dot{d}_b$ and (7.8) for $\dot{\phi}_e$, $\dot{\psi}_e$ and $\dot{\theta}_e$ gives the transformed system:

$$ \dot{s} = \frac{v\mathrm{C}\theta_e\mathrm{C}\psi_e}{1 - d_n c} \tag{7.10a} $$

$$ \dot{d}_n = d_b\tau\dot{s} + v\mathrm{C}\psi_e\mathrm{S}\theta_e \tag{7.10b} $$

$$ \dot{d}_b = -d_n\tau\dot{s} - v\mathrm{S}\psi_e \tag{7.10c} $$

$$ \dot{\phi}_e = \omega\mathrm{C}\theta - \tau\dot{s}\mathrm{C}\theta_e\mathrm{SC}\psi_e + \kappa v\mathrm{C}\phi_e\mathrm{T}\psi_e + \omega\mathrm{S}\theta\mathrm{S}\phi_e\mathrm{T}\psi_e \tag{7.10d} $$

$$ \dot{\psi}_e = \omega\mathrm{S}\theta\mathrm{C}\phi_e + \tau\dot{s}\mathrm{S}\theta_e \tag{7.10e} $$

$$ \dot{\theta}_e = \kappa v\mathrm{C}\phi_e\mathrm{SC}\psi_e + \omega\mathrm{S}\theta\mathrm{S}\phi_e\mathrm{SC}\psi_e - \dot{s}\tau\mathrm{C}\theta_e\mathrm{T}\psi_e - c\dot{s} \tag{7.10f} $$

We note that in (7.10) $|d_n| < 1/c(s)$, which means that the transformation exists if the distance between the needle tip and the desired path $\mathcal{P}$ is not too large (smaller than the lower bound of the curve radii). Also, to avoid singularities in (7.10), $\psi_e, \theta_e \in (-\pi/2, \pi/2)$. Finally, we remark that the 3D Serret-Frenet frame transformation presented here is singular if the trajectory is a straight-line, since the normal direction of the straight-line could be either right or left direction. One way to avoid the singularity is using a path with a very small curvature rather than a completely straight line. Another way for avoiding the transformation singularity is using the parallel transport frame suggested in [114]. In the next section, we will use the model in (7.10) to design a controller to stabilize the needle distance from the path, i.e, d_n and d_b, at zero. Note that by means of the transformation to the Frenet-Serret frame, the needle steering problem is converted to the stabilization of the coordinates d_n and d_b.

7.3.2 Regulation via Feedback Linearization

The objective of the needle steering controller is to synthesize a control law that allows the needle tip to follow a desired path in a stable manner, independent of the sign of the insertion velocity. We select the needle rotation velocity ω as the control input. Considering the needle insertion velocity v and its derivative are bounded, the needle steering problem consists of finding smooth feedback control laws $\omega(v, s, d_n, d_l, \phi_e, \psi_e, \theta_e)$ such that $\lim_{t\to\infty} d_n(t) = \lim_{t\to\infty} d_b(t) = 0$.

To design the controller, first the kinematic equations in (7.10) are transformed into the chain form via a change of state and control variables. The conversion of multi-input nonholonomic systems into the chained form was first presented by Bushnell *et al.* [113]. Let us determine a change of coordinates $(s, d_n, d_b, \phi_e, \theta_e, v, \omega) \to (z_1, z_2, z_3, u_1, u_2)$ allowing to transform (7.10) into the 3-dimensional chained system

$$\begin{aligned} \dot{z}_1 &= u_1 \\ \dot{z}_2 &= u_1 z_3 \\ \dot{z}_3 &= u_2 \end{aligned} \tag{7.11}$$

First, we set $z_1 = s$. Thus u_1 is given by (7.10a). Then, the second state variable is chosen as $z_2 = 0.5(d_n^2 + d_b^2)$. Using (7.10b) and (7.10c) and eliminating $\dot{s}$ by (7.10b) we have

$$\dot{z}_2 = u_1 z_3 = u_1(1 - d_n c)(d_n \mathrm{T}\theta_e - d_b \mathrm{T}\psi_e \mathrm{SC}\theta_e) \tag{7.12}$$

Taking derivative of $\dot{z}_3$ in (7.12) with respect to time and replacing $\dot{s}, \dot{d}_n, \dot{d}_b, \dot{\phi}_e, \dot{\psi}_e$ and $\dot{\theta}_e$ by their values in (7.10), the input u_2 is obtained as

$$u_2 = a_{11}\omega + a_{12} \tag{7.13}$$

where a_{11}, a_{12}, are given by

$$a_{11} = -(1 - d_n c)\Big[\mathrm{SC}\theta_e \mathrm{S}\theta \mathrm{SC}\psi_e \big(\mathrm{S}\phi_e(-d_n \mathrm{SC}\theta_e + d_b \mathrm{T}\theta_e \mathrm{T}\psi_e) + d_b \mathrm{SC}\psi_e \mathrm{C}\phi_e)\big)\Big] \tag{7.14a}$$

$$\begin{aligned} a_{12} = & \frac{v\mathrm{C}\psi_e}{1 - d_n c}\Big\{ (d_n \mathrm{S}\theta_e \mathrm{C}\psi_e - d_b \mathrm{S}\psi_e)\,(d_n c' + c d_b \tau) + \\ & (cd_n - 1)\mathrm{C}\psi_e \Big(\mathrm{SC}\theta_e \left(-(cd_n - 1)\mathrm{SC}^2\psi_e (d_b \kappa \mathrm{SC}\psi_e \mathrm{S}\phi_e + d_n \kappa \mathrm{SC}\theta_e \mathrm{C}\phi_e) + 1\right) - 1\big) + \\ & \mathrm{T}\theta_e \left(d_b \mathrm{T}\psi_e \left(\kappa(cd_n - 1)\mathrm{SC}\theta_e \mathrm{SC}^2\psi_e \mathrm{C}\phi_e + 2c\right) + (1 - 2cd_n)\mathrm{S}\theta_e\right)\Big)\Big\} \end{aligned} \tag{7.14b}$$

We note that for $|d_n| < 1/c(s)$ and any $\theta_e, \psi_e \in (-\pi/2, \pi/2)$, $(s, d_n, d_l, \phi_e, \psi_e, \theta_e) \to (z_1, z_2, z_3,)$ defines a mapping between $\mathbb{R}^4 \times (-\pi/2, \pi/2)^2$ and $\mathbb{R}^3$. Also, the control variable involves the derivative of path curvature (c'), whose value is thus needed.

The objective of the controller is to asymptotically bring $z_2 = 0.5(d_n^2 + d_b^2)$ to zero and also ensures that the constraint on the distance to the path (i.e., $|d_n| < 1/c(s)$ is satisfied along the trajectories of the controlled system. We consider the following control law:

$$u_2 = -u_1 k_1 z_2 - |u_1| k_2 z_3, \quad (k_2, k_3 > 0) \tag{7.15}$$

It is then immediate to verify that the origin of the closed-loop subsystem is asymptotically stable when $u_1 = \dot{s}$, i.e., the velocity along the path is constant.

So far, we have assumed that the insertion velocity v is either imposed or prespecified. Thus, we can use v in (7.10a) to ensure $\dot{s}$ is constant. Now, the steering angular velocity w can be computed from (7.15) as

$$\omega = a_{11}^{-1}(u_1 - a_{12}) \tag{7.16}$$

Based on (7.14a) and following our assumptions that $|d_n| < 1/c(s)$ and $\theta_e, \psi_e \in (-\pi/2, \pi/2)$, ω in (7.16) is well defined when $\theta \in (0, \pi/2)$. Based on (7.6) and considering the small curvature κ of needle in tissue, this assumption is satisfied when $\theta(0) > 0$. Thus, it suffices to select a nonzero initial condition for the needle initial pose θ. Also, ω asymptotically increases when $d_n(t) = d_b(t) = 0$. This motion, typically known as duty-cycling, mimics a drilling behavior and stabilizes the needle when the tracking error is zero. Duty-cycling can increase tissue trauma in real practice. We can limit the needle rotation velocity in the proximity of the desired path to avoid the drilling motion of the needle.

7.3.3 Simulation Results

In this section, several simulations are performed to validate the proposed needle steering strategy. We will use the feedback of needle global position (x, y, and z) to control the needle tip to follow a desired trajectory. During the needle insertion, these values can be calculated online using an imaging system. By knowing the position of the needle and the desired path parameters (s, τ and c), the steering angular velocity can be computed from (7.16).

Three clinical scenarios are simulated:

1. The needle is steered on a straight line to reach a target placed at a depth of 140 mm. This is the most common goal in needle-based interventions, where the needle should be inserted along a straight line and the needle is only rotated to compensate for deviations from the straight path.

2. A 10 mm circular obstacle is positioned at a depth of 70 mm between the needle entry point into the tissue and the target. The needle is steered to reach a target at the depth of 140 mm while avoiding the obstacle.

3. The needle is steered on a 3D arbitrary curve with a constant radius of curvature.

We note that 3D Serret-Frenet frame transform presented in Section 7.4.1 is singular if the trajectory is a straight-line. In order to avoid this singularity, we assumed that

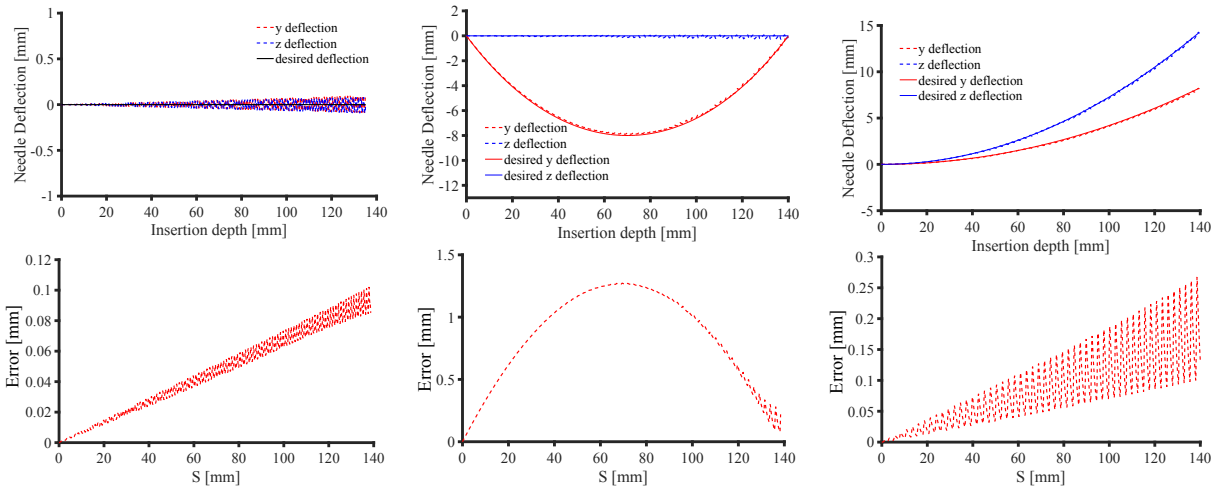

(a) (b) (c)

Figure 7.3: Simulated results of needle steering for (a) needle insertion on a straight line, (b) 2D needle insertion with obstacle avoidance, (3) tracking a 3D path with a constant curvature. desired and actual needle deflection along y and z, and mean absolute error of tracking are shown in the figures.

Table 7.1: Simulation results. Units are in mm.

	1st scenario	2nd scenario	3rd scenario
e_y	0.1	0.18	0.11
e_z	0.076	0.108	0.095
$RMSE$	0.081	0.12	0.091

the desired path in the first scenario has a very small curvature (0.0001 mm). In the 2nd scenario, the desired needle deflection in the z direction is zero and is a circular path with a radius of 130 mm in the y direction. The needle desired trajectory in the 3rd scenario is a 3D curve with constant radius of curvature of 600 mm. In the simulations, the needle curvature (κ) is set equal to 0.002 mm, which is selected based on the experimentally obtained mean radius of curvature in Section 6.2.2. We introduce 10% error in the measured value of κ to simulate uncertainty. Also, the maximum allowable rotation velocity is 10 radiant per second . The results are shown in Fig. 7.3.

Simulation results are summarized in Table 7.1. The maximum error in the y direction, e_y, the maximum error in the z direction, e_z, and the root mean squared error (RMSE) of

tracking are reported. The maximum tracking error is in the y direction in the 2nd scenario and it is equal to 0.18 mm. This error is below the accepted margin of error in clinical needle insertions ($\sim$ 5 mm). The results show that the controller is accurate, stable, and has a satisfactory performance.

7.3.4 Discussion

In this section, we presented the kinematic model of needle steering in a chained format using a transformation to the Frenet-Serret frame. Then, a feedback control law was proposed to stabilize the chained system. The proposed method was validated and analyzed through several simulations. The results show that the controller is accurate and stable. However, the controller has several drawbacks that limits its application in clinical practice.

The control law is not robust to parametric uncertainty including saturation in the actuation signal and constant perturbations such as soft tissue reaction forces. Also as the tracking error goes to zero, needle axial rotation velocity increases toward infinity. This behavior is typically known as duty-cycling, which mimics a drilling behavior and stabilizes the needle when the tracking error is zero. Duty-cycling can increase tissue trauma in real practice and is not desirable. In the next section, we propose another controller that is more robust against parameter uncertainty and uses minimal control actions in order to steer the needle toward a designated target.

7.4 Geometric 3D Needle Steering

7.4.1 Transformation to Normal Form

Here, we use a geometric tool known as *connections* and transform the system's model to a reduced form known as the *normal form* [115]. The theory of connections, which is now part of the general subject of geometric mechanics, has been helpful in the study of the behavior of systems with nonholonomic constraints [110]. The presented transformation has been studied in[116] and is formed by viewing the configuration manifold as the total

space of a fiber bundle. In the following, a simple introduction of connections with an emphasis on the aspects that apply to control theory is presented; more details can be found in [115–117].

In general, connections are associated with mappings, called bundle mappings, that project larger spaces onto smaller ones, as in Fig. 7.4. The larger space is the bundle $\mathcal{Q}$, and the smaller space is called the base B. In a trivial case (such as ours), the space $\mathcal{Q}$ is just $B \times F$, where F is the fiber. The similarity between $\mathcal{Q}$ and a product space $B \times F$ is defined using a continuous surjective projection $\Pi : \mathcal{Q} \to B$. Directions in the larger space that project to zero are called vertical directions. The connection is a specification of a set of directions, called horizontal directions, at each point, which complements the space of vertical directions [116].

One can view the motion generation in the system in (7.6) as a question of relating internal changes in a base space to net changes in the bundle. The base space is the control space in the sense that the path in the base space can be chosen by suitable control inputs. Assuming the systems configuration space $\mathcal{Q}$ is the total space of fiber bundle and the base space B, parameterized by the local coordinates b, we can divide the general coordinates to $q = (b, p) \in \mathbb{R}^2 \times \mathbb{R}^3$, where $b = [\phi \quad \theta]^T$ is the base space coordinate and $p = [x \quad y \quad z]^T$ is the fiber coordinate.

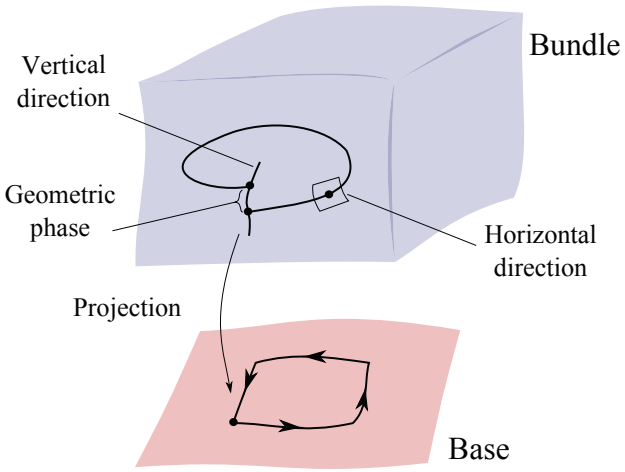

Figure 7.4: A graphical representation of the bundle and connections. A connection divides the space into vertical and horizontal directions.

Motivated by the above discussion, we use (7.6) to write the mapping from the base

coordinates b to the general coordinates q

$$\dot{q} = C^T \dot{b} \ , \tag{7.17}$$

where $C = [I \quad -J]$, I is a 2×2 identity matrix, and

$$J = \begin{bmatrix} 0 & 0 & 0 \\ -\dfrac{\mathrm{C}\theta}{\kappa} & -\dfrac{\mathrm{S}\theta\mathrm{C}\phi}{\kappa} & -\dfrac{\mathrm{S}\theta\mathrm{S}\phi}{\kappa} \end{bmatrix}. \tag{7.18}$$

Based on (7.17), the system configuration space solely depends on the evolution of base coordinates. The base space describes the internal shape of the system and cyclic paths in this space correspond to the movements that lead to transnational motion of the needle. In lieu of (7.6), we rewrite the nonholonomic model in a normal form given below using (7.17)

$$\dot{b} = u \tag{7.19a}$$

$$\dot{p} = -J^T u \tag{7.19b}$$

$$\dot{u} = U \tag{7.19c}$$

where $U = [\kappa\dot{v} \quad \dot{\omega}]$.

For a horizontal motion in the bundle corresponding to a cyclic motion in the base, the vertical motion will undergo a shift in the vertical space V, called the *geometric phase* (see Fig. 7.4). The connection $\mathbf{w} : T\mathcal{Q} \to V$ is a vector valued projection from the tangent bundle of $\mathcal{Q}$ onto its vertical part and is given by

$$\mathbf{w} = (dp + J^T db)\frac{\partial}{\partial p} \tag{7.20}$$

In terms of coordinates, $\mathbf{w}$ maps $(\dot{b}, \dot{p})$ onto $(0, \dot{p} + J^T\dot{b})$. Now, suppose we have a loop in the base with p starting at p_0, the geometric phase can be obtained by

$$p_f - p_o = -\oint J^T db \tag{7.21}$$

where p_f is the final position in the fiber. (7.21) can be also deduced from (7.19a) and (7.19b). Based on (7.21), the geometric phase shown in Fig. 7.4 depends on the area

enclosed by the path in the base space and J. Let $\gamma(\phi^*, \theta^*)$ denote the desired closed path in base space, using (7.18) and (7.21) we have

$$x_f = x_0 + \oint_\gamma \frac{\mathrm{C}\theta}{\kappa} d\theta \tag{7.22a}$$

$$y_f = y_0 + \oint_\gamma \frac{\mathrm{C}\phi\mathrm{S}\theta}{\kappa} d\theta \tag{7.22b}$$

$$z_f = z_0 + \oint_\gamma \frac{\mathrm{S}\phi\mathrm{S}\theta}{\kappa} d\theta \tag{7.22c}$$

If the closed loop is a path on a square starting at (ϕ_0, θ_0) and sequentially moving to (ϕ^*, θ_0), (ϕ^*, θ^*), $(0, \theta^*)$, $(0, \theta_0)$, and finally back to (ϕ_0, θ_0), using (7.22) we can obtain the geometric phase

$$x_f = 0 \tag{7.23a}$$

$$y_f = y_0 - \frac{1}{\kappa}\mathrm{C}\phi^*(\mathrm{C}(\theta^*) - \mathrm{C}\theta_0) + \frac{1}{\kappa}(\mathrm{C}(\theta^*) - \mathrm{C}\theta_0) \tag{7.23b}$$

$$z_f = z_0 - \frac{1}{\kappa}\mathrm{S}\phi^*(\mathrm{C}(\theta^*) - \mathrm{C}\theta_0) \tag{7.23c}$$

We note that based on (7.23), the closed path in the base space will not move the needle in x direction but shifts the needle in y and z directions. As we will show later, the selected closed path simulates a retraction/insertion motion and is expected to keep the insertion depth (i.e., x) fixed. In the remainder of Section 7.4, the geometric phase given by (7.22) and the normal form of the system in (7.19) will be used to design a retraction/insertion based needle steering controller. The goal of the controller is to first stabilize the system on an equilibrium sub-manifold of the system and later stabilize it on an equilibrium point $p_e = (x_e, y_e, z_e)$ in the manifold. The former corresponds to insertion of the needle up to a desired depth x_e and the latter is a retraction/insertion motion that guides the needle toward a desired equilibrium point in a plane fixed at x_e, i.e, p_e.

7.4.2 Controller Design

Let $q_0 = [x_0, y_0, z_0, \phi_0, \theta_0]^T$ denote an initial state. The design of a control strategy that transfers the initial state to an equilibrium point $q_e = [x_e, y_e, z_e, \phi_e, \theta_e]^T$ involves the following two-steps:

1. Stabilize the system on an equilibrium manifold. The equilibrium manifold is selected based on certain clinical metrics with the intention of steering the needle to the desired depth, x_e, while bringing the needle as close as possible to the desired equilibrium point (x_e, y_e, z_e). The coordinate of the system on the equilibrium manifold is $q_1 = [x_e, y_1, z_1, \phi_e, \theta_e]^T$. We are interested in bringing the needle tip to a desired point, not controlling the needle orientation. Thus, we have freedom in selecting the final base coordinates (ϕ_e, θ_e).

2. Traverse a closed path in the base space to produce a retraction/insertion motion that brings q_1 to q_e.

7.4.2.1 Step 1: Stabilization on a Manifold

In this section, we study the problem of smooth stabilization of the needle to an equilibrium sub-manifold of $\mathcal{Q}$. The equilibrium sub-manifold is given by

$$\mathcal{Q}_e = \{(q, \dot{q}) \mid \dot{q} = 0, f(q) = 0\} \ , \tag{7.24}$$

where $f(q)$ is a smooth vector function. We implement the results of [111] to design a feedback control law such that the closed loop has a locally asymptotically stable point on $\mathcal{Q}_e$.

Proposition 1. The control law

$$U = -\left(\frac{\partial f}{\partial q}C^T\right)^{-1}\left[\frac{\partial}{\partial q}\left(\frac{\partial f}{\partial q}C^T\dot{b}\right)C^T\dot{b} + K_1\frac{\partial f}{\partial q}C^T\dot{b} + K_2 f\right] \tag{7.25}$$

with K_1 and K_2 denoting constant symmetric positive definite 2×2 matrices renders $(q, \dot{q}) \to \mathcal{Q}_e$ if the transversality condition

$$\det\left(\frac{\partial f}{\partial b}\right)\det\left(\frac{\partial f}{\partial q}C^T\right) \neq 0 \tag{7.26}$$

is satisfied.

Proof. Considering the system in the normal form (7.19), the mapping $(b, p, \dot{b}) \to (f, p, \dot{f})$ is a diffeomorphism if

$$\det\left(\frac{\partial f}{\partial b}\right)\det\left(\frac{\partial \dot{f}}{\partial \dot{b}}\right) = \det\left(\frac{\partial f}{\partial b}\right)\det\left(\frac{\partial f}{\partial q}C^T\right) \neq 0. \tag{7.27}$$

The first and second time derivative of $f(q)$ are

$$\dot{f} = \frac{\partial f}{\partial q} C^T \dot{b} \tag{7.28a}$$

$$\ddot{f} = \frac{\partial}{\partial q}\left(\frac{\partial f}{\partial q} C^T \dot{b}\right) C^T \dot{b} + \frac{\partial f}{\partial q} C^T U \tag{7.28b}$$

We used (7.17) in derivation of (7.28) and (7.27). Now, considering the control law in (7.25), the closed-loop system

$$\ddot{f} + K_1 \dot{f} + K_2 f = 0 \tag{7.29}$$

has an asymptotically stable point at the origin, i.e, $(f, \dot{f}) \to 0$ as $t \to \infty$. Considering (7.28a) and the system in normal form in (7.19), the system remains bounded for all time, i.e, $\dot{q} \to 0$. Therefore $(q, \dot{q}) \to \mathcal{Q}_e$ as $t \to \infty$. □

To satisfy (7.26), $f(q)$ in (7.24) should be a smooth 2-dimensional vector function and include the base coordinates θ and ϕ. To define $f(q)$, we remark that in practice needles are inserted at relatively high velocities to eliminate the effect of uncertainties in targeting error [62], and later retraction/insertions can be made to compensate for targeting errors (if there is any). Denoting the desired final equilibrium point as $q_e = [x_e, y_e, z_e, \phi_e, \theta_e]^T$ and inspired by clinical needle insertion approach we define $f(q)$ as

$$f_1 = \theta + \phi + (y - y_e)^2 + (z - z_e)^2 - k_{0,1} \tag{7.30a}$$

$$f_2 = \theta + (x - x_e)^2 - k_{0,2} \tag{7.30b}$$

The first element of $f(q)$ is defined in order to minimize the targeting error in y and z directions by modulating θ and ϕ corresponding to insertion velocity and axial rotation, velocity, respectively. $k_{0,1}$ is a constant parameter that can be tuned to increase needle insertion and axial rotation velocities while minimizing the targeting error. When the system is stabilized on the equilibrium manifold, i.e.,2-dimentional $f_1 = f_2 = 0$, the final targeting error is equal to $k_{0,1} - \theta_e - \phi_e$. The second element aims to smoothly steer the needle to the desired insertion depth x_e. As $f_2 \to 0$, needle insertion depth error $\| x - x_e \|$ goes to $\pm\sqrt{k_{0,2} - \theta_e}$. From (7.22a) we can obtain $\theta_e = \text{asin}(x_e \kappa)$ at the desired insertion depth x_e. Selecting $k_{0,2} = \theta_e$, guarantees the needle insertion depth error goes to zero. It

can be easily checked that the above selected $f(q)$ satisfies the transversality condition in (7.26).

Now, considering $q_1 = [x_e, y_1, z_1, \phi_e, \theta_e]^T$ as the coordinates of the system on the manifold, in the next section we design a non-smooth controller that steers the needle from q_1 to q_e.

7.4.2.2 Step 2: Stabilization to a Point

In the previous subsection, a smooth feedback was used to asymptotically stabilize a certain smooth 2-dimensional manifold $\mathcal{Q}_e$ in $\mathcal{Q}$. The coordinate of the system on the equilibrium manifold is $q_1 = [x_e, y_1, z_1, \phi_e, \theta_e]^T$. Here, we design a switching control that brings the state of the system from q_1 to $q_e = [x_e, y_e, z_e, \phi_e, \theta_e]^T$. The control design is based on the a priori selection of a closed path in the base space.

Here, we use the concept of geometric shift introduced in Section 7.4.1 to select a desired path in base coordinate $\gamma(\phi^*, \theta^*)$ that brings the needle to a desired point. The main goal is to steer the needle in the base space (ϕ, θ) on a closed path to produce a desired geometric phase $(0, y_d, z_d)$, where $y_d = y_e - y_1$ and $z_d = z_e - z_1$.

Considering that the closed path, γ, is formed by the line segments from $b_e = (\phi_e, \theta_e)$ to $b_1 = (\phi^*, \theta_e)$, from b_1 to $b_2 = (\phi^*, \theta^*)$, from b_2 to $b_3 = (0, \theta^*)$, from b_3 to $b_4 = (0, \theta_e)$, and from b_4 back to $b_5 = b_e$. Then, the geometric phase of the parameterized family is determined by (7.23). Solving (7.23) for (ϕ^*, θ^*), one can calculate the desired path in the base. Solution of (7.23) and the corresponding selected closed path is given in the first row of Table. 7.2. Note that when $y_d = y_e - y_1 < 0$ or for $|\frac{y_d^2 + z_d^2}{y_d}| > \frac{4}{\kappa} \mathrm{S}^2 \frac{\theta_e}{2}$, θ^* is not analytic and the above described path is not applicable. Different paths can be selected for other initial conditions. The proposed paths and the corresponding base coordinates calculated by solving (7.22) in the closed form are given in Table. 7.2. We remark that these paths are not unique and the desired phase geometry can be achieved via different paths or even concatenation of a series of closed paths.

Now, considering the bundle projection map, $\Pi : (b, p, u) \to (b, u)$, we define a family

of feedback functions U_i^* such that for any $\Pi q(t_0)$ the solution of

$$\dot{b} = u \tag{7.31a}$$

$$\dot{u} = U_i^*(\Pi q) \tag{7.31b}$$

satisfies $\Pi q(t_1) = (b_i, 0)$, where $t_1 > t_0$. The feedback function is parameterized by the vectors b_i, $i = 1, ..n$, where n is the number of line segments in the path. For each b_i, there exists such a feedback function. The control algorithm is constructed by appropriate switching between members of the family of feedback functions. On each cycle of the algorithm the particular functions selected depend on the closed path parameters. We propose the following PD feedback control law

$$\begin{cases} U_i^* = -k_{1,i}(b - b_i) - k_{2,i}\dot{b}, & \text{if } \Pi q \neq (b_i, 0) \\ U_i^* = 0, & \text{if } \Pi q = (b_i, 0) \end{cases} \tag{7.32}$$

where $k_{1,i}$ and $k_{2,i}$, $i = 1, ..n$, are arbitrary positive constants. It can be easily seen that the above feedback law asymptotically stabilizes (7.31). Now, we can construct the control algorithm as follows

Algorithm 7.1: $U \leftarrow$`Control_algorithm` (q_e, q_1, ε)

```
1 while ‖q_e − q_1‖ > ε do
2     Select (φ*, θ*) from Table 7.2 to achieve desired geometric phase
3     Construct the closed path b_i, i = 1, ..n
4     for i = 1, ..., n do
5         U = U_i*(Πq) until Πq = (b_i, 0)
6     q_1 ← q
```

The inputs to the controller are the desired equilibrium point q_e, system's initial state on the equilibrium manifold q_1, and a tolerance ε which, if crossed, the goal equilibrium q_e is reached and the controller stops retraction/insertion.

Now, let us highlight a few interesting aspects of the retraction/insertion paths illustrated in Table 7.2. Conditions 1 and 2 are designed for needle retraction/insertion.

Table 7.2: Closd paths and corresponding base coordinates for retraction/insertion motion of the needle. Note: $k \in \mathbb{Z}$, $y_d = y_e - y_1$, $z_d = z_e - z_1$, and all the paths start from $b_e = (\phi_e, \theta_e)$

	Condition	Closed path	Base coordinates	Needle motion
1	$z_d \in \mathbb{R}$ & $y_d \in \mathbb{R}^+$ & $\frac{y_d^2 + z_d^2}{y_d} \leq \frac{4}{\kappa}\mathrm{S}^2\frac{\theta_e}{2}$	$b_1 = (\phi^*, \theta_e)$, $b_2 = (\phi^*, \theta^*)$, $b_3 = (0, \theta^*)$, $b_4 = (0, \theta_e)$, $b_5 = (\phi_e, \theta_e)$	$\phi^* = 2k\pi - 2\mathrm{atan}(y_d/z_d)$ $\theta^* = \mathrm{acos}(\frac{\kappa y_d^2 + \kappa z_d^2}{2y_d} + \mathrm{C}\theta_e)$	retraction–insertion
2	$z_d \in \mathbb{R}$ & $y_d \in \mathbb{R}^-$ & $\frac{y_d^2 + z_d^2}{y_d} \geq -\frac{4}{\kappa}\mathrm{S}^2\frac{\theta_e}{2}$	$b_1 = (0, \theta_e)$, $b_2 = (0, \theta^*)$, $b_3 = (\phi^*, \theta^*)$, $b_4 = (\phi^*, \theta_e)$, $b_5 = (\phi_e, \theta_e)$	$\phi^* = 2k\pi - 2\mathrm{atan}(y_d/z_d)$ $\theta^* = \mathrm{acos}(-\frac{\kappa y_d^2 + \kappa z_d^2}{2y_d} + \mathrm{C}\theta_e)$	retraction–insertion
3	$z_d \in \mathbb{R}$ & $y_d \in \mathbb{R}^+$ & $\frac{y_d^2 + z_d^2}{y_d} > \frac{4}{\kappa}\mathrm{S}^2\frac{\theta_e}{2}$	$b_1 = (0, \theta_e)$, $b_2 = (0, \theta^*)$, $b_3 = (\phi^*, \theta^*)$, $b_4 = (\phi^*, \theta_e)$, $b_5 = (\phi_e, \theta_e)$	$\phi^* = 2k\pi - 2\mathrm{atan}(y_d/z_d)$ $\theta^* = -\mathrm{acos}(-\frac{\kappa y_d^2 + \kappa z_d^2}{2y_d} + \mathrm{C}\theta_e)$	retraction–insertion
4	$z_d \in \mathbb{R}$ & $y_d \in \mathbb{R}^-$ & $\frac{y_d^2 + z_d^2}{y_d} < -\frac{4}{\kappa}\mathrm{S}^2\frac{\theta_e}{2}$	$b_1 = (\phi^*, \theta_e)$, $b_2 = (\phi^*, \theta^*)$, $b_3 = (0, \theta^*)$, $b_4 = (0, \theta_e)$, $b_5 = (\phi_e, \theta_e)$	$\phi^* = 2k\pi - 2\mathrm{atan}(y_d/z_d)$ $\theta^* = -\mathrm{acos}(\frac{\kappa y_d^2 + \kappa z_d^2}{2y_d} + \mathrm{C}\theta_e)$	retraction–insertion
5	$z_d \in \mathbb{R}$ & $y_d \in \mathbb{R}^+$ & $\frac{y_d^2 + z_d^2}{y_d} > \frac{4}{\kappa}\mathrm{S}^2\frac{\theta_e}{2}$	$b_1 = (0, \theta_e)$, $b_2 = (0, \theta^*)$, $b_3 = (\phi^*, \theta^*)$, $b_4 = (\phi^*, \theta_e)$, $b_5 = (\phi_e, \theta_e)$	$\phi^* = 2k\pi - 2\mathrm{atan}(y_d/z_d)$ $\theta^* = \mathrm{acos}(-\frac{\kappa y_d^2 + \kappa z_d^2}{2y_d} + \mathrm{C}\theta_e)$	insertion–retraction
6	$z_d \in \mathbb{R}$ & $y_d \in \mathbb{R}^-$ & $\frac{y_d^2 + z_d^2}{y_d} < -\frac{4}{\kappa}\mathrm{S}^2\frac{\theta_e}{2}$	$b_1 = (\phi^*, \theta_e)$, $b_2 = (\phi^*, \theta^*)$, $b_3 = (0, \theta^*)$, $b_4 = (0, \theta_e)$, $b_5 = (\phi_e, \theta_e)$	$\phi^* = 2k\pi - 2\mathrm{atan}(y_d/z_d)$ $\theta^* = \mathrm{acos}(\frac{\kappa y_d^2 + \kappa z_d^2}{2y_d} + \mathrm{C}\theta_e)$	insertion–retraction
7	$z_d \in \mathbb{R}$ & $y_d = 0$	$b_1 = (\phi^*, \theta_e)$, $b_2 = (\phi^*, \theta^*)$, $b_3 = (-\phi^*, \theta^*)$, $b_4 = (-\phi^*, \theta_e)$, $b_5 = (\phi_e, \theta_e)$	$\phi^* = 2k\pi + \mathrm{sign}(z_d)\pi/2$ $\theta^* = -\mathrm{acos}(-\mathrm{sign}(z_d)\frac{\kappa z_d}{2} + \mathrm{C}\theta_e)$	retraction–insertion
8	$z_d\mathrm{S}\phi_e \leq 0$ & $y_d\mathrm{C}\phi_e \leq 0$	$b_1 = (\phi_e, \theta_1^*)$, $b_2 = (\phi_1^*, \theta_1^*)$, $b_3 = (\phi_1^*, \theta_e)$, $b_4 = (\phi_1^*, \theta_2^*)$, $b_5 = (\phi_2^*, \theta_2^*)$, $b_6 = (\phi_2^*, \theta_e)$, $b_7 = (\phi_e, \theta_e)$	$\phi_1^* = \pi - \phi_e$ $\phi_2^* = \pi + \phi_e$ $\theta_1^* = \mathrm{acos}(-\frac{\kappa y_d}{2\mathrm{C}\phi_e} + \mathrm{C}\theta_e)$ $\theta_2^* = \mathrm{acos}(-\frac{\kappa z_d}{2\mathrm{S}\phi_e} + \mathrm{C}\theta_e)$	double retraction–insertion

Conditions 3 and 4 correspond to large needle retraction/insertion. Conditions 5 and 6 represent needle insertion/retraction movement. Condition 7 is used only when y_d is zero and tends to correct the error in z direction. Condition 8 is a special steering scenario demonstrating a double retraction movement on previous insertion paths.

When the desired target point is far from the needle or as the desired path curvature increases beyond the modeled curvature of the needle κ, conditions 1 and 2 in Table 7.2 are not satisfied, i.e, $|\frac{y_d^2+z_d^2}{y_d}| > \frac{2}{\kappa}\mathrm{S}^2\frac{\theta_e}{2}$. In this case, three possible options exist for needle steering: 1) Use conditions 5 and 6 to further insert the needle to a higher depth and later retract the needle toward the target. 2) Use conditions 3 and 4 to perform an extended retraction followed by a re-insertion (almost similar to a new insertion). 3) Perform multiple retractions and insertions using concatenation of a series of closed paths from conditions 1, 2, and 5. This situation can be simply avoided and rarely happens in practice for three reasons: 1) In clinical practice, preoperative images are used to select the needle point of entry as close as possible to the desired target location. 2) For steering the needle toward very divergent targets, highly flexible needles [40,55,56] with small deflection curvature (κ) can be selected to satisfy conditions 1 and 2 in Table 7.2. 3) Even if the target point is far from the needle entry point, the first step of the controller, described in Section 7.4.2.1, ensures that the desired equilibrium point is very close to the needle before the retraction begins.

Row 6 in Table 7.2 is a special steering scenario demonstrating a double retraction movement, one retraction to correct the error in y direction and another to correct insertion error in z direction. In this condition, the needle is only retracted on the previous insertion paths. This is recommended for needle retractions in stiff tissue, where the needle follows the same path it has previously traversed. In the next section, we perform several simulation studies to investigate the different conditions in Table 7.2 and validate the controller.

7.4.3 Simulation Study

Simulations are performed to check the controller parameters and verify the needle steering controller performance in steering the needle toward various points in 3D. Two scenarios are

simulated: (1) Needle insertion on a straight path: The needle is steered to reach a target placed at a depth of 140 mm, thus the desired target point is $(140, 0, 0)$. (2) Needle insertion on a curved path: Considering a 2 mm obstacle is placed at the depth of 70 mm, first, the needle is steered toward a point at $(60, 4, 4)$, next it is steered toward $(90, 4, 4)$ to pass the obstacle, and finally guided to the final destination at $(140, 0, 0)$. The needle curvature in the simulations is $\kappa = 1/400$ mm^{-1} (see Section 6.2.2). The parameters of the first step controller are $K_1 = 100I$ and $K_2 = 10I$, where I is a 2×2 identity matrix, and $k_{0,1} = 0.3$ and $k_{0,1} = \text{asin}(140\kappa)$. The parameters of the second controller are $k_{1,i} = k_{2,i} = 500$, $i = 1, .., 5$. The results of the simulations are plotted in Fig. 7.5.

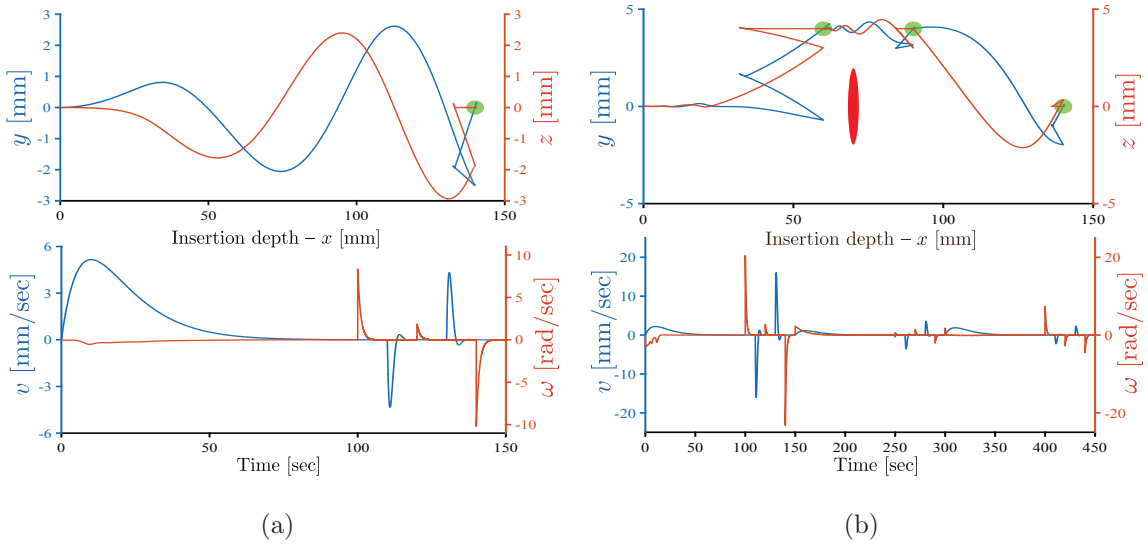

Figure 7.5: Simulated results of needle steering for (a) needle insertion on a straight path, (b) 3 point needle insertion with obstacle avoidance. Needle deflection in y and z directions as long as insertion velocity v and axial rotation velocity ω are shown. Obstacles and target points are shown with red and green, respectively.

Now, we verify the needle steering controller when conditions 1 and 2 in Table 7.2 are not satisfied, i.e, $|\frac{y_d^2+z_d^2}{y_d}| > \frac{2}{\kappa}\text{S}^2\frac{\theta_e}{2}$. In the simulations, it is assumed that the needle initial coordinate is (0,0,0) and the final target point is (0,4,10), the initial orientation ϕ_e and deflection angle θ_e are 0 and $\pi/10$, respectively. Three possible options are simulated and presented in Fig. 7.6: 1) Use conditions 3 and 4 to perform insertion-retraction–shown by dashed line. 2) Use conditions 3 and 4 to perform an extended retraction insertion–shown by solid line. 3) Perform multiple retractions and insertions. The needle is first steered from (0,0,0) to (0,4,4) using condition 1 and later to (0,4,10) using condition 5 from Table 7.2–

shown by dotted line.

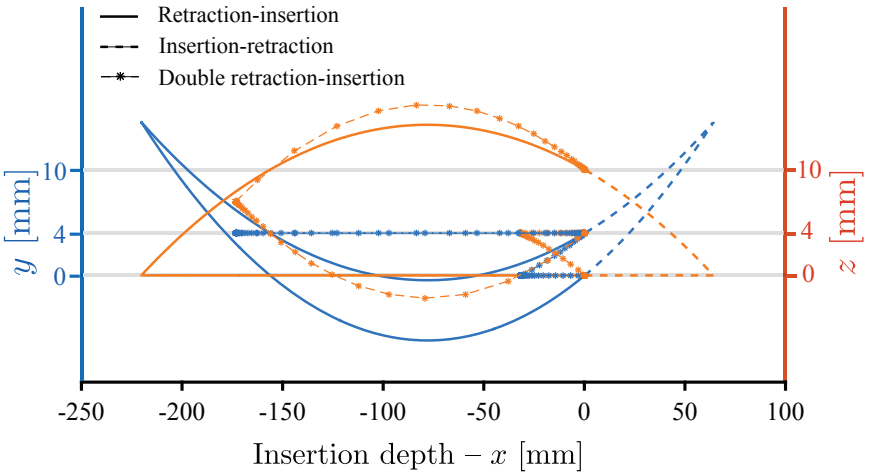

Figure 7.6: A comparison between various options for needle retraction/insertion when the target point is far from the needle initial state. The needle initial coordinate is (0,0,0) and the final target point is (0,4,10). Initial needle base coordinate is $(0,\pi/10)$.

In the last simulations, we evaluate the performance of the system in the presence of uncertainty in the model parameter κ. Due to many factors such as tissue heterogeneity the needle tip curvature might differ from the nominal identified curvature. Here, we simulate an extreme scenario in which there is $\pm 60\%$ error in the identified value of needle radius of curvature. Results are shown in Fig. 7.7. The controller is capable of steering the needle to the desired point by performing extra retractions. In the simulations, the magnitude of the targeting error at the end of the simulation (ϵ in Algorithm 7.1) was selected to be 0.1 mm. A total of 3 retractions are performed to reach the desired accuracy.

Deviations from nominal curvature often happens during the retraction, when the needle tip cannot cut the tissue and it does not follow the path predicted by the nonholonomic model. As explained above these deviations increase the number of retractions, which is undesirable. Another way to handle this is to retract the needle following the same insertion path. This scenario is realized in Condition 6 in Table 7.2. One can employ this condition only when $z_d \mathrm{S}\phi_e \leq 0$ and $y_d \mathrm{C}\phi_e \leq 0$. A schematic of 2D retraction on insertion path when $\phi_e = 0$ is shown in Fig. 7.8(a) and 7.8(b). Fig. 7.8(a) is a schematic of needle insertion when condition 6 is satisfied and retraction on insertion path is possible. However, in 7.8(b), $(y - y_1)\mathrm{C}\phi_e \geq 0$ and clearly it is impossible to reach the target with a retraction

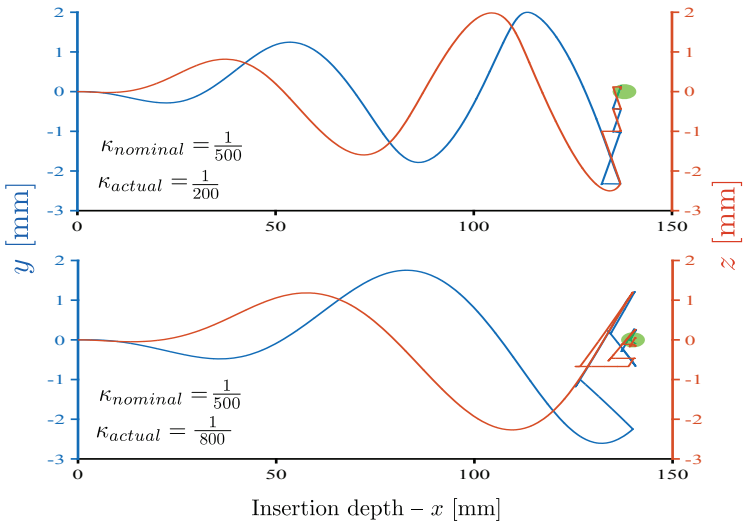

Figure 7.7: Results of the needle steering simulations with 60% uncertainty in the nominal value of radius of curvature.

on the already traversed insertion path. Results of 3D double retractions simulation for a case where condition 6 is satisfied is shown in Fig. 7.8(c).

7.4.4 Experimental Evaluation

In this section, needle insertion experiments are performed using the setup shown in Appendix A, Fig. A.1, to evaluate the designed needle steering controller. In the experiments, the ultrasound probe is robotically moved to follow the needle tip. The procedure introduced in [97] is used to calculate needle deflection along y and z directions from 2D transverse ultrasound images.

In our experiments, we used the 18-gauge flexible notched needles introduced in Chapter 6. Two types of tissue are used in the experiments, plastisol phantom tissue and ex-vivo porcine tissue. The plastisol tissue is made of 80% (by volume) liquid plastic and 20% plastic softener (M-F Manufacturing Co., USA). A phantom prostate with diameter of 50 mm is embedded in the plastisol tissue. The porcine tissue is embedded in gelatin to increase the contact surface between the ultrasound probe and the tissue and as a result reducing noise in the ultrasound images. The Young's elasticity moduli of the synthetic and ex-vivo tissues calculated using indentation tests are 30 Kpa and 50 Kpa, respectively. The elas-

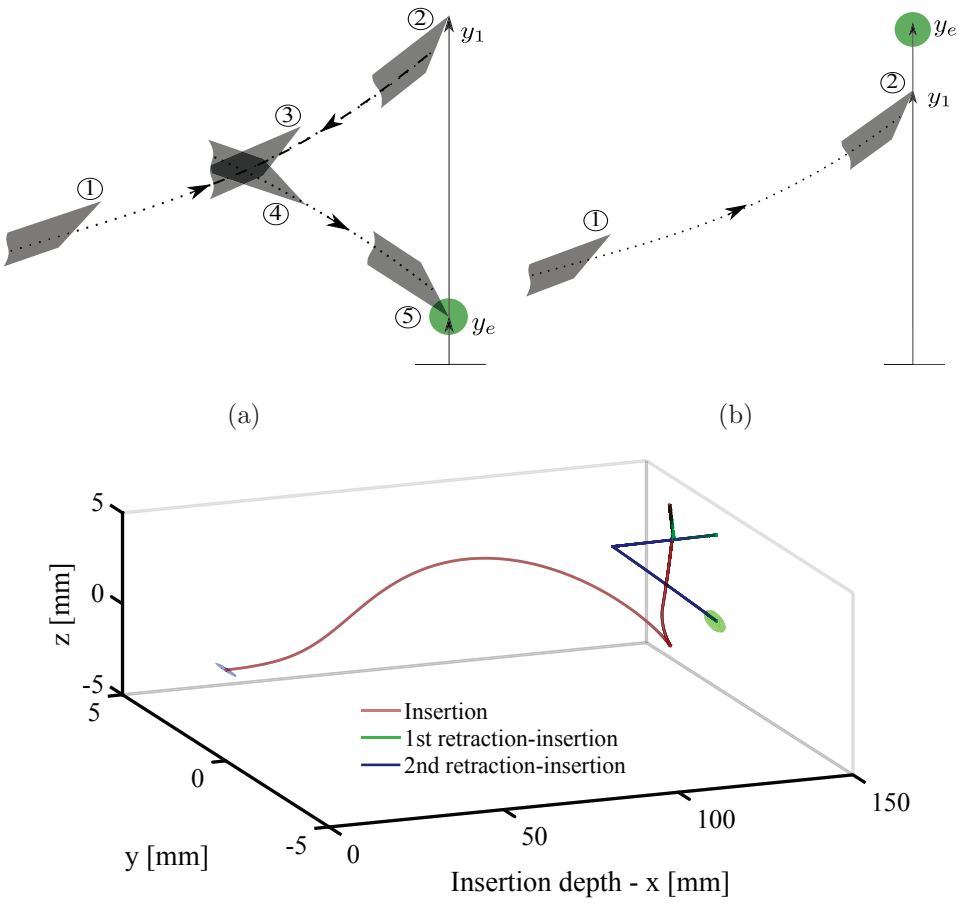

Figure 7.8: Simulation of double retractions on prior insertion paths. Schematics of 2D needle insertion and retraction for when (a) condition 6 is satisfied and retraction on prior insertion path is possible and (b) condition 6 is not satisfied. In (a) and (b) insertion and retractions are shown by dotted and dashed lines, respectively. (c) Simulation results for 3D double retraction on prior insertion paths.

ticity of the synthetic tissue are similar to what is found in muscle and connective tissues [72].

Similar to the simulations, two scenarios are used in the experiments to validate the controller.

1. The needle is steered to reach a target on a straight line placed at a depth of 140 mm.

2. The needle is steered to reach a target at the depth of 140 mm while avoiding a spherical obstacle with a diameter of 2 mm placed at the depth of 70 mm.

The 1st scenario is similar to conventional needle insertion in prostate brachytherapy, where the needle should be inserted along a straight line within the tissue. The 2nd scenario represents needle steering when there is an obstacle. Obstacles are sensitive or impenetrable anatomical regions in the proximity of the target point such as glands, blood vessels or bones. Based on preoperative medical images the clinician can specify the insertion location and target region as well as sensitive structures and obstacles. For the 2nd scenario we performed a 3 point needle steering. The needle is steered toward a point at $(60, 4, 4)$, next it is steered toward $(80, 4, 4)$ to pass the obstacle, and finally guided to the final destination at $(140, 0, 0)$.

In the experiments, needle deflections were sufficiently small to satisfy conditions 1 and 2 and we only used these two conditions. 5 insertions without rotations were performed in each tissue prior to needle steering experiments to identify the nominal curvature of the needle. κ is found by fitting the model in (7.6) to the experimental results using nonlinear least square method. The magnitude of κ for synthetic and ex-vivo tissue are 0.0023 ± 0.0004 and 0.0015 ± 0.0007 mm^{-1}, respectively. $\pm$ shows 95% confidence bounds.

Results of needle steering experiments for each scenario in two tissues are shown in Fig. 7.9. The magnitude of the targeting error (ϵ in Algorithm 7.1) is 1 mm and 1.5 mm for needle steering without and with obstacle, respectively. In the representative results shown in Fig. 7.9, one retraction is performed for needle steering on straight line in both tissues. Also, one retraction and two retractions are performed for needle steering with obstacle in plastisol and ex-vivo tissue, respectively. The experimental results for 10 trials in each tissue are summarized in Table 7.3. The maximum absolute targeting error in the first and second scenarios are 0.98 and 1.45 mm, respectively, both for insertions in ex-vivo tissue. The maximum number of retractions is 7 and occurs in needle steering with obstacle in porcine tissue.

7.5 Concluding Remarks

In this chapter, we proposed a nonholonomic model of needle steering that is fully controllable. Then, we present two different type of controllers for 3D needle steering: In

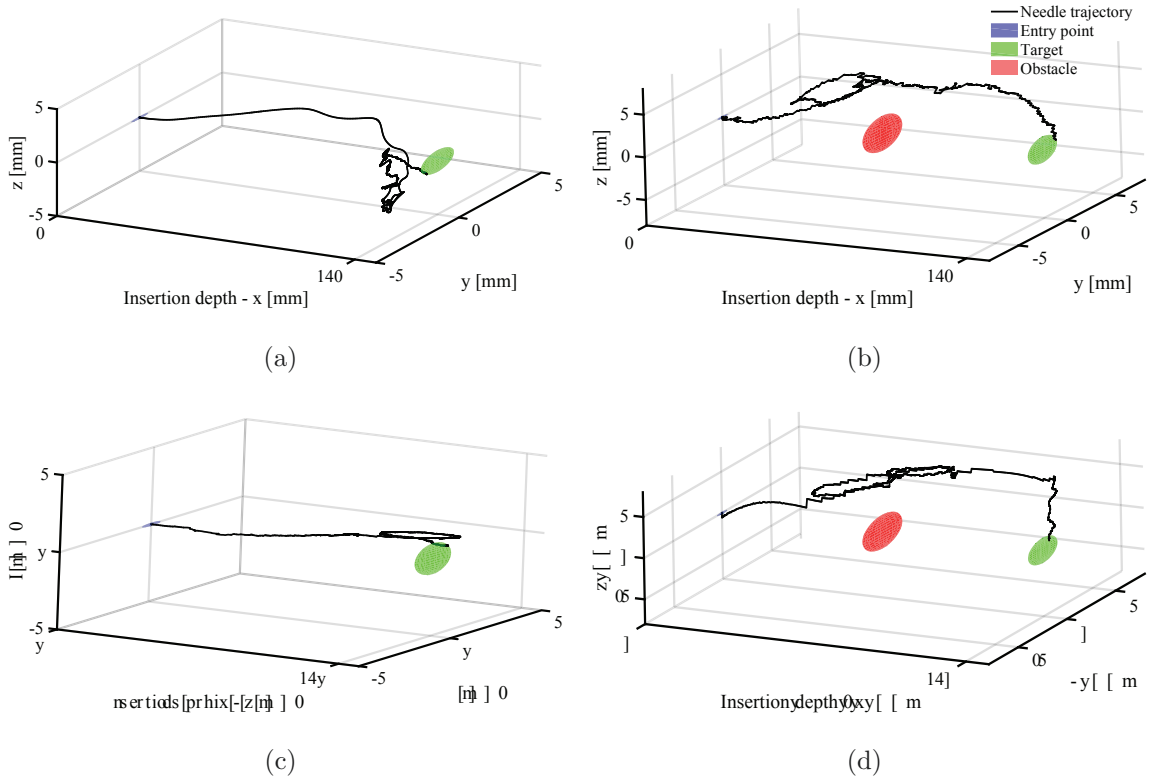

Figure 7.9: Representative experimental needle steering results for each insertion scenario in synthetic and ex-vivo tissue. (a) Needle steering in plastisol tissue without obstacle and (b) with obstacle. (c) Needle steering in ex-vivo tissue without obstacle and (d) with obstacle.

Section 7.3, a nonlinear feedback-linearization-based controller was proposed to steer the needle in 3D while avoiding anatomical obstacles. The main drawback of the proposed approach was relatively large control actions that can increase tissue trauma.

In Section 7.4, a geometric controller for 3D needle steering via retraction/insertion is proposed. The proposed approach implements needle retraction/insertion motion to correct any undesired targeting errors. The proposed 3D needle steering system can be used in all clinical needle insertion scenarios to improve needle steering accuracy and extend the application of needle-based interventions to deeper or more difficult-to-reach targets. The maximum targeting error of the proposed approach is 0.98 mm for needle insertion on a straight line. In a recent study from our group, seed placement accuracy in prostate brachytherapy is measured using post-implant ultrasound images [99]. 1619 seeds using 357 strands were implanted in 15 patients' prostate glands. Of the 1619 seeds implanted,

Table 7.3: Results of needle steering experiments for 10 trials. Mean targeting error (e_{mean}), maximum targeting error (e_{max}), standard deviation of error (σ), maximum number of retractions (Max. Ret. No.), and minimum number of retractions (Min. Ret. No.) are listed.

	Plastisol		Ex-vivo	
	1st Scenario	2nd Scenario	1st Scenario	2nd Scenario
$e_{mean}[mm]$	0.7	1.13	0.67	1.22
$e_{max}[mm]$	0.91	1.41	0.98	1.45
$\sigma[mm]$	0.25	0.22	0.31	0.18
Max. Ret. No.	3	6	4	7
Min. Ret. No.	0	1	0	2

1196 (73.87%) were confidently identified in post-implant images. The overall mean in-plane and out-of-plane displacements were 13 and 15 mm, respectively, which is higher than our proposed method. However, this error includes the image processing error, error in registering images before and after the surgery, and errors due to prostate motion and deformation.

To furthermore elaborate the effectiveness of the needle steering and for benchmarking the proposed needle insertion strategy, we have performed several fully manual needle insertions in a plastisol tissue and compared the results with the controlled needle insertion. Two skilled brachytherapist were asked to steer the needle to follow a straight line in a synthetic tissue, similar to the one used in previous experiments. The surgeon can rotate the needle axially and move the ultrasound probe to locate the needle tip. Real time visual image feedback of needle tip were provided to the surgeon during the insertions. 10 trials were performed by each surgeon. Results of the manual and controlled needle steering are compared in Fig. 7.10. The mean targeting error of the controlled needle steering is 60% less than manual needle insertion. Fig. 7.10 shows that the standard deviation of the error of the proposed approach is smaller than manual needle insertion. This means the proposed approach shows more repeatability compared to conventional needle insertion strategies.

The maximum number of performed retractions directly depend on the uncertainties

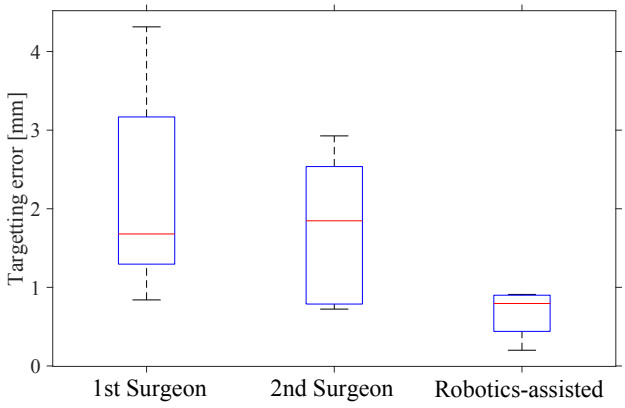

Figure 7.10: A comparison between robotics-assisted needle steering and manual needle insertion. For each group, red line indicates median error, blue box indicates 25th and 75th percentile, and whiskers indicate minimum and maximum error.

in the measured value of κ and the desired targeting error. Large uncertainties in the value of κ can increase number of needle retractions, which is undesirable. In practice, needle curvature can be measured on the fly by means of an online estimator [37]. One can also relax the constant curvature path assumption by employing a high-level controller that controls the needle curvature through duty-cycling [14, 15]. Another approach that was discussed in Section 7.4.3 is to retract the needle on prior insertion paths. This way variations in the magnitude of κ is minimized and number of retractions is decreased. We performed 5 trial insertions using condition 8 in Table 7.2, inserting the needle in ex-vivo tissue on a straight line with double retractions on prior insertion paths. A representative result is shown in Fig. 7.11. As it can be seen the controller retracts the needle on previous paths and tries to minimize the error in y direction first and z direction next. In this experiment the needle reached the target with mean error of 0.76 mm and only 2 retractions were performed in each trial.

In the presented obstacle avoidance experiments, we selected 3 arbitrary points around the obstacle and steered the needle toward these points to avoid the obstacle. We note that 3D path planning strategies such as [14, 15] can be used to calculate the location of target points more efficiently to maximize the needle distance from the obstacle and minimize number of retractions. In the experiments, the obstacle and target are fixed in space rather than fixed to the tissue itself. A small amount of deformation was observed during these

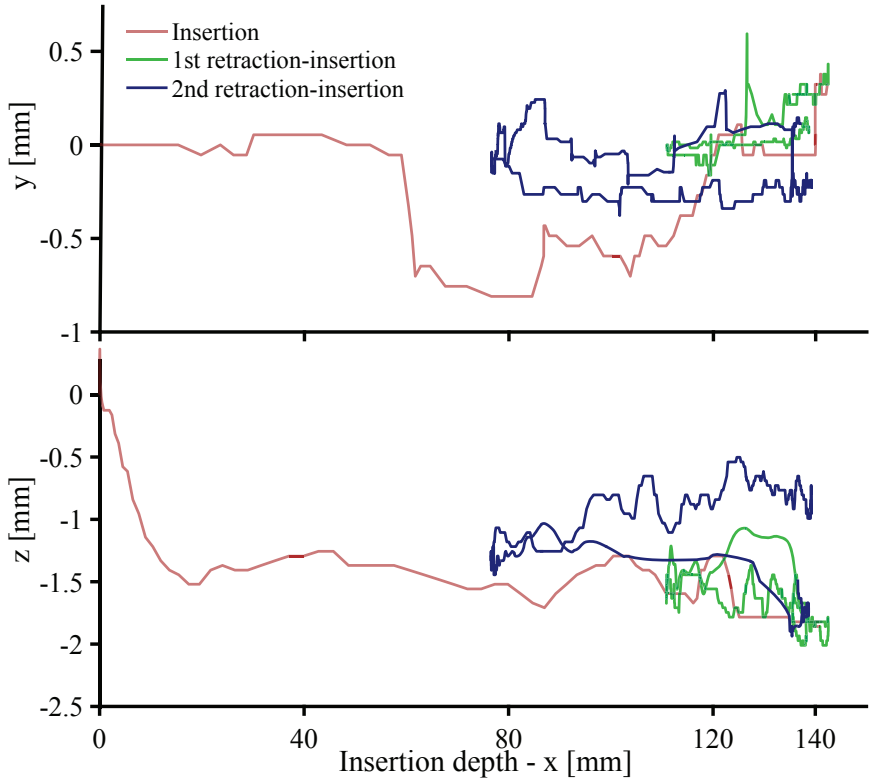

Figure 7.11: Experimental needle steering result for double retractions on prior insertion paths. Needle deflection in y and z directions are reported.

experiments, which disturbed the targeting accuracy. Future efforts will focus on validating the controller by performing experiments with biological tissue with moving target since the proposed controller is capable of correcting errors due to tissue motion via retractions.

Finally we remark that the two-steps of the proposed controller are independent. The first step controller is designed based on observations of clinical needle insertions in prostate brachytherapy, where needle is simultaneously rotated and inserted at high velocity to insert the needle on a straight line. Depending on the clinical application, this controller can be replaced by other steering strategies studied in the litrature. Second step of the controller that performs retractions can be simply combined with previous 3D [14,15,34] or 2D planar needle steering strategies [31,37] to enhance their targeting accuracy.

Chapter 8

Conclusions and Future Works

This dissertation has explored modeling and control of robotics-assisted needle steering with the aim of enhancing the performance of needle-based interventions. The core theme of this dissertation is motivated by challenging deployment of medical robotic systems in clinical environments where robots must interact with human operators. We intend to propose robotics-assisted needle steering strategies that can be implemented in the current clinical setting with minimal or no modifications. Other motivating challenges that drove these endeavors are: 1) combining the accuracy and precision of robots with judgment and skill of clinicians, 2) reducing the trauma of surgery by minimizing the control efforts required in a successful needle steering, and 3) providing new methods of reaching challenging targets to reduce number of conditions that are currently considered untreatable or inoperable.

We have developed several needle steering strategies for 2D and 3D needle steering, as well as fully robotic and semi-automated needle steering. We studied prostate brachytherapy as an example of needle-based interventions. We showed that the proposed strategies can reduce needle targeting error in various scenarios in prostate brachytherapy, which will benefit the individual patient, the surgeon, and the healthcare system. In fact, the benefits of this research improving the accuracy of needle insertions will not only be limited to prostate brachytherapy, but will also be applicable to other procedures that involve precise insertion of needles (e.g., liver ablation, interventional radiology for image guided biopsies)

8.1 Needle Steering Modeling

Toward these ends, we developed three different needle steering models that can be used to study robotics-assisted needle steering. Chapter 3 dealt with a comprehensive mechanics-based model of 2D needle steering. The model relates needle deflection to insertion velocity and axial rotation of the needle, which can be regarded as control inputs for needle steering. By means of a novel time-delayed tissue model embedded in the proposed model, the needle tip position is accurately predicted. Also, the model is computationally efficient and allows for real-time control of the needle tip position in a robotic-assisted needle insertion context. Needle insertion experiments are performed at different velocities with axial rotation(s) at different insertion depths on synthetic and ex vivo animal tissue to validate the needle steering model. The results confirm the model's accuracy and capability in capturing the effects of insertion velocity and axial needle rotation on needle deflection, thus enabling future applications in pre-surgery motion planning, optimized trajectory design, and real-time control of needle steering. Also, the proposed model can be used for the semi-automated needle insertion, in which automatic robot-assisted adjustments are performed to one of the control inputs, while other inputs are directly applied by the surgeon. The comprehensive model is designed to respond to all the needle steering inputs (i.e., axial rotation, insertion velocity, needle base force/torque), only over some of which there is robotic control.

In Chapter 5, we proposed an adaptive 2D needle steering model based on the Homotopy Analysis Method (HAM). The model uses a depth-varying radius of curvature and is able to predict uncertain changes in the needle curvature due to the variations in the insertion velocity or tissue inhomogeneity. Unlike the mechanics-based model, the HAM-based model has only one parameter, i.e., the average radius of curvature of the needle, which can be easily identified. This facilitates the implementation of the model in clinical needle steering, where non-invasive identification of model parameters is challenging.

In Chapter 7, we presented a nonholonomic model of needle steering. Unlike the previous models proposed in this dissertation, the nonholonomic model can predict needle deflection in 3D. The model is controllable and all the model states are observable via

2D imaging systems such as ultrasound. Thus it can be used to develop practical needle steering strategies that only relies only on 2D ultrasound images to steer the needle.

8.2 Fully Robotic and Semi-automated Needle Steering

Fully automatic and semi-automated needle steering are both studied in this dissertation. Typically, two main control actions are used to steer the needle, namely, axial rotation and insertion of the needle. The needle steering controller can be either fully automated, meaning that the device performs both insertion and steering actions, or semi-automated, where insertion is performed by the surgeon while needle rotation occurs automatically.

Chapter 4 addressed the 2D fully robotic needle steering. The mechanics-based needle deflection model combined with an image processing techniques, and a model predictive controller was used to accurately steer the needles inside soft tissues. In Chapter 5, a needle steering strategy for surgeon-in-the-loop semi-automated needle steering was proposed.

The HAM-based predictor is implemented in an online motion planner that steers the needle inside the tissue toward a predefined target. In the semi-automated needle steering system the robot only controls the needle axial rotation while the surgeon inserts the needle. To elaborate the effectiveness of semi-automated needle steering and for benchmarking our controlled needle insertion strategy, we performed several fully automated and manual needle insertions and compared the results with semi-automated needle insertion. The results demonstrated that the human-in-the-loop strategy is more accurate than fully robotic needle insertion. Also, the semi-automated approach gives the same performance at different trials. The mean error of the semi-automated approach is comparable to manual needle insertions performed by a skilled surgeon. However, the results are more consistent and repeatable in case of semi-automated needle steering.

8.3 Highly Flexible Steerable Needles

Chapter 6 addressed design and modeling of highly flexible notched needles. Commercially available disposable brachytherapy needles are modified to develop a needle with improved deflection curvature and enhanced maneuverability. The notched needle is developed by carving small notches on a standard needle shaft. By carving several consecutive notches on the needle shaft, the needle flexural strength and the needle's maximum achievable ROC are decreased. Thus, the needle provides a safe working channel for delivering payloads to target locations. The goal of the proposed research is not changing the current clinical setting and replacing the current needles with the new proposed notched needle. We intend to provide another option in terms of needle selection so that surgeons can perform successful needle insertions in certain clinical scenarios where high needle deflection curvature is required.

In the proposed experiments, notches were manually carved at different locations on the needle shaft using a hand-held milling machine. Future efforts can be focused on automating this process to ensure the notches are homogeneous and smooth, reducing the possibility of damaging the tissue.

Also in designing the notched needles, it is assumed that the notch width and depth are both 0.5 mm, which is smaller than the inner diameter of the needle. These design parameters are assumed constant to ensure the needle can provide a safe channel for delivering payloads with a diameter bigger than 0.5 mm, which is the case for radioactive seeds in prostate brachytherapy. However, there is a risk of leaking for delivering or preserving liquids. This can be avoided by coating the needles with super-elastic materials that does not increase needle rigidity but reduce the chance of leakage. A soft coating also reduces the contact between the notches and the tissue, thus, eliminating the possibility of damaging the tissue. Feasibility of silicone coating of surgical needles can be studied in future works.

8.4 3D Needle Steering

The main drawback of the needle steering approaches proposed in chapter 4 and 5 is that they are 2D and only control the needle deflection in the insertion plane. However, during clinical needle steering the needle tip might deviate and deflect out of plane. Many factors such as tissue inhomogeneity can cause out of plane needle deflection. In Chapter 7, a two-step geometric controller for 3D needle steering via retraction/insertion is proposed. The proposed approach implements needle retraction/insertion motion to correct any undesired targeting errors. The proposed 3D needle steering system can be used in all clinical needle insertion scenarios to improve needle steering accuracy. To elaborate the effectiveness of the needle steering and for benchmarking the proposed needle insertion strategy, we have performed several fully manual needle insertions and compared the results with the controlled 3D needle insertion. Two skilled brachytherapist were asked to steer the needle to follow a straight line in a synthetic tissue, similar to the one used in previous experiments. The surgeon can rotate the needle axially and move the ultrasound probe to locate the needle tip. Real time visual image feedback of needle tip were provided to the surgeon during the insertions. Results show that the mean targeting error of the controlled needle steering is 60% less than manual needle insertion.

The two-steps of the proposed geometric controller are independent. The first step controller is designed based on observations of clinical needle insertions in prostate brachytherapy, where needle is simultaneously rotated and inserted at high velocity to insert the needle on a straight line. Depending on the clinical application, this controller can be replaced by other steering strategies studied in the literature. Second step of the controller that performs retractions can be simply combined with previous 3D or 2D planar needle steering strategies to enhance their targeting accuracy.

In this dissertation, only fully robotic 3D needle insertion is considered. It is preferred to keep the surgeon in charge of needle insertion in the interest of ensuring the safety of the operation. Future goals in 3D needle steering include the generalization of the 2D mechanics-based model for application in 3D semi-automated needle steering. The 2D model presented in Chapter 3 can be generalized to simulate full needle axial rotation in-

stead of 180° rotation. The methodology proposed in Chapter 3 to model needle/tissue interaction forces as external excitation forces allows one to simply implement the interaction force models to any mechanics-based 3D model. Also, the 3D geometric approach presented in Chapter 7 can be modified for semi-automated needle steering. For instance, instead of robotically controlling the needle insertion/retractions, specific guidelines for insertion/retraction can be visually presented to the surgeon in real-time. Therefore, the surgeon can manually preform insertion/retractions while the robot automatically controls the axial rotation of the needle.

Future goals can include development of a simulator and trainer for assessment and improvement of targeting accuracy in needle-based interventions. Typically, the excellent success rates of brachyhtherapy are only achieved by experienced brachytherapists, as studies have shown that there is a learning curve where inexperienced surgeons have a higher risk of performing implants of suboptimal quality. Enhancing clinical awareness of these deviations and skill levels of brachytherapists is imperative for improved implant quality. A needle steering simulator can provide unlimited training opportunities and will allow inexperienced surgeons to offer brachytherapy to a wider range of patients. This will allow them to improve their skills and achieve higher quality implants without the usual learning curve.

The simulator requires a model-based virtual reality environment that can simulate needle deflection in soft tissue. The surgeons can perform multiple insertions of needles in the virtual environment and receive quantifiable performance assessments in terms of needle tip positioning and seed placement errors. Also, semi-automated needle steering controllers can be used to guide novice surgeons and improve their performance. For instance, a semi-automated controller can be used to rotate the needle when necessary if the user does not perform the action at the desired decision epoch. This dissertation has addressed many of the key pieces of such a simulator, including developing realistic model of needle deflection in soft tissue and constructing a semi-automated needle steering controller that can share the needle steering control inputs with a human user.

8.5 Clinical Translation Outlook

The proposed needle steering controllers are validated using the experimental setups shown in Appendix A. In the experiments an abdominal linear ultrasound transducer is used, which is not designed for prostate brachytherapy. Towards translating the proposed technology into clinical practice, the ultrasound transducer can be replaced with a transrectal ultrasound probe commonly used in brachytherapy. It should be noted that all the proposed steering controllers require US images of the needle that can be captured by any 2D ultrasound transducer.

In order to track the needle tip during insertion, the ultrasound probe would follow the needle tip during insertion. For brachytherapy applications, this is only viable as long as the moving parts of the ultrasound probe are not in contact with the surrounding tissue. This could be implemented with a thin, firm sleeve in which a transrectal ultrasound probe translates, such that when the transducer moves, it does not deform the prostate gland and/or adjacent anatomical structures. This feature can be found in some commercially available ultrasound systems such as the TargetScan (Envisioneering Medical, USA) in which the probe is stationary, but the transverse imaging plane can be translated internally.

Another option is the 3D-2052 anorectal ultrasound probe from BK Ultrasound, USA, which translates the axial imaging plane by 60 mm inside the ultrasound probe to construct a 3D volume. Alternatively, other means of deflection measurement can also be considered, such as force sensor based estimators [118], partial ultrasound image feedback algorithms designed to minimize the ultrasound probe motion [97], or 3D matrix transducer transrectal ultrasound probes. Clinical deployment of the system will also require handling issues regarding sterility, accuracy, and risk assessment.

In all the validation needle steering experiments, the obstacle and target are fixed in space rather than fixed to the tissue itself. A small amount of deformation was observed during these experiments, which disturbed the targeting accuracy. Future efforts can be focused on modifying the controllers for needle steering with moving target. More realistic testing scenario can be designed, where needle steering tests can be conducted on biological

tissue with moving targets. The motion of the target can be tracked in the ultrasound images or compensated in the model-based control algorithms using a soft tissue model that predicts target displacements.

Bibliography

[1] Carlos Rossa and Mahdi Tavakoli. Issues in closed-loop needle steering. *Control Engineering Practice*, 62:55 – 69, 2017.

[2] S.P. DiMaio and S.E. Salcudean. Needle steering and model-based trajectory planning. In *Medical Image Computing and Computer-Assisted Intervention - MICCAI 2003*, volume 2878, pages 33–40. Springer Berlin Heidelberg, 2003.

[3] O. Goksel, S.E. Salcudean, et al. 3D simulation of needle-tissue interaction with application to prostate brachytherapy. *Computer Aided Surgery*, 6:279–88, 2006.

[4] R. Alterovitz, A Lim, et al. Steering flexible needles under Markov motion uncertainty. In *IEEE/RSJ International Conference on Intelligent Robots and Systems*, pages 1570–1575, 2005.

[5] Nuttapong Chentanez, Ron Alterovitz, et al. Interactive simulation of surgical needle insertion and steering. In *ACM SIGGRAPH 2009 papers*, pages 1–10. ACM, 2009.

[6] Wooram Park, Jin Seob Kim, et al. Diffusion-based motion planning for a nonholonomic flexible needle model. In *Robotics and Automation, 2005. ICRA 2005. Proceedings of the 2005 IEEE International Conference on*, pages 4600–4605, 18-22 April 2005.

[7] Robert J. Webster, Jin Seob Kim, et al. Nonholonomic modeling of needle steering. *The International Journal of Robotics Research*, 25(5-6):509–525, 2006.

[8] Kaiguo Yan, Wan Sing Ng, et al. Needle steering modeling and analysis using unconstrained modal analysis. In *The First IEEE International Conference on Biomedical Robotics and Biomechatronics*, pages 87–92, 2006.

[9] Orcun Goksel, Ehsan Dehghan, et al. Modeling and simulation of flexible needles. *Medical Engineering & Physics*, 31(9):1069 – 1078, 2009.

[10] S. Misra, K.B. Reed, et al. Mechanics of flexible needles robotically steered through

soft tissue. *Int. J. Rob. Res.*, 29(13):1640–1660, 2010.

[11] R.J. Roesthuis, M. Abayazid, et al. Mechanics-based model for predicting in-plane needle deflection with multiple bends. In *4th IEEE RAS EMBS International Conference on Biomedical Robotics and Biomechatronics*, pages 69–74, 2012.

[12] K.B. Reed, A.M. Okamura, et al. Modeling and control of needles with torsional friction. *EEE Transactions on Biomedical Engineering*, 56(12):2905–2916, Dec 2009.

[13] J.P. Swensen, MingDe Lin, et al. Torsional dynamics of steerable needles: Modeling and fluoroscopic guidance. *IEEE Transactions on Biomedical Engineering*, 61(11):2707–2717, Nov 2014.

[14] Gustaaf J. Vrooijink, Momen Abayazid, et al. Needle path planning and steering in a three-dimensional non-static environment using two-dimensional ultrasound images. *The International Journal of Robotics Research*, 2014.

[15] S. Patil, J. Burgner, et al. Needle steering in 3D via rapid replanning. *IEEE Transactions on Robotics*, 30(4):853–864, Aug 2014.

[16] K.B. Reed, V. Kallem, et al. Integrated planning and image-guided control for planar needle steering. In *2nd IEEE RAS & EMBS International Conference on Biomedical Robotics and Biomechatronics, BioRob.*, pages 819–824, 2008.

[17] M. Heverly, Pierre Dupont, et al. Trajectory optimization for dynamic needle insertion. In *Proceedings of the IEEE International Conference on Robotics and Automation (ICRA)*, pages 1646–1651, 2005.

[18] Mohsen Mahvash and Vincent Hayward. Haptic rendering of cutting, a fracture mechanics approach. *Journal of Haptics Research*, 2, 2001.

[19] Allison M. Okamura, Christina Simone, et al. Force Modeling for Needle Insertion into Soft Tissue. *IEEE Transactions on Biomedical Engineering*, 51:1707–1716, 2004.

[20] S. Misra, K.B. Reed, et al. Needle-tissue interaction forces for bevel-tip steerable needles. In *2nd IEEE RAS & EMBS International Conference on Biomedical Robotics and Biomechatronics(BioRob)*, pages 224–231, 2008.

[21] Jason Z. Moore, Kostyantyn Malukhin, et al. Hollow needle tissue insertion force model. *(CIRP) Annals - Manufacturing Technology*, 60(1):157 – 160, 2011.

[22] M. Mahvash and P.E. Dupont. Mechanics of dynamic needle insertion into a biological

material. *IEEE Transactions on Biomedical Engineering*, 57(4):934–943, 2010.

[23] Andrew C. Barnett, Yuan-Shin Lee, et al. Fracture mechanics model of needle cutting tissue. *Journal of Manufacturing Science and Engineering*, 2015.

[24] B. Maurin, L. Barb, et al. In vivo study of forces during needle insertions. In *Proceedings of Medical Robotics Navigation and Visualisation Scientific Workshop (MRNV 04)*, 2004.

[25] T. Lehmann, C. Rossa, et al. Needle path control during insertion in soft tissue using a force-sensor-based deflection estimator. In *2016 IEEE International Conference on Advanced Intelligent Mechatronics (AIM)*, pages 1174–1179, 2016.

[26] C. Rossa, M. Khadem, et al. Constrained optimal control of needle deflection for semi-manual steering,. In *IEEE International Conference on Advanced Intelligent Mechatronics (AIM), Banff, Canada*, pages 1198–1203, 2016.

[27] Jijie Xu, Vincent Duindam, et al. Planning fireworks trajectories for steerable medical needles to reduce patient trauma. *Proceedings of the ... IEEE/RSJ International Conference on Intelligent Robots and Systems. IEEE/RSJ International Conference on Intelligent Robots and Systems*, 2009:4517–4522, 2009.

[28] D. Glozman and M. Shoham. Image-guided robotic flexible needle steering. *IEEE Transactions on Robotics*, 23:459–467, June 2007.

[29] Vincent Duindam, Jijie Xu, et al. 3d motion planning algorithms for steerable needles using inverse kinematics. *The International journal of robotics research*, 57:535–549, 2009.

[30] K. B. Reed, A. Majewicz, et al. Robot-assisted needle steering. *IEEE Robotics Automation Magazine*, 18(4):35–46, 2011.

[31] V. Kallem and N. J. Cowan. Image guidance of flexible tip-steerable needles. *IEEE Transactions on Robotics*, 25(1):191–196, 2009.

[32] D.S. Minhas, J.A. Engh, et al. Modeling of needle steering via duty-cycled spinning. In *29th Annual International Conference of the IEEE Engineering in Medicine and Biology Society (EMBS)*, pages 2756–2759, Aug 2007.

[33] P. Mignon, P. Poignet, et al. Beveled-tip needle-steering using 3d ultrasound, mechanical-based kalman filter and curvilinear roi prediction. In *2016 14th Inter-*

national Conference on Control, Automation, Robotics and Vision (ICARCV), pages 1–6, 2016.

[34] D.C. Rucker, J. Das, et al. Sliding mode control of steerable needles. *IEEE Transactions on Robotics*, 29(5):1289–1299, Oct 2013.

[35] T.K. Adebar, A.E. Fletcher, et al. 3-D ultrasound-guided robotic needle steering in biological tissue. *IEEE Transactions on Biomedical Engineering*, 61(12):2899–2910, Dec 2014.

[36] A. Maghsoudi and M. Jahed. Needle dynamics modelling and control in prostate brachytherapy. *IET Control Theory Applications*, 6(11):1671–1681, 2012.

[37] Pedro Moreira and Sarthak Misra. Biomechanics-based curvature estimation for ultrasound-guided flexible needle steering in biological tissues. *Annals of Biomedical Engineering*, 43(8):1716–1726, 2015.

[38] Dedong Gao, Yong Lei, et al. Needle steering for robot-assisted insertion into soft tissue: A survey. *Chinese Journal of Mechanical Engineering*, 25(4), 2012.

[39] N.J. van de Berg, D.J. van Gerwen, et al. Design choices in needle steering: A review. *IEEE/ASME Transactions o Mechatronics*, 20(5):2172–2183, Oct. 2015.

[40] T.K. Adebar, J.D. Greer, et al. Methods for improving the curvature of steerable needles in biological tissue. *IEEE Transactions on Biomedical Engineering*, PP(99):1–1, 2015.

[41] T. K. Adebar, J. D. Greer, et al. Towards robotic needle steering for percutaneous radiofrequency ablationin the liver: Procedure-specific workspace analysis. In *The Hamlyn Symposium on Medical Robotics*, pages 67–68, 2015.

[42] Nelson N Stone and Richard G Stock. Prostate brachytherapy in patients with prostate volumes $> 50\ cm^3$: dosimetic analysis of implant quality. *International Journal of Radiation Oncology*Biology*Physics*, 46(5):1199 – 1204, 2000.

[43] L. Potters. Permanent prostate brachytherapy in men with clinically localised prostate cancer. *Clinical Oncology*, 15(6):301 – 315, 2003.

[44] J. A. Engh, G. Podnar, et al. Toward effective needle steering in brain tissue. In *2006 International Conference of the IEEE Engineering in Medicine and Biology Society*, pages 559–562, 2006.

[45] L. Vancamberg, A. Sahbani, et al. Needle path planning for digital breast tomosynthesis biopsy. In *2010 IEEE International Conference on Robotics and Automation*, pages 2062–2067, 2010.

[46] A. Kuntz, P. J. Swaney, et al. Toward Transoral Peripheral Lung Access: Steering Bronchoscope-deployed Needles through Porcine Lung Tissue. In *Hamlyn Symposium on Medical Robotics*, pages 9–10, 2016.

[47] N. A. Wood, K. Shahrour, et al. Needle steering system using duty-cycled rotation for percutaneous kidney access. In *2010 Annual International Conference of the IEEE Engineering in Medicine and Biology*, pages 5432–5435, 2010.

[48] Van Khuyen Bui, Sukho Park, et al. A novel curvature-controllable steerable needle for percutaneous intervention. *Proceedings of the Institution of Mechanical Engineers, Part H: Journal of Engineering in Medicine*, 2016.

[49] S. Okazawa, R. Ebrahimi, et al. Hand-held steerable needle device. *IEEE/ASME Transactions on Mechatronics*, 10(3):285–296, June 2005.

[50] R.J. Webster, J.M. Romano, et al. Mechanics of precurved-tube continuum robots. *IEEE Transactions on Robotics*, 25(1):67–78, Feb 2009.

[51] P. Sears and Pierre Dupont. A steerable needle technology using curved concentric tubes. In *IEEE/RSJ International Conference on Intelligent Robots and Systems*, pages 2850–2856, Oct 2006.

[52] H.B. Gilbert, J. Neimat, et al. Concentric tube robots as steerable needles: Achieving follow-the-leader deployment. *IEEE Transactions on Robotics*, 31(2):246–258, April 2015.

[53] T.R. Wedlick and A.M. Okamura. Characterization of pre-curved needles for steering in tissue. In *Annual International Conference of the IEEE Engineering in Medicine and Biology Society*, pages 1200–1203, Sept 2009.

[54] Kirsten R. Henken, Peter R. Seevinck, et al. Manually controlled steerable needle for MRI-guided percutaneous interventions. *Medical & Biological Engineering & Computing*, pages 1–10, 2016.

[55] P.J. Swaney, J. Burgner, et al. A flexure-based steerable needle: High curvature with reduced tissue damage. *IEEE Transactions on Biomedical Engineering*, 60(4):906–

909, April 2013.

[56] Nick J. van de Berg, Jenny Dankelman, et al. Design of an actively controlled steerable needle with tendon actuation and FBG-based shape sensing. *Medical Engineering & Physics*, 37(6):617 – 622, 2015.

[57] P. Hagedorn and A. DasGupta. *Vibrations and Waves in Continuous Mechanical Systems*. Wiley, 2007.

[58] L. Meirovitch. Derivation of equations for flexible multibody systems in terms of quasi-coordinates from the extended Hamilton's principle. *Shock and Vibration*, 1(2):107–119, 1993.

[59] BG Galerkin. Series solution of some problems of elastic equilibrium of rods and plates. *Wjestnik Ingenerow Petrograd*, pages 897–908, 1915.

[60] G. Genta. *Vibration Dynamics and Control*. Springer, 2009.

[61] T.L. Anderson. *Fracture Mechanics: Fundamentals and Applications, Third Edition*. Taylor & Francis, 2005.

[62] T.K. Podder, D.P. Clark, et al. Effects of velocity modulation during surgical needle insertion. In *Engineering in Medicine and Biology Society, 2005. IEEE-EMBS 2005. 27th Annual International Conference of the*, pages 5766–5770, 2005.

[63] S. Li and A.L. Oldenburg. Measuring soft tissue elasticity by monitoring surface acoustic waves using image plane digital holography. In *Society of Photo-Optical Instrumentation Engineers (SPIE) Conference Series*, volume 2, page 7965, March 2011.

[64] Chunyuan Zhang. *Viscoelastic fracture mechanics*. Science Press Beijing, 2006.

[65] R.A. Schapery. Correspondence principles and a generalized J integral for large deformation and fracture analysis of viscoelastic media. *International Journal of Fracture*, 25(3):195–223, 1984.

[66] D.S. Dugdale. Yielding of steel sheets containing slits. *Journal of the Mechanics and Physics of Solids*, 8(2):100–104, 1960.

[67] J. W. Hutchinson and P. C. Paris. Stability analysis of j controlled crack growth. In *ASTM STP 668, American Society for Testing and Materials*, pages 37–64, 1979.

[68] C.C. De Wit, H. Olsson, et al. A new model for control of systems with friction.

IEEE Transactions on Automatic Control, 40(3):419–425, 1995.

[69] Ali Asadian, RajniV. Patel, et al. Dynamics of translational friction in needle tissue interaction during needle insertion. *Annals of Biomedical Engineering*, 42(1):73–85, 2014.

[70] T. Piatkowski. Dahl and lugre dynamic friction models the analysis of selected properties. *Mechanism and Machine Theory*, 73(0):91 – 100, 2014.

[71] K. Youcef-Toumi and Osamu Ito. A time delay controller for systems with unknown dynamics. In *American Control Conference, 1988*, pages 904–913, 15-17 June 1988.

[72] Alexander Leibinger, Antonio E. Forte, et al. Soft tissue phantoms for realistic needle insertion: A comparative study. *Annals of Biomedical Engineering*, 44(8):2442–2452, 2016.

[73] M.R. Kermani, R.V. Patel, et al. Friction identification and compensation in robotic manipulators. *IEEE Transactions on Instrumentation and Measurement*, 56(6):2346–2353, 2007.

[74] M. Waine, C. Rossa, et al. 3D needle shape estimation in TRUS-Guided prostate brachytherapy using 2D ultrasound images. *IEEE Journal of Biomedical and Health Informatics*, PP(99):1–1, 2015.

[75] Zhouping Wei, L. Gardi, et al. Oblique needle segmentation for 3D trus-guided robot-aided transperineal prostate brachytherapy. In *IEEE International Symposium on Biomedical Imaging: Nano to Macro*, pages 960–963, April 2004.

[76] Paul M Novotny, Jeff A Stoll, et al. GPU based real-time instrument tracking with three dimensional ultrasound. *Medical image analysis*, 11(5):458–464, 2007.

[77] H.R.S. Neshat and R.V. Patel. Real-time parametric curved needle segmentation in 3D ultrasound images. In *2nd IEEE RAS EMBS International Conference on Biomedical Robotics and Biomechatronics (BioRob)*, pages 670–675, Oct 2008.

[78] Mingyue Ding, Zhouping Wei, et al. Needle and seed segmentation in intra-operative 3D ultrasound-guided prostate brachytherapy. *Ultrasonics*, 44:331 – 336, 2006. Proceedings of Ultrasonics International and World Congress on Ultrasonics (WCU).

[79] M. Uhercik, J. Kybic, et al. Model fitting using ransac for surgical tool localization in 3-d ultrasound images. *Biomedical Engineering, IEEE Transactions on*, 57(8):1907–

1916, 2010.

[80] Stephen H. Okazawa, Richelle Ebrahimi, et al. Methods for segmenting curved needles in ultrasound images. *Medical Image Analysis*, 10:330–342, 2006.

[81] M. Kaya and O. Bebek. Needle localization using gabor filtering in 2d ultrasound images. In *IEEE International Conference on Robotics and Automation (ICRA)*, pages 4881–4886, 2014.

[82] Jay Carriere, Carlos Rossa, et al. Needle shape estimation in soft tissue based on partial ultrasound image observation. In *IEEE International Conference on Robotics and Automation (ICRA)*, pages 2277–2282, May 2015.

[83] Momen Abayazid, GustaafJ. Vrooijink, et al. Experimental evaluation of ultrasound-guided 3d needle steering in biological tissue. *International Journal of Computer Assisted Radiology and Surgery*, 9(6):931–939, 2014.

[84] M. Waine, C. Rossa, et al. 3D shape visualization of curved needles in tissue from 2d ultrasound images using RANSAC. In *IEEE International Conference on Robotics and Automation (ICRA)*, 2015.

[85] StephenM. Smith and J.Michael Brady. SUSAN–a new approach to low level image processing. *International Journal of Computer Vision*, 23(1):45–78, 1997.

[86] S. Joe Qin and Thomas A. Badgwell. A survey of industrial model predictive control technology. *Control Engineering Practice*, 11(7):733–764, 2003.

[87] L. Grne and J. Pannek. *Nonlinear Model Predictive Control*. Springer London, 2011.

[88] Ihor O Bohachevsky, Mark E Johnson, et al. Generalized simulated annealing for function optimization. *Technometrics*, 28(3):209–217, August 1986.

[89] V. Cerny. Thermodynamical approach to the traveling salesman problem: An efficient simulation algorithm. *Journal of Optimization Theory and Applications*, 45(1):41–51, 1985.

[90] W.F. Carriker, P.K. Khosla, et al. Path planning for mobile manipulators for multiple task execution. *IEEE Transactions on Robotics and Automation*, 7(3):403–408, Jun 1991.

[91] P. Caricato and A. Grieco. Using simulated annealing to design a material-handling system. *IEEE Intelligent Systems*, 20(4):26–30, July 2005.

[92] Richard Taschereau, Jean Pouliot, et al. Seed misplacement and stabilizing needles in transperineal permanent prostate implants. *Radiotherapy and Oncology*, 55(1):59 – 63, 2000.

[93] Philip Blumenfeld, Nobuhiko Hata, et al. Transperineal prostate biopsy under magnetic resonance image guidance: A needle placement accuracy study. *Journal of Magnetic Resonance Imaging*, 26(3):688–694, 2007.

[94] S. Misra, K.B. Reed, et al. Needle-tissue interaction forces for bevel-tip steerable needles. In *Biomedical Robotics and Biomechatronics, 2008. BioRob 2008. 2nd IEEE RAS EMBS International Conference on*, pages 224–231, 2008.

[95] Liao Shijun. Homotopy analysis method: A new analytic method for nonlinear problems. *Applied Mathematics and Mechanics*, 19(10):957–962, 1998.

[96] Shijun Liao. *Homotopy Analysis Method in Nonlinear Differential Equations*. Springer Berlin Heidelberg, 2012.

[97] Michael Waine, Carlos Rossa, et al. Needle tracking and deflection prediction for robot-assisted needle insertion using 2d ultrasound images. *Journal of Medical Robotics Research*, 01(01):1640001, 2016.

[98] Daniel Delling, Peter Sanders, et al. *Algorithmics of Large and Complex Networks: Design, Analysis, and Simulation*, chapter Engineering Route Planning Algorithms, pages 117–139. Springer Berlin Heidelberg, 2009.

[99] Muhammad F. Jamaluddin, Sunita Ghosh, et al. Quantifying iodine-125 placement accuracy in prostate brachytherapy using post-implant transrectal ultrasound images. *Brachytherapy*, 15:S180, 2016.

[100] O.C. Zienkiewicz, R.L. Taylor, et al. *The Finite Element Method for Solid and Structural Mechanics*. Butterworth-Heinemann, Oxford, seventh edition edition, 2014.

[101] R. Eberhart and J. Kennedy. A new optimizer using particle swarm theory. In *Proceedings of the Sixth International Symposium on Micro Machine and Human Science, 1995*, pages 39–43, 1995.

[102] R. E. Perez and K. Behdinan. Particle swarm approach for structural design optimization. *Computers and Structures*, 85(19-20):1579–1588, 2007.

[103] Gerhard Venter and Jaroslaw Sobieszczanski-Sobieski. Particle swarm optimization.

AIAA Journal, 41(8):1583–1589, 2003.

[104] Souma Chowdhury, Weiyang Tong, et al. A mixed-discrete particle swarm optimization algorithm with explicit diversity-preservation. *Structural and Multidisciplinary Optimization*, 47(3):367–388, 2013.

[105] Steven M. LaValle and James J. Kuffner. Randomized kinodynamic planning. *The International Journal of Robotics Research*, 20(5):378–400, 2001.

[106] Junichi Fukada, Naoyuki Shigematsu, et al. Predicting pubic arch interference in prostate brachytherapy on transrectal ultrasonography-computed tomography fusion images. *Journal of Radiation Research*, 53(5):753–759, 2012.

[107] Shi-Jun Zhang, Hai-Ning Qian, et al. Relationship between age and prostate size. *Asian Journal of Andrology*, 15(1):116–120, 2012.

[108] W.Lyle McClung, S.Christopher Daniel, et al. Enhancing needle durability by silicone coating of surgical needles. *The Journal of Emergency Medicine*, 13(4):515 – 518, 1995.

[109] R. W. Brockett. Asymptotic stability and feedback stabilization. In *Differential Geometric Control Theory*, pages 181–191. Birkhauser, 1983.

[110] Anthony M. Bloch. *Control of Mechanical and Nonholonomic Systems*, pages 315–365. Springer New York, New York, NY, 2015.

[111] A. M. Bloch, M. Reyhanoglu, et al. Control and stabilization of nonholonomic dynamic systems. *IEEE Transactions on Automatic Control*, 37(11):1746–1757, 1992.

[112] Daniel Liberzon. *Systems Not Stabilizable by Continuous Feedback*, pages 77–91. Birkhäuser Boston, Boston, MA, 2003.

[113] L.G. Bushnell, D.M. Tilbury, et al. Steering three-input nonholonomic systems: The fire truck example. *The International Journal of Robotics Research*, 14(4):366–381, 1995.

[114] V. Cichella, I. Kaminer, et al. Cooperative path following of multiple multirotors over time-varying networks. *IEEE Transactions on Automation Science and Engineering*, 12(3):945–957, July 2015.

[115] A. M. Bloch. *Nonholonomic Mechanics*, pages 207–276. Springer New York, 2003.

[116] Jerrold E. Marsden and Jim Ostrowski. Symmetries in motion: Geometric foun-

dations of motion control. In *Motion, Control, and Geometry: Proceedings of a Symposium*, pages 3–19, 1998.

[117] Michael Berry. Anticipations of the geometric phase. *Physics Today*, 43(12):34–40, 1990.

[118] T. Lehmann, C. Rossa, et al. A real-time estimator for needle deflection during insertion into soft tissue based on adaptive modeling of needle-tissue interactions. *IEEE/ASME Transactions on Mechatronics*, 21(6):2601–2612, 2016.

[119] Thomas Lehmann, Mahdi Tavakoli, et al. Force-sensor-based estimation of needle tip deflection in brachytherapy. *Journal of Sensors*, 2013:10, 2013.

[120] C. Rossa, N. Usmani, et al. A hand-held assistant for semi-automated percutaneous needle steering. *IEEE Transactions on Biomedical Engineering*, PP(99):1–1, 2016.

[121] L. Meirovitch. *Methods of Analytical Dynamics*. Dover Publications, 2010.

Appendices

A Experimental Needle Steering Setup

In order to perform fully robotic needle insertion into soft tissue, the setup shown in Fig. A.1 is used. The setup consists of a robotic system with two DoFs, namely the translational and rotational motions of needle [119]. Forces and torques are measured at the needle base using a 6-DOF force/torque sensor (ATI Nano 43, ATI Industrial Automation, USA). Images for needle tip and shape tracking inside transparent phantom tissues are recorded using an HD Sony camera (XCL-S800, Sony of Canada Ltd., Canada) and an Ultrasound machine (SonixTouch, Ultrasonix, Canada) is used to track needle tip position in ex-vivo tissue. The ultrasound probe is automatically moved to follow the needle tip and provide images of the needle tip cross section.

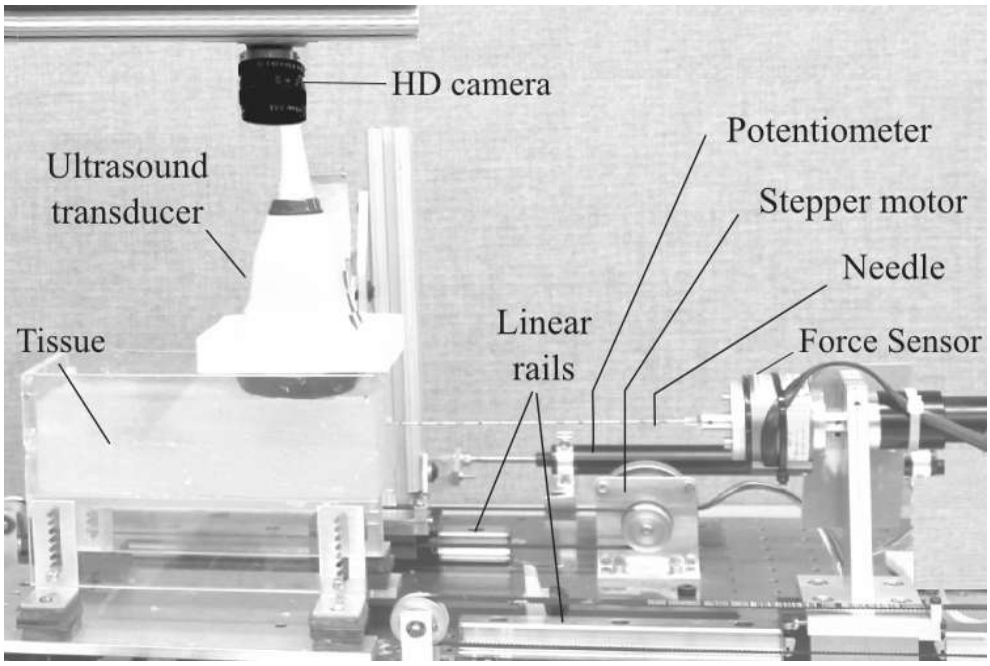

Figure A.1: Experimental setup used to perform needle insertion experiments.

In order to perform semi-automated surgeon-in-the-loop needle insertion into soft tissue, the setup shown in Fig. A.2 is used [120]. During the insertions, the ultrasound probe follows the needle tip and acquires transverse images of the needle tip in ex-vivo tissue. As the surgeon pushes the device and the needle, the device automatically rotates the needle axially at appropriate positions in order to reach a desired target. The surgeon can also control needle rotation manually using the control console. The probe of the ultrasound machine (SonixTouch, Ultrasonix, BC, Canada) is automatically moved to follow surgeon's hand and provide images of the needle tip.

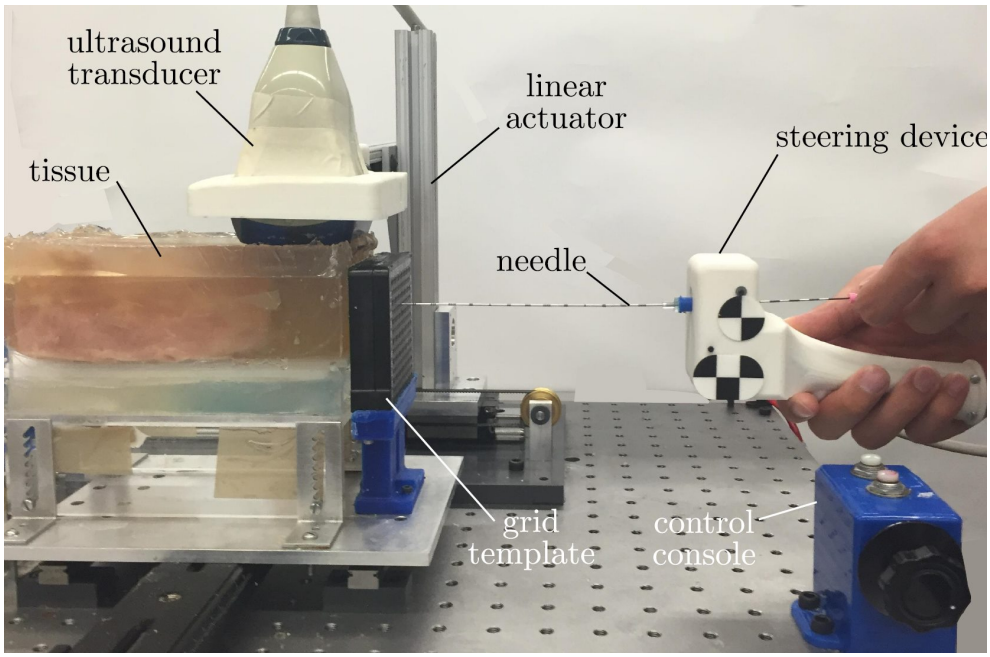

Figure A.2: The handheld needle steering assistant for semi-automated needle insertion .

B Hamilton's Principle For Needle Deflection In Terms of Psudeo-coordinates

Since in our modelling approach all the forces and moments applied to the system are written with reference to the body-fixed frame, the Hamilton's principle is best written with reference to the same frame. The extended Hamilton's principle with respect to the generalized coordinates is given by

$$\begin{aligned}\int_{t_1}^{t_2} \Big[& \delta \boldsymbol{R}^T \frac{\partial \mathcal{L}}{\partial \boldsymbol{R}} + \delta \boldsymbol{V}^T \frac{\partial \mathcal{L}}{\partial \boldsymbol{V}} + \delta \boldsymbol{\theta}^T \frac{\partial \mathcal{L}}{\partial \boldsymbol{\theta}} + \delta \dot{\boldsymbol{\theta}}^T \frac{\partial \mathcal{L}}{\partial \dot{\boldsymbol{\theta}}} \\ & + \int_0^{\ell} (\delta \boldsymbol{u}^T \frac{\partial \hat{\mathcal{L}}}{\partial \boldsymbol{u}} + \delta \dot{\boldsymbol{u}}^T \frac{\partial \hat{\mathcal{L}}}{\partial \dot{\boldsymbol{u}}} + \delta \boldsymbol{u}'^T \frac{\partial \hat{\mathcal{L}}}{\partial \boldsymbol{u}'} + \delta \boldsymbol{u}''^T \frac{\partial \hat{\mathcal{L}}}{\partial \boldsymbol{u}''}) dx \\ & + \overline{\delta \mathcal{W}} \Big] \, dt = 0 \end{aligned} \tag{B.1}$$

where $\overline{\delta \mathcal{W}}$ is the virtual work of non-conservative forces given by

$$\overline{\delta \mathcal{W}} = \delta \boldsymbol{R}^T \boldsymbol{Q}_R + \delta \boldsymbol{\theta}^T \boldsymbol{Q}_\theta + \delta \boldsymbol{u}^T \boldsymbol{Q}_u \tag{B.2}$$

where $\boldsymbol{Q}_R$, $\boldsymbol{Q}_\theta$, and $\boldsymbol{Q}_u$ are generalized forces working in direction of generalized coordinates. also $\hat{\mathcal{L}}$ in (B.1) is the Lagrangian density of the flexible body and we have

$$\mathcal{L} = \int_0^{\ell} \hat{\mathcal{L}} \, dx \tag{B.3}$$

Before proceeding any further, we note that $\boldsymbol{R}$ is in terms of inertial components X and Y, and $\boldsymbol{\theta}$ is vector of Eulerian-type angles. $\dot{\boldsymbol{\theta}}$ is the angular velocity of carrier in body-fixed frame, as the result of planar rotation of the carrier it is direct derivative of $\boldsymbol{\theta}$. However $\boldsymbol{V}$ is the pseudo-velocity vector and it can be related to derivatives of general coordinates by $\boldsymbol{V} = \mathbf{C}\dot{\boldsymbol{R}}$. Thus we can write variations of the quasi-velocity vector as

$$\delta \boldsymbol{V} = \delta \mathbf{C} \dot{\boldsymbol{R}} + \mathbf{C} \delta \dot{\boldsymbol{R}} \tag{B.4}$$

From basic dynamics we know that ([121])

$$\dot{\mathbf{C}} = \tilde{\dot{\boldsymbol{\theta}}}^T \mathbf{C} \tag{B.5}$$

Similarly we can write $\delta \mathbf{C}$ in variational form $\delta \mathbf{C} = \delta \tilde{\boldsymbol{\theta}}^T \mathbf{C}$. Now (B.4) can be rewritten as

$$\delta \boldsymbol{V} = \delta \tilde{\boldsymbol{\theta}}^T \mathbf{C} \dot{\boldsymbol{R}} + \mathbf{C} \delta \dot{\boldsymbol{R}} = \tilde{\boldsymbol{V}} \delta \boldsymbol{\theta} + \mathbf{C} \delta \dot{\boldsymbol{R}} \tag{B.6}$$

At this point we can proceed with the extended Hamilton's principle. We start by simplifying the terms in (B.1). Using (B.6) and (B.5) and by performing integration by parts we have

$$\begin{aligned}
&\int_{t_1}^{t_2} \delta \boldsymbol{V}^T \frac{\partial \mathcal{L}}{\partial \boldsymbol{V}} dt \\
&= \int_{t_1}^{t_2} (-\delta \boldsymbol{\theta}^T \tilde{\boldsymbol{V}} + \delta \dot{\boldsymbol{R}} \mathbf{C}^T) \frac{\partial \mathcal{L}}{\partial \boldsymbol{V}} dt \\
&= -\int_{t_1}^{t_2} \delta \boldsymbol{\theta}^T \tilde{\boldsymbol{V}} \frac{\partial \mathcal{L}}{\partial \boldsymbol{V}} dt + \delta \boldsymbol{R}^T \mathbf{C} \frac{\partial \mathcal{L}}{\partial \boldsymbol{V}} \Big|_{t_1}^{t_2} \\
&\quad - \int_{t_1}^{t_2} \delta \boldsymbol{R}^T \left[\dot{\mathbf{C}}^T \frac{\partial \mathcal{L}}{\partial \boldsymbol{V}} + \mathbf{C}^T \frac{d}{dt} (\frac{\partial \mathcal{L}}{\partial \boldsymbol{V}}) \right] dt \\
&= -\int_{t_1}^{t_2} \delta \boldsymbol{\theta}^T \tilde{\boldsymbol{V}} \frac{\partial \mathcal{L}}{\partial \boldsymbol{V}} dt - \int_{t_1}^{t_2} \delta \boldsymbol{R}^T \mathbf{C}^T \left[\tilde{\dot{\boldsymbol{\theta}}} \frac{\partial \mathcal{L}}{\partial \boldsymbol{V}} + \frac{d}{dt} (\frac{\partial \mathcal{L}}{\partial \boldsymbol{V}}) \right] dt
\end{aligned} \tag{B.7}$$

Note that $\delta(.)$ operator does not vary time, therefore $\delta \boldsymbol{R}^T \mathbf{C} \frac{\partial \mathcal{L}}{\partial \boldsymbol{V}} \Big|_{t_1}^{t_2}$ vanishes in (B.7). Following the same approach we can write

$$\begin{aligned}
&\int_{t_1}^{t_2} \int_o^l \delta \boldsymbol{u}''^T \frac{\partial \hat{\mathcal{L}}}{\partial \boldsymbol{u}''} dx dt \\
&= \int_{t_1}^{t_2} \left[\delta \boldsymbol{u}'^T \frac{\partial \hat{\mathcal{L}}}{\partial \boldsymbol{u}''} - \delta \boldsymbol{u}^T \frac{d^2}{dx^2} \frac{\partial \hat{\mathcal{L}}}{\partial \boldsymbol{u}''} \right] \Big|_0^\ell dt \\
&\quad + \int_{t_1}^{t_2} \int_o^l \delta \boldsymbol{u}^T \frac{d^2}{dx^2} (\frac{\partial \hat{\mathcal{L}}}{\partial \boldsymbol{u}''}) dx dt
\end{aligned} \tag{B.8}$$

$$\begin{aligned}
&\int_{t_1}^{t_2} \int_o^l \delta \boldsymbol{u}'^T \frac{\partial \hat{\mathcal{L}}}{\partial \boldsymbol{u}'} dx dt \\
&= \int_{t_1}^{t_2} (\delta \boldsymbol{u}^T \frac{\partial \hat{\mathcal{L}}}{\partial \boldsymbol{u}'} \Big|_0^\ell) dt - \int_{t_1}^{t_2} \int_o^l \delta \boldsymbol{u}^T \frac{\partial}{\partial x} (\frac{\partial \hat{\mathcal{L}}}{\partial \boldsymbol{u}'}) dx dt
\end{aligned} \tag{B.9}$$

$$\begin{aligned}
&\int_{t_1}^{t_2} \int_o^l \delta \dot{\boldsymbol{u}}^T \frac{\partial \hat{\mathcal{L}}}{\partial \dot{\boldsymbol{u}}} dx dt \\
&= -\int_{t_1}^{t_2} \int_0^\ell \delta \boldsymbol{u}^T \frac{d}{dt} (\frac{\partial \hat{\mathcal{L}}}{\partial \dot{\boldsymbol{u}}}) dt dx
\end{aligned} \tag{B.10}$$

$$\begin{aligned}
&\int_{t_1}^{t_2} \delta \dot{\boldsymbol{\theta}}^T \frac{\partial \mathcal{L}}{\partial \dot{\boldsymbol{\theta}}} dt \\
&= -\int_{t_1}^{t_2} \delta \boldsymbol{\theta}^T \frac{d}{dt} (\frac{\partial \mathcal{L}}{\partial \dot{\boldsymbol{\theta}}}) dt
\end{aligned} \tag{B.11}$$

Inserting (B.7), (B.8), (B.9), (B.10), and (B.11) in (B.1) we can rewrite the Hamilton's Principle as

$$
\begin{aligned}
&\int_{t_1}^{t_2} \left[\delta \boldsymbol{u}'^T \frac{\partial \hat{\mathcal{L}}}{\partial \boldsymbol{u}''} + \delta \boldsymbol{u}^T \left(\frac{\partial \hat{\mathcal{L}}}{\partial \boldsymbol{u}'} - \frac{d}{dx}\left(\frac{\partial \hat{\mathcal{L}}}{\partial \boldsymbol{u}''}\right) \right) \right] \Bigg|_0^{\ell} dt \\
&+ \int_{t_1}^{t_2} \left[\int_o^l \delta \boldsymbol{u}^T \left(\frac{\partial \hat{\mathcal{L}}}{\partial \boldsymbol{u}} - \frac{d}{dt}\left(\frac{\partial \hat{\mathcal{L}}}{\partial \dot{\boldsymbol{u}}}\right) - \frac{d}{dx}\left(\frac{\partial \hat{\mathcal{L}}}{\partial \boldsymbol{u}'}\right) \right. \right. \\
&\left. \left. + \frac{d^2}{dx^2}\left(\frac{\partial \hat{\mathcal{L}}}{\partial \boldsymbol{u}''}\right) \right) dx + \delta \boldsymbol{u}^T \boldsymbol{Q}_u \right] dt \\
&+ \int_{t_1}^{t_2} \delta \boldsymbol{R}^T \left[\mathbf{C}^T \left(-\frac{d}{dt}\left(\frac{\partial \mathcal{L}}{\partial \boldsymbol{V}}\right) - \tilde{\dot{\boldsymbol{\theta}}} \frac{\partial \mathcal{L}}{\partial \boldsymbol{V}} \right) + \frac{\partial \mathcal{L}}{\partial \boldsymbol{R}} + \boldsymbol{Q}_R \right] dt \\
&+ \int_{t_1}^{t_2} \delta \boldsymbol{\theta}^T \left[-\frac{d}{dt}\left(\frac{\partial \mathcal{L}}{\partial \dot{\boldsymbol{\theta}}}\right) - \tilde{\boldsymbol{V}} \frac{\partial \mathcal{L}}{\partial \boldsymbol{V}} + \frac{\partial \mathcal{L}}{\partial \boldsymbol{\theta}} + \boldsymbol{Q}_\theta \right] dt = 0
\end{aligned}
\tag{B.12}
$$

(B.12) gives the extended Hamilton's principle in terms of the pseudo-velocity $\boldsymbol{V}$. Following fundamental lemma of the calculus of variations and setting all the integrals in (B.12) equal to zero, one can obtain the equations of motion in pseudo-coordinates.

C Deriving Continuous Equation of Motion of Flexible Needle

In this section we will derive the equation of motion for the continuous part of the needle-carrier system. Rewriting the last two integrals in (3.11) in terms of coordinates of flexible needle u and ω gives

$$\begin{aligned}
&\int_{t_1}^{t_2}\int_{o}^{\ell}(-EI\omega'''' - \rho A\ddot{\omega} + f_{cy} + f_s + f_k + f_{fy})\delta\omega \; dxdt \\
&+\int_{t_1}^{t_2}\int_{o}^{\ell}(f_{cx} + f_{fx})\delta u \; dxdt \\
&+\int_{t_1}^{t_2} EI(\omega''\delta\omega' - \omega'''\delta\omega)\Big|_0^{\ell} dt = 0
\end{aligned} \tag{C.1}$$

From the kinematic model, we know that the needle has two translational and one rotational DoF. Previously we used (3.4) to eliminate the redundant rotational DoF, ψ, in the process of deriving the Lagrangian. We can do the same for the axial needle displacement u which can be related to the transverse translational DoF of the flexible needle ω, using kinematic constraint in (k56). Using (3.4), inserting derived equations for cutting force and friction from (3.9) we obtain

$$\begin{aligned}
&\int_{t_1}^{t_2}\int_{o}^{\ell}\Big[-EI\omega''''-\rho A\ddot{\omega}+F_f\omega' H_{l-X}(x) \\
&+\Big(F_{c\eta}-F_{c\xi}\omega'(l,t)\Big)\delta_\ell(x)+f_s+f_k\Big]\delta\omega \; dxdt \\
&-\int_{t_1}^{t_2}\int_{o}^{\ell}\Big[F_{c\xi}+F_{c\eta}\omega'(l,t)+\Big(\int_{x}^{\ell}F_f H_{l-X}(\zeta)d\zeta\Big)\Big]\omega'\delta\omega' \; dxdt \\
&+\int_{t_1}^{t_2} EI(\omega''\delta\omega'-\omega'''\delta\omega)\Big|_0^{\ell} dt=0
\end{aligned} \tag{C.2}$$

Now we first simplify the second integral by taking integration by part, then add and

subtract $\int_{t_1}^{t_2}\int_o^{\ell} F_{c\eta}\omega'^2\delta_\ell(x)dxdt$ to (C.2) to obtain

$$\begin{aligned}
&\int_{t_1}^{t_2}\int_o^{\ell}\Big[-EI\omega'''' - \rho A\ddot{\omega} + Q + F_f\omega' H_{l-X}(x) \\
&- F_{c\xi}\omega'(l,t)\delta_\ell(x)\Big]\delta\omega\ dxdt + \int_{t_1}^{t_2}\int_o^{\ell}\Big[F_{c\eta}\omega'^2\delta_\ell(x)\Big]dxdt \\
&- \int_{t_1}^{t_2}\int_o^{\ell}\Big[P\omega'' - (F_f H_{l-X})\omega'\Big]\delta\omega\ dxdt \\
&- \int_{t_1}^{t_2}\Big[F_{c\xi} + F_{c\eta}\omega'(l,t) + (\int_x^{\ell} F_f H_{l-X}(\zeta)d\zeta)\Big]\omega'\Big|_0^{\ell} dt \\
&+ \int_{t_1}^{t_2} EI(\omega''\delta\omega' - \omega'''\delta\omega)\Big|_0^{\ell} dt = 0
\end{aligned} \tag{C.3}$$

with

$$Q = f_s + f_k + F_{c\eta}\delta_\ell(x) - F_{c\eta}\omega'^2\delta_\ell(x) \tag{C.4a}$$

$$P = F_{c\xi} + F_{c\eta}\omega'(l,t) + ((\ell - x)F_f)\, H_{\ell-X} \tag{C.4b}$$

Simplifying and sorting out (C.3) gives

$$\begin{aligned}
&\int_{t_1}^{t_2}\int_o^{\ell}(-EI\omega'''' - \rho A\ddot{\omega} - P\omega'' + Q)\,\delta\omega\ dxdt \\
&- \int_{t_1}^{t_2}\Big\{F_{c\xi}\omega'(l,t)\delta\omega(\ell) - F_{c\eta}\omega'^2(\ell) \\
&+ \Big[F_{c\xi} + F_{c\eta}\omega'(l,t) + \Big(\int_x^{\ell} F_f H_{l-X}(\zeta)d\zeta\Big)\Big]\omega'\Big|_0^{\ell} \\
&+\ EI(\omega''\delta\omega' - \omega'''\delta\omega)\Big|_0^{\ell}\Big\}dt = 0
\end{aligned} \tag{C.5}$$

Following variations formulation and setting the first integral in (C.5) equal to zero, we can obtain the equations of motion for the needle

$$EI\omega'''' + \rho A\ddot{\omega} + P\omega'' = Q \tag{C.6}$$

Also setting the second integral equal to zero, results in the following boundary values

which are required for solving the partial differential equation in (C.5).

$$
\begin{aligned}
-\int_{t_1}^{t_2} \Bigg\{ & F_{c\xi}\omega'(l,t)\delta\omega(\ell) - F_{c\eta}\omega'^2(\ell) \\
& + \left[F_{c\xi} + F_{c\eta}\omega'(l,t) + \left(\int_x^{\ell} F_f H_{l-X}(\zeta) d\zeta \right) \right] \omega' \Bigg|_0^{\ell} \\
& + EI(\omega''\delta\omega' - \omega'''\delta\omega) \Bigg|_0^{\ell} \Bigg\} dt = 0
\end{aligned}
\tag{C.7}
$$

We intend to avoid complications involved in solving a PDE with non-homogeneous boundary conditions. To do so we simplify (C.7) by expanding some of the its terms as follows

$$
\begin{aligned}
-\int_{t_1}^{t_2} \Bigg[& -F_{c\xi}\omega'(0,t)\delta\omega(0,t) - F_{c\eta}\omega'(\ell)\omega'(0,t) \\
& + \left(\int_0^{\ell} F_f H_{l-X}(\zeta) d\zeta \right) \omega'(0,t) \\
& + EI(\omega''\delta\omega' - \omega'''\delta\omega) \Bigg|_0^{\ell} \Bigg] dt = 0
\end{aligned}
\tag{C.8}
$$

The needle is clamped to the carrier, which implies the following geometric boundary conditions at one end

$$\omega(0,t) = \omega'(0,t) = 0 \tag{C.9}$$

Now to eliminate all boundary terms we choose the two following dynamic boundary conditions at the other end of the needle

$$\omega''(\ell,t) = \omega'''(\ell,t) = 0 \tag{C.10}$$

Given boundary conditions satisfy (C.8). (C.9) suggests that the clamped side of the needle has no deflection and has a slope of zero. Also (C.10) states that the tip of the needle is assumed to experience no shear force or bending moment. Note that in the process of deriving the equations, appropriate forcing terms are added as part of the external forces Q and P to eliminate shear force and achieve homogeneous boundary conditions.